

CP violating effects
in B -meson decays with multimuon final states
– simulation study in the CMS detector

Marcin Konecki

*Thesis submitted to the Warsaw University
in partial fulfilment of the requirements
for the Ph.D. degree in Physics,
performed under supervision of Professor Jan Królikowski*



Warszawa 1997

Abstract

This thesis describe the CMS potential to observe the *gold plated*, CP violating decay $B_d \rightarrow J/\psi K_S \rightarrow \mu^+ \mu^- \pi^+ \pi^- \oplus \mu^{tag}$ and decay modes similar to that, involving J/ψ and 3 muons in the final state. The results are obtained with PYTHIA Monte-Carlo (release 5.7) with both gluon splitting and gluon fusion $b\bar{b}$ production processes simulated explicitly. The thesis are organised in chapters. At first the introduction to the CMS detector is given. Then, experimental aspects of CP violation are highlighted. In the main Chapter 3, expected number of events, signal to background ratio for CP violating channels as well as for some control channels are presented. The opportunity to measure dilution factor is investigated. Finally, the errors on both time integrated and time dependent asymmetries are presented for $B_d \rightarrow J/\psi K_S \oplus \mu^{tag}$ and $B_s \rightarrow J/\psi \phi \oplus \mu^{tag}$ channels. In the appendices, the CP violation phenomena is presented in the framework of electroweak Standard Model and the comparison of PYTHIA predictions with available data from CMS-like experiments is given.

Contents

Introduction	7
1 The CMS detector at LHC	11
1.1 The Large Hadron Collider	11
1.1.1 Motivations and Physics Goals	11
1.1.2 The machine	14
1.2 The Compact Muon Solenoid - a detector overview	17
1.2.1 The magnet	20
1.2.2 The Central Tracking System	20
1.2.2.a Track reconstruction	23
1.2.2.b Vertex reconstruction	24
1.2.2.c Efficiency of K_S reconstruction	25
1.2.3 Calorimetry	26
1.2.4 Muon system	27
1.2.4.a Muon trigger	29
1.2.5 Global Trigger and Data Acquisition	30
2 Review of the CP violation from the experimental point of view	33
2.1 CP violating asymmetries	33
2.2 Unequal $B - \bar{B}$ production	34
2.3 Dilution due to tagging	35
2.4 Influence of background	36
2.5 Need for control channels	37
2.6 The investigated channels	37
2.6.1 The $B_d \rightarrow J/\psi K_S \oplus \mu$ channel	38
2.6.2 The $B^\pm \rightarrow J/\psi K^\pm \oplus \mu$ and $B_d \rightarrow J/\psi K^* \oplus \mu$ channels	38
2.6.3 The $B_s \rightarrow J/\psi \phi \oplus \mu$ channel	39
3 The simulation	41
3.1 Description of the simulation	41
3.1.1 Generation of $b\bar{b}$ sample	41
3.1.2 Decay into investigated channel	42
3.1.3 Analysis	45
3.2 The results in the time integrated study	51
3.2.1 Expected number of signal events in the simulated channels	51
3.2.2 The expected levels of background	52
3.2.3 Dilution factor due to tagging	54

3.2.4	The predicted error on intrinsic asymmetries	56
3.3	Time dependent analysis	82
3.3.1	The predicted error on intrinsic asymmetries - perfect secondary vertex resolution	82
3.3.1.a	The $B_d \rightarrow J/\psi K_S \oplus \mu$ channel	82
3.3.1.b	The $B_s \rightarrow J/\psi \phi \oplus \mu$ channel	83
3.3.2	The influence of secondary vertex resolution	83
Summary and perspective outlook		97
A Standard Model and the CP violation		101
A.1	The $SU(2)_L \otimes U(1)_Y$ symmetric electroweak Lagrangian	102
A.1.1	The underlying gauge symmetry	103
A.1.2	The $\mathcal{L}(\Psi, W, B)$ term	103
A.1.2.a	The Charged Currents	104
A.1.2.b	The Neutral Currents	105
A.1.3	The $\mathcal{L}(W)$ and $\mathcal{L}(B)$ terms	106
A.1.4	Terms involving Higgs field: $\mathcal{L}(W, B, \phi) - V(\phi) + \mathcal{L}(\Psi, \phi)$	106
A.2	The Spontaneous Symmetry Breaking	107
A.2.1	The masses of Intermediate Bosons	108
A.2.2	Mass generation for fermions	108
A.3	The fermionic piece of electroweak Lagrangian in terms of physical fermion fields	111
A.4	The CP operation	112
A.4.1	The parity operator P for fermion fields	112
A.4.2	The charge conjugation operator C for fermion fields	113
A.4.3	The combined CP symmetry and its violation	113
B The Cabibbo-Kobayashi-Maskawa matrix		117
B.1	CKM phases, invariants and parametrisations	117
B.2	The unitary triangle	119
B.2.1	Experimental bounds to unitarity triangle	121
C CP violation in beauty meson decays		123
C.1	Direct CP violation	123
C.2	CP violation arising from mixing in neutral B meson system	124
C.2.1	Indirect CP violation	128
C.2.2	CP violation arising from the interplay between mixing and decay	129
C.2.2.a	The $B_d \rightarrow J/\psi K_S$ channel	133
C.2.2.b	The $B_s \rightarrow J/\psi \phi$ channel	134
D The credibility of simulation		137
Acknowledgements		139
Bibliography		141

Introduction

For the last few decades the human understanding of the world on sub-particle level has grown up significantly. The electromagnetic and weak interactions were unified, the weak and strong interaction mediators – the Intermediate Vector Bosons (IVB) – Z^0 , W^\pm and gluons were discovered, the number of light neutrino types has been measured to be three. The recent discovery of the top quark has closed the last but one¹ vacant on the quark-lepton list. The observed phenomena are explained within a theory known as the *Standard Model*. The Standard Model consists of the electroweak theory (Glashow, Salam and Weinberg [1]-[3]) and the Quantum Chromodynamics – QCD [4]-[6] and has been developed by many physicists from all over the world. Although the Standard Model describes precisely all known (perturbative) elementary particle phenomena, our understanding of the world is still far from being complete.

Presently, the most intriguing problem is the existence of predicted, so called Higgs particle(s) [7]-[9] (one in the original version, or several of them in extensions of the Standard Model), which has never been observed. The Higgs sector is a remnant of the Spontaneous Symmetry Breaking – the same mechanism which leads to the origin of masses. Recently the theoreticians were intensively developing a family of extensions to the Standard Model; particularly promising due to their intrinsic consistency, compactness and natural accommodation of Higgses are two Higgs doublets models and within this class, the supersymmetric (SUSY) extensions, in particular the Minimal Standard Supersymmetric Model (MSSM). The search for the Higgs particle(s) and other postulated particles in theoretically allowed mass regions requires high luminosity and high energy accelerator able to penetrate wide range of masses at high energies. It is the main motivation to build the Large Hadron Collider (LHC).

Beside the explanation of the electroweak symmetry breaking another exciting phenomenon in the field of today's elementary particle physics is the origin of CP violation. The CP symmetry consist of two discrete symmetries combined together: parity (spatial reflection) P, and charge conjugation (particle – antiparticle exchange) C. Initially, it was believed that P and C symmetries are conserved separately since people would like to have the microscopic world

¹Up to now, the conviction of the existence of another elementary particle – lepton ν_τ is still based on the indirect evidence only.

left-right and matter-antimatter symmetric. However, in 1956 Lee and Yang analysing the " $\Theta - \tau$ puzzle" suggested [10] that the parity conservation is broken in weak interactions. Later, the experiment of Wu and collaborators [11] had shown that the weak interactions do not respect parity (nor charge conjugation) – only right-handed antineutrinos are emitted in nuclear β -decay. After that, it was strongly believed that the combined product of C and P is a good symmetry (reflection left and right and at the same time matter and antimatter; left-handed neutrinos in the matter world corresponds to right-handed ones in the world made of antimatter).

In 1964 Christenson, Cronin, Fitch and Turlay [12] **unexpectedly** observed the two pionic decay mode of long-lived neutral kaons among dominant three pionic decays. If the CP is conserved, the long-lived kaon should coincide with the CP odd eigenstate, that should never go to the two pion (CP even) state. The first explanation was given by the Wolfenstein in 1964 [13] with a help of introduced extra *superweak interaction*. After more than thirty years there is no other unquestionable evidence for CP violation but the above mentioned tiny one in the $K^0 - \bar{K}^0$ system (in $\Delta S = 2$ transitions, observed with a help of nonleptonic pionic $K_L \rightarrow 2\pi$ [12],[14, 15] and semileptonic $K_L \rightarrow \pi^\pm l^\mp \nu$ [16, 17] decays), and the origin of CP violation is still not completely clear. Several processes that could induce or contribute to the phenomena was investigated [18], but up to now even the original Wolfenstein explanation is not excluded by the experiment. On the other hand it should be noticed that the consequences of observed tiny CP violation may extend to cosmology (explanation of the asymmetry between matter and antimatter [19]).

In the Standard Model the CP violation may be induced both by strong and electroweak part of the theory. In the first case however, the theoretically allowed terms that violate CP [20],[21] contribute to the electric dipole of the neutron, for which a strong experimental upper bound exists. Since the reason of the suppression is not known, this so called *strong CP problem* [22] may lead to the new physics. The clear and convincing mechanism of generation of CP violation in the electroweak sector of the Standard Model was proposed in 1973 by Kobayashi and Maskawa [23], who extended the phenomena of flavour mixing (Cabibbo [24]) up to three generations of quarks. In the electroweak Standard Model, the CP violation is governed by a single phase of the 3×3 Cabibbo-Kobayashi-Maskawa (CKM) mixing matrix. The dependence on only one (although unknown) parameter makes the model predictable. Particularly it predicts the CP violation not only in $K^0 - \bar{K}^0$ $\Delta S = 2$ transitions (observed), in $\Delta S = 1$ decays (including non-conclusive ϵ'/ϵ measurements [25],[26]), but also large effects in the decays of B mesons.

The B -physics is regarded as a possible way to clarify the mechanisms of the CP violation in the nearest future. Unluckily, the clear signatures of CP violation are expected in relatively rare decays, and a special experimental effort is required to ensure the statistical significance. The first possibility

is to build dedicated e^+e^- B -factory, another one is to use high luminosity hadronic machines. The LHC offers an unique way to study CP violation in B -meson system. Since the predicted cross-section for $b\bar{b}$ pair production is large (~ 0.5 mb, see Fig. 0.1) one should expect $\sim 10^{13}$ b -particles per year at designed initial LHC luminosity. Thus, even the general purpose experiments may measure CP violating effects with significant accuracy. This task, however, requires serious efforts to be taken in optimisation of trigger system (selection of b -events in the bulk of QCD background) as well as in track measurements (to measure the decay point of a B -meson the performant vertex detector is required).

In this thesis, the possibility to measure the CP violation in neutral B meson system in the framework of the Compact Muon Solenoid (CMS) detector at LHC is discussed. Particularly the "gold plated" CP violating channel

$$B_d \rightarrow J/\psi K_S \oplus \mu^{tag} \rightarrow 3\mu \pi^+ \pi^-$$

as well as the

$$B_s \rightarrow J/\psi \phi \oplus \mu^{tag} \rightarrow 3\mu K^+ K^-$$

channel (where a tiny CP violation is expected) are analysed. Moreover the following control channels are investigated

$$B_d \rightarrow J/\psi K^* \oplus \mu^{tag} \rightarrow 3\mu K^\pm \pi^\mp,$$

$$B^\pm \rightarrow J/\psi K^\pm \oplus \mu^{tag} \rightarrow 3\mu K^\pm.$$

Expected number of events, signal to background ratio for CP violating channels as well as for control channels are presented. The opportunity to measure dilution factor is investigated. Finally, the errors on both, time integrated and time dependent asymmetries are given for $B_d \rightarrow J/\psi K_S$ and $B_s \rightarrow J/\psi \phi$ channels.

The PYTHIA Monte-Carlo generator [28] was intensively used to simulate necessary events that were later processed using the CMS detector parametrisations. The branching fractions implemented in the simulation are based on the *Review of Particle Physics* [29].

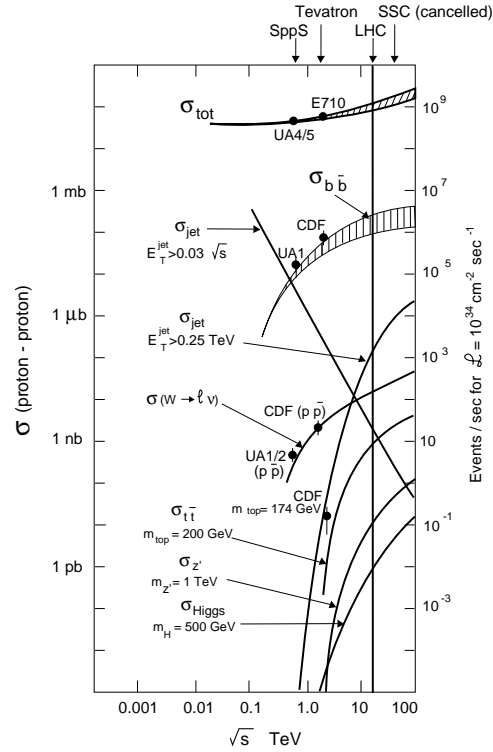


Figure 0.1: Evaluation of cross-sections in pp colliders [27].

The thesis is organised in chapters. After this Introduction, in Chapter 1 the overview of the LHC, its physics potential followed with a short description of the CMS detector is given. The detector features of the primary importance to the performed task are brought into prominence. Chapter 2 contains the short introduction to measurement of CP violation from the experimental point of view and the most important aspects of measurement. Chapter 3 – the main one – contains description of the simulation and the results. Apart of that, four Appendices are enclosed. In Appendix A the construction of the electroweak Standard Model Lagrangian leading to the CP violation phenomena is presented. In Appendix B some of the properties of CKM matrix are shown. In Appendix C the phenomenological review of CP violation in the sector of B -mesons is given. Finally, in Appendix D the comparison of PYTHIA predictions with the data from the UA1, D0 and CDF experiments is shown.

The author of this thesis is a member of the CMS collaboration involved in the project of the RPC based muon trigger, responsible particularly for the RPC simulation software, calculation and parametrisation of trigger efficiencies. Simultaneously, the author takes a part in the works of CMS B -physics group, giving leading contribution to the PYTHIA based simulation package developed for the purposes of the CMS B -physics group. The author own work contributing to this thesis are the provided trigger parametrisation functions as well as the simulation study described in Chapter 3.

Chapter 1

The CMS detector at LHC

1.1 The Large Hadron Collider

1.1.1 Motivations and Physics Goals

The Large Hadron Collider (LHC) is designed [30]-[34] and approved [35] accelerator at European Laboratory for Particle Physics - CERN¹. The main motivation for building the LHC is to penetrate a totally unexplored energy region up to TeV range (on the parton level). This is exactly the most attractive regime for Higgs searchers. It is well known that even in the minimal Standard Model the mass of Higgs particle is not calculable. However, since the perturbative theory breaks down for $m_H \geq 1 \text{ TeV}/c^2$ it cannot be too heavy.

The LHC has been designed to be as much universal as possible. There are three modes of operation foreseen. The main, and initial one is to collide protons (p-p option). Also, the heavy ion (up to Pb-Pb) collisions are foreseen. Finally, possibility to collide proton beam with the electron one from the LEP accelerator (so called LHC⊗LEP option) is kept open. The main physics searches in p-p colliding mode might be summarised [36]-[38] as follows:

- Explanation of electroweak symmetry breaking.

- The minimal Standard Model Higgs scenario.

The search for the minimal Standard Model Higgs is one of the primary motivations, goals and design constraints for LHC experiments. Depending on the mass, there are several decay modes that should be investigated:

$$\begin{array}{ll} \star H \rightarrow WW \rightarrow l\nu jj & (600\text{GeV}/c^2 < m_H < 1000\text{GeV}/c^2) \\ \star H \rightarrow ZZ \rightarrow 2l^+2l^- & (2m_Z < m_H < 800\text{GeV}/c^2) \\ \star H \rightarrow ZZ^* \rightarrow 2l^+2l^- & (130\text{GeV}/c^2 < m_H < 2m_Z) \\ \star H \rightarrow \gamma\gamma & (80\text{GeV}/c^2 < m_H < 150\text{GeV}/c^2) \end{array}$$

¹The abbreviation CERN stands for *Conseil Européen pour la Recherche Nucleaire* – a French name of the initial establishment body

- The supersymmetric scenario.

In all supersymmetric extensions to the Standard Model at least two Higgs doublets are necessary to induce masses to upper and lower fermions. In the case of the Minimal Supersymmetric Standard Model (for reviews and references see, for example [39]-[42]), five Higgs particles are present: light neutral scalar h^0 , heavy neutral scalar H^0 , pseudoscalar A^0 and charged H^\pm . Depending on the masses of Higgs particles several decay modes might result in the discovery. One can mention [43]:

$$\begin{aligned} &\star h, H \rightarrow \gamma\gamma \\ &\star H \rightarrow ZZ^{(*)}, h \rightarrow ZZ^* \\ &\star h, H, A \rightarrow \tau\tau \\ &\star t \rightarrow H^\pm b, H^\pm \rightarrow \tau\bar{\nu}_\tau \\ &\star h, H, A \rightarrow \mu\mu \end{aligned}$$

- Alternative Symmetry Breaking (without Higgses) scenarios.

The Spontaneous Symmetry Breaking may be effectively generated by Strongly Interacting Symmetry Breaking Sector. This assumes absence of any physical state belonging to Symmetry Breaking Sector other than the longitudinal Weak Bosons. Weak longitudinal polarised Intermediate Vector Bosons (states with helicity zero) are absent in the symmetric limit where their mass vanishes. Thus, they are directly related to the Symmetry Breaking mechanism. Study of their properties might be attractive way to attack the Symmetry Breaking problem. Several approaches are made. The BESS model [44] postulates a triplet of new vector resonances (V^0, V^\pm) having large couplings to longitudinal W 's and Z 's. In the DHT model [45, 46] several scenarios are possible and the symmetry breaking dynamics may be studied through scattering of longitudinal component of weak bosons.

It is quite possible that a Higgs particle(s) might be discovered at LEP200 before LHC will be turned on. However, the investigation of its properties requires high statistics, available only at LHC. Thus, the LHC would explore Higgs nature, ascribing it to SM, MSSM or others, and possibly explaining the origins of the Spontaneous Symmetry Breaking.

- Supersymmetry.

The search for Supersymmetry particles (other than Higgses) is an exciting point of LHC physics. Besides of the extension to the Higgs sector the Supersymmetry introduces a set of new particles (*sparticles*): *gauginos* – spin 1/2 superpartner of SM bosons, *squarks* and *sleptons* – spin 0 superpartners of elementary fermions and *higgsinos* – spin 1/2 superpartners of Higgses. One of the assumptions of MSSM of a great importance for the experimental physics [37, 47] is a conservation of R-parity

(sparticles have $R=-1$ whereas particles $R=1$). Thus the sparticles can only be produced in pairs, each sparticle may decay only to odd number of lighter one(s), the lightest is absolutely stable. Gluinos and squarks are the most promising candidates to be discovered at LHC. Depending on the masses of sparticles and MSSM parameters several decay modes might be studied [38, 43]. In all cases the final states are of the form: *Jets* (+*Leptons*) + E_t^{miss} . Due to conserved R-parity no sparticles mass peaks can be observed in the searches. Instead, the evidence for SUSY particles might be based on analysis of event topology and obtained *Jets/Leptons*/ E_t^{miss} spectra. A good understanding of background including shape and magnitude is crucial for these searches.

- The Heavy Quark Physics.

The LHC exploration of top quark physics will concentrate on its identification, precise mass measurement, and measurement of decay modes. The relatively high cross section for $b\bar{b}$ pair production makes LHC a huge b-factory. This offers an opportunity to study the CP violation in the beauty quark sector, that had not been observed up to now. Earlier observation of CP violation by experiments under preparation² is foreseen. LHC would have possibility to study CP violation with better accuracy. Besides of CP violation phenomena, a measurement of quark-antiquark mixing in B_d and B_s systems is possible.

- Neutrino Physics.

The ν_τ is the only particle in the list of elementary fermions that has been never observed directly³. The LHC gives potential opportunity [49] to observe the $\nu_\tau \rightarrow \tau$ transition in $\nu_\tau N \rightarrow \tau X$ reaction both in beam-dump and beam-beam mode.

- Precise measurements and tests of known processes.

There are several important quantities, of great interest which are foreseen to be measured. One could mention total and elastic cross sections. The high accuracy measurement of strong coupling constant is foreseen. LHC gives a possibility to test QCD over 10 orders of magnitude with jets, and 8 to 9 orders with direct photons. Furthermore, high p_t W, Z production, a background to other interesting processes, would be an interesting test of QCD. It is foreseen to test triple-gauge couplings $WW\gamma$ and WWZ , since they have not been tested with satisfactory precision. Possible deviations from the Standard Model will be investigated.

²HERA-B at HERA in DESY, Belle at KEKB in KEK, BaBar at PEP-II in SLAC, CDF and D0 at Tevatron in FNAL

³The evidence for existence of ν_τ comes from several sources [48]. It is convincing but indirect.

- New Heavy Vector Bosons.

Various extensions of the Standard Model predict the existence of new Gauge Bosons. Their discovery at high energy and high luminosity collider seems to be possible for masses up to about 5 TeV/c² [50]. One should mention the most attractive channels: $W' \rightarrow l\nu$, $Z' \rightarrow l^+l^-$, and for relatively light W' : $W' \rightarrow ZW$.

- Exotica.

Several exotic solutions of symmetry breaking puzzle are already mentioned. One should add a study of Baryon and Lepton number violation, instantons, compositeness effects, quark and lepton excited states and more [51]. Hopefully, the reality will be more exotic and unexpected than predictions.

The mentioned goals requires universal, high precision detectors, able to operate at maximal achievable energies and luminosities. It has been decided to build two general purpose experiments: ATLAS [52] with toroidal magnet and CMS [53] with the solenoidal one. Additionally, heavy ion experiment – ALICE [54] and LHCb [55]– dedicated for B-physics are foreseen.

1.1.2 The machine

The Large Hadron collider is designed to collide protons with the energy up to $\sqrt{s} = 14$ TeV with the desired luminosity of 10^{34} cm⁻²s⁻¹ (see Table 1.1 [34] for parameter specification). The p-p collisions is an initial option for accelerator operation. After that the accelerator would be operated in heavy ion mode colliding ions as heavy as lead with an energy $\sqrt{s} = 1148$ TeV (2.76 TeV/nucleon) and luminosity of 10^{27} cm⁻²s⁻¹.

The LHC accelerator will be build and operated on basis of existing CERN infrastructure. The LHC will be located in the LEP tunnel of 27 km circumference. Thus, before LHC will be installed, the LEP ring should be removed. The space for eventual LEP reinstallation will be left above the LHC ring. Such an option would provide e-p collisions if the physics case justify it. The desired high energy for a given circumference (limited by the size of LEP tunnel) requires high magnetic field. The designed dipole magnet will be cooled down to 1.9 K by the superfluid helium, to achieve magnetic field of 8.4 Tesla. Furthermore, cost considerations and space limitation dictate two-in-one design, where two beam channels are incorporated into a single iron yoke and cryostat.

The LHC will be injected by the existing CERN accelerator chain (Figure 1.1), namely 50 MeV linac, 1 GeV Booster, the 26 GeV Proton Synchrotron and finally the 450 GeV Super Proton Synchrotron.

In the Figure 1.2 a schematic view of the LHC ring is shown, with marked places foreseen for the experimental areas and for machine operation. Four beam-beam crossing points are designed: Point 1 (the Point number reflects

<i>feature</i>	<i>value</i>
Energy	7.0 TeV
Luminosity	$10^{34} \text{ cm}^{-2}\text{s}^{-1}$
Bunch spacing	25 ns
R.m.s bunch length	7.5 cm
Beam radius	$16 \mu\text{m}$
Particles per bunch	$1 \cdot 10^{11}$
Beam lifetime	22 h
Luminosity lifetime	10 h
Full crossing angle	$200 \mu\text{rad}$
Injection Energy	450 GeV
Circumference	26.659 km
Beta function at interaction points	0.5 m
Dipole Field	8.4 T
Circulating current/beam	0.54 A
Energy loss per turn	6.7 keV

Table 1.1: The main parameters for LHC operation in p-p mode

the Octant number in Figure 1.2 in which the Point is located) – reserved for ATLAS, Point 5 where CMS will be placed, Point 2 (ALICE) and Point 8 (B-physics). Other possible interaction points do not have bunch crossings. The beams are injected in Points 2 and 8, beam cleaning is performed in Points 3 and 7. In Point 6 the beam abort system will be located, while Point 4 remains vacant.

It is clear that the full desired luminosity cannot be obtained at once. It is expected that LHC will start the operation with initial luminosity of $a \text{ few} \times 10^{32} \text{ cm}^{-2}\text{s}^{-1}$ that will be soon increased to $\sim 10^{33} \text{ cm}^{-2}\text{s}^{-1}$, while the full luminosity of $10^{34} \text{ cm}^{-2}\text{s}^{-1}$ will be achieved within a couple of years. The low luminosity mode of LHC operation ($10^{33} \text{ cm}^{-2}\text{s}^{-1}$) is optimal for the B -physics study, because the production of $b\bar{b}$ pairs is large enough while the combinatorial background is low (small pile-up of events).

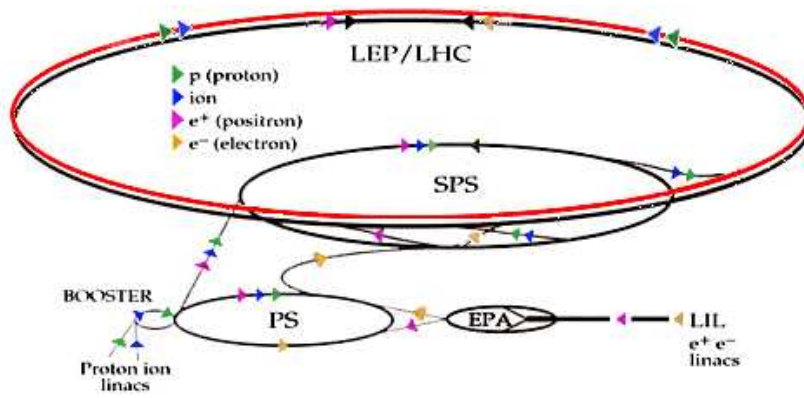


Figure 1.1: The CERN accelerator complex. Protons are produced in proton-ion linacs then follow through booster, PS (Proton Synchrotron), SPS (Super Proton Synchrotron), and finally injected into LHC with energy of 450 GeV.

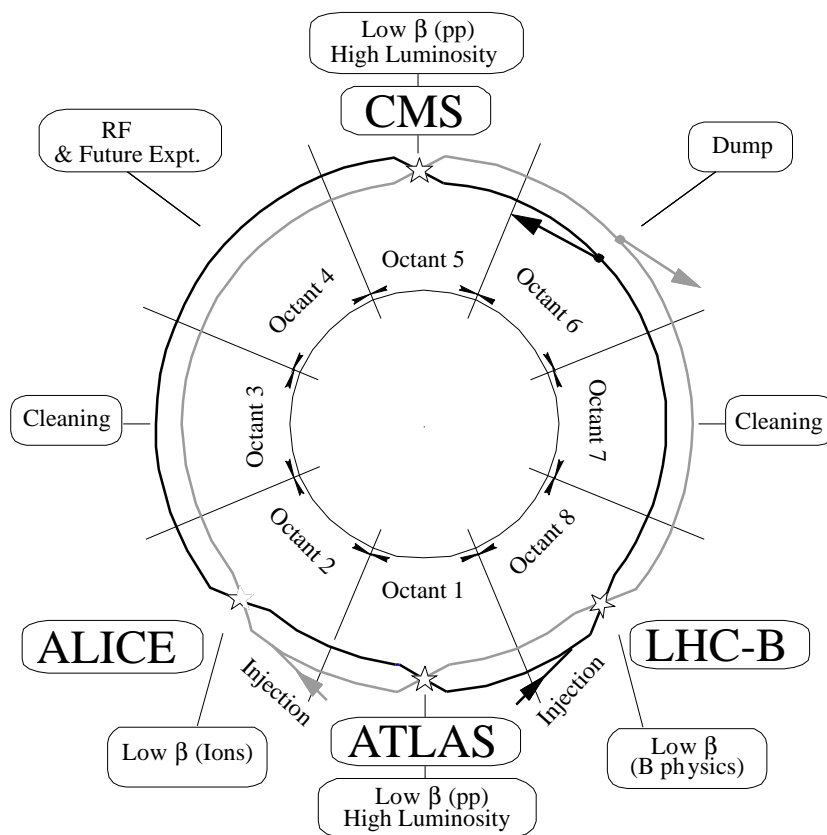


Figure 1.2: The schematic layout of the LHC. The ring is divided into 8 octants. In four of them there are beam-crossing points where the experiments will be located.

1.2 The Compact Muon Solenoid - a detector overview

The⁴ CMS (Compact Muon Solenoid) detector is a proposed [56, 57, 53, 43] and approved [58] general purpose detector at LHC. It is designed to make discoveries at highest luminosities of LHC. As the name suggests, design concepts were optimised for good muon identification and measurement, since muons are one of the most important signatures of hard processes at hadron colliders. To enlarge a discovery potential, a special emphasis have been put on a precise measurement of electrons and photons. A strong solenoidal field has been chosen, giving the compactness to the overall design. The CMS general design principles may be summarised as follows [43]:

1. a very good and redundant muon system,
2. the best possible electromagnetic calorimeter consistent with 1),
3. a high quality central tracking to achieve 1) and 2),
4. a financially affordable detector.

In the Figure 1.3 a perspective view of the CMS detector is presented. One can see the Inner Tracker covering the beam pipe at the interaction region. The Inner Tracker is surrounded with an electromagnetic calorimeter (ECAL) marked in green and a hadronic calorimeter (HCAL) in blue. These mentioned subdetectors are positioned in a 4 Tesla magnetic field generated by a CMS superconducting solenoidal coil. The magnetic field is closed with an iron Return Yoke (yellow) splitted into a few layers by the four Muon Stations (in red). The pseudorapidity coverage of the detector is about $|\eta| < 2.4$ for Muon Stations, $|\eta| < 2.6$ for Tracker and $|\eta| < 3.0$ for ECAL and HCAL. The energy hermeticity of the detector is completed with Very Forward Hadronic Calorimeters (VCAL, in violet) supplementing pseudorapidity coverage up to $|\eta| < 5.0$. Generally, parts of the detector situated parallel to proton beams are called *barrel* (or the central) part of the detector, whereas *endcaps* (or forward part of the detector) have subdetectors positioned perpendicularly to the beam pipe.

An overall CMS weight is 12500 ton, whereas a length 21.6 meters (excluding VCALs) and a diameter 15 meters. The transverse and longitudinal cuts of the CMS detector are shown in the Figures 1.4 and 1.5 respectively.

⁴The CMS detector is still in planing phase. Thus its geometry details and performance parameters are still changing. This section describes the detector at the stage of detector Technical Proposal [43] submitted to LHCC committee in the end of 1994, supplemented with the available documentation from the CMS Resources Review Boards, CMS collaboration meetings and various CMS notes. One should note that some of the alternative solutions kept open at the moment are to be fixed in the series of incoming Technical Design Reports expected in 1997–1998.

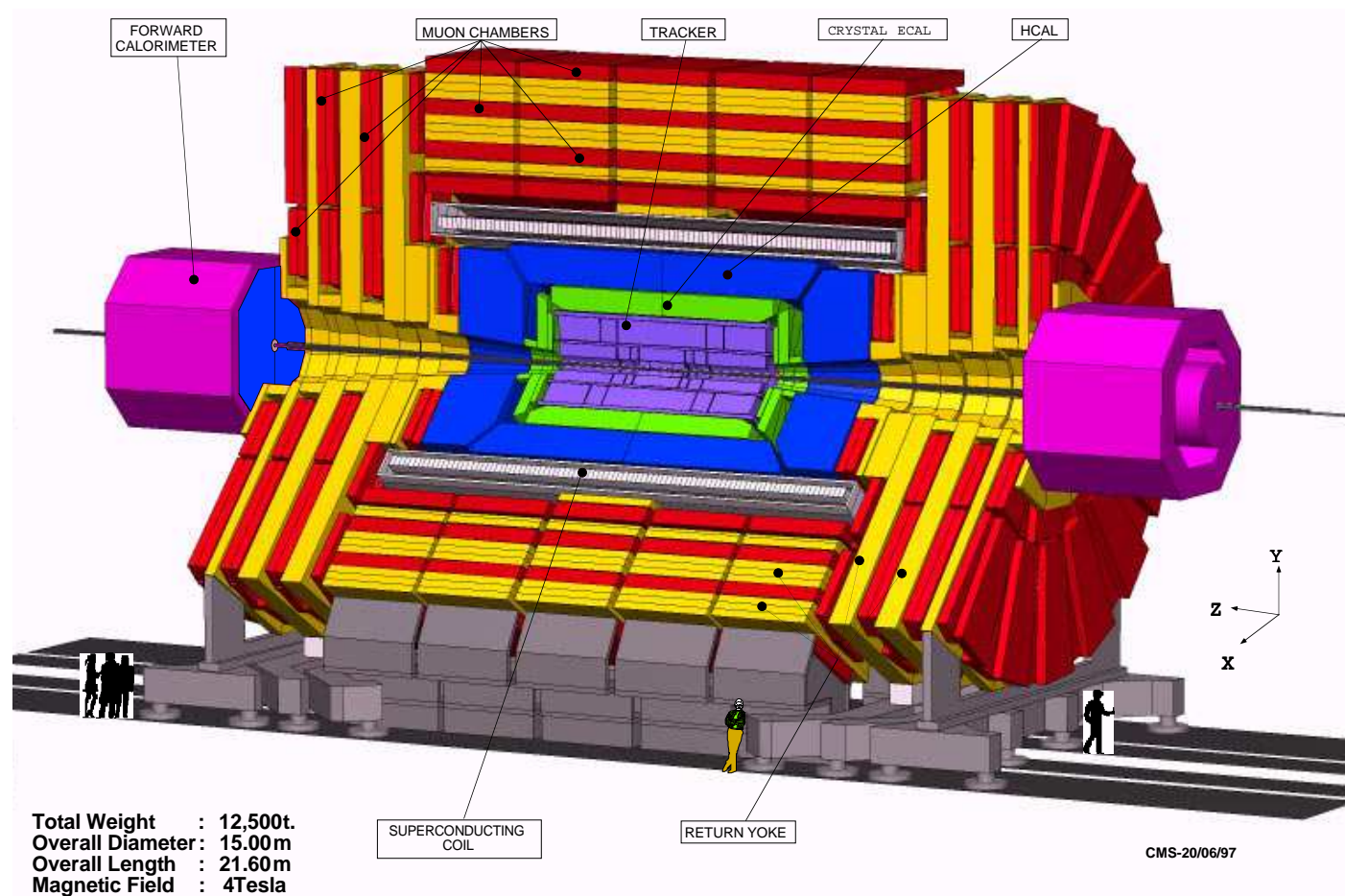


Figure 1.3: The perspective view of the CMS detector. Its main constituents are marked.

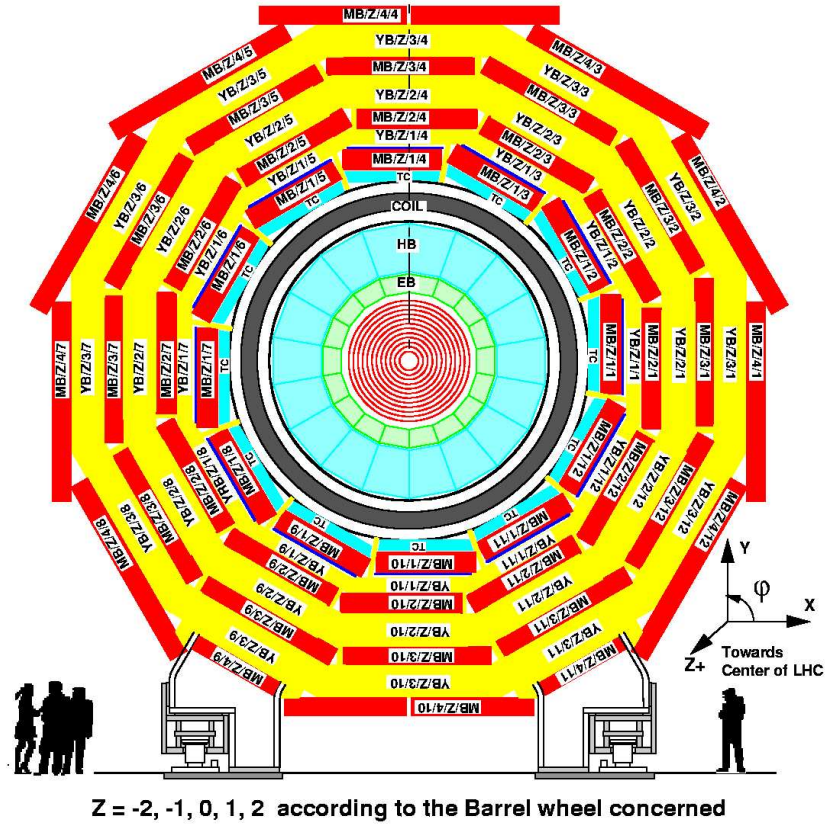


Figure 1.4: The transverse view of the CMS detector.

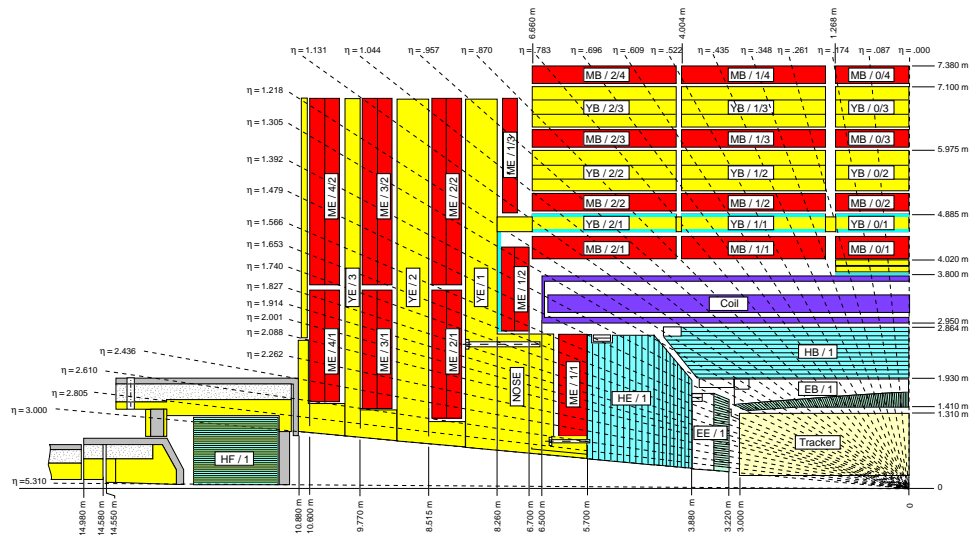


Figure 1.5: The longitudinal view of the CMS detector.

1.2.1 The magnet

The magnet system is the major part of the detector. The CMS collaboration has chosen solenoidal type of magnetic field (Figure 1.6) with strong, 4 Tesla, field inside a long superconducting coil. The uniform, cylindrical magnetic field facilitate track reconstruction, while the coil length - 13 m ensures efficient bending of charged particles tracks up to pseudorapidity of 2.4 making any additional forward toroids unnecessary. Simultaneously, the large inner radius (2.95 m) of the superconducting coil is sufficient to lodge the Inner Tracker and the calorimeters. The magnetic field is closed with iron Return Yoke where the field has a strength of 1.8 T (saturated iron). The Return Yoke is designed as 12-sided structure equipped with muon stations (see Figure 1.4). Its shape is a compromise between flat planes of muon station, technical requirements and intended cylindrical symmetry of magnetic field. The bending power of the CMS magnet varies from 17 Tm in the barrel to 6 Tm at $|\eta|=2.5$.

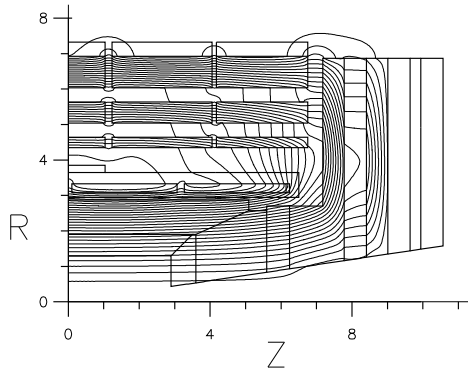


Figure 1.6: Lines of a magnetic field in the CMS detector. The magnetic field has a strength of 4 Tesla inside a coil and 1.8 Tesla in Return Yoke.

1.2.2 The Central Tracking System

A precise momentum measuring system, gaining in good invariant mass resolution is very important feature of hadron collider detectors, due to large combinatorial background. The measurement of isolated particles and particles in jets is necessary for many physics task. Additionally, a secondary vertex identification capability (microvertex device) is recommended for the b -physics. All these features should be provided by a good tracking system.

The design goal of the CMS collaboration is to reconstruct high p_t tracks with an efficiency better than 90% for particles in jets, and better than 95% for isolated tracks, providing both excellent momentum resolution ($\Delta p_t/p_t \approx 0.1 p_t$, p_t in TeV/c for high p_t charged leptons) and the impact parameter resolution (20 μm in the transverse plane and 100 μm in the z coordinate for high p_t particles). The desired performance requires excellent precision for track measurement. Since small cell size is favourite, the large number of read-out channels is implied.

The track measurement in CMS is based on the Central (Inner) Tracker, although the muon detectors located outside a coil provide a few additional measurement points for muon tracks. The schematic layout of the Central Tracker (version 3) is shown in Figure 1.7.

The high magnetic field makes possible usage of only a few high accuracy

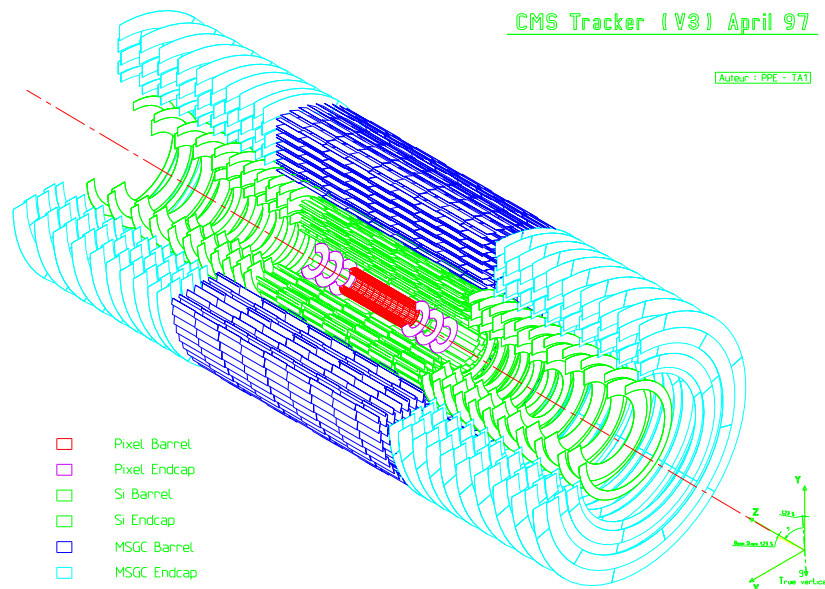


Figure 1.7: A schematic view of CMS Tracker (version 3 of the geometry). The beam pipe is surrounded with silicon pixel detector having role of microvertex detector, followed by silicon microstrips and finally with MSGC. The desired coverage of the overall Tracker is up to pseudorapidity 2.6

measured points per track for momentum assignment. On the other hand a large number of hit planes enables unique track definition. The dedicated simulation defines the optimal number of measurement points to be 10-12 in each direction. It is preferred to situate the high precision detector near the interaction region because multiple scattering does not influence the measurement. Moreover, the high resolution near the interaction point provides a precise information for reconstruction of decay points of charm and beauty particles. At higher radii, the multiple scattering justify the usage of less accurate detectors. Following this consideration, optimising the cost and performance, the Central Tracker is composed of three types of subdetectors.

The Silicon Pixel detector is the part of the Tracker closest to the beam pipe. It consist of square shaped silicon pixels arranged in cylindrical surfaces in barrel and in disks in endcaps. The size of the pixel is about $125\mu\text{m} \times 125\mu\text{m}$ but its space resolution is enhanced by analogue signal interpolation to approximately $15\mu\text{m}$ both in $r \cdot \varphi$ and z coordinates.

The method is based on weighting of signal measured in more than one cell due to substantial charge spreading (Figure 1.8). The initial number of surfaces is

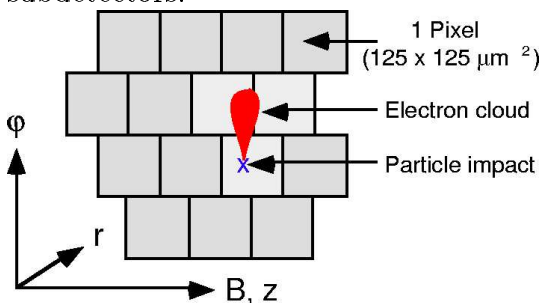


Figure 1.8: A schematic picture illustrating the charge sharing in the barrel pixel units.

two for the "low luminosity mode" (located at radii 4.25 cm and 7.2 cm) but the mechanical structure allows the installation of the outer "high luminosity mode" layer [59] (at 11 cm) possibly replacing the inner one. This allow us to obtain high precision measurement points in barrel close to the vertex. In the endcaps, there are two layers optimised for the geometrical acceptance and space resolution, supplementing the rapidity coverage of Pixel subdetector up to $|\eta| \leq 2.45$. The total number of channels is huge ($\sim 5 \cdot 10^7$) forcing the sparsified readout (with zero suppression).

The main profit from the Silicon Pixel subdetector is a good primary and secondary vertex resolution. Furthermore, the pixels provide substantial improvement in z coordinate resolution. The main difficulty is that the Silicon Pixel detector situated very close to the interaction vertex will be exposed to the serious radiation dose. Their radiation hardness is still under study but it is expected that the radiation damage may force us to remove (or replace) this subdetector after several years of LHC operation.

The Silicon Pixels are followed with the Silicon Microstrip subdetector formed of long and narrow strips of silicon. It is intended to operate at highest LHC luminosities resolving different interaction vertices. It is by itself a powerful device for finding vertices in the plane transverse to the beam pipe. Two detector types are foreseen: single sided strips and double sided (stereo) strips (small crossing angle ~ 100 mrad). The motivation to use stereo strips is their improved z -coordinate resolution in comparison to the single sided ones. The strips are arranged in the four cylinders (version 3) in the barrel ($r \approx 20$ -50 cm) and in eleven disks in endcaps. Barrel and endcap parts meets at $|\eta| \approx 1.8$. The narrow rectangular shaped strips in the barrel are 12.5 cm long, whereas in the forward part strips have wedge (projective) shape of varying length. The readout pitch is $100 \mu\text{m}$ for single sided strips while the double sided units have an axial pitch of $66 \mu\text{m}$ and the stereo pitch of $200 \mu\text{m}$. The achievable resolution of the Microstrip subdetector is comparable with that of pixels in the $r \cdot \varphi$ coordinate and better than 1 mm in z coordinate (stereo detectors). The total number of channels in silicon microstrip detectors is about $3.6 \cdot 10^6$.

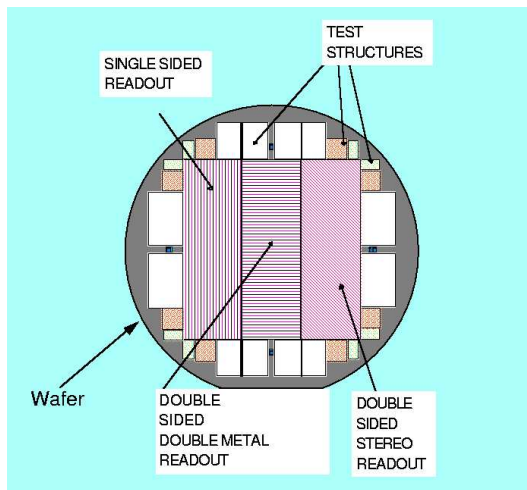


Figure 1.9: A schematic view of Silicon Microstrip testing unit. Several readout techniques were investigated.

The outermost part of the Tracker is instrumented with the Microstrip Gas Chambers (MSGC). They form a set of seven cylindrical layers in the barrel part, and ten disks in the forward part. The MSGC subdetector extends the

inner tracker radius to approximately 120 cm and $|z|$ to about 290 cm. The MSGC chamber consists of the glass substrate and the drift plane covering 1.5–3 mm gas gap (Figure 1.10). The glass substrate supports rectangular anode (9 μm width) and cathode (70 μm width) strips. The strips length depends on the location with a typical value of 12.5 cm. The readout pitch is 200 μm for single sided layers (and it is doubled for stereo readout). This allows to obtain the resolutions 40 μm in $r \cdot \varphi$ and about 2 mm in z coordinate. The total number of channels in gas microstrip detectors is about $7.7 \cdot 10^6$.

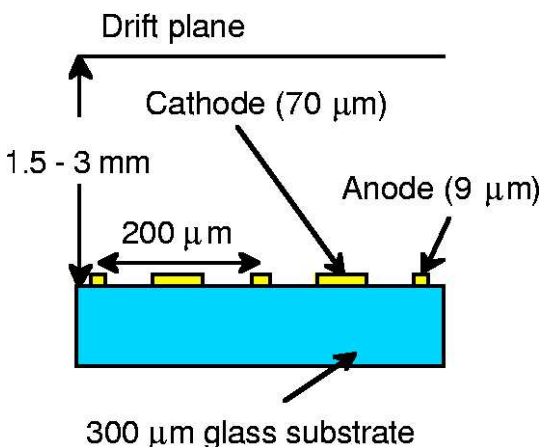


Figure 1.10: The schematic layout of MSGCs (1995 version).

It should be stressed that overall resolution depends on intrinsic resolutions described above and the alignment precision. The final alignment will be performed using real tracks, and the alignment error is expected to be smaller than 15 μm . Combining with the intrinsic resolution, the effective resolution is expected to be 20 μm in the transverse plane for silicon detectors, and about 60 μm for MSGCs. The z -coordinate alignment precision should be of order of 30 μm for barrel pixels.

The described layout of Microstrip detector and MSGC corresponds to the version 3 [60] of its geometry. Since the price of the silicon is still decreasing the most modern (still under discussion) version extends the silicon part up to six layers in the barrel (leading to the total area of 150 m^2 of the silicon).

The next three subsections describe tracker performance parameters that are essential for b -physics.

1.2.2.a Track reconstruction

The track reconstruction at LHC, where the number of produced particles in single pp collision exceeds a hundred, and the average number of hits in a tracker from one bunch crossing exceeds 10^5 , is an enormously difficult task. Several algorithms have been developed and applied [61, 62] to reduce combinatorial patterns. The algorithms were tested in the realistic GEANT description of the CMS detector using the QCD events generated with PYTHIA Monte-Carlo. In order to reproduce initial LHC conditions, both noise and event pile-up was taken into account making simulation reliable. The results shown in [43] prove that design goals are well satisfied since the track finding efficiency extends 94-98% for isolated tracks, and 93-98% for tracks in high p_t jets, keeping the number of produced ghosts at the percent level.

The momentum resolution was estimated with the GEANE package taking into account realistic detector accuracy (statistical and systematical effects). The results are shown in Figure 1.11. The momentum resolution is shown for selected values of pseudorapidity as a function of transverse momentum of incoming particle. The primary vertex constraint is excluded from the fit. The obtained resolution degrades with increasing η due to decreasing bending power. The parametrised results are intensively used in the simulation described in next chapters.

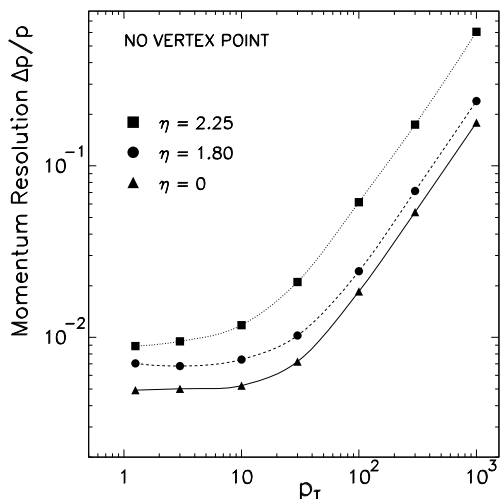


Figure 1.11: Momentum resolution obtained with a detailed detector simulation. Three curves corresponds to different pseudorapidity regions. No vertex constraint is used.

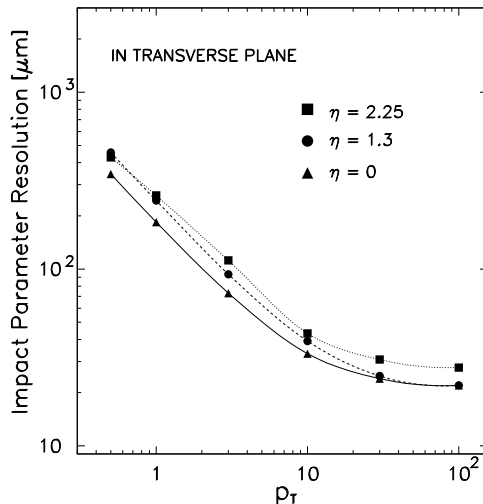


Figure 1.12: Impact parameter resolution in transverse plane. The resolution dependence on p_t is strong while on η weaker. The typical value related to B -physics is $100 \mu\text{m}$.

1.2.2.b Vertex reconstruction

The physics performance of the impact parameter resolution as well as primary and secondary vertex resolution is limited by the pixel microvertex detector and is dominated by the size of pixels and their distance from the beam. The vertex measurements are of primary importance to B -physics, tagging of b -jets, modes involving τ 's but also may resolve individual pp interactions in a single bunch crossing reducing the combinatorial background. The b -tagging played an essential role in the recent discovery of top. The impact parameter resolution was intensively studied with reliable GEANT description of the detector. Some of the obtained results are presented in Figure 1.12, where the dependence of impact parameter resolution in transverse plane is plotted as a function of transverse momentum of incoming particle.

1.2.2.c Efficiency of K_S reconstruction

A K_S is a very special particle because its decay time ($\tau_{K_S} \approx 0.89 \cdot 10^{-10}\text{s}$) convoluted with a typical LHC kinematics may lead to decay path varying from millimetres up to meters. Since a K_S is produced in CP violating decay $B_d^{(-)} \rightarrow J/\psi K_S$, efforts were made [63] to develop the reconstruction techniques. The task is addressed to the whole tracker and requires the proper identification of pions from $K_S \rightarrow \pi^+\pi^-$ decay. The decay length allow us to eliminate a bulk of combinatorial background by setting the lower bound. On the other hand, some of K_S 's cannot be identified and measured since their decay point is too far from the vertex causing the number of hits along the pionic tracks to be too small to reconstruct them.

In the analysis presented below it was assumed that the K_S decay vertex should be separated by more than 2 cm in the transverse plane from the interaction point. The minimal number of hit planes necessary for efficient track reconstruction was estimated to be six per pion track. The spiralling pions were rejected by setting the p_t cut to 700 MeV/c. Nevertheless, in many cases pion track measurement is based only on MSGC's response, and the momentum resolution is much worse than in the case of high p_t particles produced at the interaction vertex. This effect is amplified when the relatively soft pion tracks cross MSGCs in direction non-perpendicular to chamber surfaces, which causes the serious degradation of momentum resolution [64].

Taking into account the above limitations, inclusive decays of b -hadrons were generated, and the Tracker response was simulated. The distributions of $\pi^+\pi^-$ invariant mass is shown in Figure 1.13. The resolution of K_S mass is $\sigma \approx 8.6 \text{ MeV}/c^2$ with signal to background ratio of 2:1. The background shown comes from combination of charged tracks belonging to the same event assuming they are pions. The design K_S reconstruction efficiency was 35%, and, as was shown recently, it is achievable [65] in CMS.

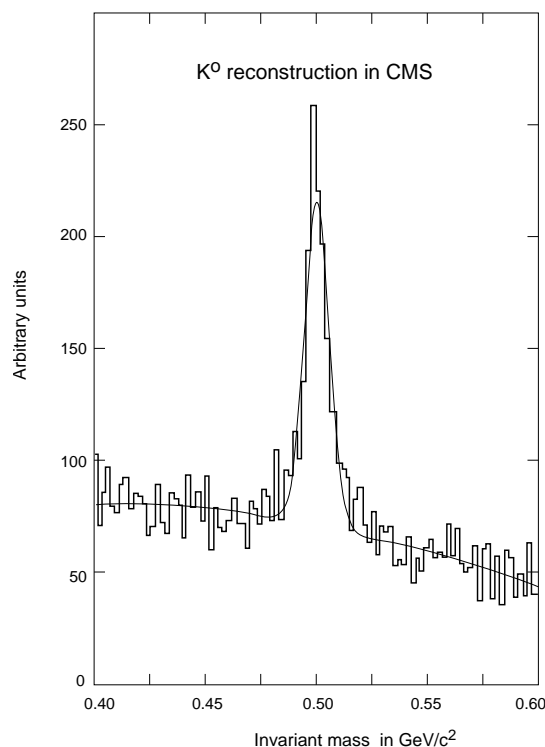


Figure 1.13: K_S invariant mass spectrum on the top of the combinatorial background

1.2.3 Calorimetry

The calorimetry system of CMS consist of three types of calorimeters: electromagnetic (ECAL), hadronic (HCAL) and very forward calorimeter (VCAL). The benchmark for the electromagnetic calorimeter performance is the diphoton mass resolution to optimise the search of Higgs particle in the possible $H \rightarrow \gamma\gamma$ channel. Since the low mass Higgs is narrow the observed signal depends on the experimental mass resolution. Both excellent energy and angular resolution may play a key role in the discovery. The CMS collaboration has chosen the homogeneous type of ECAL made of lead tungstate crystals (PbWO_4). The lead tungstate is very high density material, leading to a short radiation length ($X_0=9$ mm) and a small Moliere radius (2 cm). Thus, the compact size of ECAL may be kept. Also, the short scintillation decay time (10 ns) matched well to the LHC bunch crossing interval. One of disadvantages of PbWO_4 is the low (but still useful) light-yield that should be overcome using Si avalanche photodiodes. The length of the crystals is $25.8 X_0$ (and 1.1 nuclear interaction length λ) and the lateral granularity $\Delta\eta \times \Delta\phi \approx 0.014 \times 0.014$ (at $\eta=0$) i.e. $\approx 2 \text{ cm} \times 2 \text{ cm}$ giving about 11 m^3 of total volume ($\sim 10^5$ rectangular crystals). The achievable energy resolution of CMS ECAL in the central part of the detector may be parametrised as follows:

$$\frac{\sigma_E}{E} = \frac{2\%}{\sqrt{E}} \oplus 0.5\% \oplus \frac{0.15}{E},$$

where energy E is in GeV and the sums are quadratic. With increasing pseudorapidity the stochastic term degenerates to approximately 5% while the noise term up to 250 MeV. To improve the $\gamma\gamma$ mass resolution the preshower detector is added in the front of ECAL. It consist of the thin ($\approx 3X_0$) plane of lead followed with a layer of silicon strips. Another layer of silicon is positioned in the crystal matrix. The aim of the silicon is to measure photon shower position at two depth. The predicted angular resolution $\sigma_\theta/E \approx 50 \text{ mrad}/\sqrt{E}$ (energy in GeV) enables keeping the overall mass resolution of low mass Higgs below 1 GeV.

The electromagnetic calorimeter is surrounded by a hadronic one, sampling calorimeter made out of copper absorber interlaced with plastic scintillators. The lateral granularity is $\Delta\eta \times \Delta\phi = 0.087 \times 0.087$ (multiple of ECAL) covering the pseudorapidity interval $|\eta| < 3.0$ with the absorption length of 5λ at $\eta = 0$ to 10.5λ in endcaps (ECAL not included). Since, especially in barrel the hadronic calorimeter is too thin for efficient measurement of large showers, a kind of "tail catcher" is added to ensure adequate absorption depth (1–3 additional layers of scintillators with an iron of return yoke having a role of an absorber).

The extension of HCAL is the very forward calorimeter positioned at $|z| \approx 11 \text{ m}$ with a depth of 3 m, in a very high radiation and a very high rate environment. Its main aim is to extend the hermeticity of CMS detector up to $|\eta| < 5.0$. The VCAL is a sampling calorimeter (10λ) based on the copper

absorber matrix interlaced with quartz fibres (sensitive to Cerenkov light) as the active medium (a high purity quartz is one of the most radiation hard substances known).

The expected resolution of hadronic calorimeter is $\sigma_E/E = 65\%/\sqrt{E} \oplus 5\%$ in barrel, and degenerates with pseudorapidity to $\sigma_E/E = 100\%/\sqrt{E} \oplus 5\%$ in VCAL, allowing efficient study of QCD jets, t -quark physics and also processes leading to missing transverse energy.

1.2.4 Muon system

There are several top priority physics processes leading to one or more muons in the final state. Due to the muon long penetration length, its identification is relatively easy, providing a way to observe very rare phenomena, even in the heavy bulk of background at highest luminosities. The muon system takes care of muon measurements. It should provide a robust muon trigger, muon identification, momentum measurement, and finally, a possibility of matching of the reconstructed muon track with hits in the Inner Tracker.

The CMS muon system consist of four muon stations located inside the Return Yoke (Figures 1.3-1.5). The yoke serves not only as an mechanical support but also as an efficient absorbent improving muon identification. The returned magnetic flux is a source of additional bending power, improving the momentum resolution.

Muon stations are instrumented with muon detectors. Several different techniques were considered to obtain desired precision and optimise cost-performance ratio. In the barrel, where the magnetic field in muon station is tiny, rates and occupancies are relatively low, the Drift Tubes (DT) are chosen. In the forward, the choice was Cathode Strip Chambers (CSC), because of non negligible magnetic field in muon stations combined with expected significant occupancies and rates. Both types of the detectors are expected to provide good position measurement, trigger capability and unambiguous bunch crossing identification. Nevertheless, a dedicated trigger detector, based on Resistive Plate Chambers (RPC) is foreseen to make a muon trigger system more flexible and robust.

Drift Tube is a wire chamber. A single drift cell (Figure 1.14) of a transverse size $4\text{ cm} \times 1.1\text{ cm}$ has varying length, typically 2-4 m. The readout is taken from $50\text{ }\mu\text{m}$ diameter anode wires stretched out along the tube. The chamber is operated with the Ar-CO₂ mixture giving the maximal drift time a few hundred nanoseconds, and the position accuracy of $\approx 150\text{ }\mu\text{m}$ from one tube.

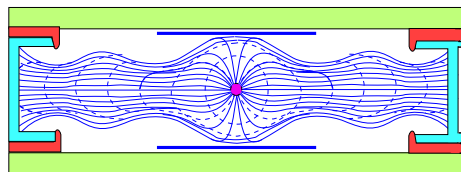


Figure 1.14: The lines of electric field inside a single cell of Drift Tube.

The drift tubes in a single muon station are organised into layers and superlayers. Each muon station (marked MB in Figure 1.5) contains 12 layers of DTs grouped into 3 superlayers (4 layers of DTs each). The inner and the outer superlayer consist of DTs with wires parallel to the beam measuring bending in $r - \phi$ coordinate, whereas the middle has wires perpendicular to the beam measuring the z coordinate.

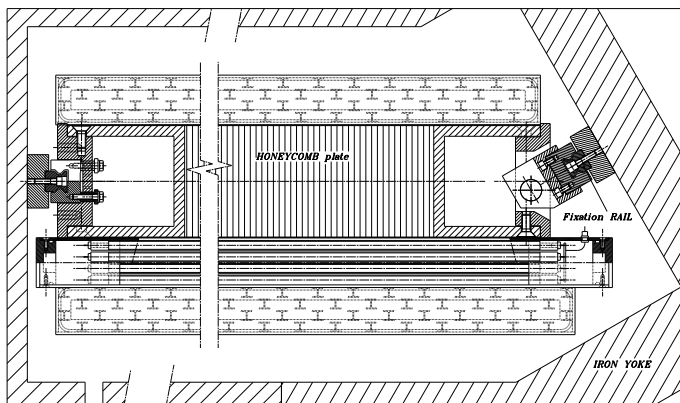


Figure 1.15: Cross section of the muon station in the barrel. The beam direction is perpendicular to the picture. DT based chamber is mounted on iron Return Yoke support and consist of (from bottom to top of the picture): a superlayer of DTs with wires parallel to the beam, a superlayer with wires perpendicular to the beam, a honeycomb plate giving required stiffness and the outer, again parallel superlayer. At the top and bottom space is foreseen for the RPCs

On top of the precise muon track measurement, the DTs provide information required by the first level trigger. A dedicated meantimer technique has been developed for bunch crossing identification and fast track parameters measurement. The meantimer circuit is suitable to measure the bending angle with accuracy better than 60 mrad (per superlayer) and a position with 1.25 mm resolution. The position - bending angle track parameters provided by the meantimer in the inner superlayer is combined with information from the outer one (the combined angular resolution increase up to about 10 mrad). The track candidates from the whole chamber are sorted and the two tracks closest to the radial direction are forwarded to trigger track finder.

In the endcaps, four muon station ME1-ME4 (see Figure 1.5) form disks located at $|z| = 5.7 - 10.5$ m, covering pseudorapidity $0.9 < |\eta| < 2.4$. Stations are instrumented with Cathode Strip Chambers – variation of multiwire proportional chamber with two readout electrodes – strips and wires, positioned in perpendicular directions to make possible measurement of both coordinates. The chamber is operated with Ar-CO₂-CF₄ with a maximal drift time about 40 – 50 ns. The single station is equipped with a six layers of wires and strips interlaced with honeycomb support. The desired position resolution

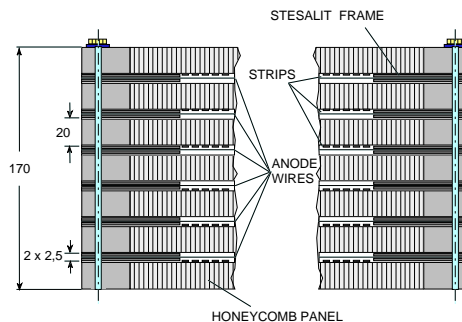


Figure 1.16: Cross-section through six-layers standard CSC. The strips are positioned radially (measuring the azimuthal angle), whereas wires – perpendicular to beam and strips measure the polar angle. The dimensions are given in mm.

is $75 \mu\text{m}$ and $150 \mu\text{m}$ in station ME1 and ME2-ME4 respectively; it was well achieved in the tests with the 5 mm strip width. The chamber is operational in a strong magnetic field up to $\approx 4 \text{ T}$, and in the high charged particle rate up to 1.5 kHz/cm^2 . For the purpose of triggering a fast readout of the chamber based on the comparator technique enables the effective measurement of position with the half strip precision. The information from the whole station is collected, and, if at least four hits match the locally predefined pattern, the track candidate is formed. Additionally, the bunch crossing identification is performed on the basis of wire information.

The third type of muon detector are Resistive Plate Chambers (RPC) – optimised for purpose of triggering. Chambers are placed in muon stations accompanying DT or CSC covering the $|\eta| < 2.1$ region (initial, staged version; the placed is kept for eventual extensions up to $|\eta| = 2.4$).

Each RPC plane is instrumented with strips (about $5/16^\circ$ width each) positioned parallel to the beam in barrel and radially in endcaps. The space resolution is not crucial and it is limited by the strip size. The required time resolution of order of a few nanoseconds was obtained in the tests.

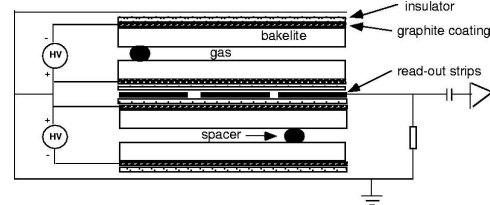


Figure 1.17: Cross-section of the double gas gap RPC.

1.2.4.a Muon trigger

The information delivered by Drift Tubes and Cathode Strip Chambers to trigger processors should be very similar since in the intermediate part of the detector the necessary information must be collected from both types of chambers. In the current design, at first the DT and CSC electronics processes the information locally (in one muon station). Both DT based local processor (mean-timer technique) and CSC local pattern comparator predefine a local track segment. Then the output from all stations is handled by the Track Finder. Using the measured $r\phi$ and local bending angle several extrapolations are needed to reconstruct a trajectory and finally assign a transverse momentum.

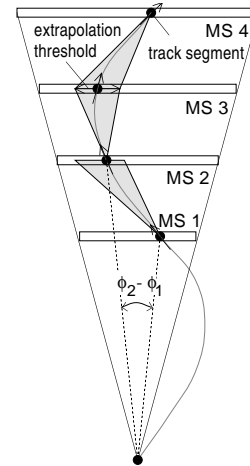


Figure 1.18: Illustration of DT and CSC track finding algorithm.

The RPC based trigger PACT (Pattern Comparator Trigger) operates on four (logical) trigger planes. A muon, bent in the solenoidal magnetic field of the detector, crosses RPCs, lighting strips on its way. The correlation of transverse momentum with the lighted strip configuration (pattern) enables triggering. PACT

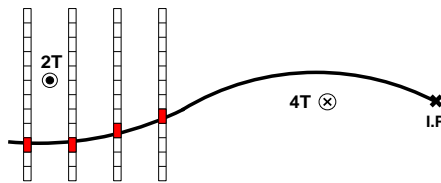


Figure 1.19: The principles of operation of RPC based PACT trigger processor

consist of groups of internal comparators, and if at least three hits of a pattern coincide with the predefined ones a p_t value is assigned. Typically, one RPC plane is positioned in one muon station, however in the barrel in the first two muon stations additional planes are added to enable low p_t (< 6 GeV/c) triggering based on the same trigger logic.

For the maximal flexibility the muon trigger does not apply any cut itself but sends information with roughly estimated momenta of muon candidates and the bunch crossing identification to the global 1st level trigger. Then information is combined with an input from calorimeters and decision to keep or reject an event is taken. Such a solution enables easy tuning of cuts and operand modes for the purposes of physics priorities. The main trigger modes of the muon trigger alone are single muon trigger and dimuon trigger (although many reconstructed muons per event may be sent to global trigger). In the single muon mode one expects the trigger rate to be a few kHz with a 15-20 GeV/c threshold at desired luminosity, but the required safety margin due to the rate uncertainties implies the need for tunable cuts in the 50-100 GeV/c range. On the other hand, for the multimMuon triggers the lowest possible cut should not be limited by the trigger logic and performance but by the muon ability to penetrate at least four muon stations. This sets the lower limit to ≈ 4 GeV/c in barrel decreasing to ≈ 2 GeV/c in the most forward direction. The b -physics programme at initial low luminosities benefits very much (Figure 1.20) from this option.

1.2.5 Global Trigger and Data Acquisition

Running at the design LHC luminosity one should expect the average interaction rate of 1 GHz. On the other hand, the maximum rate that could be archived for the off-line analysis does not exceed 100 Hz. Thus the reduction factor of 10^7 is required. The reduction will be performed in two steps (see Figure 1.21).

Initially, the front end (FE) electronic generates an input for the first level detector triggers (L1T), collected in the global first level trigger (GTS). Since no dead time is allowed, every bunch crossing has to be processed. Furthermore, the overall first level trigger processing time should stay within the length of tracker pipeline i.e. 128 bunch crossings ($3.2 \mu\text{s}$). The maximal output rate is limited by the second level trigger input rate of 100 kHz. Since a large

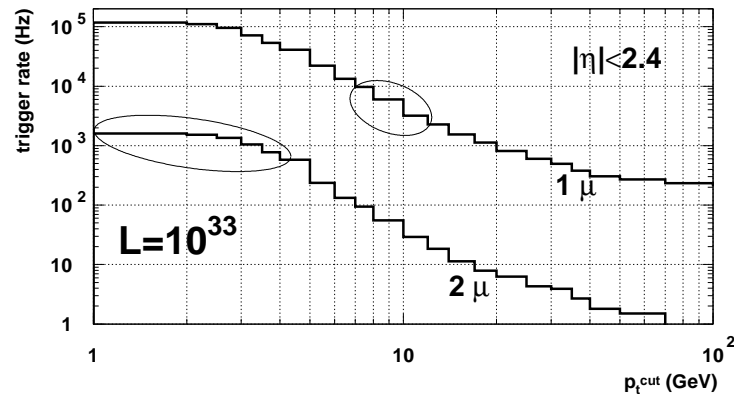


Figure 1.20: Single and double muon rates in initial low luminosity mode. The ellipses indicate approximate safety margins of operation.

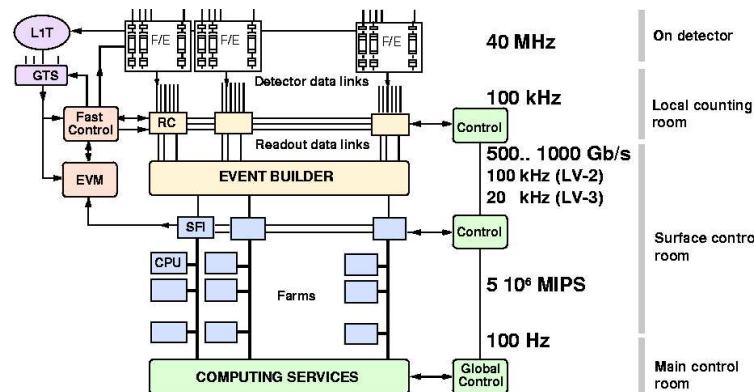


Figure 1.21: A scheme of CMS trigger and data acquisition.

safety margin should be kept, the 1st level trigger output rate (calorimeters and muons) is designed not to exceed 30 kHz.

At the second step, the event is analysed by an online processor farm. The event data reading from the front-end electronic is performed with the Event Builder governing the readout crates (RC). The information from the whole detector is then directed by the Event Builder switch through a Switch-Farm Interface (SFI) to a processor (CPU). Events for further analysis are collected and archived by Computing Services (e.g. disks and tape drivers). The second level trigger is managed by Event Manager (EVM) and several control units. The overall reduction factor of 2nd level trigger is $\approx 10^3$. Convoluting the output rate with the event size ($\approx 1\text{MB}$) one should expect several TB (10^{12} Bytes) archived data per day.

Chapter 2

Review of the CP violation from the experimental point of view

2.1 CP violating asymmetries

The^{1,2} B -physics offers an unique way to study a CP violation in many B -decay channels. Particularly, the CP violation may be observed in different decays widths of produced B^0 and \bar{B}^0 to the same final CP eigenstate f_{CP}

$$\begin{aligned}\Gamma(B^0(t) \rightarrow f_{CP}) &\propto e^{-t/\tau} (1 - \text{Im}(r_{CP}) \cdot \sin xt/\tau) \\ \Gamma(\bar{B}^0(t) \rightarrow f_{CP}) &\propto e^{-t/\tau} (1 + \text{Im}(r_{CP}) \cdot \sin xt/\tau),\end{aligned}\quad (2.1)$$

where B^0/\bar{B}^0 is B_d^0/\bar{B}_d^0 or B_s^0/\bar{B}_s^0 , x is x_d or x_s respectively (B -meson mixing parameter), and r_{CP} is defined in equation (C.42) in terms of Cabibbo-Kabayashi-Maskawa matrix elements. The CP violation is manifested by $\text{Im}(r_{CP}) \neq 0$. The most frequently used method is to look at the asymmetries in number of decays

time dependent $a(t)$

$$a(t)_{B \rightarrow f_{CP}} = \frac{N(B^0(t) \rightarrow f_{CP}) - N(\bar{B}^0(t) \rightarrow f_{CP})}{N(B^0(t) \rightarrow f_{CP}) + N(\bar{B}^0(t) \rightarrow f_{CP})} = -\text{Im}(r_{CP}) \cdot \sin xt/\tau \quad (2.2)$$

time integrated A

$$A_{B \rightarrow f_{CP}} = \frac{N(B^0 \rightarrow f_{CP}) - N(\bar{B}^0 \rightarrow f_{CP})}{N(B^0 \rightarrow f_{CP}) + N(\bar{B}^0 \rightarrow f_{CP})} = -\frac{x}{1+x^2} \cdot \text{Im}(r_{CP}) \quad (2.3)$$

¹Dedicated theoretical discussion of the CP violation phenomena is given in the Appendix C, where the notation used in this chapter is also defined.

²This chapter is written on the basis of CMS technical note [66] written by the author of this thesis.

In both methods B^0/\bar{B}^0 refers to the flavour of *initially produced* B , and the assumption is that mesons of opposite flavours are produced in equal amounts. In the time dependent studies one measures the number of decays as a function of the time of the decay. Thus the precise reconstruction of the decay vertex is crucial. In principle this is not necessary in the time integrated studies, where only the total number of decays is counted. The price paid for that is the extra $\frac{x}{1+x^2}$ factor (successor of the integration of equations (2.1) over time), which dilutes asymmetry – thus it is called *dilution factor due to integration* (D_{int}).

2.2 Unequal $B - \bar{B}$ production

Since LHC is pp collider one may expect an asymmetry in B vs. \bar{B} production (B denotes $\bar{b}q$ whereas \bar{B} : $b\bar{q}$). Protons do not contain valence antiquarks, thus B_d^0 can be produced in two ways: $\bar{b}d_{sea}, \bar{b}d_{val}$ whereas \bar{B}_d^0 can be produced only in one way: $b\bar{d}_{sea}$. Thus we expect more B_d^0 than \bar{B}_d^0 . Similar arguments suggest higher numbers of B^+ than B^- and Λ_b than $\bar{\Lambda}_b$. Because more \bar{b} than b quarks are absorbed in $B_{u,d}$ one expects an overproduction of \bar{B}_s ($b\bar{s}$) compared with B_s ($\bar{b}s$). Since formulae (2.2) and (2.3) are derived under the assumption of equal $B - \bar{B}$ production, in case of non negligible production asymmetry some corrections are needed. To correct the asymmetry (2.3) one may calculate (the correction to (2.2) goes in the same manner):

$$\begin{aligned}
A &= \frac{N(B \rightarrow f) - N(\bar{B} \rightarrow f)}{N(B \rightarrow f) + N(\bar{B} \rightarrow f)} = \frac{N_B \Gamma_B - N_{\bar{B}} \Gamma_{\bar{B}}}{N_B \Gamma_B + N_{\bar{B}} \Gamma_{\bar{B}}} \\
&= \frac{\frac{1}{2} (N_B + N_B + N_{\bar{B}} - N_{\bar{B}}) \Gamma_B - \frac{1}{2} (N_{\bar{B}} + N_{\bar{B}} + N_B - N_B) \Gamma_{\bar{B}}}{\frac{1}{2} (N_B + N_B + N_{\bar{B}} - N_{\bar{B}}) \Gamma_B + \frac{1}{2} (N_{\bar{B}} + N_{\bar{B}} + N_B - N_B) \Gamma_{\bar{B}}} \\
&= \frac{(N_B + N_{\bar{B}})(\Gamma_B - \Gamma_{\bar{B}}) + (N_B - N_{\bar{B}})(\Gamma_B + \Gamma_{\bar{B}})}{(N_B + N_{\bar{B}})(\Gamma_B + \Gamma_{\bar{B}}) + (N_B - N_{\bar{B}})(\Gamma_B - \Gamma_{\bar{B}})} \\
&= \frac{A_{prod} + A_{B \rightarrow f_{CP}}}{1 + A_{prod} A_{B \rightarrow f_{CP}}} \simeq A_{prod} + A_{B \rightarrow f_{CP}} \quad (2.4)
\end{aligned}$$

where $N_B, N_{\bar{B}}, \Gamma_B, \Gamma_{\bar{B}}$ (for simplicity) stands for $N(B^0), N(\bar{B}^0), \int_0^\infty dt \Gamma(B(t) \rightarrow f), \int_0^\infty dt \Gamma(\bar{B}(t) \rightarrow f)$ respectively, and:

$$A_{prod} = \frac{N(B^0) - N(\bar{B}^0)}{N(B^0) + N(\bar{B}^0)} - \text{the production asymmetry}$$

The $A_{B \rightarrow f_{CP}}$ is the intrinsic asymmetry caused by CP violation (given by the formula (2.3)). The theoretical hints [67] and Monte-Carlo investigations [68] show that differences at the production level are minor (of order 1%) in the p_t and η range of interest in CMS, however this should be checked by the experimental measurement. The simulation study in the framework of CMS [69, 70] shows that the asymmetry at the production level can be controlled at reasonable level. It is neglected in this thesis.

2.3 Dilution due to tagging

The final CP eigenstate f_{CP} does not allow us to guess the flavour of the initial B species, since both B and \bar{B} may decay to it. Fortunately, since b quarks in strong interactions are produced in pairs, one may try to observe the flavour of an associated b -hadron (the discussion below is given for the time integrated asymmetry A , the correspondence for $a(t)$ is straightforward).

$$A_{B \rightarrow f_{CP}} = \frac{N(B \rightarrow f_{CP}) - N(\bar{B} \rightarrow f_{CP})}{N(B \rightarrow f_{CP}) + N(\bar{B} \rightarrow f_{CP})} = \frac{N(f_{CP}, b) - N(f_{CP}, \bar{b})}{N(f_{CP}, b) + N(f_{CP}, \bar{b})} \quad (2.5)$$

One way to do that, is to look for associated (tagging) μ (generally lepton) supposedly coming from weak decays of this b -hadron ($b \rightarrow \mu^-; \bar{b} \rightarrow \mu^+$). Finally, the asymmetry one can try to look at is

$$A_{f_{CP} \oplus \mu} = \frac{N(f_{CP} \oplus \mu^-) - N(f_{CP} \oplus \mu^+)}{N(f_{CP} \oplus \mu^-) + N(f_{CP} \oplus \mu^+)}, \quad (2.6)$$

where the $\oplus \mu$ emphasise that the associated muon accompanies the investigated decay. If the charge of the detected muon could always make known the flavour of the associated beauty quark the measurable asymmetry $A_{f_{CP} \oplus \mu}$ would be equal to the asymmetry one wants to measure $A_{B \rightarrow f_{CP}}$. However, there are several sources of mistaggings (false ascribing of the flavour of initially produced b based only on the charge of detected associated muon). It is useful to denote w - fraction of wrong tags, $r = 1 - w$ - fraction of right tags:

$$\begin{aligned} w &= \frac{\text{number of "wrong" assignments of flavour of produced } B/\bar{B} \text{ decaying latter to } f}{\text{number of all assignments of flavour of produced } B/\bar{B} \text{ decaying latter to } f} \\ &= \frac{N(B \rightarrow f \oplus \mu^+)}{N(B \rightarrow f \oplus \mu^\pm)} = \frac{N(\bar{B} \rightarrow f \oplus \mu^-)}{N(\bar{B} \rightarrow f \oplus \mu^\pm)} \\ r &= \frac{\text{number of "right" assignments of flavour of produced } B/\bar{B} \text{ decaying latter to } f}{\text{number of all assignments of flavour of produced } B/\bar{B} \text{ decaying latter to } f} \\ &= \frac{N(B \rightarrow f \oplus \mu^-)}{N(B \rightarrow f \oplus \mu^\pm)} = \frac{N(\bar{B} \rightarrow f \oplus \mu^+)}{N(\bar{B} \rightarrow f \oplus \mu^\pm)} \end{aligned} \quad (2.7)$$

Thus

$$\begin{aligned} N(f \oplus \mu^-) &= N(B \rightarrow f \oplus \mu^\pm) \cdot r + N(\bar{B} \rightarrow f \oplus \mu^\pm) \cdot w \\ N(f \oplus \mu^+) &= N(\bar{B} \rightarrow f \oplus \mu^\pm) \cdot r + N(B \rightarrow f \oplus \mu^\pm) \cdot w, \end{aligned} \quad (2.8)$$

and the asymmetry $A_{f_{CP} \oplus \mu}$ could be expressed as:

$$\begin{aligned} A_{f_{CP} \oplus \mu} &= \frac{N(B \rightarrow f_{CP}) \cdot r + N(\bar{B} \rightarrow f_{CP}) \cdot w - N(\bar{B} \rightarrow f_{CP}) \cdot r - N(B \rightarrow f_{CP}) \cdot w}{N(B \rightarrow f_{CP}) \cdot r + N(\bar{B} \rightarrow f_{CP}) \cdot w + N(\bar{B} \rightarrow f_{CP}) \cdot r + N(B \rightarrow f_{CP}) \cdot w} \\ &= \frac{[N(B \rightarrow f_{CP}) - N(\bar{B} \rightarrow f_{CP})] \cdot r - [N(B \rightarrow f_{CP}) - N(\bar{B} \rightarrow f_{CP})] \cdot w}{[N(B \rightarrow f_{CP}) + N(\bar{B} \rightarrow f_{CP})] \cdot r + [N(B \rightarrow f_{CP}) + N(\bar{B} \rightarrow f_{CP})] \cdot w} \\ &= \frac{r-w}{r+w} \cdot \frac{N(B \rightarrow f_{CP}) - N(\bar{B} \rightarrow f_{CP})}{N(B \rightarrow f_{CP}) + N(\bar{B} \rightarrow f_{CP})} \\ &= D_{tag} \cdot A_{B \rightarrow f_{CP}} \end{aligned} \quad (2.9)$$

The measurable asymmetry is just proportional to the genuine asymmetry $A_{B \rightarrow f_{CP}}$. The proportional factor D_{tag} is:

$$\begin{aligned} D_{tag} &= \frac{(\text{number of "right" tags}) - (\text{number of "wrong" tags})}{(\text{number of all tags})} \\ &= \frac{r - w}{r + w} = 1 - 2w, \end{aligned} \quad (2.10)$$

Since $0 < w < 1$ the D_{tag} factor is always smaller than one³. It dilutes the asymmetry and thus is called *the dilution factor due to tagging*. There are several sources of mistaggings, contributing to the dilution factor:

- mixing; because of the mixing an (associated) neutral B meson may change its flavour before the decay (ex. $B_d^0 \rightarrow \bar{B}_d^0 \rightarrow \mu^-$ instead of usual transition $B_d^0 \rightarrow \mu^+$); the fraction of wrong tags due to mixing is nothing else but χ_B measured experimentally (see C.7)

$$w_{mix} = f_{B_d} \chi_d + f_{B_s} \chi_s + (1 - f_{B_d} - f_{B_s}) \cdot 0 = \chi_B$$

- cascade decays; this source occurs when *beauty* \rightarrow *charm* \rightarrow μ transition takes place. The charge of the muon from $b \rightarrow c \rightarrow \mu$ is opposite to that of $b \rightarrow \mu$,
- additional b, c production and K, π decays. In this study muons from such sources are treated as an irreducible noise. One should expected that the fraction of right and wrong tags from these sources are equal $\frac{1}{2}$.

One may notice that, in a good approximation the D_{tag} may be factorized into two main sources *dilution due to cascade decays* (D_{cas}) and *dilution due to mixing* (D_{mix})

$$D_{tag} \approx D_{cas} \cdot D_{mix} \quad (2.11)$$

The described dilution factor arises as a consequence of tagging initially produced B -meson using the charge of detected muon (or more generally lepton). This is not the only possible method. Another one is to reconstruct the flavour of associated b -quark using the jet tagging. Also, one may separate the sample of $B^0 \rightarrow f_{CP}$ where B^0 comes from decay of other charged, excited B -meson. The reconstruction of the charge of the initial B would also tag the flavour of B^0 (this is known as the self tagging method).

2.4 Influence of background

It is clear, that the unavoidable presence of background (anything faking $B \rightarrow f_{CP} \oplus \mu$) influences the above formulae. Assuming that backgrounds

³Note that $-1 < D_{tag} < 1$ but in realistic case one would expect $0 < w < 1/2$ and thus $0 < D_{tag} < 1$.

gives equal contamination to positively and negatively charged tags, the numerators of equation (2.6) are unaffected, whereas the denominators are increased by a factor $(N_{signal} + N_{background})/N_{signal}$. Thus the measurable asymmetries become

$$\begin{aligned} A_{meas} &= \frac{N^{tot}(f_{CP} \oplus \mu^-) - N^{tot}(f_{CP} \oplus \mu^+)}{N^{tot}(f_{CP} \oplus \mu^-) + N^{tot}(f_{CP} \oplus \mu^+)} \\ &= -D_{bgd} \cdot D_{tag} \cdot D_{int} \cdot \text{Im}(r_{CP}) \end{aligned} \quad (2.12)$$

$$\begin{aligned} a(t)_{meas} &= \frac{N^{tot}(f_{CP}(t) \oplus \mu^-) - N^{tot}(f_{CP}(t) \oplus \mu^+)}{N^{tot}(f_{CP}(t) \oplus \mu^-) + N^{tot}(f_{CP}(t) \oplus \mu^+)} \\ &= -D_{bgd} \cdot D_{tag} \cdot \text{Im}(r_{CP}) \cdot \sin(x \cdot t/\tau) \end{aligned} \quad (2.13)$$

In the above equations, the N^{tot} stands for total number of events (i.e. with background included). The influence of background is reflected by the *Dilution factor due to background* D_{bgd}

$$D_{bgd} = \frac{N_{signal}}{N_{signal} + N_{background}} \quad (2.14)$$

2.5 Need for control channels

It is clear that the dilution factor due to tagging cannot be determined, basing only on the information obtained from investigated $B \rightarrow f_{CP} \oplus \mu$ channel itself. Furthermore, it is necessary to measure independently possible B/\bar{B} production asymmetry and possible instrumental asymmetries for the tagging muon. These are the main purposes to study [66, 69] so called *control channels* with similar (to investigated CP violating channel) final state particles and decay kinematic.

2.6 The investigated channels

The easiest way to confirm CP violation in B -sector at LHC is to measure the time integrated asymmetry in the "gold plated" $B_d \rightarrow J/\psi K_S$ channel using the muonic tag. This motivated the author to study also the channels similar kinematically to the gold plated one, i.e. $B_d \rightarrow J/\psi K^* \oplus \mu$, $B^\pm \rightarrow J/\psi K^\pm \oplus \mu$ and $B_s \rightarrow J/\psi \phi \oplus \mu$ from which some information related to CP-violation may be obtained.

The J/ψ particle can be relatively easily detected by looking for its $\mu\mu$ decay channel. Furthermore, another muon is required as a tag. These leads to easy to detect and trigger $\mu^+\mu^-\mu^\pm$ (+hadrons) signature (see Table 2.1). In the $B \rightarrow J/\psi X \oplus \mu$ channels with 3 muons in the final state the multi-muon trigger is favoured. In the particular situation where the luminosity is low ($10^{33} \frac{1}{\text{cm}^2\text{s}}$) the dimuon trigger reduce the rate to acceptable level (see section 1.2.5). One triggering muon is expected to come from the J/ψ whereas the other may be the second muon from J/ψ decay or the tagging (associated) one.

2.6.1 The $B_d \rightarrow J/\psi K_S \oplus \mu$ channel

To measure the CP violation in $B_d \rightarrow J/\psi K_S$ channels one may measure the (time integrated or time dependent) asymmetries between number of decays B_d^0 and \bar{B}_d^0 to $J/\psi K_S$ CP eigenstate with a help of muonic tag. The theoretical formulae lead to (see Appendix C.2.2.a for more details)

$$\text{Im}(r_{CP}) = \sin 2\beta \quad (2.15)$$

(the above relation takes into account the fact that $J/\psi K_S$ is the CP odd state). Hence the CP-violating asymmetries are

$$A_{B_d \rightarrow J/\psi K_S} = -\frac{x_d}{1+x_d^2} \sin 2\beta \quad a(t)_{B_d \rightarrow J/\psi K_S} = -\sin 2\beta \cdot \sin x_d t / \tau \quad (2.16)$$

To recognise the K_S one can look at its $\pi^+ \pi^-$ decays. Thus the full signature of an event is $\mu^+ \mu^- \mu^\pm \pi^+ \pi^-$.

2.6.2 The $B^\pm \rightarrow J/\psi K^\pm \oplus \mu$ and $B_d \rightarrow J/\psi K^* \oplus \mu$ channels

$B^\pm \rightarrow J/\psi K^\pm \oplus \mu$ and $B_d \rightarrow J/\psi K^* \oplus \mu$ channels are good candidates for the control channel to $B_d \rightarrow J/\psi K_S \oplus \mu$ (and possibly to $B_s \rightarrow J/\psi \phi \oplus \mu$). Both channels have similar kinematics and reasonable branching ratios. Thus one may expect the satisfactory accuracy without uncontrolled biasing.

In the $B^\pm \rightarrow J/\psi K^\pm$ decay the charge of a kaon tags the flavour of initially produced b -quark. Thus one knows what is the expected charge of the associated muon. Comparing it with that of measured muon, one may calculate the fraction of wrong tags and thus a dilution factor due to tagging D_{tag} . It is necessary to check for the correlation (that should be of course measured in an independent way) between production of B^\pm and B_d (one may easily imagine that produced B_d^0 is more frequently accompanied with B^- than \bar{B}_d^0 whereas B^+ with \bar{B}_d^0 than B^-) since such a correlation may have an influence on the measured factor. This possible correlation is neglected in this thesis. Since K^\pm is long lived, the final signature of the event is $\mu^+ \mu^- \mu^\pm K^\pm$.

On the other hand, the $B_d \rightarrow J/\psi K^*$ channel is free of correlation uncertainties. Here K^{*0} tags B_d^0 at the time of its decay, whereas \bar{K}^{*0} corresponds to \bar{B}_d^0 . Again, one can extract the dilution factor due to tagging comparing the species of K^* with the charge of the associated muon. Since the flavour of K^* tags B_d at decay time one has to take into account the probability χ_d (given by (C.23)) that produced B_d changes the flavour before the decay. The fraction of wrong $K^* \oplus \mu$ pairs is related to w_{tag} with the following relation

$$\frac{N(K^{*0} \oplus \mu^+)}{N(K^{*0} \oplus \mu^\pm)} = \frac{N(\bar{K}^{*0} \oplus \mu^-)}{N(\bar{K}^{*0} \oplus \mu^\pm)} = w_{tag}(1 - \chi_d) + (1 - w_{tag})\chi_d \quad (2.17)$$

Is necessary to distinguish between produced K^{*0} and \bar{K}^{*0} . One can achieve that looking for the K^* decays to charged $K\pi$ ($K^{*0} \rightarrow K^+ \pi^-$; $\bar{K}^{*0} \rightarrow K^- \pi^+$). Thus the signature of the event is $\mu^+ \mu^- \mu^\pm K^\pm \pi^\mp$.

Although CMS will have no particle identification, the K^{*0}/\bar{K}^{*0} distinction may be based on the calculation of two invariant masses for considered hadrons: $m(h_K^+ h_\pi^-)$ vs. $m(h_\pi^+ h_K^-)$, where h_K (h_π) means assuming hadron to be a kaon (pion). Only events with unambiguous identification are kept.

2.6.3 The $B_s \rightarrow J/\psi \phi \oplus \mu$ channel

At a first glance $B_s \rightarrow J/\psi \phi$ looks exactly like $B_d \rightarrow J/\psi K_S$ (one *down* quark in B_d is replaced with the *strange* one in B_s). However, this is not the case for the asymmetries. In the first order of the approximate Wolfenstein parameterisations of CKM matrix the asymmetry in the $B_s \rightarrow J/\psi \phi$ vanishes. The more careful calculations shows (Appendix C.2.2.b) that Standard Model predicts small but non vanishing asymmetry there

$$\text{Im}(r_{CP}) = 2\lambda^2 \eta \approx 0.03 \quad (2.18)$$

where λ, η are parameters in Wolfenstein parameterisation of CKM matrix. One can rewrite the above equations in terms of γ angle of the unitary triangle

$$2\lambda^2 \eta = 2\lambda^2 \sqrt{\rho^2 + \eta^2} \cdot \sin \gamma \quad (2.19)$$

The time dependent and time integrated asymmetries appear to be

$$A_{B_s \rightarrow J/\psi \phi} \approx -\frac{x_s}{1+x_s^2} \cdot 2\lambda^2 \eta \approx O(10^{-3}) \quad a(t)_{B_s \rightarrow J/\psi \phi} \approx -2\lambda^2 \eta \cdot \sin x_s t / \tau \quad (2.20)$$

As it is shown later, the predicted time integrated asymmetry is well below the CMS sensitivity (for $x_s \sim 10$). Thus this channel may be used as a control channel to $B_d \rightarrow J/\psi K_S$ monitoring possible fake instrumental asymmetries. More accurate results may be achieved in the time dependent analysis. Excellent secondary vertex resolution is crucial in this case. It should be emphasised that this channels is also very interesting because any large asymmetry measured there would mean effects beyond the Standard Model.

Since ϕ decays to $K^+ K^-$, the observed signature of such an event is $-\mu^+ \mu^- \mu^\pm K^+ K^-$.

<i>channel</i>	<i>signature</i>
$B_d \rightarrow J/\psi K_S \oplus \mu$	$\mu^- \mu^+ \mu^\pm \pi^+ \pi^-$
$B_d \rightarrow J/\psi K^* \oplus \mu$	$\mu^- \mu^+ \mu^\pm K^\pm \pi^\mp$
$B^\pm \rightarrow J/\psi K^\pm \oplus \mu$	$\mu^- \mu^+ \mu^\pm K^\pm$
$B_s \rightarrow J/\psi \phi \oplus \mu$	$\mu^- \mu^+ \mu^\pm K^+ K^-$

Table 2.1: The signatures of the investigated channels

Chapter 3

The simulation

3.1 Description of the simulation

The simulation was performed with Monte-Carlo generator PYTHIA (release 5.7) [28] interfaced with JETSET (release 7.4) [28] under the control of steering package [71] developed for purposes of the CMS b-physics group¹. It consist of three separate steps:

3.1.1 Generation of $b\bar{b}$ sample

The $b\bar{b}$ events were generated at the desired LHC centre of mass energy $\sqrt{s} = 14$ TeV. The CTEQ2L[72] structure functions and SLAC (Peterson) [73] fragmentation function with $\epsilon_b = 0.005$ were chosen. An efforts was made to generate all main $b\bar{b}$ production processes explicitly. To achieve that (non elastic, non diffractive) minimum bias events were generated (with PYTHIA steering variable MSEL=1). This PYTHIA minimum bias option includes the

process	(number)	cross-section [mb]	
$q_i q_j \rightarrow q_i q_j$	(11)	1.5	} generated
$q_i \bar{q}_i \rightarrow q_k \bar{q}_k$	(12)	$O(10^{-2})$	
$q_i \bar{q}_i \rightarrow gg$	(13)	$O(10^{-2})$	
$q_i g \rightarrow q_i g$	(28)	16.6	
$gg \rightarrow q_k \bar{q}_k$	(53)	0.9	
$gg \rightarrow gg$	(68)	36.2	
Elastic scattering		22.2	
Single diffractive		14.3	
Double diffractive		9.8	

Table 3.1: Processes contributing to the total pp cross-section of 101.5 mb. The Semi-hard QCD part (used in simulation, $\sigma \approx 55.2$ mb) is separated from the elastic and diffractive scattering which do not contribute to $b\bar{b}$ production. The PYTHIA internal process number is shown for generated processes.

¹Description of earlier version of the simulation, leading however to similar results may be found in [66].

following processes giving important contribution to $b\bar{b}$ pairs production

- $q_i g \rightarrow q_i g, gg \rightarrow gg$ with $g \rightarrow b\bar{b}$ (gluon splitting)
- $q_i q_i \rightarrow b\bar{b}, gg \rightarrow b\bar{b}$ (fusion)

It should be emphasised that to keep unbiased sample no kinematic cuts at the parton generation level were used. To obtain the most flexible sample (keeping in mind minimisation of the computing time and disk space consumption) the event generation is stopped at the level of generated partons. The information on produced flavours is already accessible at that step. If the inspection for presence of $b\bar{b}$ pairs succeeds, the whole event is saved on disk. The described procedure allows us to keep only interesting b -events, picked up from the bulk of simulated minimum bias collisions. Since the event is saved before the hadronisation going on, one may have hope too use the generated b -events several times ensuring minimal biasing of the results.

Approximately 111,000,000 pp collisions were generated at CERN (13,000,000), in Pisa (23,000,000) and in Warsaw (75,000,000). At this step, $\sim 863,000$ $b\bar{b}$ events were found (thus PYTHIA predictions for $b\bar{b}$ cross sections is $\sigma_{b\bar{b}} \approx 420\mu\text{b}$).

3.1.2 Decay into investigated channel

The next step was to read generated $b\bar{b}$ events and to decay them into wanted channel. Two classes of dedicated jobs were developed. The first one simulating given exclusive channel, i.e. $B_d \rightarrow J/\psi K_S \oplus \mu$, $B_d \rightarrow J/\psi K^* \oplus \mu$, $B^\pm \rightarrow J/\psi K^\pm \oplus \mu$ and $B_s \rightarrow J/\psi \phi \oplus \mu$ separately. In the second class inclusive $B \rightarrow J/\psi X \oplus \mu$ decays were performed. The first class was intended to give accurate number of events, dilution factor and some inputs to time dependent study. The second one was to calculate signal to background ratio. In both classes the presence of the additional muon accompanying the investigated decay was required (marked with $\oplus \mu$).

At first, generated events were loaded, hadronisation was performed and b -hadrons were decayed to quasi stable ones (ex. $B^* \rightarrow B\gamma$). The example spectra of p_t of B_d mesons are shown in the Figure 3.1 with marked contribution from the processes listed in table 3.1. As one may observe the gluon splitting part in respect to gluon fusion contribute with a ratio of roughly 2:1.

Then, in each generated event one b -hadron was picked up. In the case of exclusive channel simulation, if the flavour of B matched the one in investigated channel the picked meson was forced to decay into the signal channel. On the other hand in inclusive job, one B was randomly picked up in each event and decayed according to provided decay table (see Tab. 3.2). The table contains only allowed $B \rightarrow [\text{charmonium}]X$ channels and approximately reproduces the PDG [29] branching rations collected from $\Upsilon(4S)$ experiments (see table 3.3).

In the exclusive (dedicated for specific process) channel simulation, products of initial B decay were further forced to decay to the final preferred observable state, i.e.:

B_d	Br.Ratio	B^\pm	Br.Ratio
$J/\psi K^0$	0.04808	$J/\psi K^\pm$	0.06410
$J/\psi K^*$	0.10256	$J/\psi \bar{s}u$	0.44744
$J/\psi \bar{s}d$	0.36090	$J/\psi \bar{d}u$	0.02692
$J/\psi \bar{d}d$	0.02692	$\psi' \bar{s}u$	0.21314
$\psi' \bar{s}d$	0.21314	$\psi' \bar{d}u$	0.01122
$\psi' \bar{d}d$	0.01122	$\chi_{c1} \bar{s}u$	0.22532
$\chi_{c1} \bar{s}d$	0.22532	$\chi_{c1} \bar{d}u$	0.01186
$\chi_{c1} \bar{d}d$	0.01186		

Table 3.2: The example decay table for $B_d, B^\pm \rightarrow J/\psi X$ inclusive decays. The quoted numbers are defined with respect to $\text{Br}(B \rightarrow J/\psi X)[\text{direct}] + \text{Br}(B \rightarrow \psi' X) + \text{Br}(B \rightarrow \chi_{c1} X)[\text{direct}] = 1.56 \cdot 10^{-2}$ to reproduce the PDG value $\text{Br}(B \rightarrow J/\psi X) = (1.14 \pm 0.06)\%$. Similar tables are implemented for other b -hadrons. For the J/ψ all the 2 body decays are listed explicitly, whereas ≥ 3 body decays are described in terms of quarks. For χ_{c1}, ψ' there are no additional conditions for number of particles in the final state.

- $B_d \rightarrow J/\psi K_S \implies K_S \rightarrow \pi^+ \pi^-, J/\psi \rightarrow \mu^+ \mu^-$
- $B_d \rightarrow J/\psi K^* \implies K^* \rightarrow K^\pm \pi^\mp, J/\psi \rightarrow \mu^+ \mu^-$
- $B^\pm \rightarrow J/\psi K^\pm \implies J/\psi \rightarrow \mu^+ \mu^-$
- $B_s \rightarrow J/\psi \phi \implies \phi \rightarrow K^+ K^-, J/\psi \rightarrow \mu^+ \mu^-$

Since it is clear that for very soft tracks, track finding efficiency deteriorates, the appearing stable hadrons were required to pass kinematic cuts² $p_t(\text{hadron}) > 0.5 \text{ GeV}/c$ and $|\eta| < 2.4$, otherwise the event was skipped. In the corresponding step of inclusive simulation there was no constraint on products if B chain decays (except of J/ψ) and the event was not skipped if the products did not pass the above kinematic cut. In both inclusive and exclusive classes J/ψ was forced to decay into a $\mu^+ \mu^-$ state. For each μ its acceptance was checked and only events with both muons passing acceptance criteria were kept. For the acceptance, the standard CMS ACCMRPC [74] routine was used, which returned the acceptance probability that muon would be observed in at least two muon stations (it is assumed that it is equivalent to its identification). Additionally for each of two muons probability to give a trigger (lowest possible cut) was checked using the standard CMS EFFMRPC [74] routine³. If none of them gave the trigger, event was skipped.

At this step, an event record consisted of one B decayed in the investigated channel (or inclusively into $J/\psi X$) down to stable particles, other short-living

²In this thesis it is assumed that hadrons with p_t above $0.5 \text{ GeV}/c$ are well reconstructed. The usually taken safety threshold is $0.7 \text{ GeV}/c$. It is also assumed that the region of efficient tracking is limited to $|\eta| < 2.4$.

³Both ACCMRPC and EFFMRPC were primarily developed for the RPC trigger study, however for low p_t cuts are representative for the whole muon trigger system.

mode	PDG Br. Ratio	simulated BR
J/ψ anything	$(1.14 \pm 0.06)\%$	
J/ψ anything [direct]	$(8.0 \pm 0.8) \times 10^{-3}$	8.4×10^{-3}
ψ' anything	$(3.5 \pm 0.5) \times 10^{-3}$	3.5×10^{-3}
χ_{c1} anything	$(4.2 \pm 0.7) \times 10^{-3}$	
χ_{c1} anything [direct]	$(3.7 \pm 0.7) \times 10^{-3}$	3.7×10^{-3}
χ_{c2} anything	$< 3.8 \times 10^{-3}$	
η_c anything	$< 9 \times 10^{-3}$	

Table 3.3: The charmonium decay modes of B_d/B^\pm listed in [29], and the ones used in the simulation. In the simulation the $B \rightarrow J/\psi$ anything [direct] branching ratio was tuned to obtained the overall $B \rightarrow J/\psi$ anything branching ratio of 1.14% (with $\text{BR}(\psi' \rightarrow J/\psi \text{ anything})=57\%$ and $\text{BR}(\chi_{c1} \rightarrow J/\psi \text{ anything})=27.3\%$).

(exited) b -hadrons decayed to the quasi-stable ones, while the rest of the particles was still undecayed.

The next step was to decay not yet decayed particles looking for an associated muon. The standard PYTHIA decay table was used. To do that in the inclusive simulation the PYTHIA table of valid decay modes for b -hadrons was changed twice per event – initially only entries to Table 3.2 were selected, later (in order to get associated muon) the default PYTHIA modes were restored.

Unfortunately, the probability to find an associated muon passing all the selection criteria is small. Hence for each event this step was repeated 1000 times for exclusive jobs or 100 times in case of inclusive jobs. In most of events at least one associated muon was found (see Figure 3.2), while the computer time consumption was only increased by a small factor⁴, since most of its time was used to read the event and perform initial fragmentation.

If more than one muon was found in one of the repeated decays, the hardest was chosen. Its acceptance and trigger capability were checked, similarly to muons from J/ψ decay. As it was mentioned (sections 1.2.5 and 2.6) in the low luminosity LHC mode the dimuon trigger is sufficient to reduce rate to the acceptable level. Thus, although in the investigated channels there are three muons in the final state, only two of them are required to give a trigger. The third one is expected to be accepted only.

There was, however, additional requirement for an associated muon. It originated from the idea of minimising the influence of possible fake asymmetries introduced by the detector. For each η and p_t , the ISYMRPC [74] (see Figure 3.3) routine decided if the muon may introduce fake asymmetries or not (in other words it was checked if the direction of motion of the muon and its p_t was in the range, where acceptance and trigger probability were equal for positively and negatively charged muons). The use of ISYMRPC function

⁴The relative CPU times to generate 1:10:100:1000 decays of the same event in order to find associated muon were 1 : 1.03 : 1.37 : 4.6

eliminates the need of additional cuts. If ISYMRPC (applied to associated muon only) accepts the event it means that the associated muon of opposite charge would be accepted too. The number of associated muons passing the above fake asymmetry cut, acceptance criteria and (together with muons from J/ψ) dimuon trigger requirements, was the weight of the event.

In the typical LHC event, even at luminosity of $10^{33}\text{cm}^{-2}\text{s}^{-1}$ there are several pp collisions in one bunch crossing. Hence, in the background dedicated simulation, to reproduce initial conditions at the LHC, hadrons from additionally generated minimum bias events (without any b -quarks) joined the event record. The number of minimum bias events was calculated from the Poisson distribution with a mean of $n_{\text{min. bias}} = 1.4$.

After this step, an event record (passed to analysing program) was composed of B decaying to one of the investigated states (or inclusively), the products of its chain decay (including muons from J/ψ decay) and a list of associated muons found in 1000 (100) decays. Additionally, in the inclusive jobs the list of all charged, stable hadrons in $|\eta| < 2.4$ and with $p_t > 0.5$ was superimposed (from the $b\bar{b}$ event itself and additional minimum bias events). This list was made when first associated muon passed all applied cuts and was used to form the combinatorial background in background analysing job.

Since the collected statistic appeared not to be sufficient for the background analysis (inclusive decays) all the generated events were processed 20 times (introducing a negligible bias).

3.1.3 Analysis

The next step was to simulate CMS reconstruction sensitivities. In order to do that, momenta of all charged particles were smeared with the TSMEARP routine [75], developed to parameterise momentum measurement of particles from the primary vertex or nearby. With the smeared momenta, the invariant masses were calculated. They were required to be within the predefined window around the true masses of reconstructed particles.

The allowed mass regions are given in Table 3.4. They were obtained studying the mass resolution in signal channels (see Figures 3.4–3.7) and cover approximately 95% of signal events. The exception are the mass windows around resonances (K^* , ϕ) where more narrow mass bounds were used (75% and 90% respectively). Moreover, the TSMEARP do not work correctly for reconstruction of pions from a K_S decay, since a K_S may decay far from the primary vertex. In this case the mass window was taken from the dedicated simulation described in section 1.2.2.c. Moreover, calculating the B masses, the mass constraints on the intermediate particles were taken into account (see caption of Figure 3.4).

On top of that, the following assumed reconstruction efficiencies were superimposed

particle (channel)	allowed mass window [MeV/c ²]
J/ψ (all channels)	± 35
ϕ ($B_s \rightarrow J/\psi \phi$)	± 8
K^* ($B_d \rightarrow J/\psi K^*$)	± 50
K_S ($B_d \rightarrow J/\psi K_S$)	± 17.2
B_d ($B_d \rightarrow J/\psi K_S, K^*$)	± 26
B^\pm ($B^\pm \rightarrow J/\psi K^\pm$)	± 30
B_s ($B_s \rightarrow J/\psi \phi$)	± 23

Table 3.4: The allowed mass bounds for reconstructed particles.

- reconstruction efficiency for each muon: $\epsilon(\mu) = 0.95$,
- reconstruction efficiency for charged hadrons (other than forming K_S): $\epsilon(h^\pm) = 0.9$,
- reconstruction efficiency of K_S (including decay probability in sensitive volume), $\epsilon(K_S) = 0.35$; pions from $K_S \rightarrow \pi^+\pi^-$ should independently pass hadron kinematic cuts,
- reconstruction efficiency for fake (combinatorial) K_S : $\epsilon(h^+h^-) = 0.035$, (rejection factor of 10 with respect to real K_S).

The final normalisation took into account assumed $b\bar{b}$ production cross-section $500\mu\text{b}$ (a standard value recommended by LHC Committee for LHC experiments) and branching ratios of forced decays (Tab. 3.5)

<i>channel</i>	<i>Branching Ratio</i>
$B_d \rightarrow J/\psi K_S$	$3.75 \cdot 10^{-4}$
$B_d \rightarrow J/\psi K^*$	$1.6 \cdot 10^{-3}$
$B^\pm \rightarrow J/\psi K^\pm$	$1 \cdot 10^{-3}$
$B_s \rightarrow J/\psi \phi$	$1 \cdot 10^{-3}$
$B \rightarrow (J/\psi, \psi', \chi_{c1})[\text{direct}]X$	0.0156

Table 3.5: Branching ratios used for the normalisation of exclusive jobs (upper part of the table) and inclusive ones (lower part of the table).

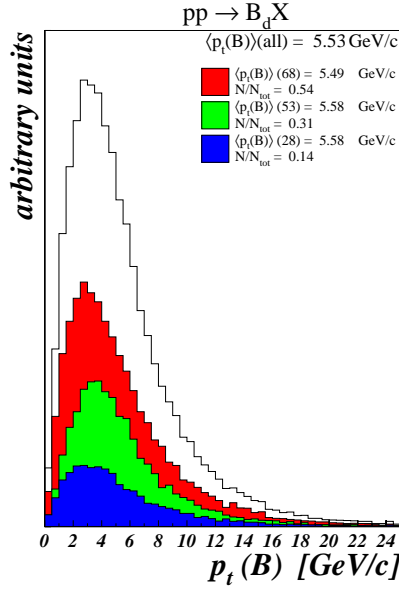


Figure 3.1: The obtained spectra of B_d mesons. The contribution from three most important processes (numbers in parentheses correspond to that given in Table 3.1) are shown. The ratio of b production due to gluon splitting (proc. 68 and 28) and gluon fusion (proc. 53) are roughly 2:1

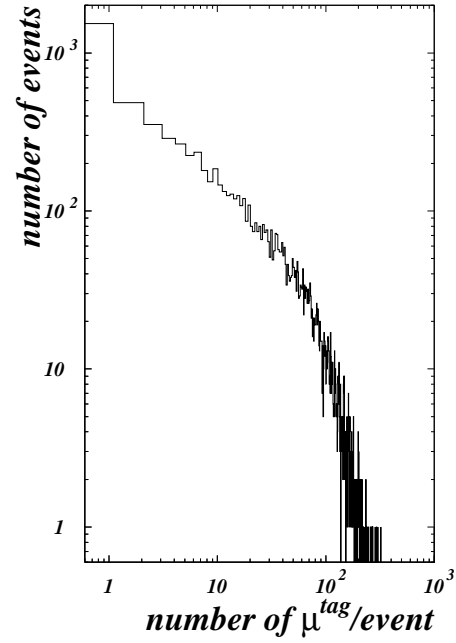
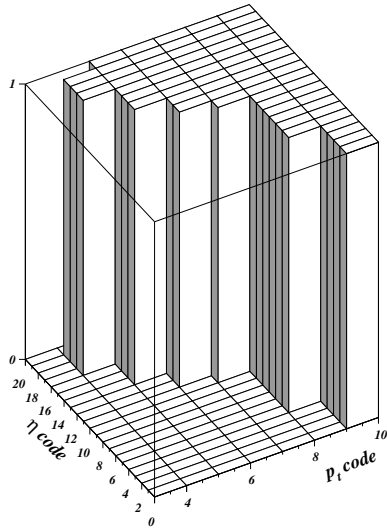


Figure 3.2: The obtained number of associated muons per one event. There were 1000 chances



η_{code}	η interval	η_{code}	η interval
0	0. - 0.09	10	1.30 - 1.40
1	0.09 - 0.28	11	1.40 - 1.50
2	0.28 - 0.47	12	1.50 - 1.60
3	0.47 - 0.63	13	1.60 - 1.75
4	0.63 - 0.78	14	1.75 - 1.87
5	0.78 - 0.92	15	1.87 - 1.99
6	0.92 - 1.04	16	1.99 - 2.10
7	1.04 - 1.14	17	2.10 - 2.20
8	1.14 - 1.22	18	2.20 - 2.30
9	1.22 - 1.30	19	2.30 - 2.40

bin	p_t interval (GeV)
3	1.5 - 2.0
4	2.0 - 2.5
5	2.5 - 3.0
6	3.0 - 3.5
7	3.5 - 4.0
8	4. - 5.
9	5. - ∞

Figure 3.3: The region in the η, p_t space where acceptance and probability of the trigger are equal for μ^+ and μ^- .

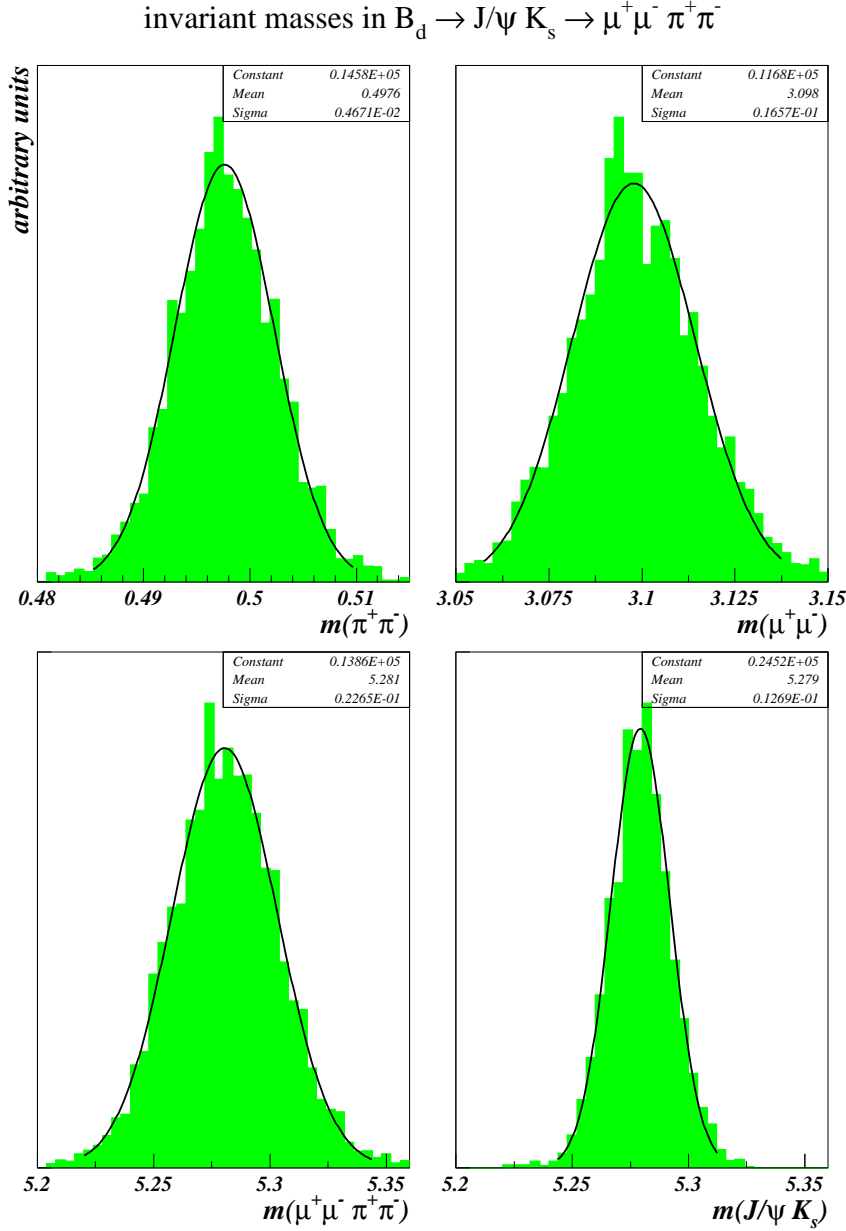


Figure 3.4: The invariant mass distributions in the $B_d \rightarrow J/\psi K_S \rightarrow \mu^+ \mu^- \pi^+ \pi^-$ channel. In left-top plot, the invariant mass of $\pi^+ \pi^-$ pair is shown. Since the smearing routine assumes that the track originates from the vertex or nearby the mass distribution is narrower than the one obtained in detailed simulation (section 1.2.2.c). In the right-top plot, the invariant mass of muons from J/ψ decays is shown. In the bottom histograms the final stable products are combined to B_d mass without (left-bottom histogram) or with (right-bottom histogram) mass constraints on the intermediate particles. The Gaussian fit to the centre of histograms is superimposed on each histogram. Using the mass constraints, instead of calculation of final-body (4-body in this case) invariant mass, the intermediate-body (2-body) invariant mass is calculated, with standard, tabular mass values of intermediate particles and momentum calculated on basis of final products (momentum of J/ψ is a sum of muonic momenta, momentum of K_S is a sum of pionic momenta), i.e. $m_{B_d}^2 = (E_{K_S} + E_{J/\psi})^2 - (\vec{p}_{\pi^+} + \vec{p}_{\pi^-} + \vec{p}_{\mu^+} + \vec{p}_{\mu^-})^2$ with $E_{K_S}^2 = m_{K_S}^2 + (\vec{p}_{\pi^+} + \vec{p}_{\pi^-})^2$, $E_{J/\psi}^2 = m_{J/\psi}^2 + (\vec{p}_{\mu^+} + \vec{p}_{\mu^-})^2$.

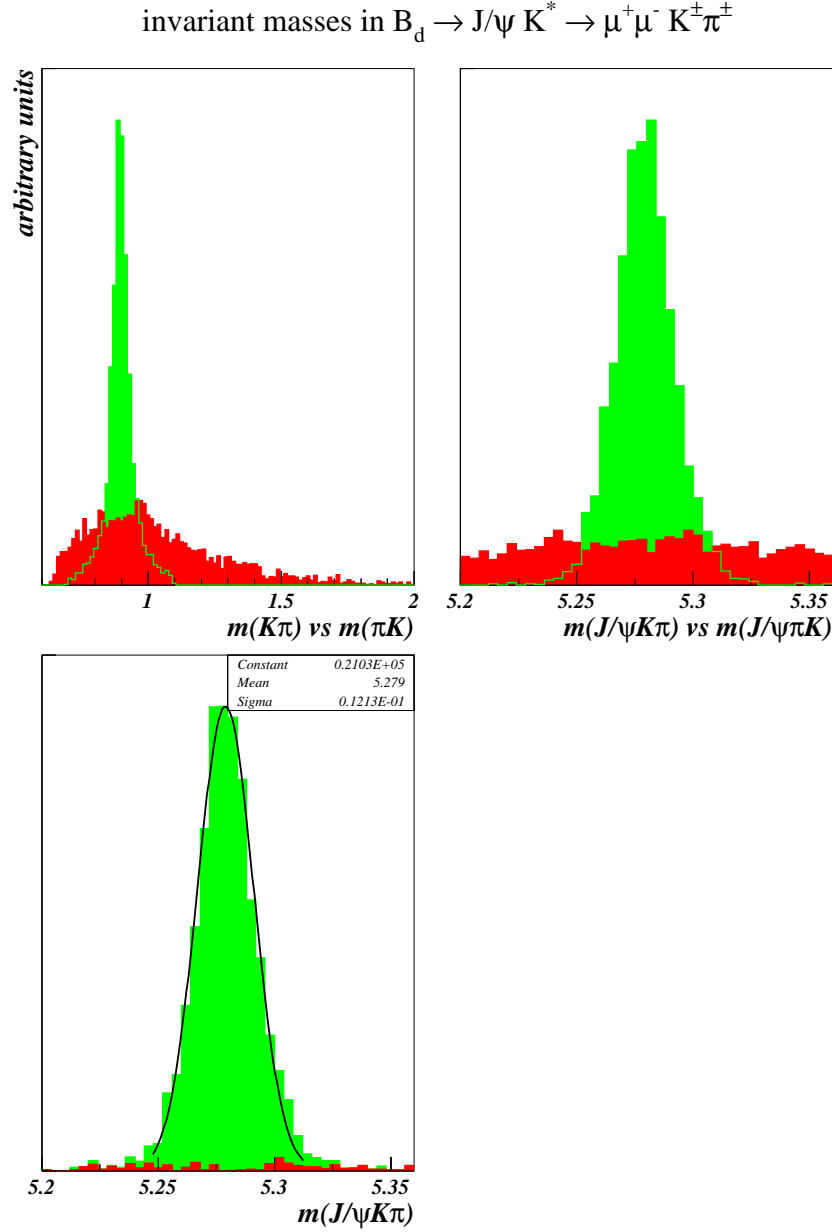


Figure 3.5: The invariant mass distributions in the $B_d \rightarrow J/\psi K^* \rightarrow \mu^+ \mu^- K^\pm \pi^\pm$ channel. In left-top plot the invariant mass of $K^\pm \pi^\mp$ pair is shown for the right $K-\pi$ identification (narrow peak) and for the wrong $K-\pi$ identification (wide distribution). In the right-top plot the invariant mass of B_d is shown for right (peaked distribution) and wrong (flat distribution) $K-\pi$ identification. At the bottom plot the B_d mass distribution is shown for events with unambiguous K^* identification. The (negligible) contribution from the wrong $K-\pi$ identification is marked. The J/ψ mass constraint is used for B_d mass calculation.

invariant masses in $B^\pm \rightarrow J/\psi K^\pm \rightarrow \mu^+ \mu^- K^\pm$

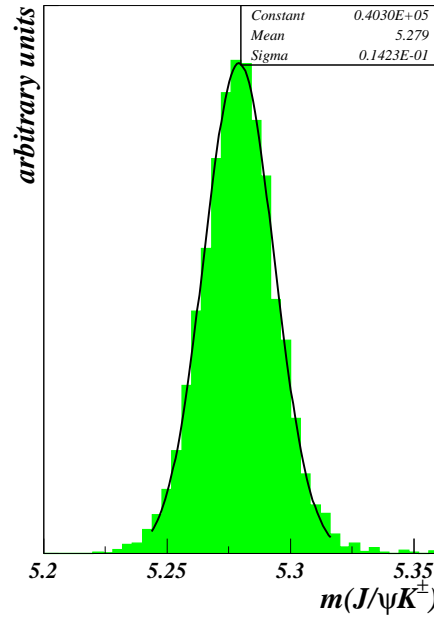


Figure 3.6: The invariant mass distributions in the $B^\pm \rightarrow J/\psi K^\pm \rightarrow \mu^+ \mu^- K^\pm$ channel. The J/ψ mass constraint is used for B^\pm mass calculation.

invariant masses in $B_s \rightarrow J/\psi \Phi \rightarrow \mu^+ \mu^- K^+ K^-$

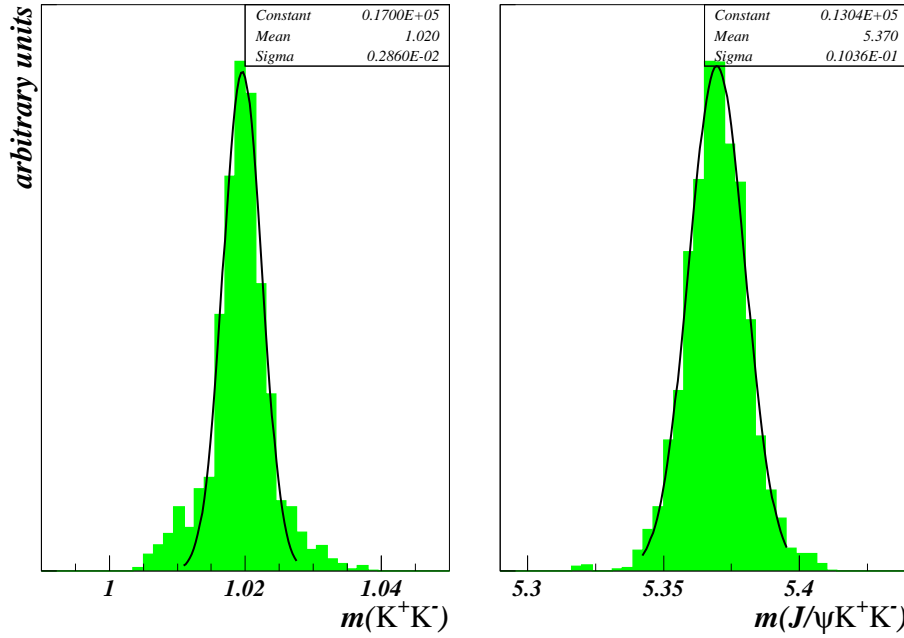


Figure 3.7: The invariant mass distributions in the $B_s \rightarrow J/\psi \phi \rightarrow \mu^+ \mu^- K^+ K^-$ channel. On the left plot, the invariant mass of $K^+ K^-$ pair is shown. The Breit-Wigner shape dominates over the Gaussian smearing. On the right plot, the B_s mass distribution is shown. The J/ψ mass constraint is used.

3.2 The results in the time integrated study

It should be stressed, that the number of signal events in thesis refers to the number of reconstructed decays in a given mode (for example $B^0 \rightarrow J/\psi K_S \rightarrow \mu^+ \mu^- \pi^+ \pi^-$) with an **ASSOCIATED MUON** coming from **ANY SOURCE**. It is not required to have any b ancestor. Such a treatment is in accordance with introduced formulae – the mistaggings are described by the dilution factor.

Although several cuts have already been introduced (since they are detector induced), the final number of events may still be a function of several variables (or additionally introduced cuts). The cuts should be chosen to get a minimal expected error on the CP violating asymmetries. For example, it is clear that, the dilution factor goes to one with the increasing p_t of an associated muon (fraction of mistaggings becomes smaller). At the same time the number of events becomes smaller. On the other hand, the harder final hadrons the less important the combinatorial background (thus D_{bgd} is closer to one) but again it is reflected in the signal statistic. Thus one have to look for the compromise.

The number of events after preselections, cuts and normalisation procedure (described in Section 3.1.3) was investigated as a function of p_t^{cut} on hadrons and p_t^{cut} on an associated muon to allow us to perform some (simplified) cut optimisation. One should notice that the probability of charged particle track reconstruction drops down significantly for tracks with p_t below 0.8 GeV/c. Additionally the requirement for an associated muon to pass the "acceptance symmetry" cut (as defined by ISYMRPC function) rejects associated muons with p_t below approximately 2-3 GeV/c in the forward region, and p_t below 4-5 GeV/c in the barrel (see Figure 3.3 and reference [74]).

The expected numbers of events were calculated for one LHC year in the low (initial) luminosity mode (10^7 seconds at $10^{33} \text{cm}^{-2} \text{s}^{-1}$, which corresponds to 10^4pb^{-1}). The numbers quoted below are number of events after normalisation, taking into account proper efficiencies, etc. Thus they are numbers of events that may be observed in the CMS experiment.

3.2.1 Expected number of signal events in the simulated channels

To investigate number of events in each of the channels, the exclusive class of jobs were used.

In the Figure 3.8, the expected number of events in $B_d^{0(-)} \rightarrow J/\psi K_S \rightarrow \mu^+ \mu^- \pi^+ \pi^-$ with an associated muon found is shown in a table-like plot as a function of cut on p_t of an associated muon (horizontal axis) and p_t of softer of pions from K_S decay (vertical axis). The statistical error of the simulation is shown in Figure 3.16. In the Figure 3.9, the number of events is presented as a function of p_t^{cut} on the associated muon. The fixed $p_t^{cut} = 0.75$ GeV for both pions was applied. The signal is split according to sources of additional (associated)

muon. Muons come not only from a $b \rightarrow \mu$ transitions (red histogram) but one can find substantial contributions from $b \rightarrow c \rightarrow \mu$ decays (blue histogram) and additionally produced $c \rightarrow \mu$ transitions (greens histogram). Furthermore, not negligible contribution is expected from muons coming from source not mentioned above (yellow histogram), namely mostly $K\pi$ decays. One can see that histograms become flat for low p_t^{cut} on the associated muon. This is because the ISYMRPC function was applied.

To analyse the $B_d^{(-)} \rightarrow J/\psi K^*$ followed with $K^{*0} \rightarrow K^+\pi^-$ ($\bar{K}^{*0} \rightarrow K^-\pi^+$) it is necessary to identify the flavour of K^* since it tags the flavour of initially produced⁵ B_d ($B_d^0 \rightarrow J/\psi K^{*0}$ while $\bar{B}_d^0 \rightarrow J/\psi \bar{K}^{*0}$). Unfortunately, CMS does not have particle identification. Thus the distinction can be made only on basis of the invariant mass calculation (see Figure 3.5). Assuming two hadrons of opposite charge h^+ and h^- were found, one may calculate two invariant masses - assuming h^+ is K^+ , h^- is K^- and vice versa. Both masses should be compared with the true value of K^* mass. If only one of them lay within the predefined K^* mass bound one may guess that the right combination was found. Such a combination is called unambiguous.

The expected number of events in $B_d^{(-)} \rightarrow J/\psi K^* \rightarrow \mu^+\mu^- K^\pm \pi^\mp$ decay with an associated muon is shown in the Figures 3.10 (errors in Figure 3.16) and 3.11 in a way similar to the $B_d \rightarrow J/\psi K_S$ channel. The quoted number of events corresponds to unambiguous K^* identification

In the same manner expected number of events in $B^\pm \rightarrow J/\psi K^\pm \rightarrow \mu^+\mu^- K^\pm$ and $B_s \rightarrow J/\psi \phi \rightarrow \mu^+\mu^- K^+K^-$ – both with an associated muon reconstructed are presented on Figures 3.12, 3.13 and 3.14, 3.15 respectively. The statistical errors of the simulation are shown in Figure 3.16.

3.2.2 The expected levels of background

It seems that the main source of background to investigated channels are events composed of real J/ψ 's combined with accidental muons and some hadrons to fulfill the signature of an event (Table 2.1). There are several sources of J/ψ 's

- Weak decays of b -hadrons. Since a b -quark usually decays to a c -quark and the \bar{c} -quark may come from a decay of virtual W , one may expect significant fraction of J/ψ that occurs in decays of b -hadrons. One should also note the possibility of a transition: b -hadrons $\rightarrow \psi' \rightarrow J/\psi$,
- Direct production of $c\bar{c}$ bound states. Note that all of them may subsequently decay to J/ψ ,
- Production of $c\bar{c}$ quarks that occasionally (small phase space) may form (collapse to) J/ψ .

⁵Since the produced B_d may mix before the decay this tagging is not perfect – it is diluted.

In the present simulation only the first item was taken into account. The contribution from other sources of real J/ψ is strongly suppressed by the required accompanied associated muon. Moreover in other real (and fake) sources the J/ψ is produced in the primary interaction point whereas J/ψ from B -meson decays are separated by the B decay path.

Inclusive b -hadron decays were simulated with its charmonium decay modes as in Table 3.2 (thus signal and background were simulated together). The final state particles were classified according to the signatures from Table 2.1, and appropriate invariant masses were calculated.

In the Figures 3.17-3.21, the expected number of events in the $B_d \rightarrow J/\psi K_S \rightarrow \mu^+ \mu^- \pi^+ \pi^-$ plus an associated muon μ^{tag} is shown in a presence of background. The numbers are presented as a function of cuts on the p_t of associated muon and the p_t of a softer hadron. In the upper table-like plot of the Figure 3.17 the number of true background events (i.e. signal events appearing in inclusive analysis are excluded) is shown. In the bottom table-like plot the statistical precision of the above result is given. Next, in the Figure 3.18 signal to background ratio is shown. It is clearly seen that the level of background decreases substantially with increasing p_t^{cut} on hadrons, while the dependence on the p_t^{cut} of the associated muon is weaker. As an example for $p_t^{cut}(hadrons) = 0.75$ GeV/c the signal to background ratio varies in the range $5.0 \div 6.4$ for $p_t^{cut}(\mu^{tag})$ $2.0 \div 7.0$ GeV/c but for fixed $p_t^{cut}(\mu^{tag}) = 5$ GeV/c the signal to background ratio changes between ~ 2 up to ~ 10 in the $p_t^{cut}(hadrons)$ range $0.5 \div 1.25$ GeV/c. The number of signal events used to calculate signal to background ratio is taken directly from dedicated signal simulation (Figure 3.8). Nevertheless, as an cross-check one may obtained number of signal events from background-dedicated (inclusive) study, what is shown in Figure 3.19 with an statistical error about twice larger than in the dedicated signal study (the number of signal events in the inclusive decays is small).

Since only the background with real J/ψ 's was investigated, the $B_d \rightarrow J/\psi K_S$ channel might have been faked by a real J/ψ plus a real K_S , or the real J/ψ plus a fake K_S . In the first case the K_S may be any real K_S coming from any source – for example from $B_d \rightarrow J/\psi K_S \pi^0$ as well as any K_S coming from the superimposed minimum bias events. In the second case, the K_S is faked by any two hadrons of opposite charge (they are assumed to be pions) passing the K_S mass bounds. These two hadrons may even come from decays of two K_S (the first pion is taken from one K_S cuts and the second pion from another one). It is assumed that the reconstruction efficiency of real K_S is 35%. It is clear that in the case of two hadrons which fake a K_S , this reconstruction efficiency is smaller, since they do not have the same production vertex or they may come from the primary vertex. The value of 3.5% was taken in this case. This is presented in Figure 3.20, where the background events of Figure 3.17 are split to real K_S (upper plot) and fake K_S (lower plot).

The typical shape of invariant mass distribution for the reconstructed decay $B_d \rightarrow J/\psi K_S \oplus \mu$ with fixed $p_t^{cut}(\mu^{tag}) = 3.0$ GeV/c and several cuts on hadronic transverse momenta is shown in the Figure 3.21. A clear mass peak is well

visible over combinatorial background even for softer investigated hadronic cut.

In the same way as in $B_d \rightarrow J/\psi K_S \rightarrow \mu^+ \mu^- \pi^+ \pi^- \oplus \mu$ channel, the level of background was analysed in $B_d \rightarrow J/\psi K^* \rightarrow \mu^+ \mu^- K^\pm \pi^\mp \oplus \mu$, $B^\pm \rightarrow J/\psi K^\pm \rightarrow \mu^- \mu^+ K^\pm \oplus \mu$ and $B_s \rightarrow J/\psi \phi \rightarrow \mu^+ \mu^- K^+ K^- \oplus \mu$ channels. The reconstructed number of background events with the statistical errors is shown in Figures 3.22, 3.25 and 3.28 respectively; the signal to background ratio in Figures 3.23, 3.26 and 3.29. Finally, the typical shapes of invariant mass distributions for the mentioned processes are shown in Figures 3.24, 3.27 and 3.30.

3.2.3 Dilution factor due to tagging

As described in Chapter 2, the dilution due to tagging reflects the possibility of wrong flavour identification of initially produced B -meson which decays to the reconstructed CP eigenstate. Specifying the value of the dilution factor due to tagging is equivalent to quoting the fractions of wrong tags (number of wrong tags divided by the number of all reconstructed tags), since they are related by (see formula 2.10) $D_{tag} = 1 - 2w$, where w stands for probability of mistagging (wrong tag).

As explained in Section 2.3 the fraction of wrong tags cannot be measured using the products of CP eigenstate in the investigated CP violating process. Instead, it should be predicted by looking at the processes of similar type and kinematics (control channels) with the same (or similar) sources of mistaggings. Nevertheless, the simulation offers the possibility to cross-check how well the fraction of wrong tags measured in control channels matches the original one. This is because in the simulation the flavour of initially produced B -meson is known in contrast to real data.

Since the mixing of associated B -mesons influences the wrong tags, it is necessary to quote the values of mixing parameters. In the presented simulation the values chosen were⁶: $x_d = 0.7$ and $x_s = 10$.

The fraction of wrong tags in the investigated channels is calculated in the exclusive (signal dedicated) simulations. The muon is classified as a wrong tag if its charge differs from the one expected on the basis of the flavour (at the production time) of B decaying later to the investigated state. The results of the simulation are presented in the table-like plots of the Figure 3.31 (statistical error given in Figure 3.32). The typical value for the channel $B_d \rightarrow J/\psi K_S \oplus \mu$ for $p_t^{cut}(\mu^{tag}) = 5$ GeV and $p_t^{cut}(pions) = 0.75$ GeV is approximately 0.25 giving the dilution factor $D_{tag} \approx 0.5$. It is clear that in the case of $B_d \rightarrow J/\psi K_S \oplus \mu$ and $B_s \rightarrow J/\psi \phi \oplus \mu$ channels the numbers presented are not measurable exper-

⁶The PDG reports [29] $x_d = 0.73 \pm 0.05$ and $x_s > 9.5$ (95% C.L.). The newer results [76] suggests slightly lower central value of x_d and stronger bounds to x_s (> 14 95% C.L.). One should note however, that even with $x_s = 10$ the mixing of B_s is maximal, because $\chi_s = \frac{x_s^2}{2+2x_s^2} = \frac{1}{2} \frac{100}{101} \approx \frac{1}{2}$

imentally. On the other hand in $B^\pm \rightarrow J/\psi K^\pm \oplus \mu$ the charge of kaon tags the charge of initially produced B^\pm . The situation is more complicated in the case of $B_d \rightarrow J/\psi K^* \oplus \mu$. Here, the unique K^* identification tags the flavour of B_d at the time of decay, which may differ from the flavour of initially produced B_d due to oscillations. As explained in section 2.6.2 this ambiguity is reflected by the (known) extra dilution factor increasing the measurable fraction of wrong tags.

The comparison between fractions of wrong tags in the Figure 3.32 cannot be done directly, since the decay kinematic slightly differs from channel to channel. It is shown in the Figure 3.33, where the distribution of transverse momentum of B -meson decaying in the investigated channel is shown. In all the channels the same cuts ($p_t^{cut}(hadrons) = 0.75$ GeV/c and $p_t^{cut}(\mu^{tag}) = 3$ GeV/c) were applied. Only reconstructed events are shown in histograms.

To make the fractions of wrong tags comparable one has to unify the underlying distribution of $\langle p_t(B) \rangle$. One solution is to tune the p_t^{cut} cuts on hadrons. This procedure is shown in Figure 3.34. In the left column the mean transverse momentum of B decaying to reconstructed state is shown as a function of cut on final hadrons. The horizontal line in left column is at $\langle p_t(B) \rangle \simeq 21.6$ GeV/c which is the mean $p_t(B)$ at $p_t^{cut}(hadrons) = 0.75$ GeV/c in the $B_d \rightarrow J/\psi K_S \oplus \mu$ channel (Figure 3.33). The vertical line suggest the hadronic cuts $p_t^{cut}(hadrons) \approx 0.75$ GeV/c, 2.5 GeV/c and 1.5 GeV/c in the channels $B_d \rightarrow J/\psi K^* \oplus \mu$, $B^\pm \rightarrow J/\psi K^\pm \oplus \mu$ and $B_s \rightarrow J/\psi \phi \oplus \mu$ respectively to reproduce the conditions of $B_d \rightarrow J/\psi K_S \oplus \mu$ with the cut $p_t^{cut}(hadrons) \approx 0.75$ GeV/c.

The same result may be obtained in slightly different way. The kinematic of the primary decay (not to final observable hadrons but just the decay of B -meson) should be very similar because K_S , K^* , K^\pm and ϕ are light comparing to J/ψ . Hence one may expect that distributions of p_t of B -meson in various decay channels should be more similar using the p_t of primary hadron rather than the cut on final hadrons. This expected behaviour is shown in the middle column of the Figure 3.34. In the right column of Figure 3.34 the distribution of mean of the p_t of the primary hadron is shown as a function of p_t cut on final hadrons. Specifying the $p_t^{cut}(hadrons) = 0.75$ GeV/c in the $B_d \rightarrow J/\psi K_S \oplus \mu$ channel one uses the sample with the mean p_t of K_S approximately 7.85 GeV/c. Forcing the same mean p_t of primary hadron in other channels implies the same (listed above) cuts in other channels (see vertical and horizontal lines in the right column of the Figure 3.34).

A closer look at the fraction of wrong tags may be taken by looking at Figures 3.35-3.38, where the wrong tags are split into sources. The contributions from separated classes of tags are similar in the investigated channels. In the Figure 3.39, the probability of right and wrong tag in the given tag source is investigated. Here, the number of wrong tags is divided just by a number of right tags in the same class (not by the total number of tags as previously). Thus value of one means that the probability of having a good tag and a wrong one are equal.

The final result of this analysis is the comparison of the dilution factors taken as a function of $p_t^{cut}(\mu^{tag})$ for the hadronic cuts fixed by the requirement of the B -meson distribution with the same mean. It is shown in the Figure 3.40 where the $\pm 1\sigma$ corridors of the dilution factor are shown for the investigated channels. The agreement is satisfactory. Thus the dilution factor in the channels where the fraction of wrong tags is unmeasurable ($B_d \rightarrow J/\psi K_S \oplus \mu$ and $B_s \rightarrow J/\psi \phi \oplus \mu$) may be provided by the measurement in the control channels.

3.2.4 The predicted error on intrinsic asymmetries

The expected number of events, level of background and a probability of observing a wrong tag allow us to calculate (with formula 2.12) the intrinsic (raw) asymmetry by measuring a number of positively and negatively charged tracks. It is possible to quote the expected error. A (simplified) calculation of an error leads to [68]

$$\delta(\text{Im}r_{CP}) = \frac{1}{D_{int} \cdot D_{tag} \cdot D_{bgd} \cdot \sqrt{N_{tot}}} \quad (3.1)$$

To calculate an error on intrinsic asymmetry in $B_d \rightarrow J/\psi K_S \oplus \mu$, where the intrinsic asymmetry is $\text{Im}(r_{CP}) = \sin 2\beta$, the value of $x_d = 0.7$ was used (to calculate D_{int}). N_{tot} is a sum of signal and background events i.e. sum of tables in Figures 3.8 and 3.17. D_{bgd} was calculated by dividing number of signal events in the table in Figure 3.8 by N_{tot} . D_{tag} is calculated on the basis of the most upper table in the Figure 3.31. The result is shown as a table-like plot in Figure 3.41. The minimal error on $\sin 2\beta$ is $\delta(\sin 2\beta)_{min} = 0.054$ for low $p_t^{cut}(\mu^{tag})$ and $p_t^{cut}(pions)$. One should note that the minimum is rather flat and there is a relatively wide area where the error on $\sin 2\beta$ is below 0.06.

To calculate an error on intrinsic asymmetry in $B_s \rightarrow J/\psi \phi \oplus \mu$, where the intrinsic asymmetry is expected to be small ($few \cdot 10^{-2}$), the value of $x_s = 10$ was used. N_{tot} is taken from tables in Figures 3.14 and 3.28, D_{bgd} is a product of division table in Figure 3.14 by N_{tot} . D_{tag} is based on fraction of wrong tags from the most lower table in Figure 3.31. The overall result is shown as a table-like plot in Figure 3.42. The minimal error is $\delta(\text{Im}r_{CP}) \approx 0.23$, much above the value predicted by the Standard Model. Thus the $B_s \rightarrow J/\psi \phi \oplus \mu$ channel in the time integrated study **cannot be used** to measure $\sin \gamma$.

The similar number of events, dilution factor due to tagging and small fraction of background makes the $B_d \rightarrow J/\psi K_S \oplus \mu$ and $B_s \rightarrow J/\psi \phi \oplus \mu$ channels looking very similar. The large difference of the precision of measurement of intrinsic asymmetry (roughly factor of five) originates from the difference of D_{int} in equation (3.1) which is ≈ 0.47 for $B_d \rightarrow J/\psi K_S \oplus \mu$ and ≈ 0.1 in the case of $B_s \rightarrow J/\psi \phi \oplus \mu$. The larger the mixing is the less sensitive is the time integrated study. Increasing the x_s up to 20 would reflect in the minimal error as big as approximately 0.5.

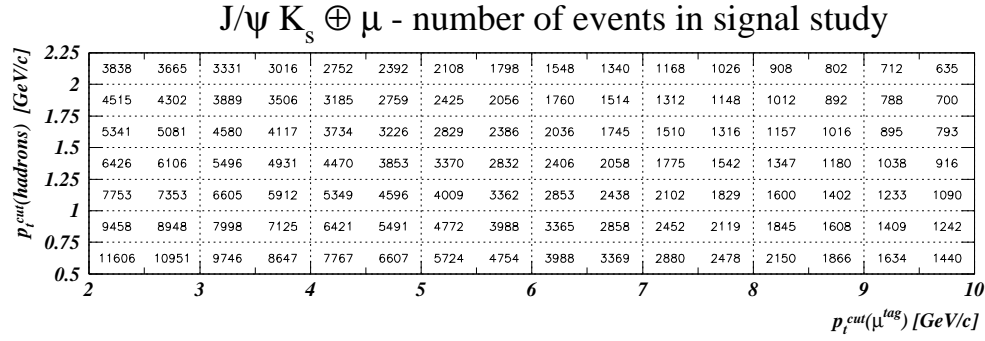


Figure 3.8: The expected number of fully reconstructed events in $B_d \rightarrow J/\psi K_S$ channel followed by $J/\psi \rightarrow \mu^+\mu^-$ and $K_S \rightarrow \pi^+\pi^-$, with an associated muon found. The number of events is presented as a function of the cut on p_t of an associated muon and the cut on p_t of the softer pion.

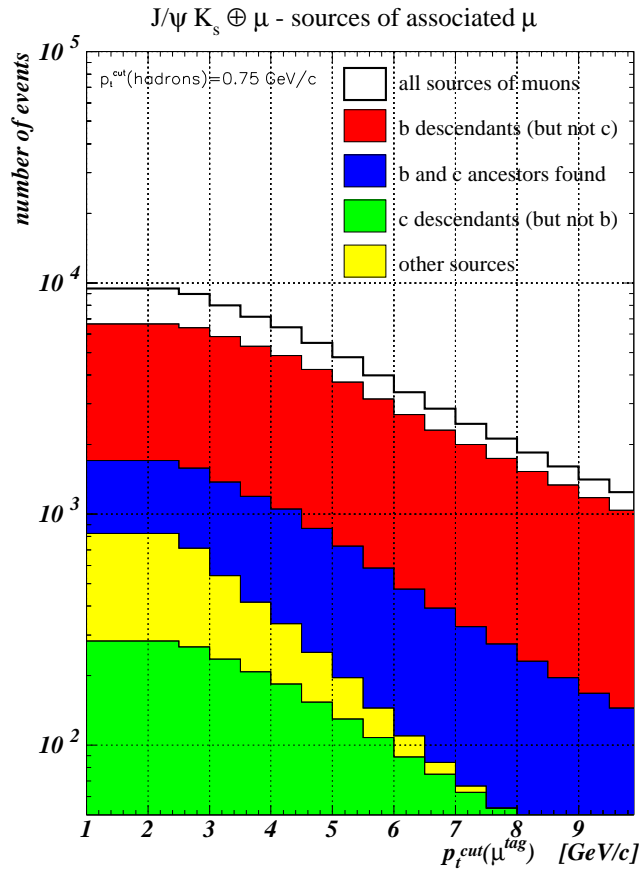


Figure 3.9: The expected number of reconstructed events in $B_d \rightarrow J/\psi K_S \oplus \mu$ channel as a function of p_t^{cut} on associated muon for fixed p_t^{cut} on pions. The various sources of an associated muons are shown.

$J/\psi K^* \oplus \mu$ - number of events in signal study

$p_t^{cut}(\text{hadrons})$ [GeV/c]	2.25	2	1.75	1.5	1.25	1	0.75	0.5									
	25283	24133	21887	19713	17889	15486	13577	11509	9805	8369	7212	6218	5441	4735	4177	3699	
	29932	28547	25876	23326	21153	18325	16090	13600	11594	9915	8558	7392	6475	5648	4987	4424	
	35249	33554	30317	27263	24682	21315	18668	15741	13393	11430	9847	8510	7438	6473	5698	5045	
	42750	40639	36610	32837	29709	25566	22348	18718	15856	13474	11565	9931	8630	7489	6555	5779	
	51078	48490	43543	38959	35170	30164	26294	21960	18529	15693	13410	11473	9941	8604	7514	6596	
	61132	57898	51806	46280	41667	35613	30955	25808	21697	18335	15660	13382	11554	9988	8709	7626	
	74285	70165	62518	55606	49922	42432	36769	30467	25432	21394	18148	15438	13292	11444	9965	8699	
$p_t^{cut}(\mu^{tag})$ [GeV/c]	2	3	4	5	6	7	8	9	10								

Figure 3.10: The expected number of fully reconstructed events in $B_d \rightarrow J/\psi K^*$ channel followed by $J/\psi \rightarrow \mu^+ \mu^-$ and $K^* \rightarrow K^\pm \pi^\mp$, with an associated muon found. The number of events is presented as a function of the cut on p_t of an associated muon and the cut on p_t of the softer hadron.

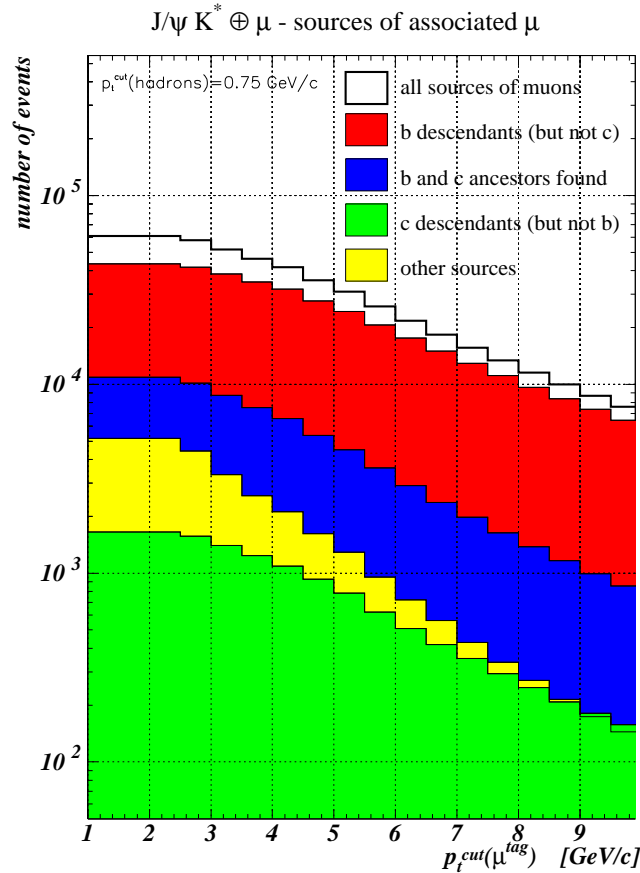


Figure 3.11: The expected number of reconstructed events in $B_d \rightarrow J/\psi K^* \oplus \mu$ channel as a function of p_t^{cut} on associated muon for fixed p_t^{cut} on hadrons. The various sources of an associated muons are shown.

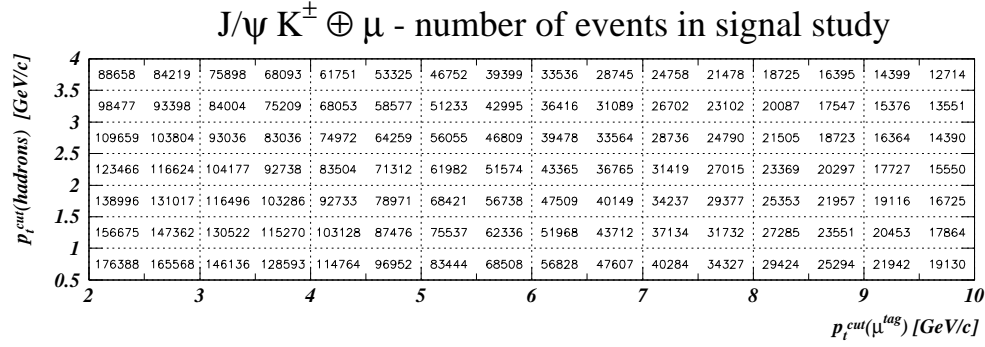


Figure 3.12: The expected number of fully reconstructed events in $B^\pm \rightarrow J/\psi K^\pm$ channel followed by $J/\psi \rightarrow \mu^+ \mu^-$, with an associated muon found. The number of events is presented as a function of the cut on p_t of an associated muon and the cut on p_t of the observed kaon.

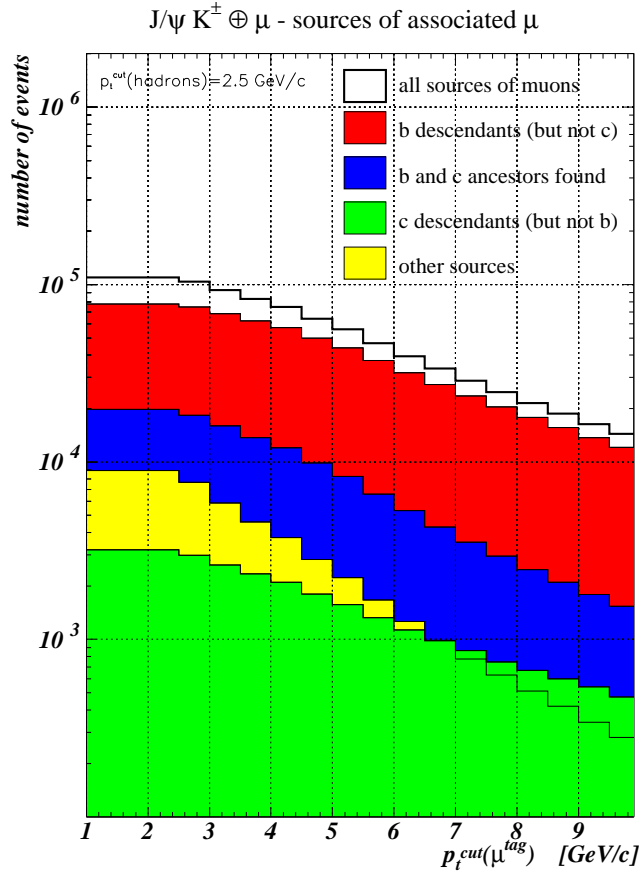


Figure 3.13: The expected number of reconstructed events in $B^\pm \rightarrow J/\psi K^\pm \oplus \mu$ channel as a function of p_t^{cut} on associated muon for fixed p_t^{cut} on observed kaon. The various sources of an associated muons are shown.

$J/\psi \Phi \oplus \mu$ - number of events in signal study

$p_t^{cut}(\text{hadrons})$ [GeV/c]	2.25	8151	7750	6951	6227	5637	4875	4296	3611	3053	2607	2234	1931	1679	1466	1291	1134
	2	9196	8727	7807	6979	6294	5429	4770	4003	3377	2878	2461	2121	1841	1598	1399	1223
	1.75	10749	10204	9134	8158	7347	6326	5556	4665	3931	3346	2855	2458	2130	1845	1616	1413
	1.5	12241	11606	10368	9237	8299	7113	6214	5194	4361	3697	3145	2698	2331	2014	1756	1535
	1.25	13828	13084	11654	10366	9301	7946	6924	5772	4838	4095	3477	2982	2575	2226	1946	1706
	1	15923	15047	13377	11872	10642	9063	7873	6528	5449	4601	3894	3329	2870	2469	2154	1886
	0.75	17727	16710	14822	13106	11736	9950	8605	7095	5889	4937	4160	3545	3045	2609	2267	1977
	0.5																
		2	3	4	5	6	7	8	9	10							
	$p_t^{cut}(\mu^{tag})$ [GeV/c]																

Figure 3.14: The expected number of fully reconstructed events in $B_s \rightarrow J/\psi \phi$ channel followed by $J/\psi \rightarrow \mu^+ \mu^-$ and $\phi \rightarrow K^+ K^-$, with an associated muon found. The number of events is presented as a function of the cut on p_t of an associated muon and the cut on p_t of the softer hadron.

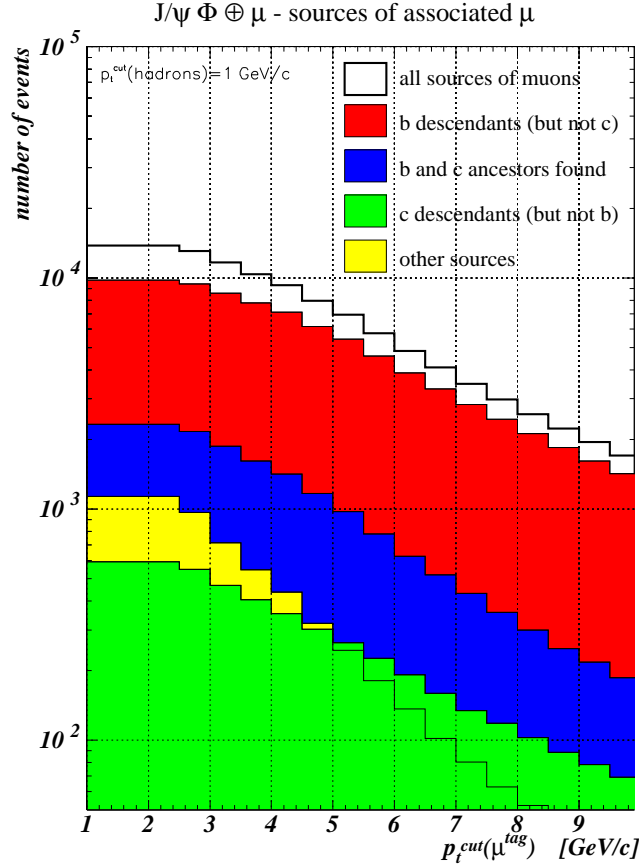


Figure 3.15: The expected number of reconstructed events in $B_s \rightarrow J/\psi \phi \oplus \mu$ channel as a function of p_t^{cut} on associated muon for fixed p_t^{cut} on final hadrons. The various sources of an associated muons are shown.

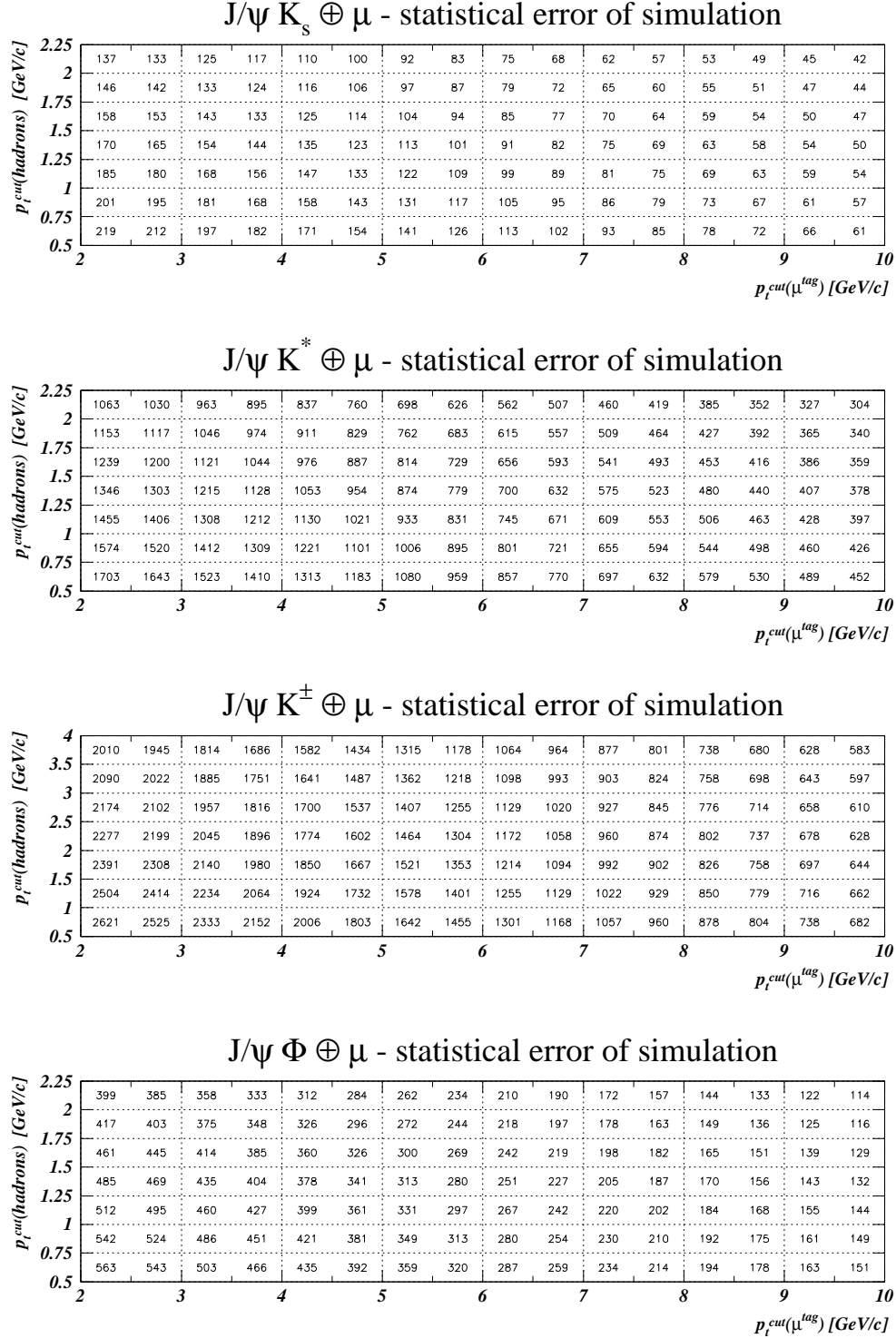


Figure 3.16: The statistical error of the simulation for the investigated signal channels, expressed in number of events. To be compared with Fig. 3.8, 3.10, 3.12 and 3.14.

$J/\psi K_S \oplus \mu$ - background study

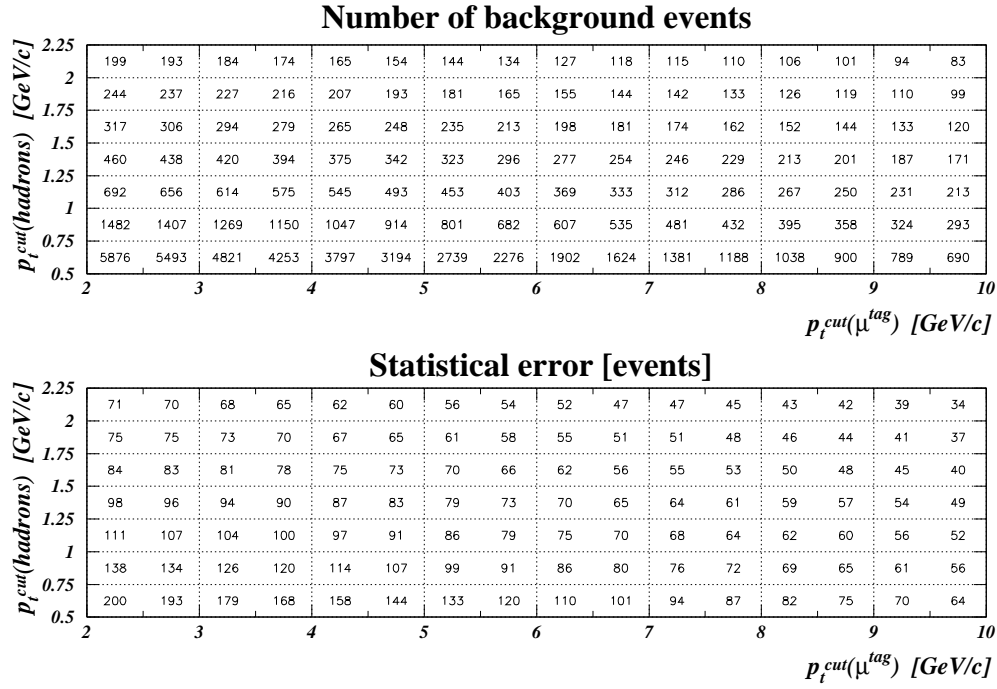


Figure 3.17: The background contributing to $B_d \rightarrow J/\psi K_S \oplus \mu$ channel obtained in the inclusive simulation. In the upper table-like plot the expected number of background events is shown, whereas the lower plot presents the statistical error of the simulation.

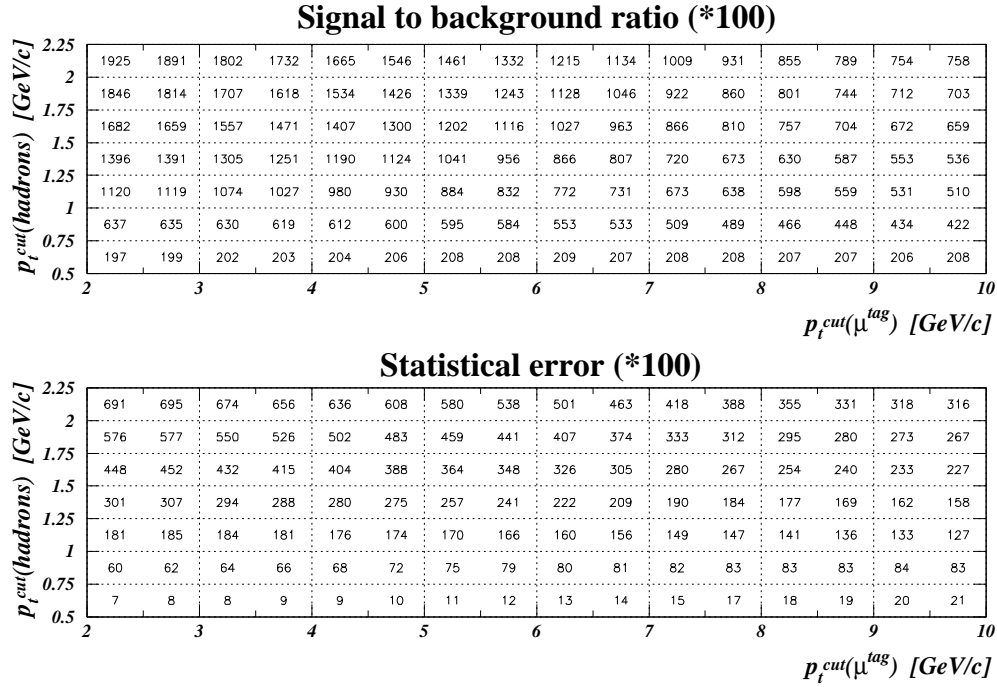


Figure 3.18: Signal to background ratio and its statistical error in the $B_d \rightarrow J/\psi K_S \oplus \mu$ channel.

J/ψ K_S ⊕ μ - background study

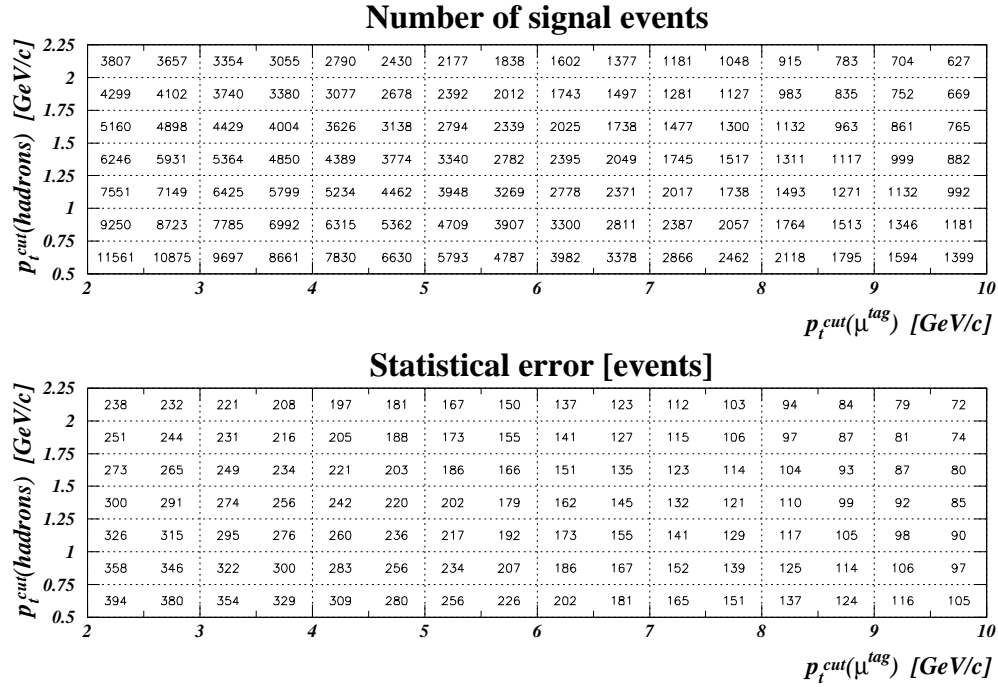


Figure 3.19: The signal events appearing in $B_d \rightarrow J/\psi K_S \oplus \mu$ analysis of the inclusive simulation.

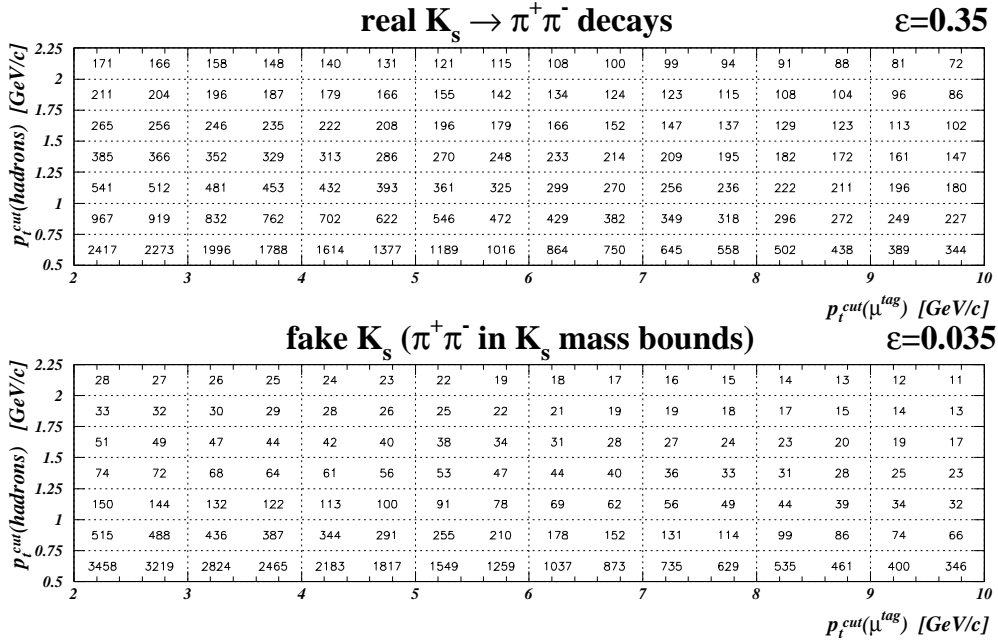


Figure 3.20: The contributions to background for $B_d \rightarrow J/\psi K_S \oplus \mu$ channel. In the upper table-like plot background events with real K_S are shown. The reconstruction efficiency was assumed to be 35%. In the lower plot contribution from hadrons faking the K_S is shown. The reconstruction efficiency was assumed to be ten times lower than in previous case.

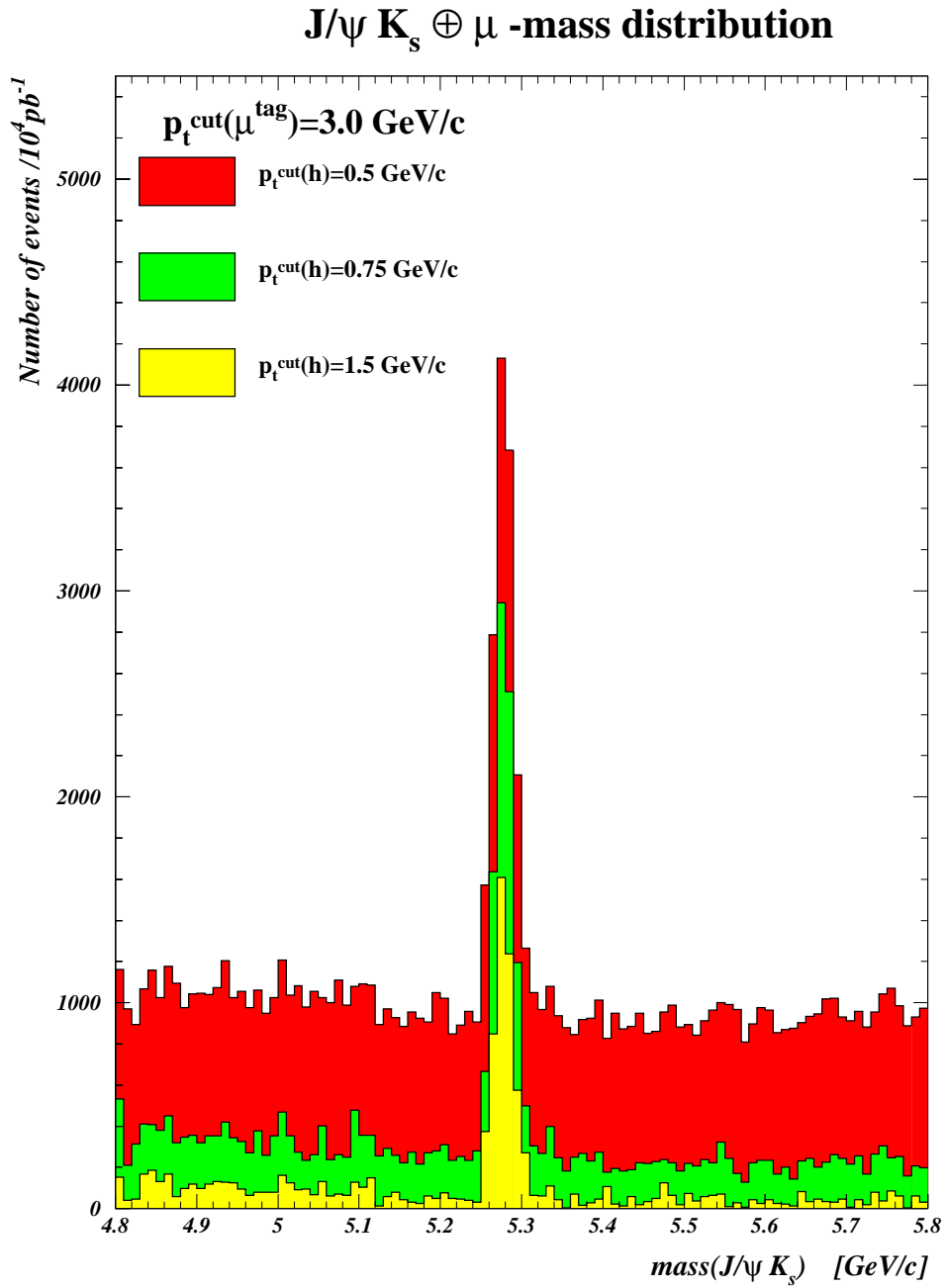


Figure 3.21: The typical views of the invariant mass distribution in the $B_d \rightarrow J/\psi K_s \oplus \mu$ channel.

$J/\psi K^* \oplus \mu$ - background study

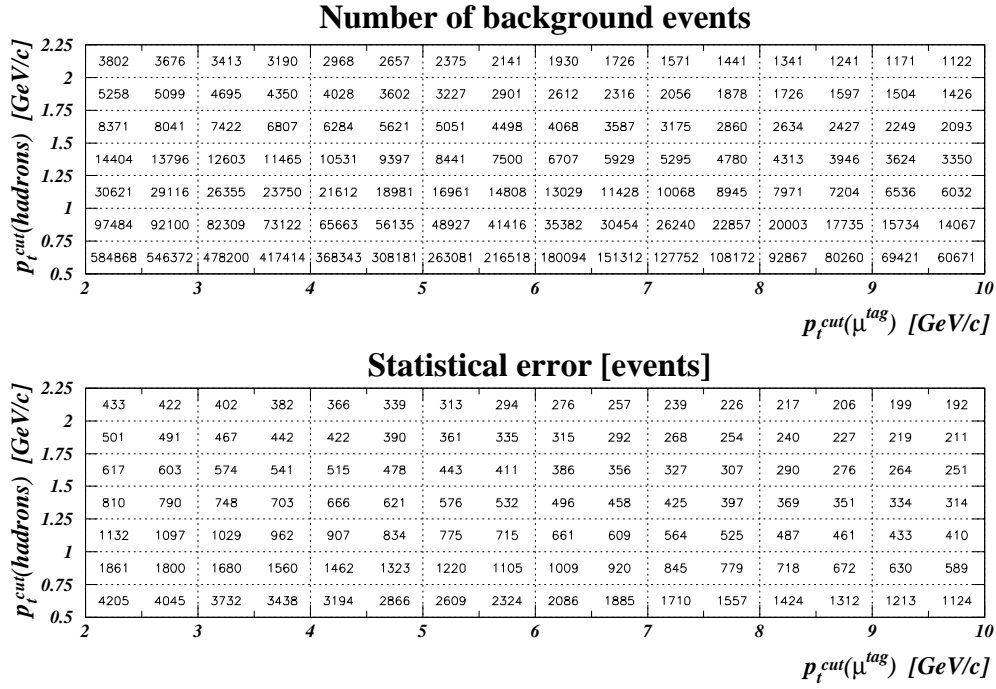


Figure 3.22: The background contributing to $B_d \rightarrow J/\psi K^* \oplus \mu$ channel obtained in the inclusive simulation. In the upper table-like plot the expected number of background events is shown, whereas the lower plot presents the statistical error of the simulation.

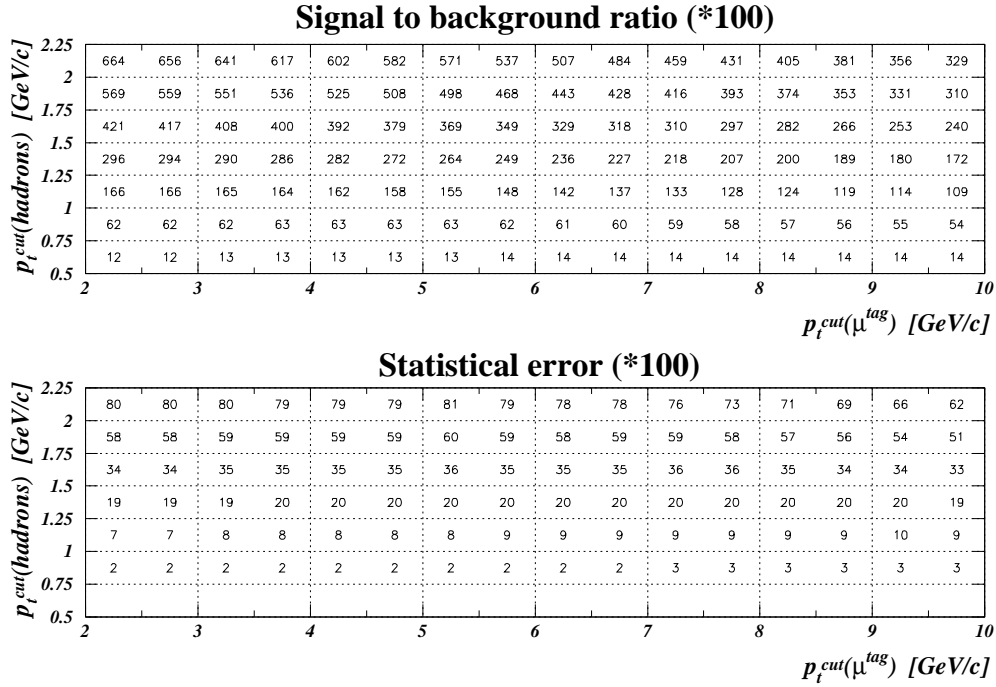


Figure 3.23: Signal to background ratio and its statistical error in the $B_d \rightarrow J/\psi K^* \oplus \mu$ channel.

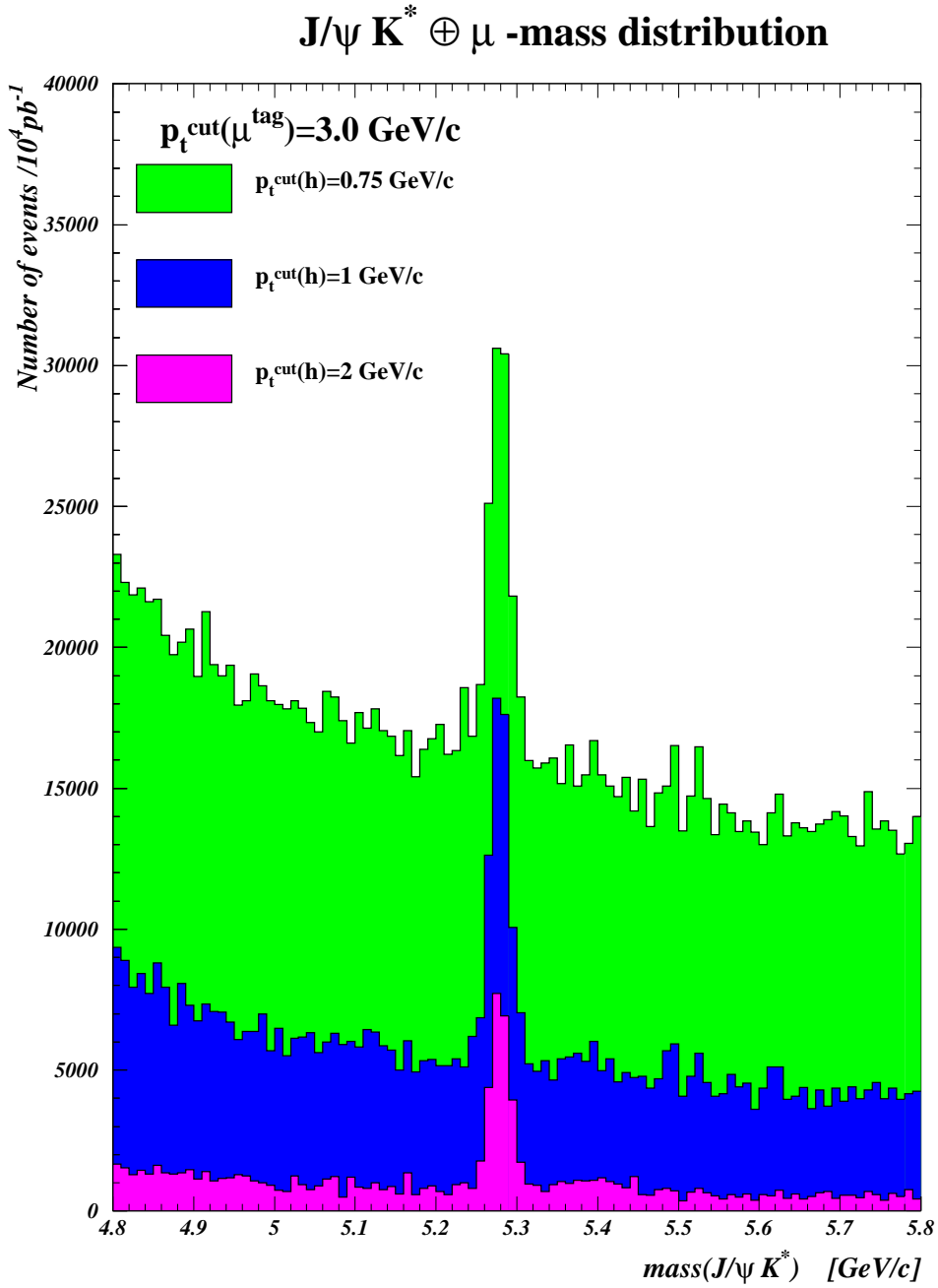


Figure 3.24: The typical views of the invariant mass distribution in the $B_d \rightarrow J/\psi K^* \oplus \mu$ channel.

$J/\psi K^\pm \oplus \mu$ - background study

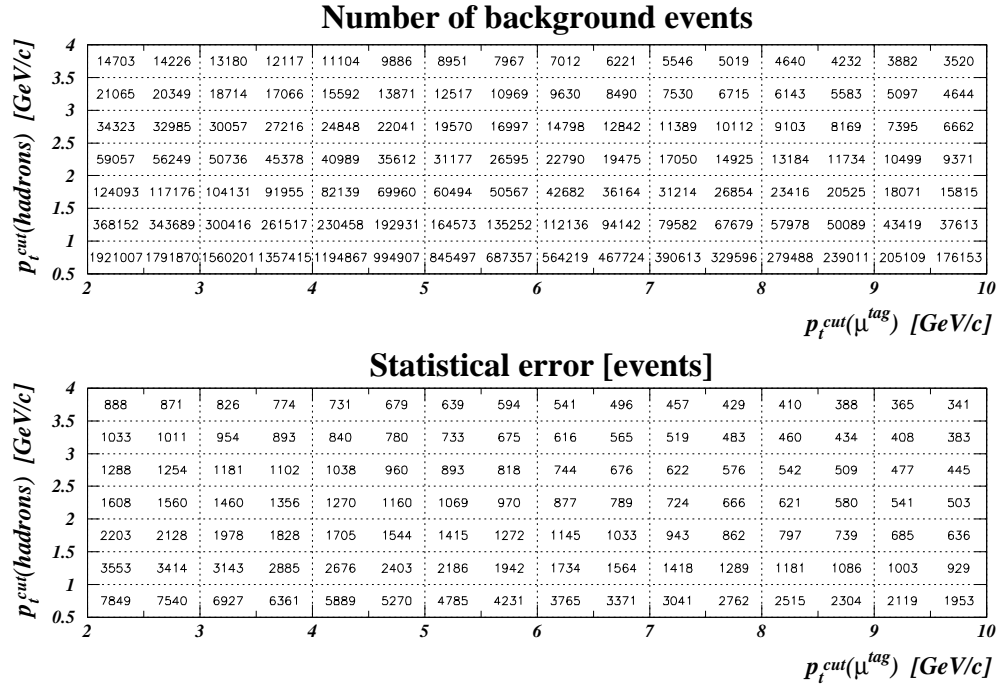


Figure 3.25: The background contributing to $B^\pm \rightarrow J/\psi K^\pm \oplus \mu$ channel obtained in the inclusive simulation. In the upper table-like plot the expected number of background events is shown, whereas the lower plot presents the statistical error of the simulation.

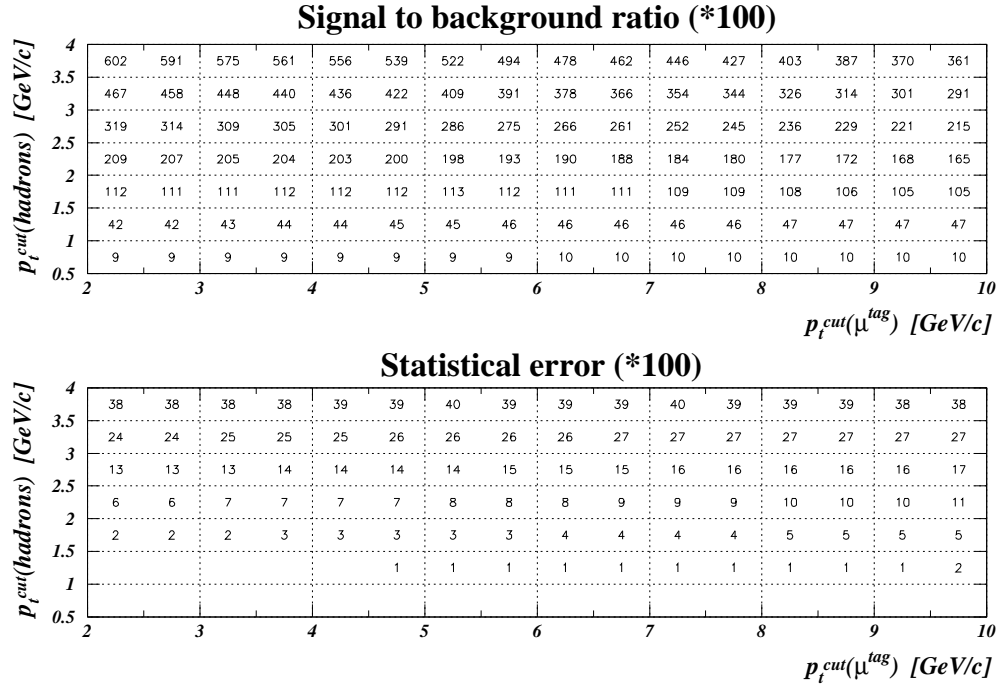


Figure 3.26: Signal to background ratio and its statistical error in the $B^\pm \rightarrow J/\psi K^\pm \oplus \mu$ channel.

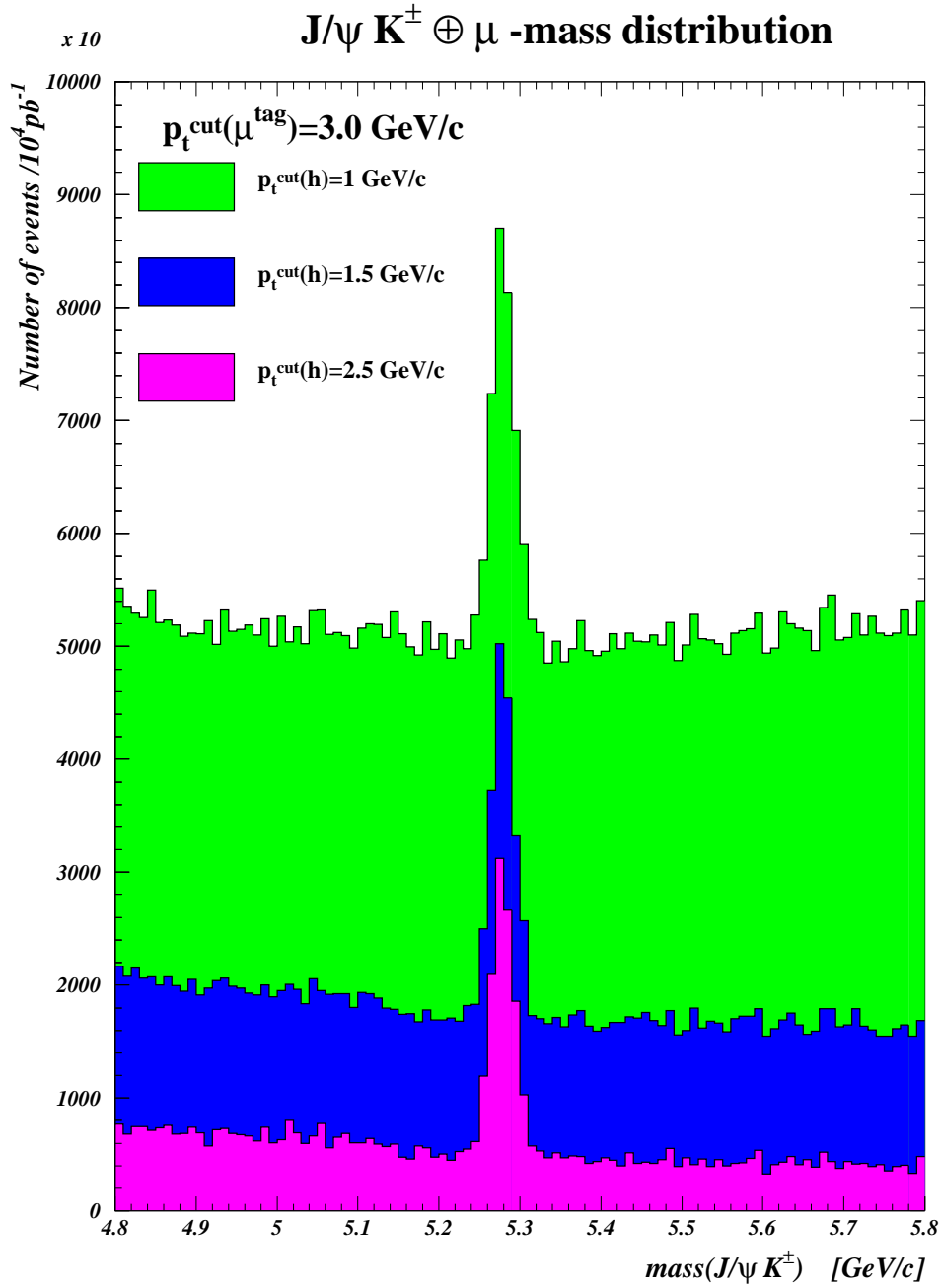


Figure 3.27: The typical views of the invariant mass distribution in the $B^\pm \rightarrow J/\psi K^\pm \oplus \mu$ channel.

J/ψ Φ ⊕ μ - background study

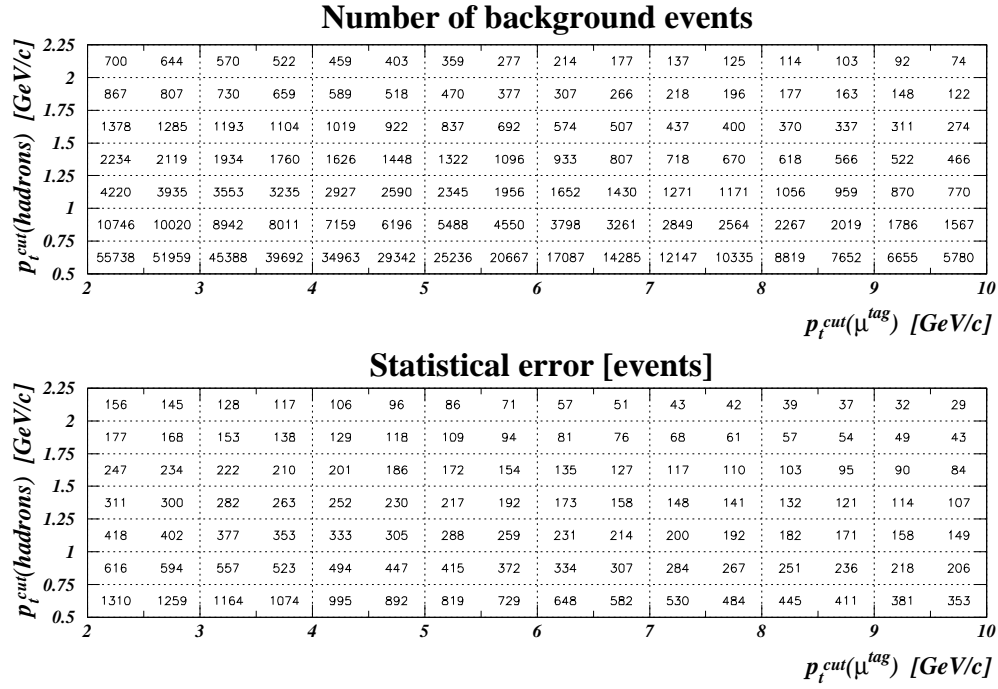


Figure 3.28: The background contributing to $B_s \rightarrow J/\psi \phi \oplus \mu$ channel obtained in the inclusive simulation. In the upper table-like plot the expected number of background events is shown, whereas the lower plot presents the statistical error of the simulation.

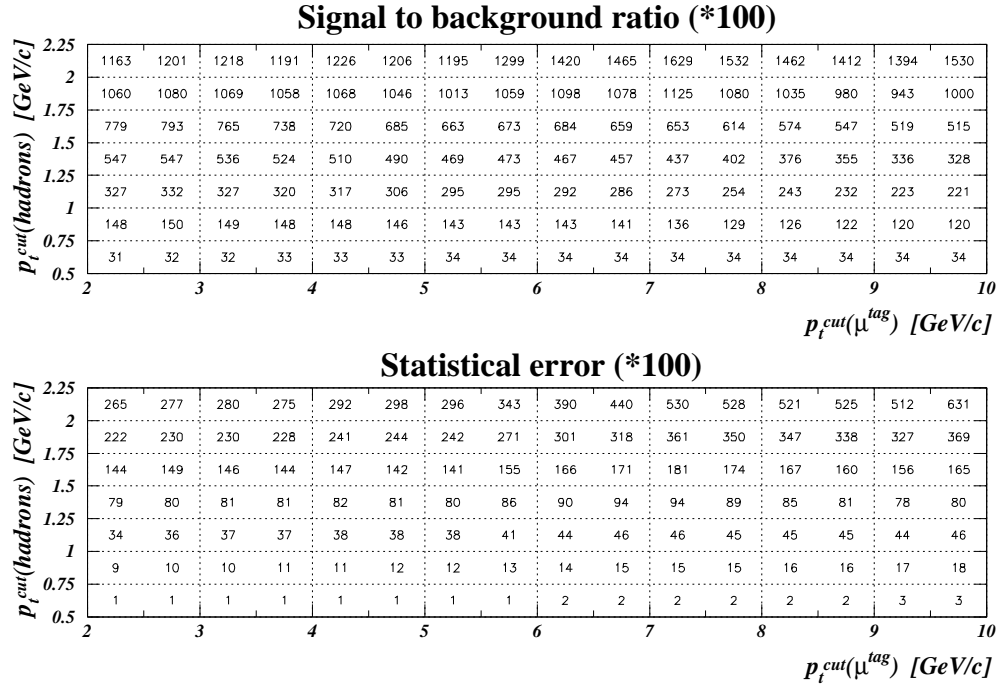


Figure 3.29: Signal to background ratio and its statistical error in the $B_s \rightarrow J/\psi \phi \oplus \mu$ channel.

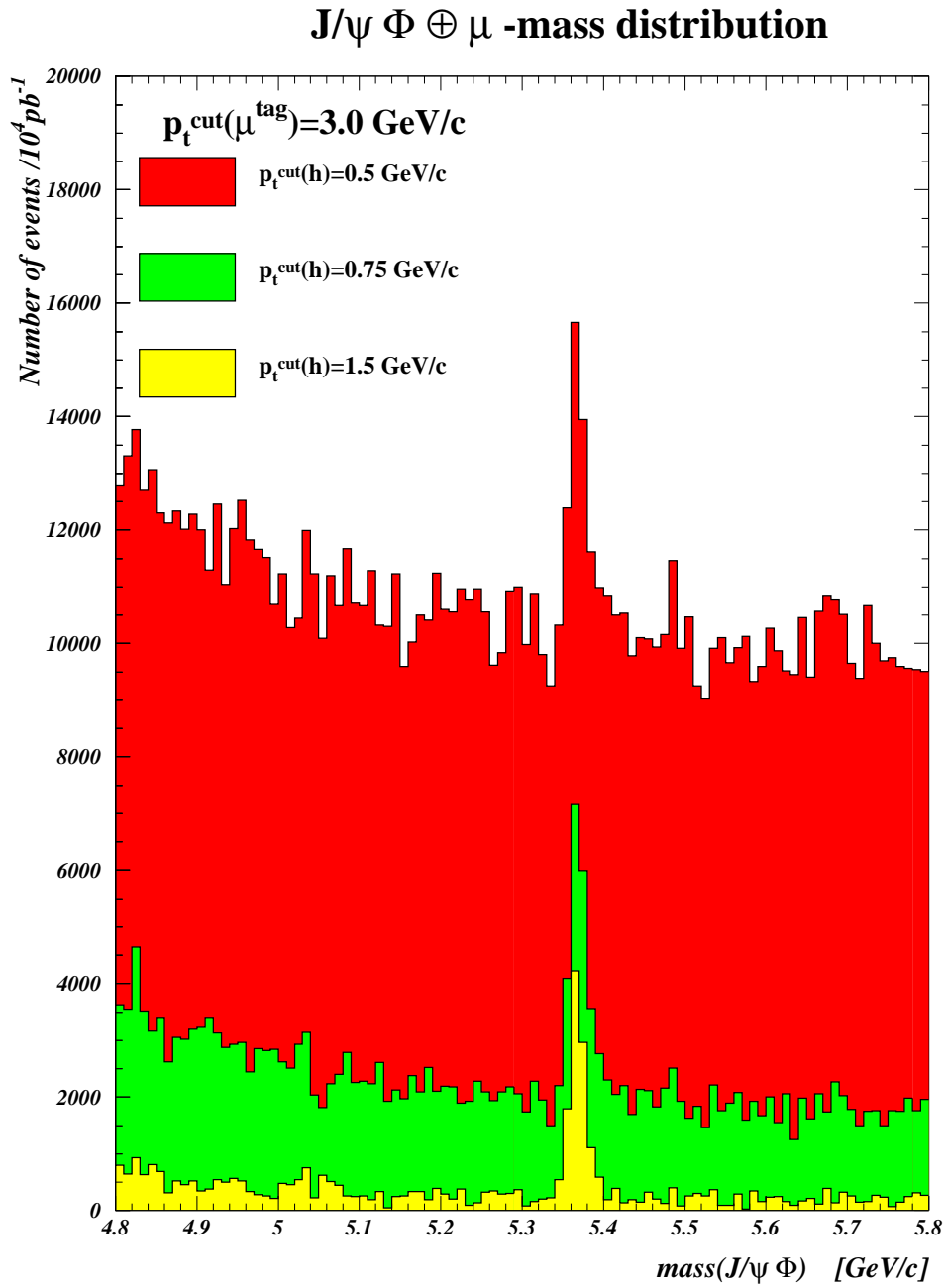


Figure 3.30: The typical views of the invariant mass distribution in the $B_s \rightarrow J/\psi \phi \oplus \mu$ channel.

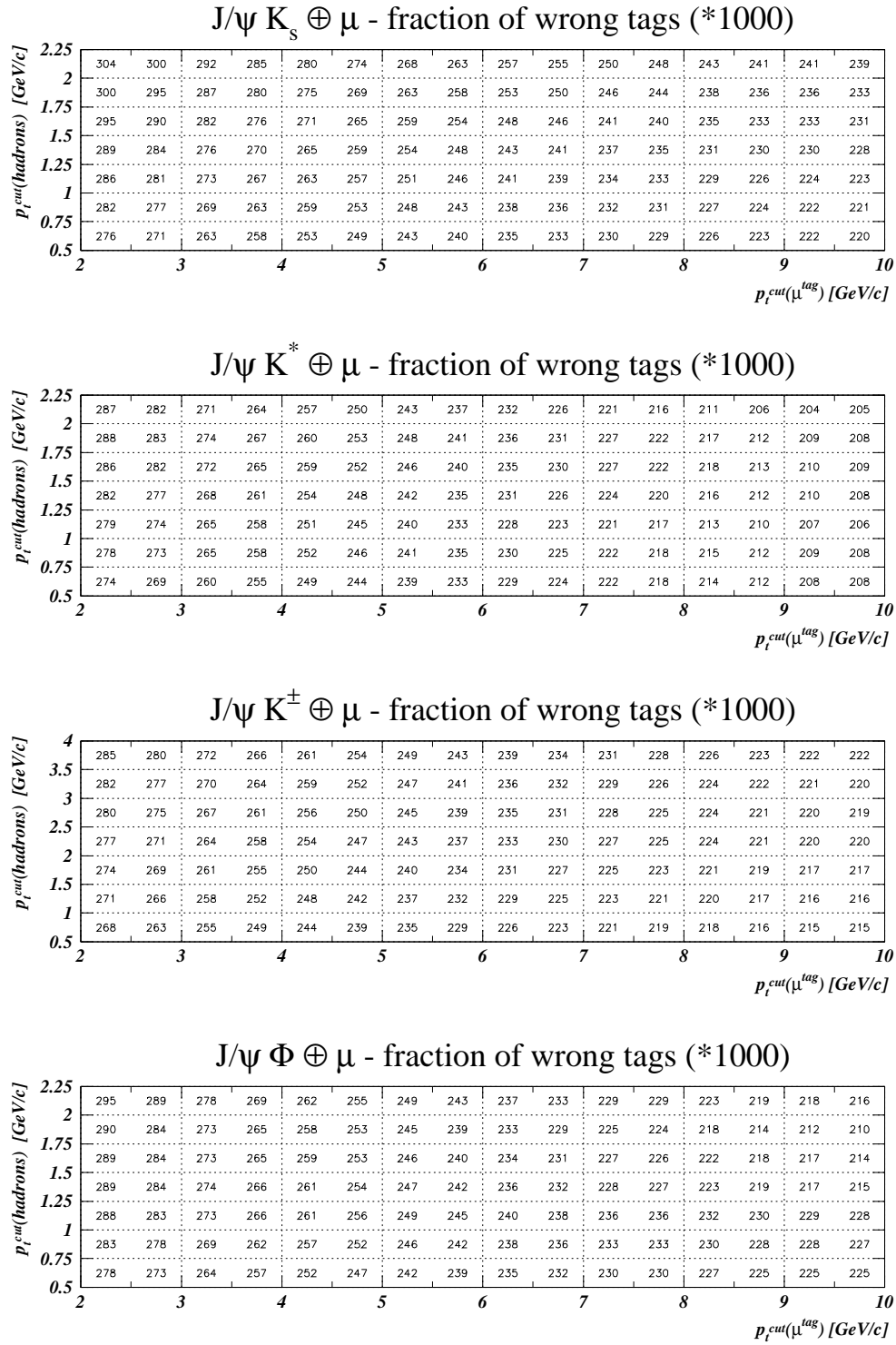


Figure 3.31: The expected fraction of wrong tags in investigated channels as a function of cuts on p_t of an associated muon and p_t of observed hadron(s).

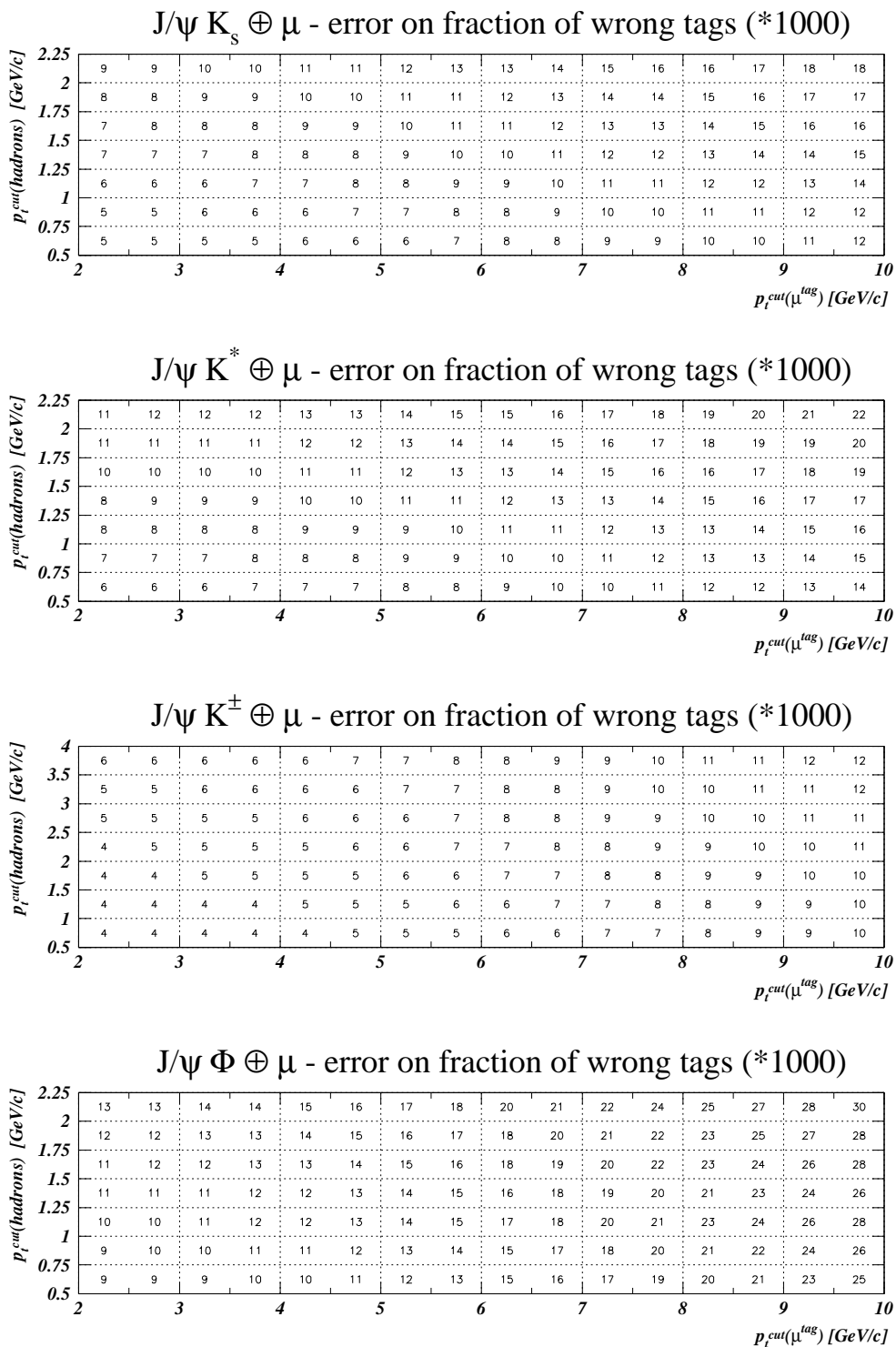


Figure 3.32: Statistical error on fraction of wrong tags corresponding to tables in Figure 3.31.

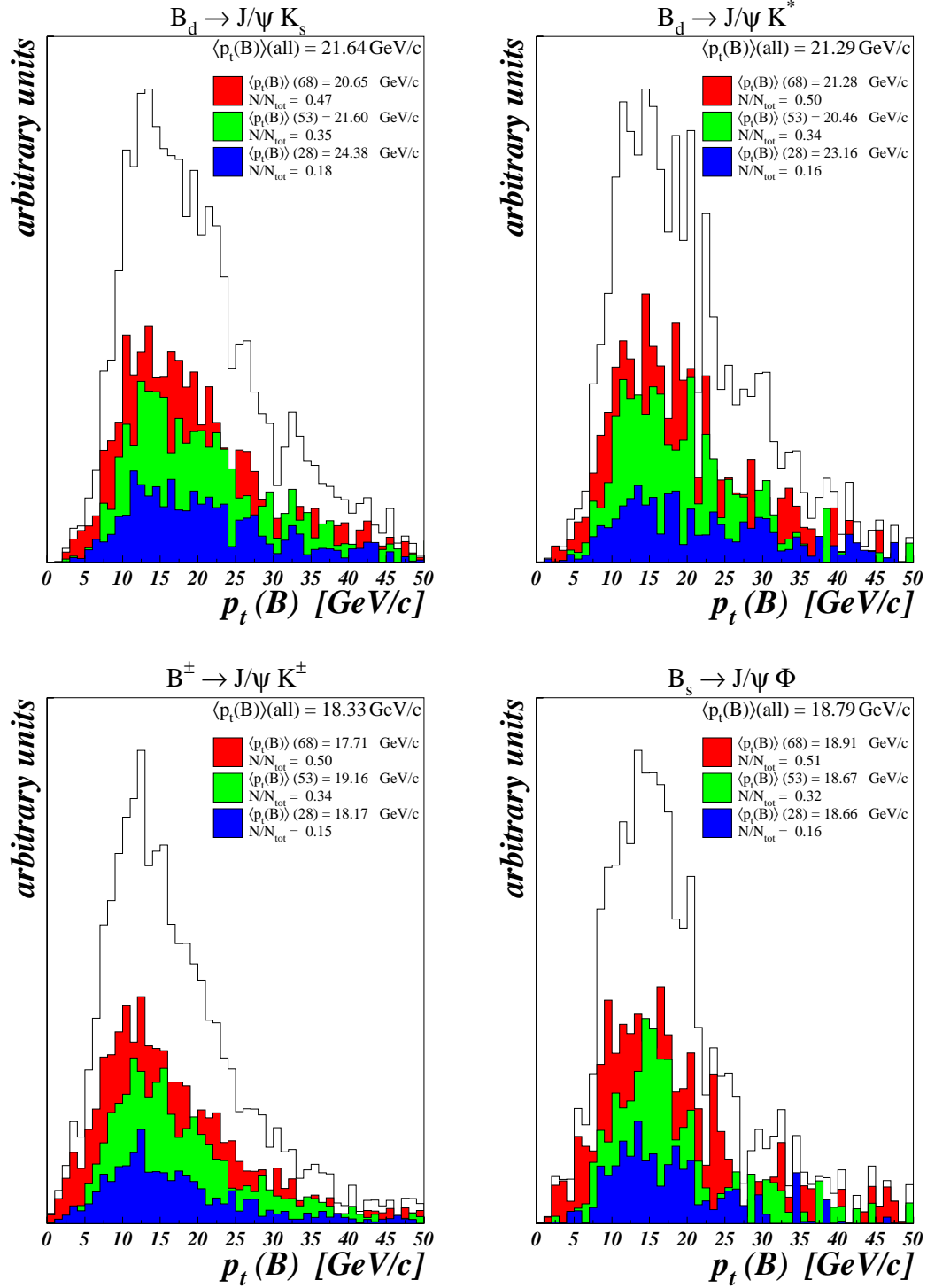


Figure 3.33: The spectra of B -mesons contribution to reconstructed events in the investigated channels. Numbers in parentheses signify the generation processes given in Table 3.1. To be compared with Figure 3.1.

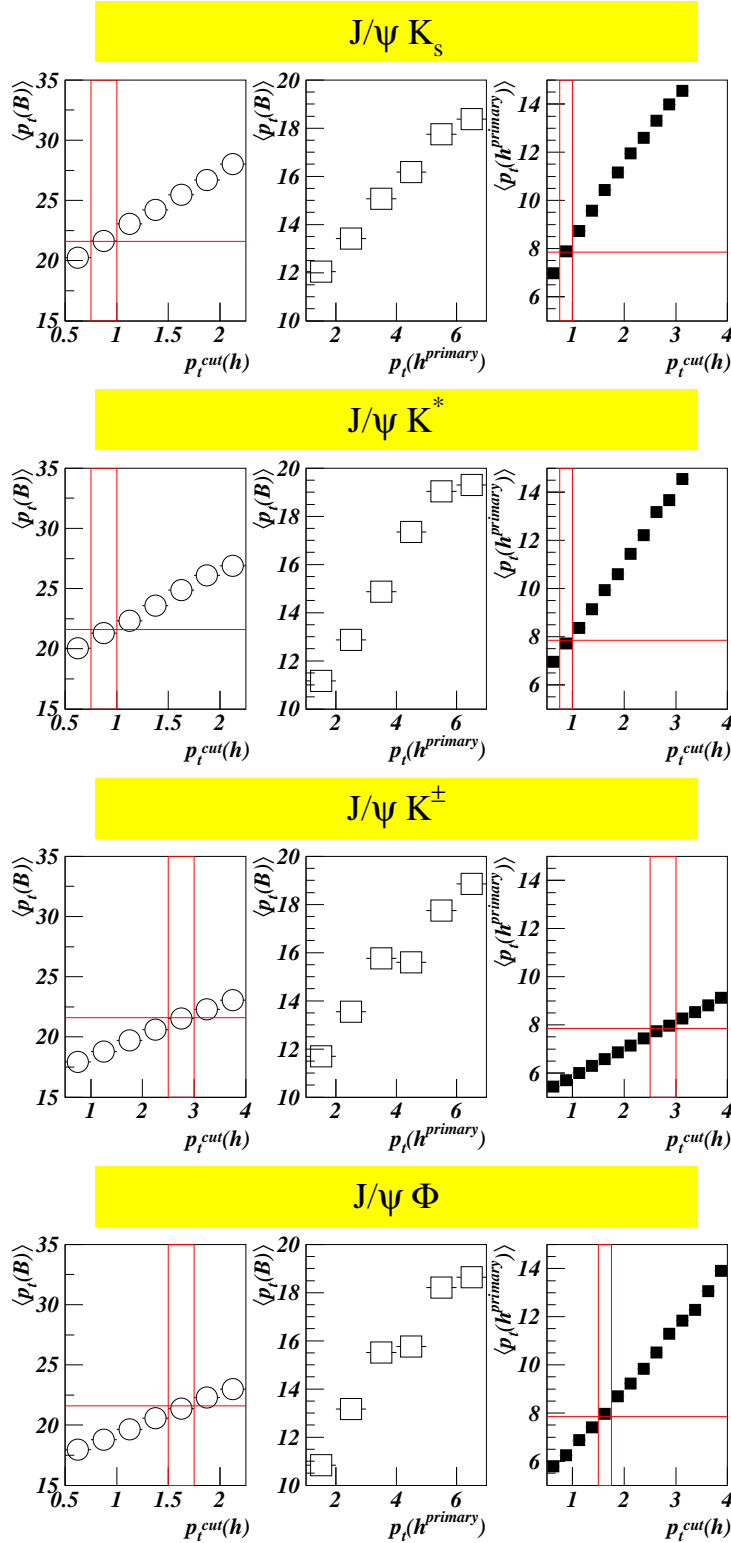


Figure 3.34: The comparison of event kinematics in investigated channels. In the left column the mean transverse momentum $\langle p_t(B) \rangle$ of reconstructed B -meson is shown as a function of the cut on transverse momentum of final hadrons $p_t^{cut}(hadrons)$. In the middle column the $\langle p_t(B) \rangle$ is shown as a function of transverse momentum of the hadron in primary decay of B -meson (the one accompanying the J/ψ). In the right column the mean p_t of primary hadron is shown as a function of $p_t^{cut}(hadrons)$. The horizontal and vertical lines fix the cut in $B_d \rightarrow J/\psi K^*$, $B^\pm \rightarrow J/\psi K^\pm$ and $B_s \rightarrow J/\psi \phi$ corresponding to that used in $B_d \rightarrow J/\psi K_s$ channel.

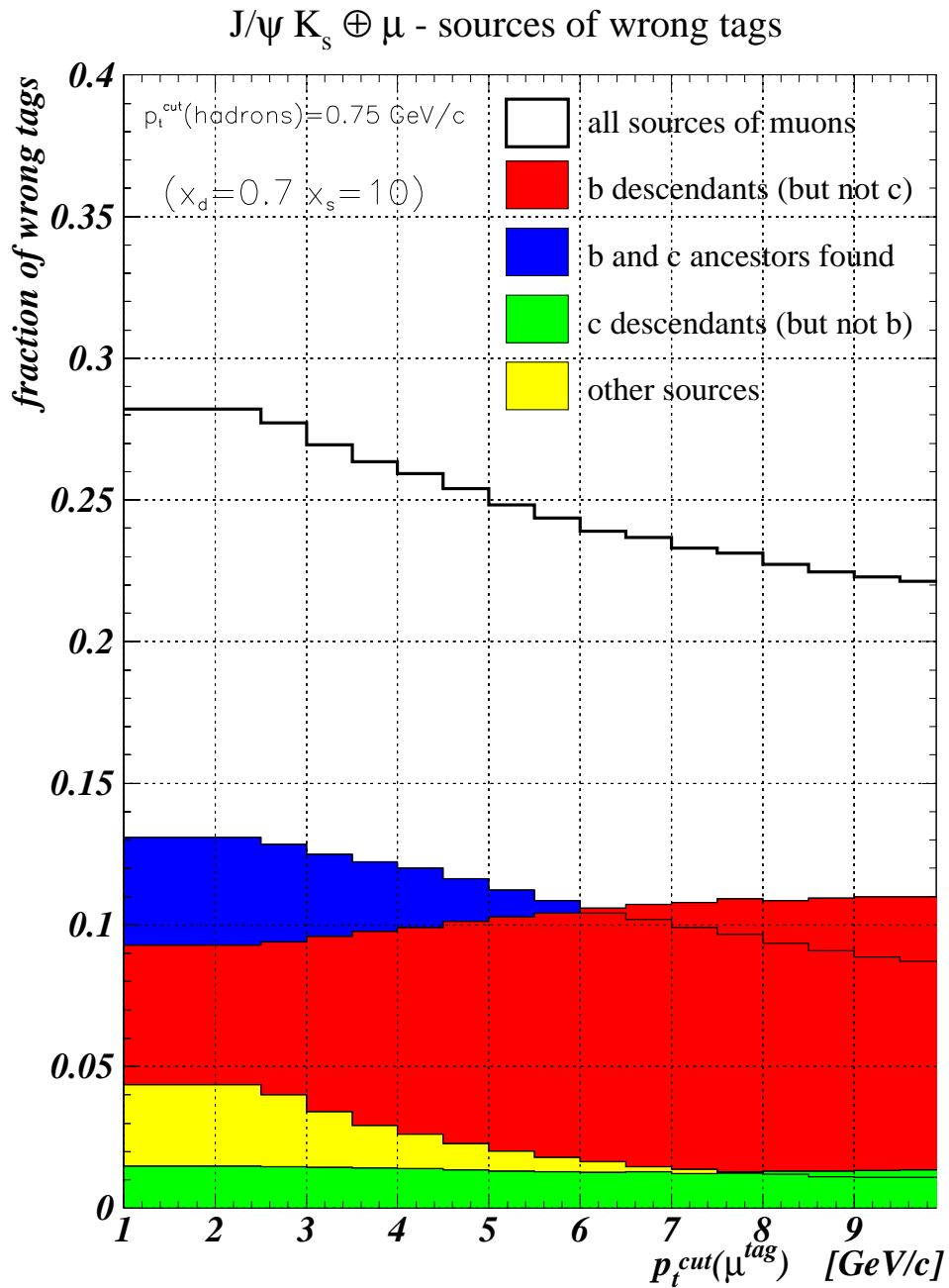


Figure 3.35: The expected fraction of wrong tags as a function of p_t cut on the associated muon in $B_d \rightarrow J/\psi K_S \oplus \mu$ channel. The contributions from several sources are marked with different colours.

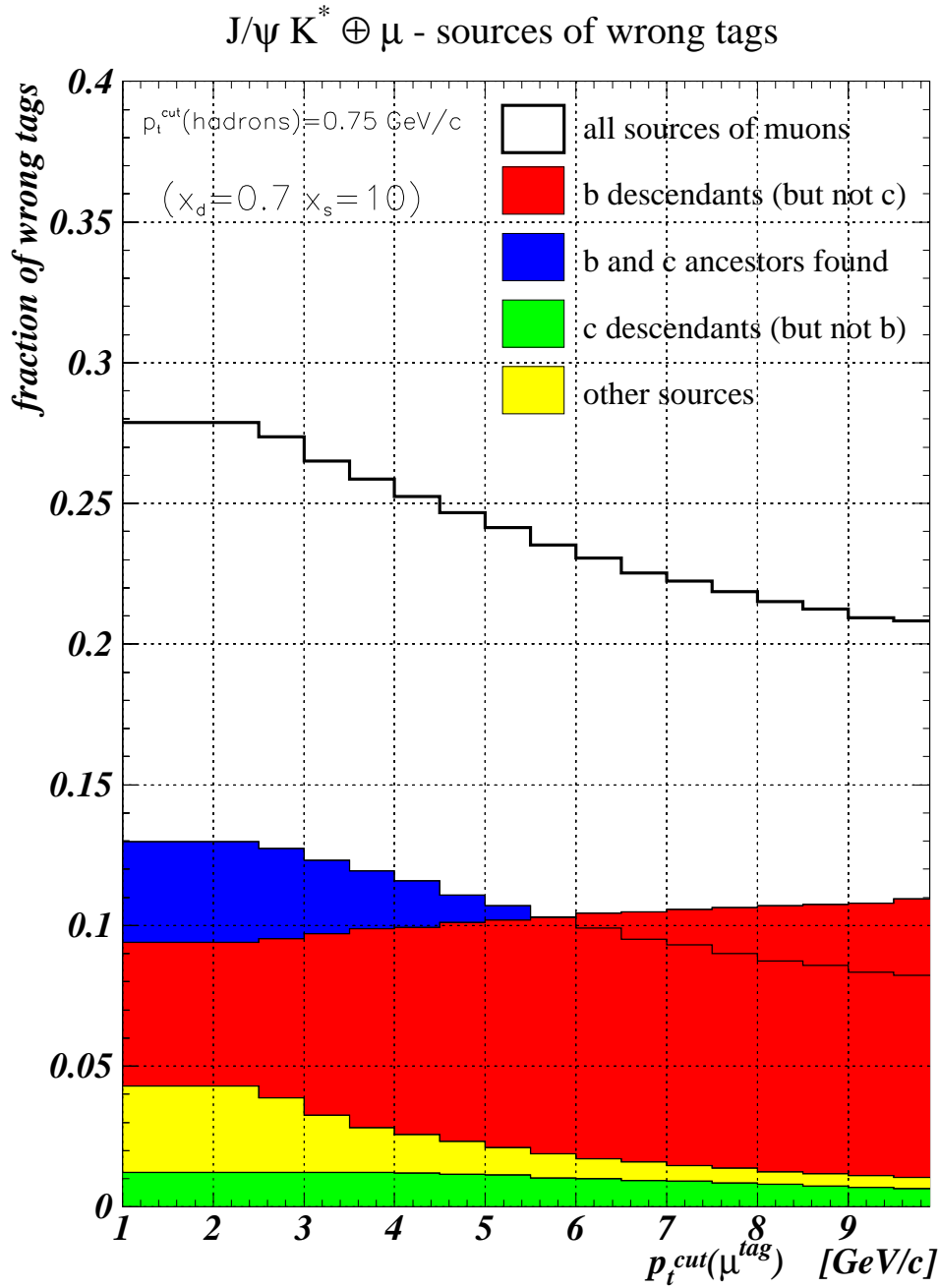


Figure 3.36: The expected fraction of wrong tags as a function of p_t cut on the associated muon in $B_d \rightarrow J/\psi K^* \oplus \mu$ channel. The contributions from several sources are marked with different colours.

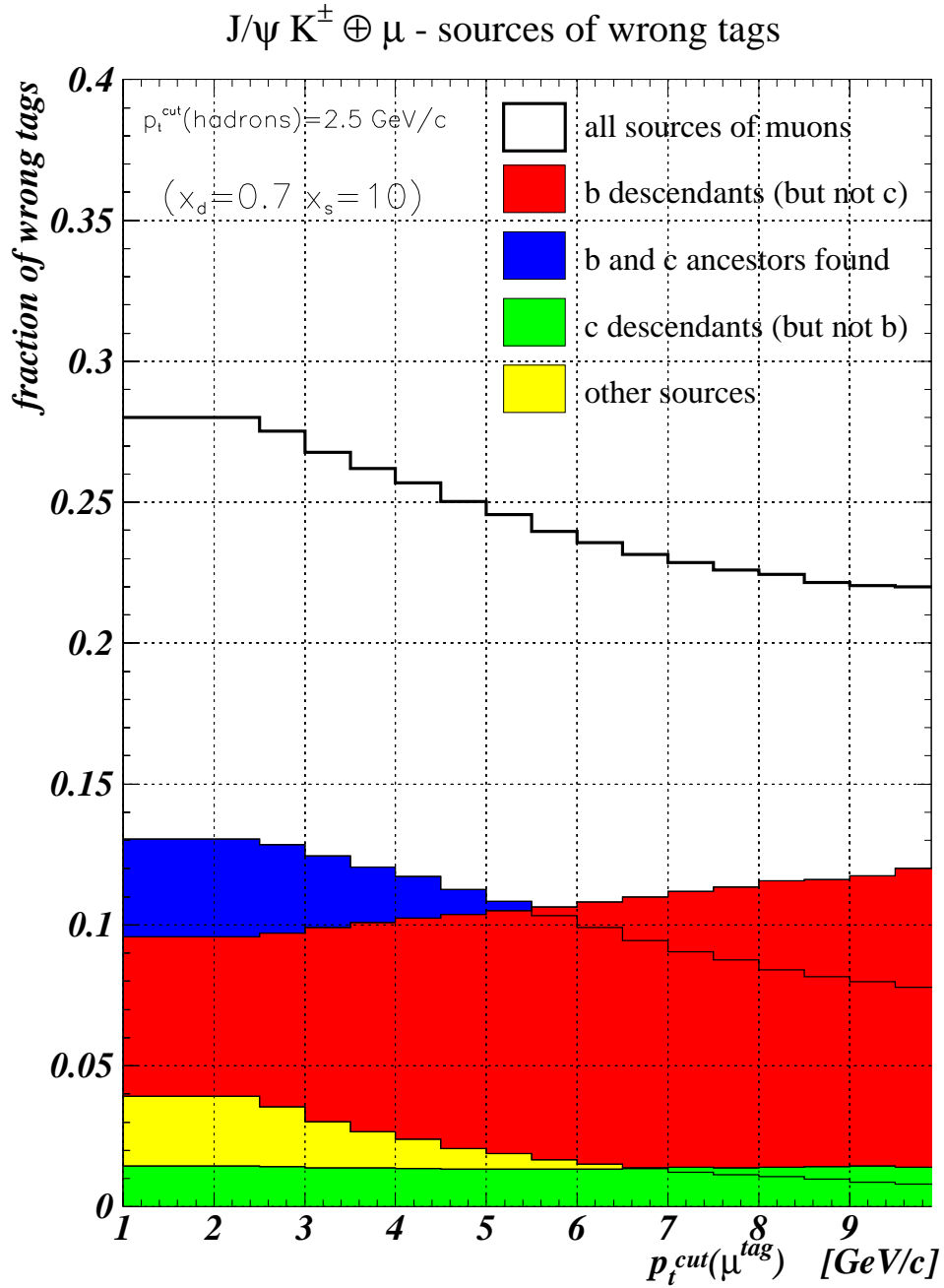


Figure 3.37: The expected fraction of wrong tags as a function of p_t cut on the associated muon in $B^\pm \rightarrow J/\psi K^\pm \oplus \mu$ channel. The contributions from several sources are marked with different colours.

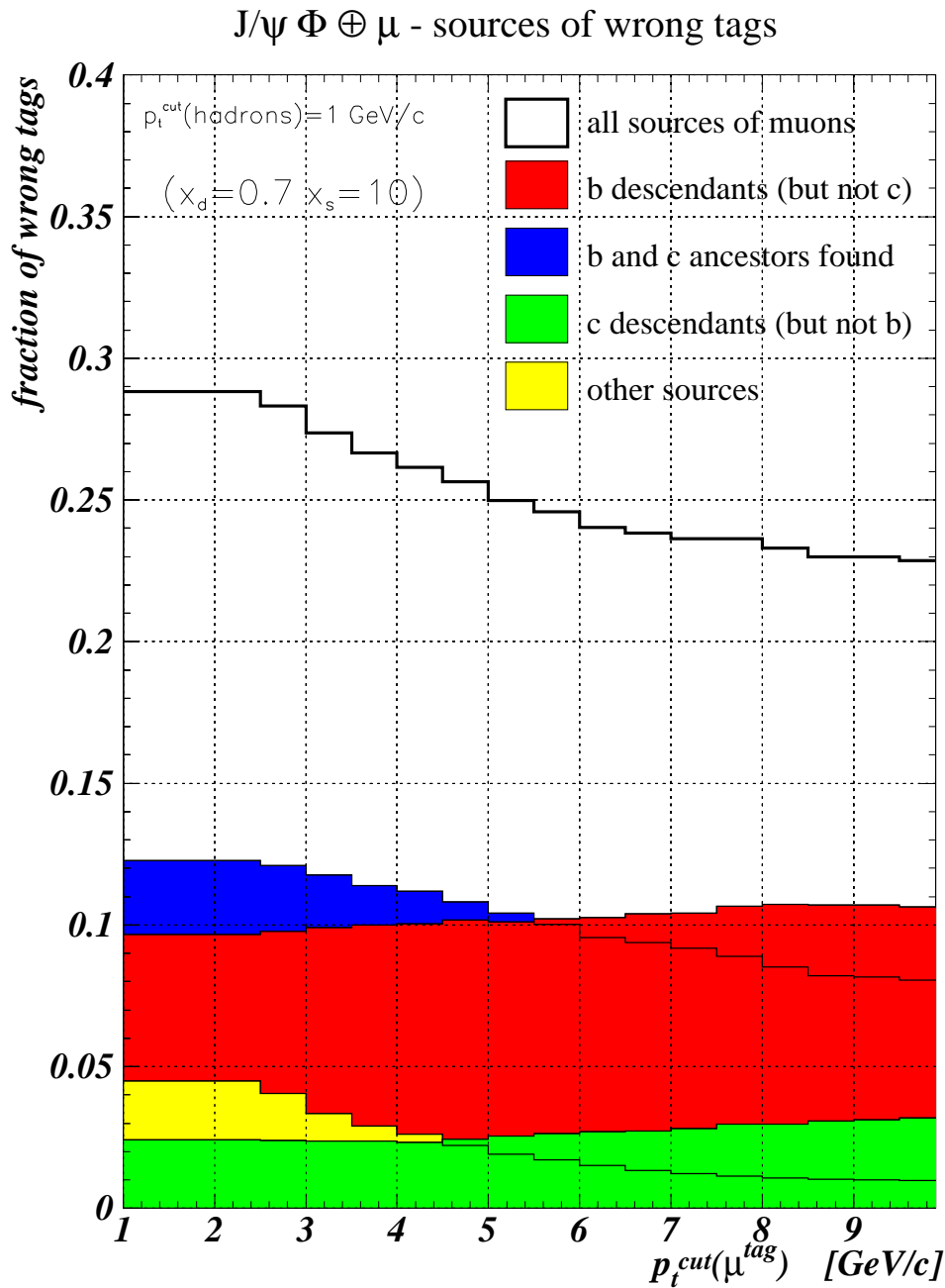


Figure 3.38: The expected fraction of wrong tags as a function of p_t cut on the associated muon in $B_s \rightarrow J/\psi \phi \oplus \mu$ channel. The contributions from several sources are marked with different colours.

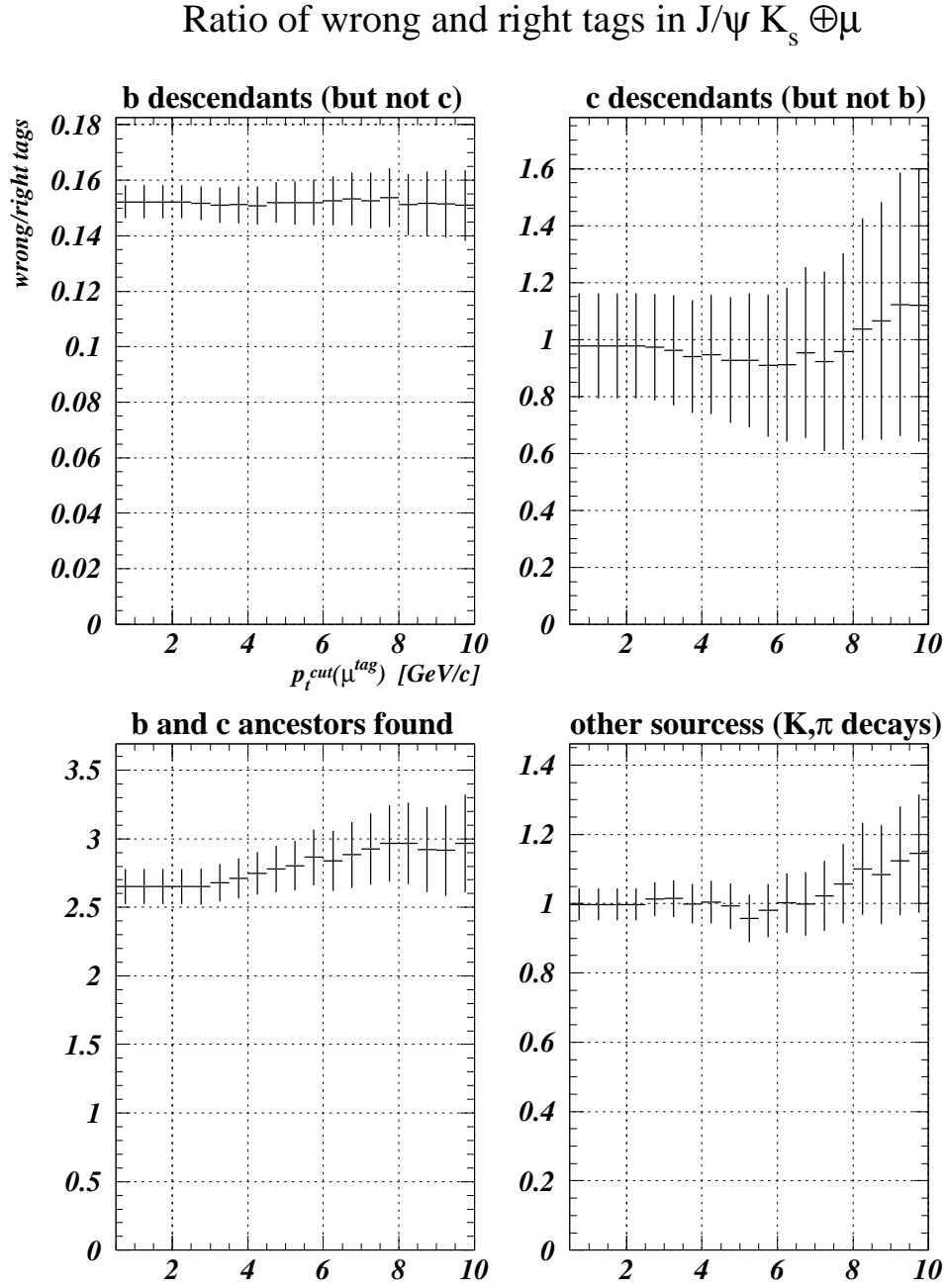


Figure 3.39: The ratio of good and wrong tags for several separated classes of tags in $B_d \rightarrow J/\psi K_S \oplus \mu$ channel.

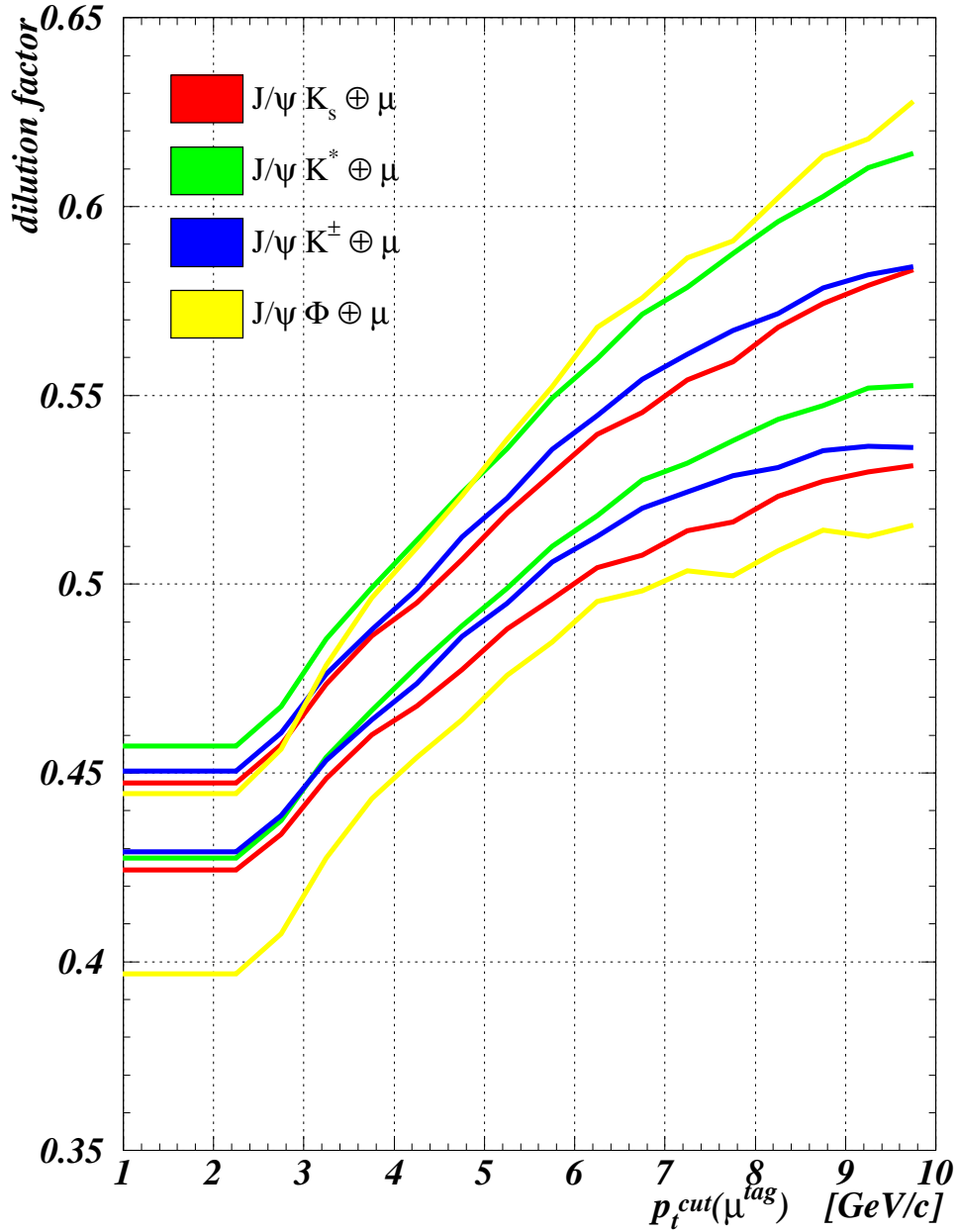


Figure 3.40: The comparison of dilution factors in the investigated channels. The different cuts on final hadrons ($p_t^{cut}(hadrons)=0.75, 0.75, 2.5, 1.5$ GeV/c in the channels $B_d \rightarrow J/\psi K_S \oplus \mu$, $B_d \rightarrow J/\psi K^* \oplus \mu$, $B^\pm \rightarrow J/\psi K^\pm \oplus \mu$ and $B_s \rightarrow J/\psi \phi \oplus \mu$ respectively) were used in order to minimise the difference in event kinematic. The bounds of $\pm 1\sigma$ corridor around the central value in each channel are marked with two lines of the same colour.

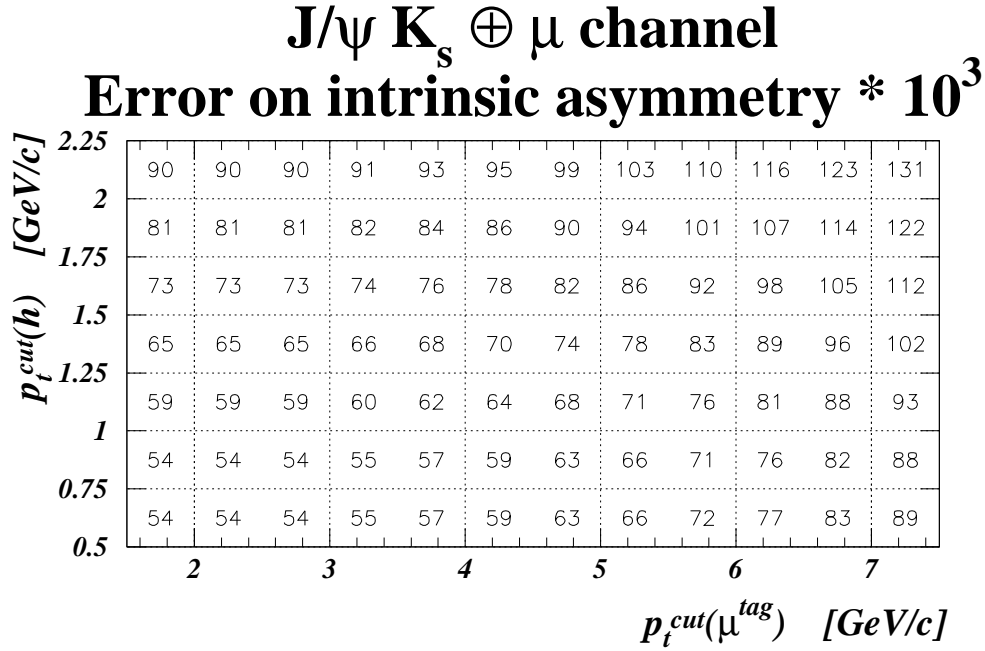


Figure 3.41: The expected error on an intrinsic asymmetry in $B_d \rightarrow J/\psi K_S \oplus \mu$ channel as a function of p_t cut on the associated muon and on final hadrons. The minimum is $\delta(\sin 2\beta) = 0.054$ at the lowest possible cuts, but there is a wide area with an error below 0.06.

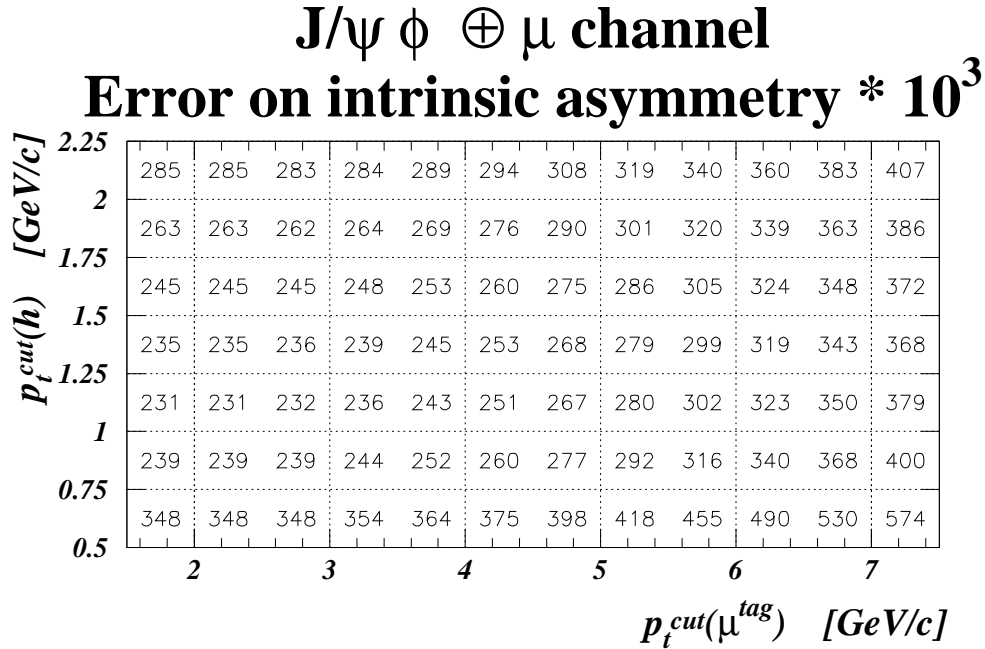


Figure 3.42: The expected error on an intrinsic asymmetry in $B_s \rightarrow J/\psi \phi \oplus \mu$ channel as a function of p_t cuts on associated muons and final hadrons. The minimal error is $\delta(asymmetry) \approx 0.23$, much above the value predicted by the Standard Model.

3.3 Time dependent analysis

To determine sensitivities to CP violating parameters in the time dependent study of channels $B_d \rightarrow J/\psi K_S \oplus \mu$ and $B_s \rightarrow J/\psi \phi \oplus \mu$ some information obtained from time integrated study was used, i.e. the number of signal events, the level of background and the probability of observing a wrong tag. The number of simulated events for the time dependent analysis was equal to number of events expected to observe (i.e. the weight of an event was one).

For each signal event the flavour of \bar{B}^0 and its decay vertex were generated with a help of formula (2.1). Similarly, for each background event its decay vertex were generated. For background events, the sign of an associated muon was taken with equal probability for both charges, whereas for signal events the charge of the muon was generated according to known probability of having right or wrong tag. Then the asymmetries (formula 2.13) were calculated.

In the case of $B_d \rightarrow J/\psi K_S$ the values of mixing parameters was fixed to $x_d = 0.7$ whereas in the case of $B_s \rightarrow J/\psi \phi$ channels two values were examined $x_s = 10$ and 20 .

3.3.1 The predicted error on intrinsic asymmetries - perfect secondary vertex resolution

3.3.1.a The $B_d \rightarrow J/\psi K_S \oplus \mu$ channel

In the investigation of $B_d \rightarrow J/\psi K_S \oplus \mu$ the number of used signal events was $N_{sig} = 9500$ (corresponding to 10^4pb^{-1} – one year of data taking at the initial LHC luminosity), the dilution due to background $D_{bgd} = 0.86$ (corresponding to signal to background ratio $N_{sig}/N_{bgd} \approx 6.4$) and the dilution factor due to tagging $D_{tag} = 0.44$. Moreover, the $x_d = 0.7$, and, since the reconstruction of secondary vertex was initially assumed to be perfect, the $\sigma_{\text{sec. vtx.}} = 0$. The intrinsic CP violation asymmetry was set to $\sin 2\beta = 0.6$.

In the Figure 3.43 the generated asymmetry is presented in terms of $B_d^0 \rightarrow f_{CP}$ and $\bar{B}_d^0 \rightarrow f_{CP}$ with an associated muon found. The charge of the muon is not important at that step. The distribution of time of the B decay is shown for B_d^0 and \bar{B}_d^0 separately in the upper-left plot. The distributions are not exponential (due to CP violating terms), but for the sum the exponential behaviour still holds (upper-right plot). In the lower plot the time dependent asymmetry is shown. This is the asymmetry between number of $B_d^0 \rightarrow J/\psi K_S$ and $\bar{B}_d^0 \rightarrow J/\psi K_S$ decays and it corresponds to formula $a(t) = -\sin 2\beta \cdot \sin(x_d \frac{t}{\tau})$. The fit with a function $(\text{amplitude}) \cdot \sin(x_d \frac{t}{\tau})$ is performed with one free parameter – amplitude. The parameter x_d is treated as known. The result of the fit reproduces the initial asymmetry with an error $\delta(\sin 2\beta) = 0.015$. Although the error corresponds to expected statistic this asymmetry cannot be observed, because the flavour of initial B -meson is not known in real data.

In more realistic case the generated asymmetry is presented in terms of number of muons of opposite sign (Figure 3.44). At that step no background is included. In the lower plot reconstructed asymmetry is presented. This is the asymmetry between the number of negatively and positively charged muons accompanying $B_d^{(-)} \rightarrow J/\psi K_S$ decay and the asymmetry corresponds to $a(t) = D_{tag} \cdot -\sin 2\beta \cdot \sin(x_d \frac{t}{\tau})$. The fit to $(amplitude) \cdot \sin(x_d \frac{t}{\tau})$ is performed and its error corresponds to $\delta(\sin 2\beta) = 0.040$.

In the realistic case the generated asymmetry is presented in terms of number of muons of opposite sign (Figure 3.45). At that step the background is already included. At the lower plot reconstructed asymmetry is presented. This is the asymmetry between number of negatively and positively charged muons accompanying $B_d^{(-)} \rightarrow J/\psi K_S$ decay and the asymmetry corresponds to $a(t) = D_{tag} \cdot D_{bgd} \cdot -\sin 2\beta \cdot \sin(x_d \frac{t}{\tau})$. The fit to $(amplitude) \cdot \sin(x_d \frac{t}{\tau})$ is performed, and its error corresponds to $\delta(\sin 2\beta) = 0.043$. With the approximation of perfect reconstruction of the secondary vertex this is the error one should expect in real experiment.

3.3.1.b The $B_s \rightarrow J/\psi \phi \oplus \mu$ channel

In the investigation of $B_s \rightarrow J/\psi \phi \oplus \mu$ the number of signal events used was $N_{sig} = 28000$ (corresponding to $2 \cdot 10^4 \text{pb}^{-1}$ – **two years** of taking data at initial LHC luminosity), the $D_{bgd} = 0.77$ (corresponding to signal to background ratio $N_{sig}/N_{bgd} = 3.3$). For the dilution factor the value of $D_{tag} = 0.42$ was used. The above parameters roughly corresponds to $p_t^{cut}(hadrons) = 1 \text{ GeV}/c$. Moreover, $x_s = 20$ was assumed, and, since the reconstruction of secondary vertex was assumed to be perfect, the $\sigma_{sec. vtx.} = 0$. The intrinsic CP violation asymmetry was set to 0.03.

Similarly to Figures 3.43-3.45, the Figures 3.46-3.48 are provided for $B_s \rightarrow J/\psi \phi \oplus \mu$ channel. The errors on the reconstructed asymmetry are $\delta(asymmetry) = 0.009, 0.022, 0.025$ for the asymmetries (respectively): $B_s^0 \rightarrow f_{CP}$ vs. $\bar{B}_s^0 \rightarrow f_{CP}$ (plus μ^{tag}); μ^- vs. μ^+ (with $B_s \rightarrow J/\psi \phi$) without and with a background superimposed. Thus, after two years of running one cannot measure the CP violation predicted by Standard Model with good enough accuracy (note that precision of the secondary vertex reconstruction is still not taken into account).

3.3.2 The influence of secondary vertex resolution

To get some feeling about the influence of secondary vertex reconstruction, in the PYTHIA based, exclusive simulation ($B_d \rightarrow J/\psi K_S$) the decay vertex of B_d was smeared with $\sigma_{sec. vtx.} = 100 \mu\text{m}$ (a very rough approximation of the CMS vertex detector resolution in transverse plane). The smearing was done in one dimension only. The result is shown in Figure 3.49. The 100 microns smearing of secondary vertex reflects as the $\sigma \approx 0.1$ in the proper time distribu-

tion t/τ . Applying that resolution to the simulation performed above one may observed (see Figures 3.50 and 3.51, to be compared with 3.45 and 3.48) the moving of reconstructed central value of asymmetry from $\sin 2\beta = 0.630$ to $\sin 2\beta = 0.621$ for $B_d \rightarrow J/\psi K_S \oplus \mu$ and $asymmetry = 0.035$ to 0.025 in $B_s \rightarrow J/\psi \phi \oplus \mu$. Although this shift is inside the errors it is somehow significant since Figures 3.45 and 3.50 as well as 3.48 and 3.51 are not independent – the decay points used there are the same, thus the shift is really induced by the introduced smearing.

To further check the influence of secondary vertex resolution, more advanced study has been done. In the plot on Figure 3.52 the reconstructed asymmetry is presented as a function of generated one, for a huge sample of events (corresponding to one year of taking data at **full LHC luminosity**) for $B_d \rightarrow J/\psi K_S \oplus \mu$ channel. The values of dilution factors due to tagging and due to background were chosen as in section 3.3.1.a. The full and empty circles represent the cases of resolution $\sigma_{\text{sec. vtx.}} = 100 \mu\text{m}$, and the perfect one respectively. In the $B_d \rightarrow J/\psi K_S \oplus \mu$ channel the influence of not perfect resolution is minor.

This is not the case for $B_s \rightarrow J/\psi \phi \oplus \mu$ channel where the rapid oscillations may be well followed with perfect microvertex device only. The values of $x_s = 10$ and 20 were examined with the samples corresponding to two and five years of taking data at **full LHC luminosity** respectively. The values of dilution factors due to tagging and due to background were chosen as in section 3.3.1.b. The full circles in Figure 3.53 are significantly below the empty ones in both cases. Thus the measured asymmetry should be corrected for secondary vertex resolution, multiplying the measured value roughly by a factor 1.5 (a factor of 6) for $x_s = 10$ ($x_s = 20$). Thus also the error on the asymmetry (for $\int L dt = 10^4 \text{pb}^{-1}$) increases from $\delta(asymmetry) = 0.025$ to about $\delta(asymmetry) = 0.037$ or up to $\delta(asymmetry) = 0.15$ for two examined values of x_s .

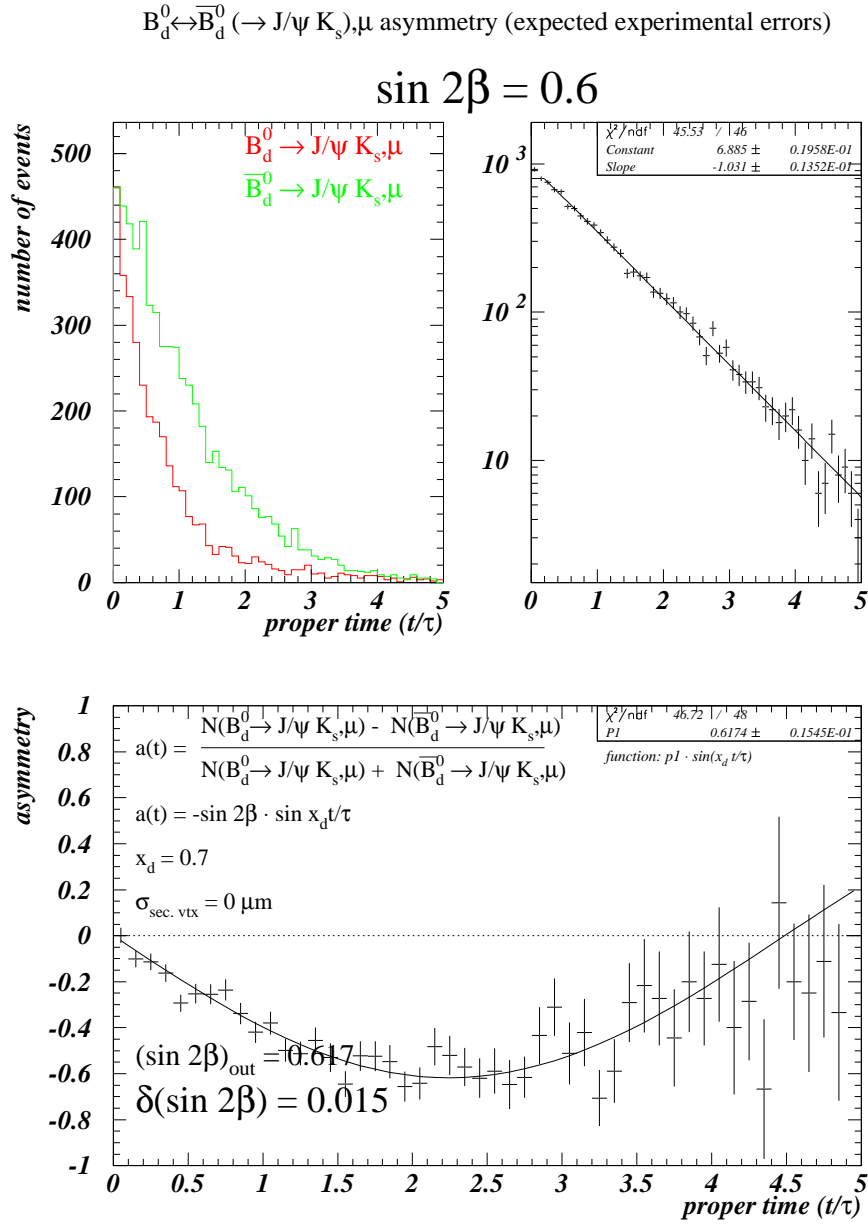


Figure 3.43: The time dependent study in $B_d \rightarrow J/\psi K_S \oplus \mu$ channel. The histograms are presented in terms of initially produced B_d^0 or \bar{B}_d^0 decaying to f_{CP} . The assumed value of the asymmetry was $\sin 2\beta = 0.6$. In the upper-left plot the distribution of the time of B decay is presented for two kinds of B separately, while in the upper-right plot their exponential sum is shown. In the lower plot the asymmetry between number of B_d^0 and \bar{B}_d^0 decaying to $J/\psi K_S$ state with an accompanying muon is shown. In such a case the asymmetry may be reconstructed with a precision of $\delta(\sin 2\beta) = 0.015$.

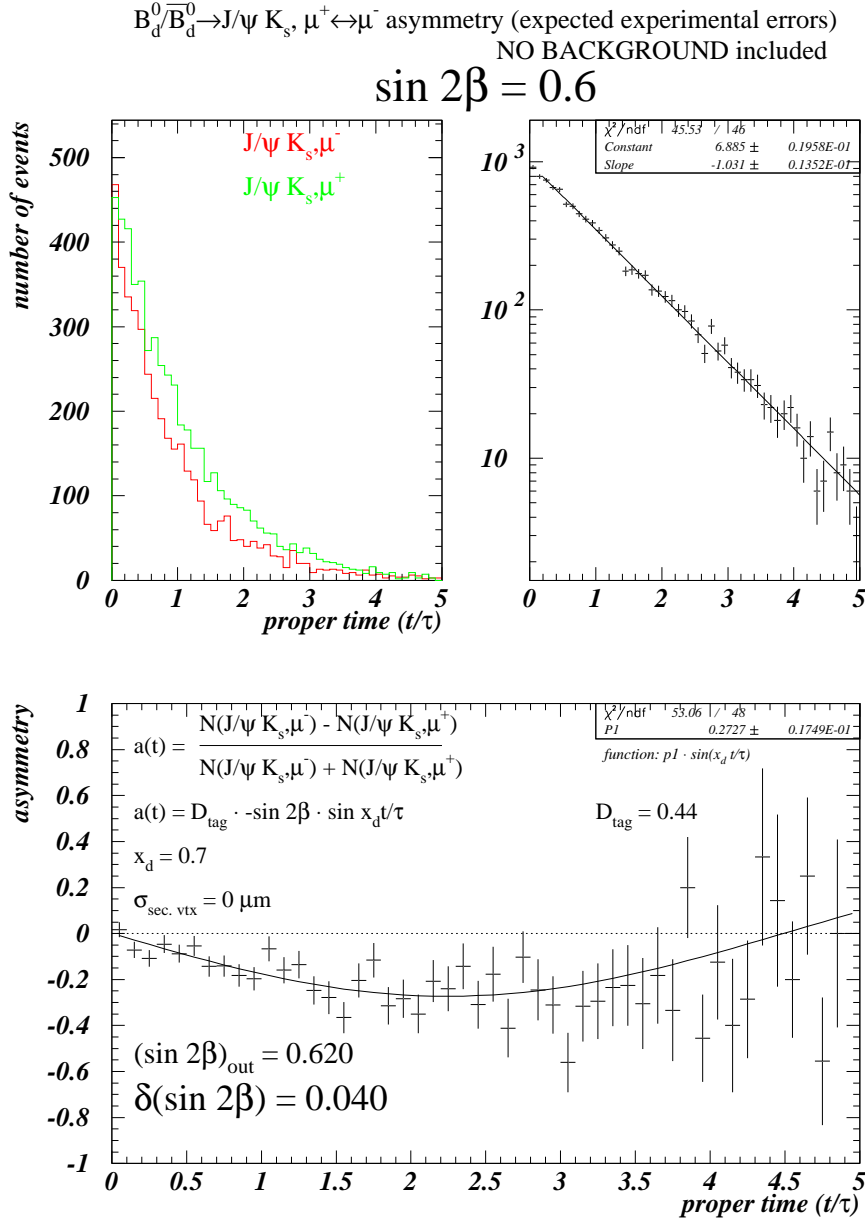


Figure 3.44: The time dependent study in $B_d \rightarrow J/\psi K_S \oplus \mu$ channel. The histograms are presented in terms of charges of associated muons. The assumed value of the intrinsic asymmetry was $\sin 2\beta = 0.6$. The background was neglected at that step, and the perfect reconstruction of the secondary vertex was assumed. In the upper-left plot the distribution of the time of B decay is presented for muons of different charges separately, while in the upper-right plot their exponential sum is shown. In the lower plot the asymmetry between number of μ^- and μ^+ accompanying the $B_d \rightarrow J/\psi K_S$ decay is shown. In such a case the asymmetry may be reconstructed with a precision of $\delta(\sin 2\beta) = 0.040$.

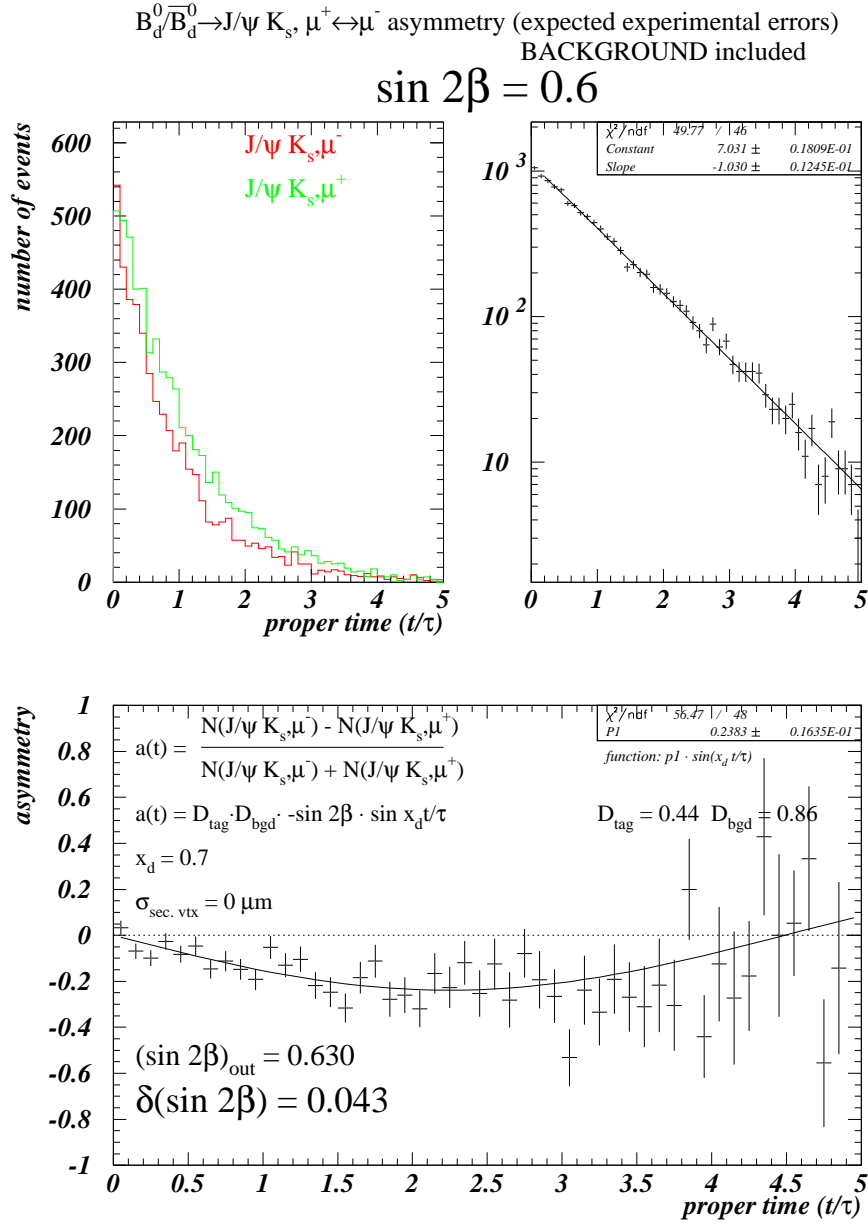


Figure 3.45: The time dependent study in $B_d \rightarrow J/\psi K_S \oplus \mu$ channel. The histograms are presented in terms of charges of associated muons. The assumed value of the intrinsic asymmetry was $\sin 2\beta = 0.6$. The background at the level of 16% of the signal was taken into account. The perfect reconstruction of the secondary vertex was assumed. In the upper-left plot the distribution of the time of B decay is presented for muons of different charges separately, while in the upper-right plot their exponential sum is shown. In the lower plot the asymmetry between number of μ^- and μ^+ accompanying the $B_d \rightarrow J/\psi K_S$ decay is shown. In such a case the asymmetry may be reconstructed with a precision of $\delta(\sin 2\beta) = 0.043$.

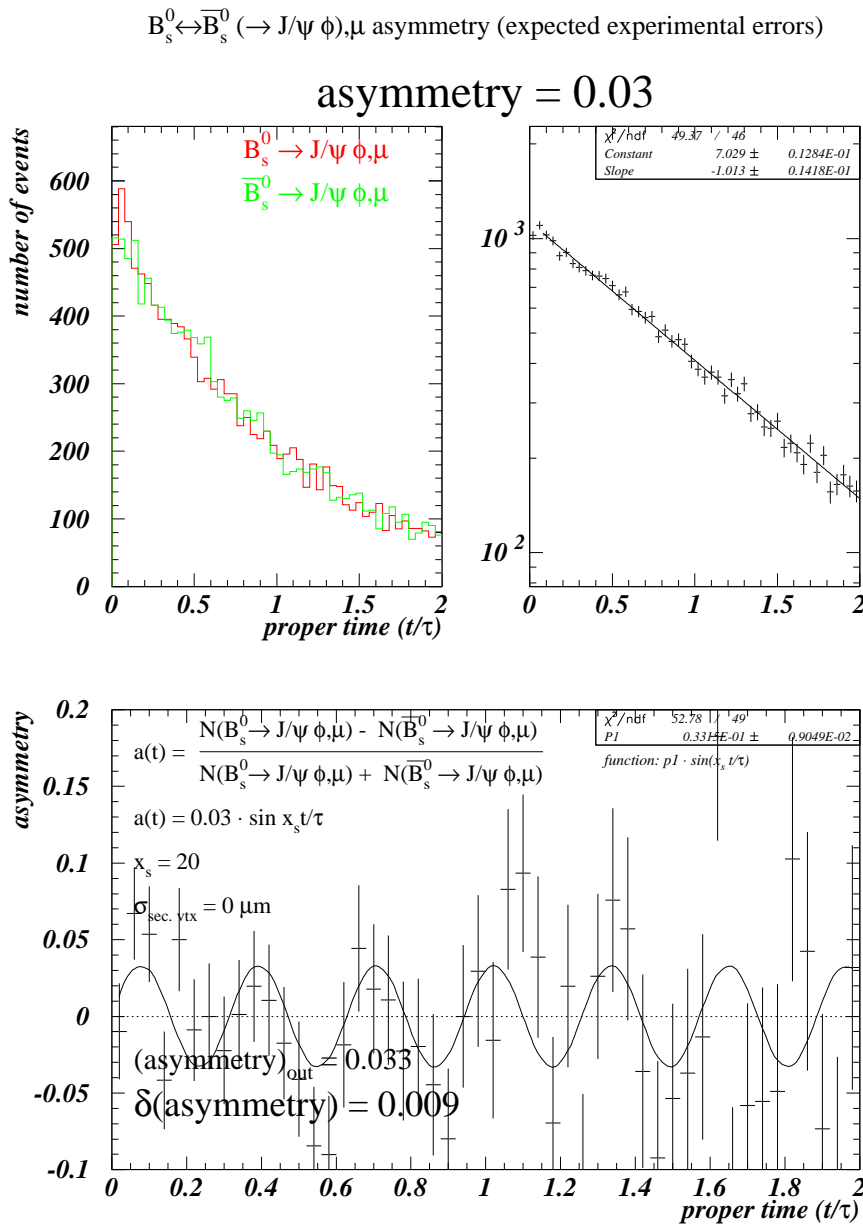


Figure 3.46: The time dependent study in $B_s \rightarrow J/\psi \phi \oplus \mu$ channel. The histograms are presented in terms of initially produced B_s^0 or \bar{B}_s^0 decaying to f_{CP} . The asymmetry of a value 0.03 was generated. In the upper-left plot the distribution of the time of B decay is presented for two kinds of B separately, while in the upper-right plot their exponential sum is shown. In the lower plot the asymmetry between number of B_s^0 and \bar{B}_s^0 decaying to $J/\psi \phi$ state with an accompanying muon is shown. In such a case the asymmetry may be reconstructed with a precision of $\delta(\text{asymmetry}) = 0.009$.

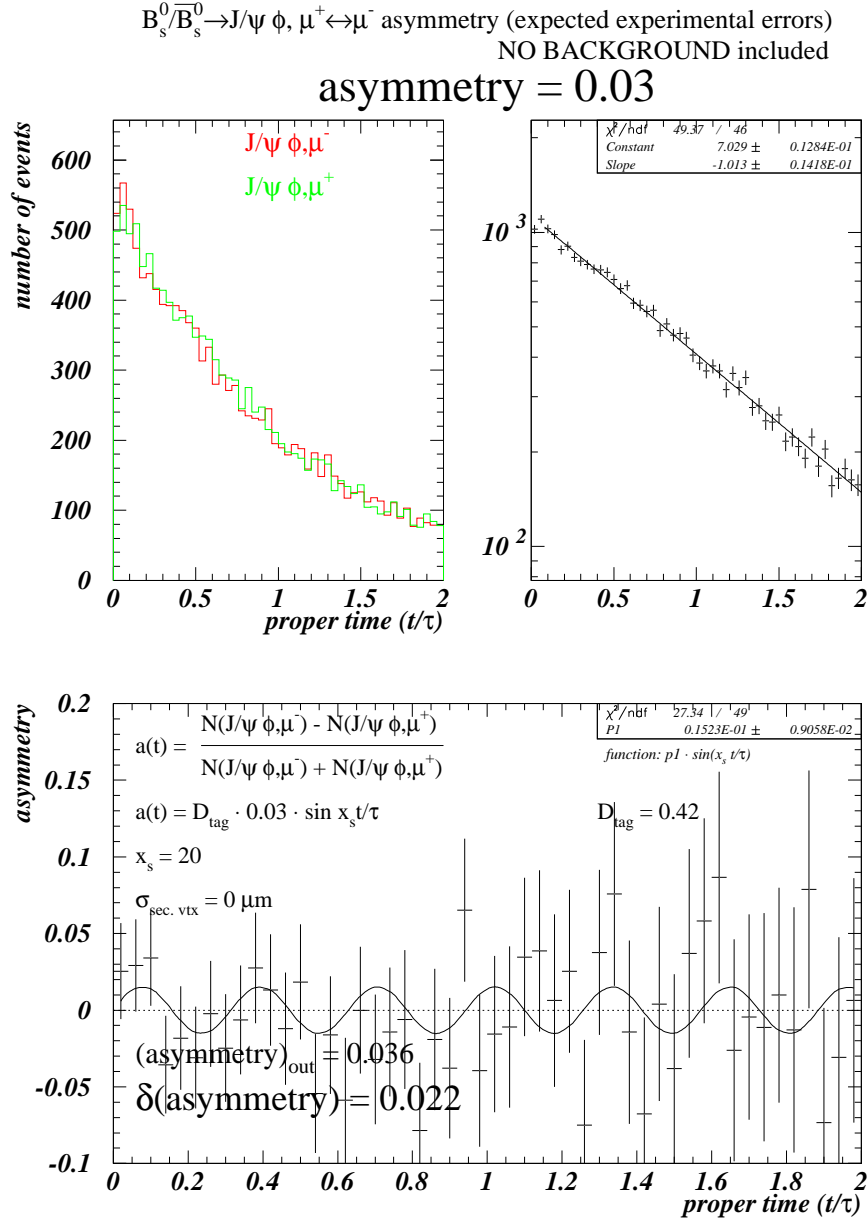


Figure 3.47: The time dependent study in $B_s \rightarrow J/\psi \phi \oplus \mu$ channel. The histograms are presented in terms of charges of associated muons. The intrinsic asymmetry of a value of 0.03 was generated. The background was neglected at that step, and the perfect reconstruction of the secondary vertex was assumed. In the upper-left plot the distribution of the time of B decay is presented for muons of different charges separately, while in the upper-right plot their exponential sum is shown. In the lower plot the asymmetry between number of μ^- and μ^+ accompanying the $B_s \rightarrow J/\psi \phi$ decay is shown. In such a case the asymmetry may be reconstructed with a precision of $\delta(\text{asymmetry}) = 0.022$.

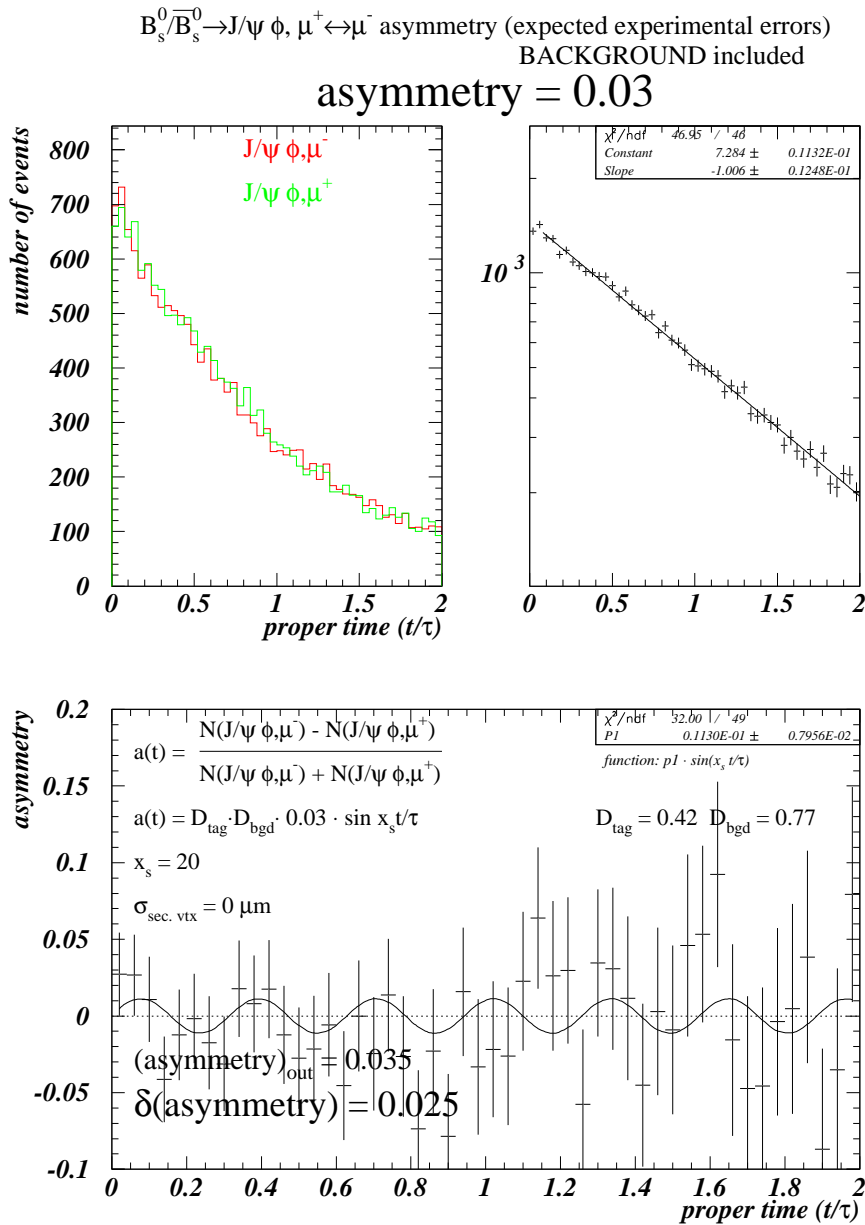


Figure 3.48: The time dependent study in $B_s \rightarrow J/\psi \phi \oplus \mu$ channel. The histograms are presented in terms of charges of associated muons. The intrinsic asymmetry of a value of 0.03 was generated. The background at the level of 30% of the signal was taken into account. The perfect reconstruction of the secondary vertex was assumed. In the upper-left plot the distribution of the time of B decay is presented for muons of different charges separately, while in the upper-right plot their exponential sum is shown. In the lower plot the asymmetry between number of μ^- and μ^+ accompanying the $B_s \rightarrow J/\psi \phi$ decay is shown. In such a case the asymmetry may be reconstructed with a precision of $\delta(\text{asymmetry}) = 0.025$.

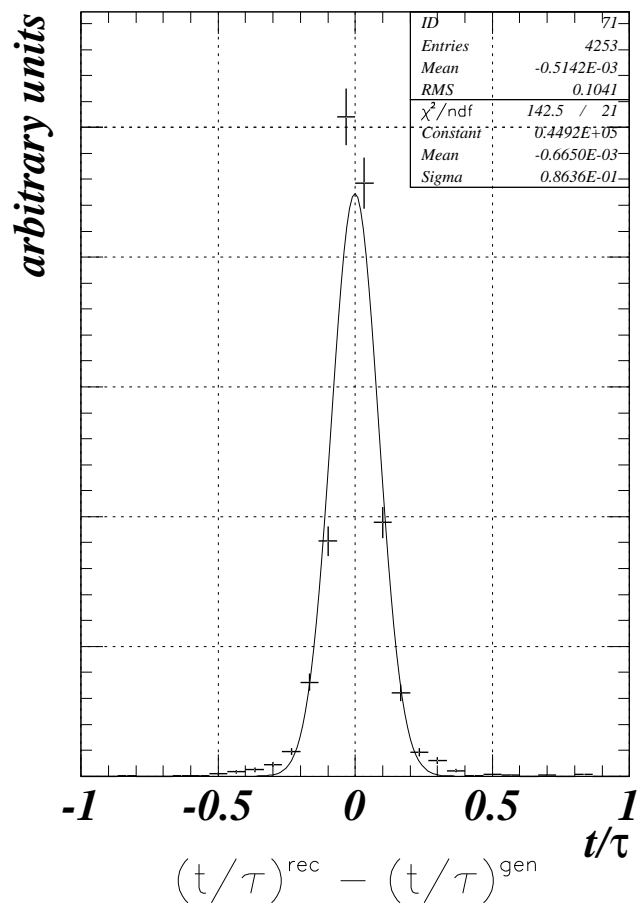


Figure 3.49: The distribution of time of the B_d decay in the $B_d \rightarrow J/\psi K_S \oplus \mu$ channel. The generated secondary vertex was smeared with $\sigma_{\text{sec. vtx.}} = 100 \mu\text{m}$. This corresponds to the CMS sensitivity to t/τ equal to about 0.1.

$B_d^0/\bar{B}_d^0 \rightarrow J/\psi K_S, \mu^+ \leftrightarrow \mu^-$ asymmetry (expected experimental errors)

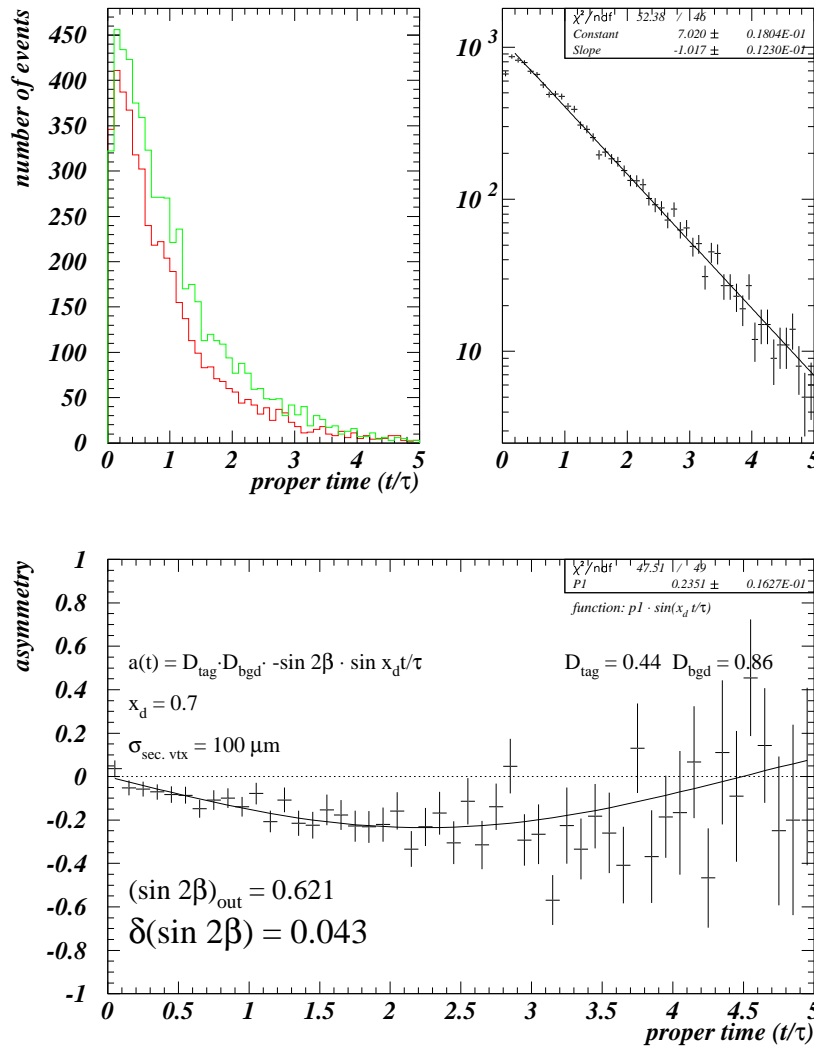


Figure 3.50: The time dependent study in $B_d \rightarrow J/\psi K_S \oplus \mu$ channel. The histograms are presented in terms of charges of associated muons. The assumed value of the intrinsic asymmetry was $\sin 2\beta = 0.6$. The background at the level of 16% of the signal was taken into account. The secondary vertex resolution of $100\mu\text{m}$ is faked by a t/τ smearing with $\sigma(t/\tau) = 0.1$. In the upper-left plot the distribution of the time of B decay is presented for muons of different charges separately, while in the upper-right plot their exponential sum is shown. In the lower plot the asymmetry between number of μ^- and μ^+ accompanying the $B_d \rightarrow J/\psi K_S$ decay is shown. In such a case the asymmetry may be reconstructed with a precision of $\delta(\sin 2\beta) = 0.043$ and the non-perfect secondary vertex reconstruction reflects in the minor shift of central value of the reconstructed asymmetry.

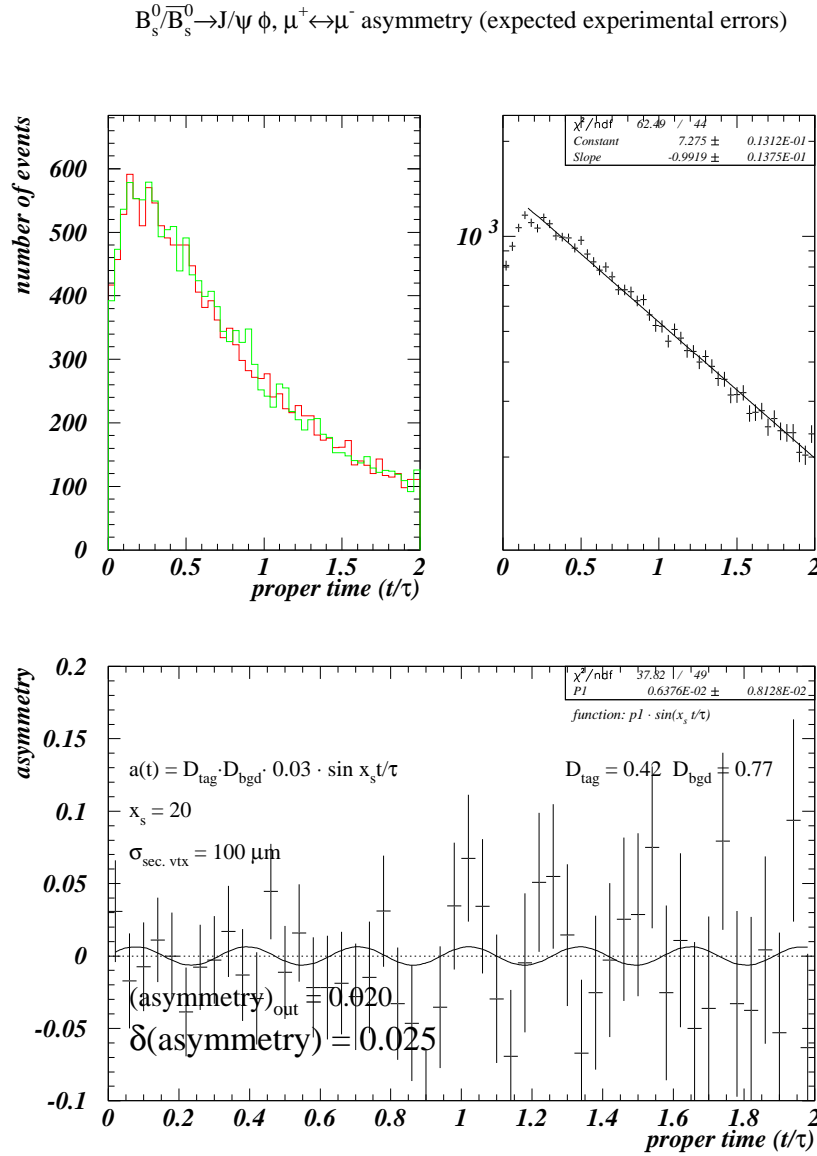


Figure 3.51: The time dependent study in $B_s \rightarrow J/\psi \phi \oplus \mu$ channel. The histograms are presented in terms of charges of associated muons. The intrinsic asymmetry of a value of 0.03 was generated. The background at the level of 30% of the signal was taken into account. The secondary vertex resolution of $100\mu\text{m}$ is faked by a t/τ smearing with $\sigma(t/\tau) = 0.1$. In the upper-left plot the distribution of the time of B decay is presented for muons of different charges separately, while in the upper-right plot their exponential sum is shown. In the lower plot the asymmetry between number of μ^- and μ^+ accompanying the $B_s \rightarrow J/\psi \phi$ decay is shown. In such a case the asymmetry may be reconstructed with a precision of $\delta(\text{asymmetry}) = 0.025$. One should note that the non-perfect secondary vertex reconstruction reflects in the shift of central value of the reconstructed asymmetry.

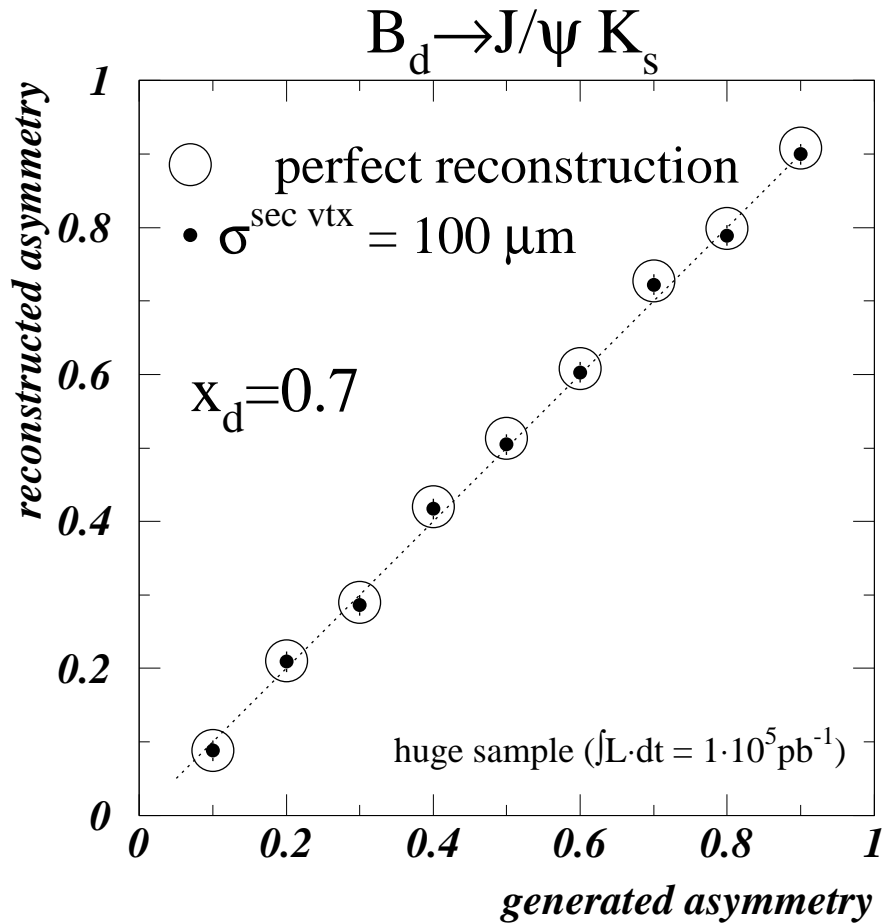


Figure 3.52: The influence of secondary vertex reconstruction for a value of reconstructed asymmetry in $B_d \rightarrow J/\psi K_S \oplus \mu$ channel. The secondary vertex resolution of $100 \mu\text{m}$ is faked by a t/τ smearing with $\sigma(t/\tau) = 0.1$. The reconstructed asymmetry in a case of perfect secondary vertex resolution is given by an empty circle, whereas the case of $\sigma_{\text{sec. vtx.}} = 100 \mu\text{m}$ is marked with full circles. A large sample of events corresponding to one year at full LHC luminosity was used. The displacement of the full point from the centre of the empty circle is a measure of the effect of the secondary vertex smearing. The errors for full and empty circles are equal.

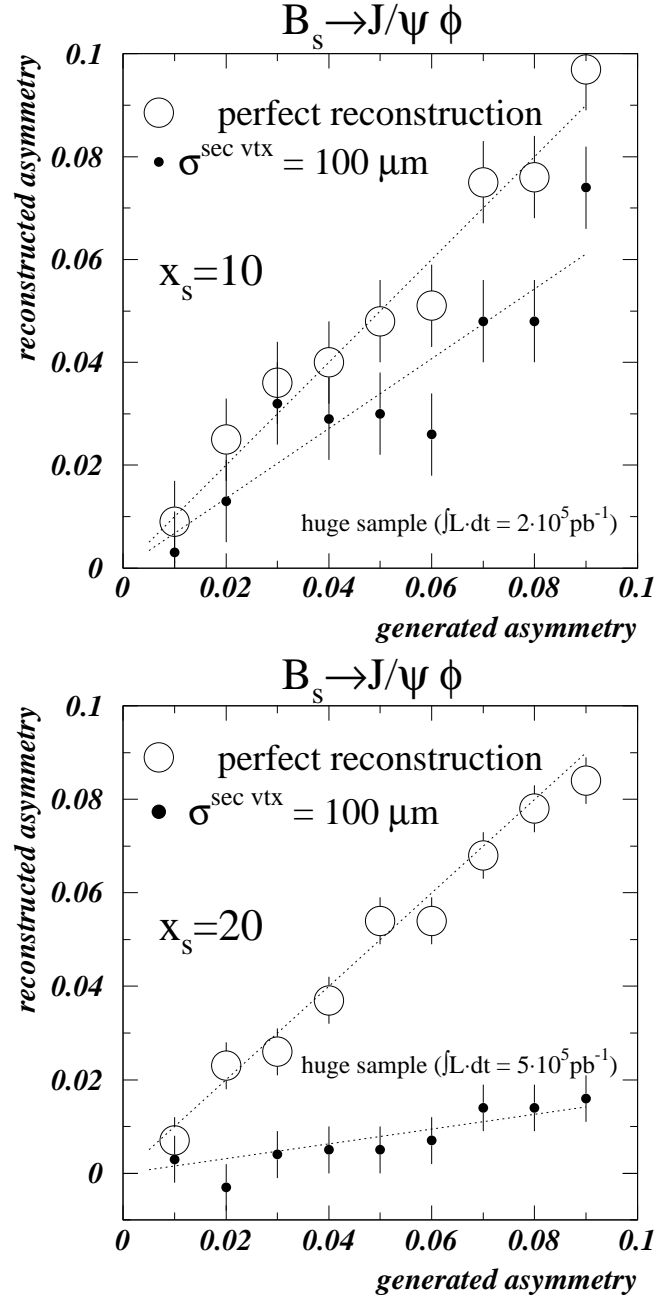


Figure 3.53: The influence of secondary vertex reconstruction for a value of reconstructed asymmetry in $B_s \rightarrow J/\psi \phi \oplus \mu$ channel for the two investigated values of $x_s = 10$ and 20. The secondary vertex resolution of $100 \mu\text{m}$ is faked by a t/τ smearing with $\sigma(t/\tau) = 0.1$. The reconstructed asymmetry in a case of perfect secondary vertex resolution is given by empty circles, whereas the case of $\sigma_{\text{sec. vtx.}} = 100 \mu\text{m}$ is marked with full circles. A large sample of events corresponding to several years of LHC running at maximal luminosity was used.

Summary and perspective outlook

The goal of this thesis was to present the simulation study of the CMS potential to measure the CP violation in B -meson decays in the modes similar to the *gold plated* $B_d \rightarrow J/\psi K_S \oplus \mu^{tag}$ channel followed with easy to trigger and reconstruct $J/\psi \rightarrow \mu^+ \mu^-$ decay mode. The time integrated studies were performed using the package developed for the purposes of CMS B -physics group with the underlying PYTHIA event generator. The detector response was faked with the parameterisation functions, most of them obtained with the detailed CMS simulation with CMSIM package interfaced with the GEANT package. The simplified kinematic cut optimisation was investigated, calculating the errors on CP violation asymmetries as a function of minimal transverse momentum of hadrons and associated (tagging) muon. The output from detailed simulation was used in the stand alone computer program derivate for the time dependent study. The results of the studies may be summarised as follows:

- The obtained minimal error on the intrinsic asymmetry $\delta(\text{Im}r_{CP}) = \delta(\sin 2\beta)$ in the time integrated study of the channel $B_d \rightarrow J/\psi K_S \oplus \mu \rightarrow \mu^+ \mu^- \pi^+ \pi^- \oplus \mu$ is 0.054 for low p_t cuts on associated muon and final pions, e.g. $p_t^{cut}(\mu^{tag}) = 2 \text{ GeV}/c$, $p_t^{cut}(\pi^\pm) = 0.75 \text{ GeV}/c$. One should note that the minimum is rather flat and the area of $\delta(\sin 2\beta) \leq 0.6$ is approximately bounded with $p_t^{cut}(\mu^{tag}) = 4 \text{ GeV}/c$ and $p_t^{cut}(\pi^\pm) = 1 \text{ GeV}/c$. The calculation of the error assumes exact knowledge of the dilution factors due to integration, tagging and background and takes into account statistical fluctuations of the number of events. The expected number of events at the above "working point" is about 11000 (for the integrated luminosity $\int L dt = 10^4 \text{ pb}^{-1}$) about 9500 of them signal ($D_{bgd} \approx 0.86$). The obtained fraction of wrong tags $w_{tag} \approx 0.28$ (mixing included) corresponds to the $D_{tag} \approx 0.44$.
- The expected minimal error on the intrinsic asymmetry $\delta(\text{Im}r_{CP})$ in the time integrated study of the $B_s \rightarrow J/\psi \phi \oplus \mu \rightarrow \mu^+ \mu^- K^+ K^- \oplus \mu$ channel is 0.23. This value was obtained for the lowest p_t cuts on associated muon $p_t^{cut}(\mu^{tag}) = 2 \text{ GeV}/c$ and the $p_t^{cut}(K^\pm) = 1 \text{ GeV}/c$. This large (compared to $B_d \rightarrow J/\psi K_S \oplus \mu$) error reflects the large value of x_s ($x_s = 10$ was used in the simulation). It is much above the value predicted in the framework

of the Standard Model. The expected number of events for the kinematic cuts coinciding with the minimal error is about 18000 total (14000 true signal events). The obtained fraction of wrong tags is $w_{tag} \approx 0.29$ (mixing included) corresponding to the $D_{tag} \approx 0.42$

- Within the statistical errors of the simulation the fraction of wrong tags (thus the dilution factor due to tagging) in the investigated B decay to CP eigenstate ($B_d \rightarrow J/\psi K_S \oplus \mu$, $B_s \rightarrow J/\psi \phi \oplus \mu$) can be provided by the control channels ($B_d \rightarrow J/\psi K^* \oplus \mu$, $B^\pm \rightarrow J/\psi K^\pm \oplus \mu$) using simple cut on the transverse momentum of final hadrons, which is intended to uniform the conditions of initial B decay. As an example, to reproduce the fraction of wrong tags at "working point" in $B_d \rightarrow J/\psi K_S \rightarrow \mu^+ \mu^- \pi^+ \pi^- \oplus \mu$ ($p_t^{cut}(\pi^\pm) = 0.75$ GeV/c) one should use $p_t^{cut}(K^\pm, \pi^\pm) = 0.75, 2.5$ GeV/c in the $B_d \rightarrow J/\psi K^* \rightarrow \mu^+ \mu^- K^\pm \pi^\mp \oplus \mu$ and $B^\pm \rightarrow J/\psi K^\pm \rightarrow \mu^+ \mu^- K^\pm \oplus \mu$ channels respectively.
- The simplified study of the time dependent method of measurement of $\sin 2\beta$ in $B_d \rightarrow J/\psi K_S$ shows that the error on intrinsic asymmetry could be cut down to $\delta(\sin 2\beta) \approx 0.043$ for the integrated luminosity of $\int L \cdot dt = 10^4$ pb $^{-1}$. This result was obtained faking the resolution of secondary vertex $\sigma_{sec.vtx.} = 100$ μ m with $\sigma(t/\tau) = 0.1$. The simulation shows, that the difference between perfect and smeared position of secondary vertex is minor in this channel.
- The simplified study of the time dependent method in the $B_s \rightarrow J/\psi \phi$ shows that the error on the intrinsic asymmetry $\text{Im}(r_{CP})$ is $\delta(\text{Im}r_{CP}) \approx 0.025$ for $\int L \cdot dt = 2 \cdot 10^4$ pb $^{-1}$, i.e. of the order of the value predicted by the Standard Model. This, however, assumes perfect knowledge of secondary vertex. In more realistic case, for two examined values of $x_s = 10$ ($x_s = 20$) it was obtained that the achievable error increases up to approximately 0.037 (0.15) reflecting the faked CMS resolution of the secondary vertex $\sigma_{sec.vtx.} = 100$ μ m.

It should be stressed that investigated $B \rightarrow J/\psi X \oplus \mu^{tag}$ decays are only a part of CMS B -physics program [43, 77]. Concerning the measurement of $\sin 2\beta$ with $B_d \rightarrow J/\psi K_S$ an efforts are taken to allow for the dilepton trigger and lepton tag, i.e. combining muons with electrons [78]. The self-tagging mode ($B^{*\pm} \rightarrow B_d^{(\pm)} \pi^\pm$) is very promising [79], but the underlying branching ratios are still very inexact. The CP violation in CMS is also to be measured ($\sin 2\alpha$) in the $B_d \rightarrow \pi^+ \pi^-$ channel [79], using the high p_t lepton as a trigger and a tag. Although the main issue of B -physics is to observe and measure the CP violation, other topics would not be given up. One should mention the search for rare decays (like $B_s \rightarrow \mu^+ \mu^-$) [70], measurement of x_s [80, 81, 82] – or essential for some SUSY/Higgs scenarios [83] – tagging of b -jets [84].

The CMS is a member of B -physics worldwide community, and the ten incoming years will be years of fruitful competition in a field of exploration of CP

violation phenomena. Several experiments with different beam configurations are involved. There are experiments at the e^-e^+ asymmetric $\Upsilon(4S)$ factories, namely BaBar at PEP II collider (9 GeV against 3.1 GeV) at SLAC, and Belle at KEKB at KEK (8 GeV against 3.5 GeV). There are general purpose detectors at hadron machines – CDF and D0 at TEVATRON ($p\bar{p}$ collider with $\sqrt{s} = 1.8$ TeV) in Fermilab and ATLAS and CMS at LHC in CERN. There are also dedicated B -experiments at general purpose colliders – HERA-B (fix target experiment) at 820 GeV proton beam of HERA ep collider in DESY, BTeV at TEVATRON (forward collider mode) and LHC-B at LHC (forward collider mode).

Some of the mentioned experiments are under construction. Data taking [85] would be initialised by HERA-B in 1998, soon followed (1999) by BaBar, BELLE and experiments at Fermilab. Theses experiments are expected to observe CP violation, by measuring $\sin 2\beta$ and $\sin 2\alpha$ at significant confidence level. The more precision measurement would come with LHC experiments when LHC will be turned on. The LHC-B will be able to measure γ of CKM unitarity triangle (measuring direct CP violation with $B_d \rightarrow DK^*$ and $B_s \rightarrow D_s K$ decays).

<i>Experiment</i>	$\delta \sin 2\beta$ ($B_d \rightarrow J/\psi K_S$)	$\delta \sin 2\alpha$ ($B_d \rightarrow \pi^+ \pi^-$)
HERA-B	0.13	0.14
BaBar	0.10	0.20
BELLE	0.08	0.15
CDF/D0	0.10	0.10
ATLAS	0.018 ¹	0.05
CMS	0.054/0.043 ²	0.06
LHC-B	0.023	0.04

Table 0.1: Error on $\sin 2\beta$ and $\sin 2\alpha$ for various future experiments. The upper part of table groups experiments that are expected to provide first evidences of CP violation in B -meson system (statistical errors are given for one year at their design luminosities). In the lower part of the table the sensitivities for LHC experiments are shown. Statistical errors are given for one year of data taking at luminosities $10^{33}\text{cm}^{-2}\text{s}^{-1}$ for ATLAS and CMS and $1.5 \cdot 10^{32}\text{cm}^{-2}\text{s}^{-1}$ in case of LHC-B.

¹This number corresponds to ATLAS electron and muon combined mode, increasing statistics approximately by a factor of four compared to analysis presented in this thesis.

²This thesis. Using decay mode with 3 muons in the final state only. Two cited values corresponds to time integrated and time dependent study respectively. For ATLAS 3 muonic mode, the error of the time integrated method is 0.036.

Appendix A

Standard Model and the CP violation

The¹ Standard Model is a Lagrangian field theory with underlying local gauge symmetry $SU(3)_C \otimes SU(2)_L \otimes U(1)_Y$. It is intended to describe strong, weak and electromagnetic interactions of fundamental fermions – quarks and leptons. The $SU(3)_C$ group (where C stands for colour) is responsible for a strong (QCD) sector of the Standard Model, with 8 massless gluons (spin-1 bosons) as the strong force mediators. The $SU(2)_L \otimes U(1)_Y$ part describes unified weak and electromagnetic (called together electroweak) part of the theory. There are 3 intermediate boson fields associated with weak isospin $SU(2)$ symmetry group and a single one corresponding to weak hypercharge group $U(1)_Y$. The $SU(2)_L \otimes U(1)_Y$ symmetric Standard Model is a massless theory. There is no way to introduce mass terms for quarks and leptons and for intermediate bosons, since the mass terms of usual form violate the underlying gauge symmetry, and - in case of intermediate bosons - make the theory non-renormalizable.

The masses for intermediate bosons of electroweak part are introduced by the so called Spontaneous Symmetry Breaking (SSB). The symmetry is broken by the non-symmetric vacuum. The electroweak group is reduced to its electromagnetic subgroup [86]:

$$SU(3)_C \otimes SU(2)_L \otimes U(1)_Y \xrightarrow{SSB} SU(3)_C \otimes U(1)_{QED}$$

The Spontaneous Symmetry Breaking, apart from the mass generation for (3 out of 4) electroweak, intermediate bosons introduces at least one massive scalar particle – so called Higgs particle.

Thus, there are three types of objects in The Standard Model:

- fundamental spin 1/2 fermions (quark and leptons),

¹The part of this Appendix devoted to introduction of the Standard Model Lagrangian is based on the reviews [86]-[88]. The sections dedicated to CP conjugation are based on [89]-[90].

- force mediators – spin 1 bosons,
- the Higgs particle(s).

The fermion-Higgs couplings allow us to incorporate fermion masses in possible quark mixing phenomena in a compact and clear way. Finally, the quark mixing via Cabibbo-Kobayashi-Maskawa matrix is a source of potential CP violation in the electroweak Standard Model framework.

A.1 The $SU(2)_L \otimes U(1)_Y$ symmetric electroweak Lagrangian

The Electroweak Standard Model is based on (or is invariant under) the local $SU(2)$ gauge symmetry of weak isospin combined with the local $U(1)$ symmetry of weak hypercharge. There are four gauge (vector) bosons induced by the assumed symmetry: W_μ^i ($i = 1 \dots 3$) and B_μ .

There is a clear experimental evidence that there are different rules for interactions of left-handed and right-handed fermion components. Thus in the Electroweak Model fermions are decomposed to left- and right-handed fields. The left-handed fermions are grouped in pairs which transform as doublets under weak $SU(2)_L$ group (that is what index L stands for), whereas right-handed components are singlets. One can distinguish the following fermion fields in the Standard Model Lagrangian (the formulae define the notation which will be used in this Appendix):

$$\left. \begin{array}{ll} \text{leptons} & \begin{array}{l} \nu_l = \{\nu_e, \nu_\mu, \nu_\tau\} \\ l = \{e, \mu, \tau\} \end{array} \end{array} \rightarrow \left(\begin{array}{c} \nu_l \\ l^- \end{array} \right)_L, l_R^- \right\} \Psi_L^i = \left(\begin{array}{c} f \\ f' \end{array} \right)_L, \Psi_R^i = f_R, f_R' \\ \text{quarks} & \begin{array}{l} q = \{u, c, t\} \\ q' = \{d, s, b\} \end{array} \end{array} \rightarrow \left(\begin{array}{c} q \\ q' \end{array} \right)_L, q_R, q_R' \right\}$$

The left and right fermions are created by the action of left and right projection operators on initial fermion field f , i.e.:

$$f_L = \underbrace{\frac{1}{2}(1 - \gamma^5)}_{\text{left projection}} f \qquad f_R = \underbrace{\frac{1}{2}(1 + \gamma^5)}_{\text{right projection}} f \qquad (\text{A.1})$$

The number of fermion generations in the basic version of The Standard Model is three, since it seems that it is the choice of Nature. This number may be however easily extended in the theory if necessary. One may also notice that there are no right-handed neutrinos in The Standard Model, since - up to now - there is no experimental evidence for their existence. This is also a matter of choice that can be easily extended if necessary (leading to massive neutrinos and possible lepton mixing).

Another object that appears in the Standard Model Lagrangian is a Higgs field. In the $SU(2)_L \otimes U(1)_Y$ invariant theory, the Higgs field appears as a doublet (under weak isospin group) denoted with a symbol ϕ :

$$\phi = \begin{pmatrix} \phi^+ \\ \phi^0 \end{pmatrix} = \frac{1}{\sqrt{2}} \begin{pmatrix} \phi_1 + i\phi_2 \\ \phi_3 + i\phi_4 \end{pmatrix}, \quad (\text{A.2})$$

where ϕ_i ($i = 1 \dots 4$) are four real scalar fields.

The $SU(2)_L \otimes U(1)_Y$ invariant Electroweak Lagrangian may be symbolically decomposed into 6 terms, each of them depending on a different set of fields [87]:

$$\mathcal{L} = \mathcal{L}(\Psi, W, B) + \mathcal{L}(W) + \mathcal{L}(B) + \mathcal{L}(W, B, \phi) - V(\phi) + \mathcal{L}(\Psi, \phi) \quad (\text{A.3})$$

These terms will be discussed in more details in sections A.1.2 – A.1.4.

A.1.1 The underlying gauge symmetry

The central principle of the gauge theories is that the Lagrangian remains invariant under some local (space-time dependent) transformations.

The $U(1)_Y$ symmetry operator acts on the fermion field Ψ as follows:

$$\Psi \xrightarrow{U(1)_Y} \Psi' = U_1 \Psi = e^{i\alpha Y} \Psi, \quad (\text{A.4})$$

where $\alpha(x)$ is arbitrary, space-time dependent (i.e. local) real function, Y – the hypercharge operator. The fermion fields are the eigenstates of the hypercharge operator with eigenvalue y_Ψ ($Y\Psi = y_\Psi\Psi$)

The action of $SU(2)_L$ group on fermion field is more complex. For the left components of fermion fields:

$$\Psi_L \xrightarrow{SU(2)_L} \Psi'_L = U_2 \begin{pmatrix} f \\ f' \end{pmatrix}_L = e^{i\vec{\alpha}(x) \cdot \vec{T}} \begin{pmatrix} f \\ f' \end{pmatrix}_L, \quad (\text{A.5})$$

whereas the right components remain untouched by the $SU(2)_L$ action. The $\vec{\alpha}(x)$ is an arbitrary vector of real functions. $\vec{T} = \{T_1, T_2, T_3\}$ is a set of 3 group generators. In usually used (Pauli matrix) representation $T_i = \frac{\sigma_i}{2}$. Thus the upper components of Ψ_L^j have the T_3 eigenvalue $t_3^j = \frac{1}{2}$ while their lower partners have $t_3^j = -\frac{1}{2}$. The sum of T_3 and Y forms the charge operator

$$Q = T_3 + Y$$

A.1.2 The $\mathcal{L}(\Psi, W, B)$ term

The purely kinetic Lagrangian for free fermions has a form

$$\mathcal{L}_0 = \sum_{\text{fermions}} i\bar{\Psi}^j \gamma^\mu \partial_\mu \Psi^j \quad (\text{A.6})$$

that is not invariant under combined $U_1 \cdot U_2$ gauge operation. A way for obtaining an invariant formula is to replace the ordinary derivative with the covariant one:

$$\partial_\mu \rightarrow D_\mu = \partial_\mu + ig\vec{T}\vec{W}_\mu + ig'Y B_\mu \quad (\text{A.7})$$

(the rules for transformation of B and W are given in next section), where g and g' are coupling constants for W_μ^i and B_μ gauge bosons respectively. Then the (A.6) expands to:

$$\begin{aligned} \mathcal{L}(\Psi, W, B) &= \sum_{\text{fermions}} i \bar{\Psi}^j \gamma^\mu D_\mu \Psi^j \\ &= \sum_{\text{fermions}} \bar{\Psi}_L^j \gamma^\mu \left[i\partial_\mu - g\vec{T}\vec{W}_\mu - g'Y B_\mu \right] \Psi_L^j \\ &+ \sum_{\text{fermions}} \bar{\Psi}_R^j \gamma^\mu [i\partial_\mu - g'Y B_\mu] \Psi_R^j \end{aligned} \quad (\text{A.8})$$

These terms describe a motion of the fundamental fermions as well as their interactions with gauge fields B, W . The fermion-boson couplings appears as a consequence of gauge invariance.

A.1.2.a The Charged Currents

The B and \vec{W} fields representing intermediate bosons in (A.3) are not those observed experimentally. Instead, the W^+, W^-, Z^0 and γ (with corresponding field A_μ) are well known intermediate bosons. In the Standard Model they are described as the mixture of \vec{W} and B . Out of 3 W_i bosons, W_1 and W_2 are used to form a charged combinations W^+ and W^- , whereas the third, neutral W_3 is mixed with the neutral B to form Z^0 and γ . Their interactions with fermions are characterised with so called Charged Currents (CC) and Neutral Currents (NC) pieces of the Lagrangian. From (A.8) one can extract terms which contain W_1 and W_2

$$\begin{aligned} \mathcal{L}_{CC} &= - \sum_{\text{fermions}} \bar{\Psi}_L^j g \gamma^\mu (T^1 W_\mu^1 + T^2 W_\mu^2) \Psi_L^j \\ &= - \sum \frac{g}{2} \bar{\Psi}_L^j \gamma^\mu \begin{pmatrix} 0 & W_\mu^1 - iW_\mu^2 \\ W_\mu^1 + iW_\mu^2 & 0 \end{pmatrix} \Psi_L^j \\ &= - \sum \frac{g}{\sqrt{2}} \bar{\Psi}_L^j \gamma^\mu (T^+ W_\mu^+ + T^- W_\mu^-) \Psi_L^j \\ &= - \sum \frac{g}{\sqrt{2}} (\bar{f}_L^j \gamma^\mu W_\mu^+ f_L^j + \bar{f}_L^j \gamma^\mu W_\mu^- f_L^j) \\ &= - \frac{g}{2\sqrt{2}} \left(J_{CC}^\mu W_\mu^+ + J_{CC}^{\mu\dagger} W_\mu^- \right) \end{aligned} \quad (\text{A.9})$$

where $W_\mu^\pm = \frac{W_\mu^1 \mp iW_\mu^2}{\sqrt{2}}$ are charged weak boson fields, $J_{CC} = \sum \bar{f} \gamma^\mu (1 - \gamma^5) f'$ – the charged current (in terms of weak eigenstates). The $T^+ = \begin{pmatrix} 0 & 1 \\ 0 & 0 \end{pmatrix}$

and $T^- = \begin{pmatrix} 0 & 0 \\ 1 & 0 \end{pmatrix}$ matrices are weak isospin rising and lowering operators.

Due to them, the upper components of $SU(2)_L$ fermion doublet are coupled to the lower ones (and vice versa) with a help of intermediate bosons W^+ , W^- . At this stage the \mathcal{L}_{CC} expressed in terms of gauge eigenstates is diagonal in generations (i.e. family conserving).

A.1.2.b The Neutral Currents

The W_μ^3 and B_μ in $\mathcal{L}(\Psi, W, B)$ are orthogonal mixtures of experimentally observed Z_μ and A_μ fields, connected through the relation:

$$\begin{pmatrix} W_\mu^3 \\ B_\mu \end{pmatrix} = \begin{pmatrix} \cos \theta_W & \sin \theta_W \\ -\sin \theta_W & \cos \theta_W \end{pmatrix} \begin{pmatrix} Z_\mu \\ A_\mu \end{pmatrix} \quad (\text{A.10})$$

Pieces of the Lagrangian (A.8) which contain W^3 and B may be rewritten as:

$$\begin{aligned} \mathcal{L}_{NC} &= - \sum_{\text{fermions}} \bar{\Psi}_L^j \gamma^\mu (g T^3 W_\mu^3 + g' Y B_\mu) \Psi_L^j \\ &\quad - \sum_{\text{fermions}} \bar{\Psi}_R^j \gamma^\mu g' y_j B_\mu \Psi_R^j \\ &= - \sum_{\text{fermions}} f^{(\prime)j}_{L,R} \gamma^\mu (g t_j^3 W_\mu^3 + g' y_j B_\mu) f^{(\prime)j}_{L,R}, \end{aligned} \quad (\text{A.11})$$

with $t_j^3 = \pm \frac{1}{2}$ for members of $SU(2)_L$ doublet and $t_j^3 = 0$ for f_R, f'_R . Substituting A_μ and Z_μ in (A.11) on gets:

$$\begin{aligned} \mathcal{L}_{NC} &= - \sum_{\text{fermions}} f^{(\prime)j}_{L,R} \gamma^\mu A_\mu \underbrace{(t_j^3 g \sin \theta_W + y_j g' \cos \theta_W)}_{eq_j} f^{(\prime)j}_{L,R} \\ &\quad - \sum_{\text{fermions}} f^{(\prime)j}_{L,R} \gamma^\mu Z_\mu (t_j^3 g \cos \theta_W - g' y_j \sin \theta_W) f^{(\prime)j}_{L,R} \end{aligned} \quad (\text{A.12})$$

In order to recognise the QED Lagrangian, one has to fix g and g' couplings in terms of e (e stands for the positron electric charge) and θ_W . Thus imposing relation $e = g \sin \theta_W = g' \cos \theta_W$ with correspondence $q_j = t_j^3 + y_j$ one gets:

$$\mathcal{L}_{NC} = -e A_\mu \sum_{\text{fermions}} f^{(\prime)j} \gamma^\mu q_j f^{(\prime)j} \quad (\text{A.13})$$

$$\begin{aligned} &- \frac{g}{2 \cos \theta_W} Z_\mu \sum_{\text{fermions}} f^{(\prime)j} \gamma^\mu \left(\underbrace{t_{jL}^3 - 2q_j \sin^2 \theta_W}_{g_j^V} - \underbrace{t_{jL}^3}_{g_j^A} \gamma^5 \right) f^{(\prime)j} \\ &= -e A_\mu J_{EM}^\mu - \frac{g}{2 \cos \theta_W} Z_\mu J_Z^\mu = \mathcal{L}_{NC}^{QED} + \mathcal{L}_{NC}^Z \end{aligned} \quad (\text{A.14})$$

The neutral currents in the above equation describe fermion-fermion transitions with a help of intermediate bosons. The fermion flavours (hence the fermion family) remains unchanged – Neutral Currents are flavour conserving.

A.1.3 The $\mathcal{L}(W)$ and $\mathcal{L}(B)$ terms

In order to supplement the created fermion - boson couplings one has to add the kinetic terms for boson fields. The invariance of Lagrangian (A.3) implies the certain form of transformation of B and W fields. One can check that the transformations of a form:

$$\begin{aligned} B_\mu &\rightarrow B'_\mu = B_\mu - \frac{1}{g'} \partial_\mu \alpha \\ \vec{W}_\mu &\rightarrow \vec{W}'_\mu = \vec{W}_\mu - \frac{1}{g} \partial_\mu \vec{\alpha} - \vec{\alpha} \times \vec{W}_\mu \end{aligned} \quad (\text{A.15})$$

guarantee the $SU(2)_L \otimes U(1)_Y$ invariance of Lagrangian (A.3).

With the help of the above transformations, $SU(2)_L \otimes U(1)_Y$ invariant kinetic part of the Lagrangian may be written as:

$$\begin{aligned} \mathcal{L}(B) &= -\frac{1}{4} F_{\mu\nu} F^{\mu\nu} \\ \mathcal{L}(W) &= -\frac{1}{4} \vec{G}_{\mu\nu} \vec{G}^{\mu\nu}, \end{aligned} \quad (\text{A.16})$$

with

$$\begin{aligned} F_{\mu\nu} &= \partial_\mu B_\nu - \partial_\nu B_\mu \\ \vec{G}_{\mu\nu} &= \partial_\mu \vec{W}_\nu - \partial_\nu \vec{W}_\mu - g \vec{W}_\mu \times \vec{W}_\nu \end{aligned}$$

The $\mathcal{L}(B)$ is the standard QED Lagrangian for a moving boson field, whereas the $\mathcal{L}(W)$ apart of purely kinetic term, involves self interaction of bosons (boson - boson couplings). The last feature is a consequence of non-Abelian properties of the $SU(2)$ group.

A.1.4 Terms involving Higgs field:

$$\mathcal{L}(W, B, \phi) = V(\phi) + \mathcal{L}(\Psi, \phi)$$

The introduced Higgs doublet offers a possibility to construct more terms with suitable transformation properties. One can write down invariant Higgs field potential of the form:

$$V(\phi) = \mu^2 \phi^\dagger \phi + h(\phi^\dagger \phi)^2 \quad (\text{A.17})$$

and the corresponding invariant kinetic like term

$$\mathcal{L}(W, B, \phi) = (D_\mu \phi)^\dagger (D^\mu \phi) \quad (\text{A.18})$$

(the higher order terms in potential are forbidden by renormalization requirements). The use of a covariant derivative of a form (A.7), which ensures correct transformation properties of a Higgs doublet, introduces Higgs-Intermediate Boson couplings that are responsible for Intermediate Bosons mass generation (see the next subsection).

Apart from that, the fermion – Higgs coupling are admitted by Yukawa type Lagrangian

$$\begin{aligned} \mathcal{L}(\Psi, \phi) = & \sum_{\text{quarks}} c'_{jk} \bar{\Psi}_{jL} \phi f'_{kR} + c_{jk} \bar{\Psi}_{jL} \phi^C f_{kR} + h.c. \\ & + \sum_{\text{leptons}} c'_{jk} \bar{\Psi}_{jL} \phi f'_{kR} + c_{jk} \bar{\Psi}_{jL} \phi^C f_{kR} + h.c. \end{aligned} \quad (\text{A.19})$$

The $\phi^C = i\sigma_2\phi^*$ in the above equation is a ϕ hypercharge couple (i.e. its hypercharge eigenvalue is $y_{\phi^C} = -\frac{1}{2}$, whereas $y_{\phi} = +\frac{1}{2}$). All the terms in equation (A.19) correspond to Higgs-fermion-fermion vertices, and the charge and isospin conservation forbids terms like $\bar{\Psi}_L \phi^C f'_R$ as well as the quark-Higgs-lepton pieces.

It has to be emphasised that for the (not yet complete) description of the observed phenomena it is sufficient to keep only $\mathcal{L}(\Psi, W, B)$ and $\mathcal{L}(W) + \mathcal{L}(B)$ pieces of the electroweak Lagrangian. The introduction of Higgs field with a plenty of additional parameters and couplings is superfluous, since it does not lead to improvement of description of observed phenomena. The situation changes if Spontaneous Symmetry Breaking is considered.

A.2 The Spontaneous Symmetry Breaking

The fully symmetric Lagrangian described above guarantees the renormalizability of the theory, but does not allow us to introduce masses for fermions or for intermediate bosons. The solution is to disturb the symmetry in such a way as to get non-symmetric results from symmetric theory. This disturbance is effected by the specific choice of the parameters in the manifestly invariant term of Higgs field potential (A.17).

Generally, the parameter h should be greater than zero, otherwise the potential has no minimum and the theory has no ground state. Concerning the μ^2 - if it is positive the ground state is $\phi = 0$ and the theory remains symmetric, in other case (that seems to be made real by Nature) the μ^2 is negative, leading to an infinite degenerate set of non trivial minima (ground states). Indeed, for $h > 0$ and $\mu^2 < 0$ the condition for the minimum of the potential (A.17) with Higgs field given by (A.2) is:

$$\frac{1}{2}(\phi_1^2 + \phi_2^2 + \phi_3^2 + \phi_4^2) = \frac{-\mu^2}{2h}, \quad (\text{A.20})$$

It is a choice of Nature which one of the infinite number of equivalent minima is realised. This choice is called Spontaneous Symmetry Breaking (SSB). Since in Quantum Field Theory the ground state represents the vacuum one can say that the SSB appears if one has the symmetric Lagrangian but the non symmetric vacuum. It is convenient to choose a ground state ϕ^V at

$$\phi^V = \frac{1}{\sqrt{2}} \begin{pmatrix} 0 \\ v \end{pmatrix}, \quad v = \sqrt{\frac{-\mu^2}{h}} \quad (\text{A.21})$$

After the ground state is fixed² the theory is shifted to chosen minimum (or, in other words the theory is expanded around it). Hence the ϕ of (A.2) may be parameterised as follows

$$\phi = \phi^V + \phi' = \frac{1}{\sqrt{2}} e^{i\vec{T} \cdot \vec{\Theta}(x)} \begin{pmatrix} 0 \\ v + H(x) \end{pmatrix}, \quad (\text{A.22})$$

where $\vec{\Theta}(x)$ and $H(x)$ denotes four real scalar fields. Writing down the potential (A.17) one gets (neglecting constant terms)

$$V(H) = -\mu^2 H^2 + hvH^3 + \frac{h}{4} H^4, \quad (\text{A.23})$$

in which one can associated a mass $m_H = \sqrt{-2\mu^2}$ with the scalar field $H(x)$, whereas the remaining $\vec{\Theta}(x)$ fields are massless (Goldstone bosons). The explicit choice of appropriate gauging may gauge them away, which shows that they are not physical (as they disappear from theory). Finally the Spontaneous Symmetry Breaking appears as the global replacement of four scalar fields ϕ with a single scalar field $H(x)$. The replacement has a form:

$$\phi \longrightarrow \begin{pmatrix} 0 \\ v + H(x) \end{pmatrix} \quad (\text{A.24})$$

A.2.1 The masses of Intermediate Bosons

The masses of Intermediate Bosons are generated from $SU(2)_L \otimes U(1)_Y$ invariant kinetic term $(D^\mu \phi)^\dagger (D_\mu \phi)$ by the replacement (A.24):

$$\begin{aligned} (D^\mu \phi)^\dagger (D_\mu \phi) &= \dots + \left| (g\vec{T} \cdot \vec{W} + g'YB) \frac{1}{\sqrt{2}} \begin{pmatrix} 0 \\ v \end{pmatrix} \right|^2 + \dots \\ &= \dots + \frac{g^2 v^2}{8} [(W^1)^2 + (W^2)^2] + \frac{v^2}{2} \left(-\frac{g}{2} W^3 + g'Y_V B \right)^2 + \dots \\ &= \dots + \frac{g^2 v^2}{8} (W_\mu^+)^\dagger W^{+\mu} + \frac{g^2 v^2}{8} (W_\mu^-)^\dagger W^{-\mu} + \frac{g^2 v^2}{8 \cos^2 \theta_W} Z_\mu Z^\mu + \dots \end{aligned} \quad (\text{A.25})$$

Thus, among others, the mass terms of intermediate boson appear. The SSB generates masses for W^+ , W^- and Z^0 intermediate vector bosons, whereas the photon remains massless, as it should be (in fact this constraints A.10).

A.2.2 Mass generation for fermions

The mass term of fermions of the usual form $m_f \bar{f} f$ expressed in terms of left and right fermion fields mix both types of components: $\bar{f} f = \bar{f}_L f_R + \bar{f}_R f_L$. Since left-handed fermions are combined in doublets while right are singlets

²Note, that the choice of a particular ground state is irrelevant since different solutions may be transformed into each other through the choice of specific gauging.

under $SU(2)$ transformations the usual fermion mass term would violate the underlying symmetry. Thus within the fully symmetric $SU(2)_L \otimes U(1)_Y$ Lagrangian (i.e. before SSB is involved in the construction) the masses of fermions do not appear.

The situation changes when one considers Yukawa type fermion-Higgs interactions of the form (A.19). The left fermions are coupled with the right ones with a help of a Higgs doublet. The Spontaneous Symmetry Breaking in some of Yukawa terms replaces Higgs scalar with a vacuum expectation parameter v , generating mass-like terms, coupling left and right components of fermion fields, namely

$$\begin{aligned}
& c'_{kk} \bar{\Psi}_{kL} \phi f'_{kR} + \\
& c_{kk} \bar{\Psi}_{kL} \phi^C f_{kR} + \xrightarrow{SSB} \dots + c'_{kk} \bar{\Psi}_{kL} \begin{pmatrix} 0 \\ \frac{v}{\sqrt{2}} \end{pmatrix} f'_{kR} + \\
& c'_{kk} \bar{f}'_{kR} \phi^T \Psi_{kL} + c_{kk} \bar{\Psi}_{kL} \begin{pmatrix} \frac{v}{\sqrt{2}} \\ 0 \end{pmatrix} f_{kR} + \\
& c'_{kk} \bar{f}'_{kR} \begin{pmatrix} 0 & \frac{v}{\sqrt{2}} \end{pmatrix} \Psi_{kL} + \\
& c_{kk} \bar{f}_{kR} \begin{pmatrix} \frac{v}{\sqrt{2}} & 0 \end{pmatrix} \Psi_{kL} \\
& = \dots + \frac{c'_{kk} v}{\sqrt{2}} (\bar{f}'_{kL} f'_{kR} + \bar{f}'_{kR} f'_{kL}) + \frac{c_{kk} v}{\sqrt{2}} (\bar{f}_{kL} f_{kR} + \bar{f}_{kR} f_{kL}) \\
& = \dots - (m'_{kk} \bar{f}'_k f'_k + m_{kk} \bar{f}_k f_k) \tag{A.26}
\end{aligned}$$

As one can see, mass-like terms appear³. Since c_{jk}, c'_{jk} for $j \neq k$ in equation (A.19) are arbitrary complex numbers, additional terms involving fields belonging to different generation appear. The full Yukawa piece of the $SU(2)_L \otimes U(1)_Y$ Lagrangian after SSB becomes

$$\begin{aligned}
\mathcal{L}_Y &= -(1 + \frac{H}{v}) \left\{ \sum_{\text{quarks}} \bar{f}_{jL} m_{jk} f_{kR} + \bar{f}'_{jL} m'_{jk} f'_{kR} + h.c. + \right. \\
&\quad \left. \sum_{\text{leptons}} \bar{f}_{jL} m_{jk} f_{kR} + \bar{f}'_{jL} m'_{jk} f'_{kR} + h.c. \right\} \\
&= -(1 + \frac{H}{v}) \left\{ \begin{aligned} & (\bar{u} \quad \bar{c} \quad \bar{t})_L \mathbf{m}_U \begin{pmatrix} u \\ c \\ t \end{pmatrix}_R + (\bar{u} \quad \bar{c} \quad \bar{t})_R (\mathbf{m}_U)^\dagger \begin{pmatrix} u \\ c \\ t \end{pmatrix}_L + \\ & (\bar{d} \quad \bar{s} \quad \bar{b})_L \mathbf{m}_D \begin{pmatrix} d \\ s \\ b \end{pmatrix}_R + (\bar{d} \quad \bar{s} \quad \bar{b})_R (\mathbf{m}_D)^\dagger \begin{pmatrix} d \\ s \\ b \end{pmatrix}_L + \\ & (\bar{e} \quad \bar{\mu} \quad \bar{\tau})_L \mathbf{m}_L \begin{pmatrix} e \\ \mu \\ \tau \end{pmatrix}_R + (\bar{e} \quad \bar{\mu} \quad \bar{\tau})_R (\mathbf{m}_L)^\dagger \begin{pmatrix} e \\ \mu \\ \tau \end{pmatrix}_L \end{aligned} \right\}
\end{aligned}$$

³Note that (A.26) is correct if one redefine fields f'_R and f_R to make c, c' real.

$$= -(1 + \frac{H}{v}) \left\{ \sum_{fermions} \bar{\mathcal{F}}_L \mathbf{m}_{\mathcal{F}} \mathcal{F}_R + \bar{\mathcal{F}}_R \mathbf{m}_{\mathcal{F}}^\dagger \mathcal{F}_L \right\}, \quad (\text{A.27})$$

$$\text{with } \mathcal{F} = \{\mathcal{U}, \mathcal{D}, \mathcal{L}\} = \left\{ \begin{pmatrix} u \\ c \\ t \end{pmatrix}, \begin{pmatrix} d \\ s \\ b \end{pmatrix}, \begin{pmatrix} e \\ \mu \\ \tau \end{pmatrix} \right\}.$$

The $\mathbf{m}_{\mathcal{F}}$ are 3x3 unitary mass matrices⁴ of arbitrary complex numbers. The mass matrices may be diagonalized with a help of binormal transformation:

$$\mathbf{M}_{\mathcal{F}} = \begin{bmatrix} m_1 & \cdot & \cdot \\ \cdot & m_2 & \cdot \\ \cdot & \cdot & m_3 \end{bmatrix} = \mathbf{V}_{\mathcal{F}} \mathbf{m}_{\mathcal{F}} \mathbf{V}_{\mathcal{F}}'^\dagger \quad (\text{A.28})$$

Furthermore, the proper choice of phases of quark fields leads to real and positive $\mathbf{M}_{\mathcal{F}}$. Substituting $\mathbf{m}_{\mathcal{F}} = \mathbf{V}_{\mathcal{F}}^\dagger \mathbf{M}_{\mathcal{F}} \mathbf{V}_{\mathcal{F}}'$ in (A.27) the Yukawa piece of the Standard Model Lagrangian becomes:

$$\begin{aligned} \mathcal{L}_Y &= -(1 + \frac{H}{v}) \{ (\bar{\mathcal{U}}_L \mathbf{V}_{\mathcal{U}}^\dagger) \mathbf{M}_{\mathcal{U}} (\mathbf{V}_{\mathcal{U}}' \mathcal{U}_R) + (\bar{\mathcal{U}}_R \mathbf{V}_{\mathcal{U}}'^\dagger) \mathbf{M}_{\mathcal{U}} (\mathbf{V}_{\mathcal{U}} \mathcal{U}_L) + \\ &\quad (\bar{\mathcal{D}}_L \mathbf{V}_{\mathcal{D}}^\dagger) \mathbf{M}_{\mathcal{D}} (\mathbf{V}_{\mathcal{D}}' \mathcal{D}_R) + (\bar{\mathcal{D}}_R \mathbf{V}_{\mathcal{D}}'^\dagger) \mathbf{M}_{\mathcal{D}} (\mathbf{V}_{\mathcal{D}} \mathcal{D}_L) + \\ &\quad (\bar{\mathcal{L}}_L \mathbf{V}_{\mathcal{L}}^\dagger) \mathbf{M}_{\mathcal{L}} (\mathbf{V}_{\mathcal{L}}' \mathcal{L}_R) + (\bar{\mathcal{L}}_R \mathbf{V}_{\mathcal{L}}'^\dagger) \mathbf{M}_{\mathcal{L}} (\mathbf{V}_{\mathcal{L}} \mathcal{L}_L) \} \\ &= -(1 + \frac{H}{v}) \left\{ \sum_{fermions} \bar{\mathcal{F}}^P \mathbf{M}_{\mathcal{F}} \mathcal{F}^P \right\} \end{aligned} \quad (\text{A.29})$$

It turns out that the fermion weak (gauge) eigenstates \mathcal{F} involved in the charged currents diagonal in generations (as in equation A.9) differ from physical (mass) eigenstates \mathcal{F}^P ($\mathcal{F}^P = \mathcal{F}_L^P + \mathcal{F}_R^P$), where:

$$\begin{aligned} \mathcal{F}_L^P &= \mathbf{V}_{\mathcal{F}} \mathcal{F}_L, \\ \mathcal{F}_R^P &= \mathbf{V}_{\mathcal{F}}' \mathcal{F}_R. \end{aligned} \quad (\text{A.30})$$

It is convenient to choose:

$$\mathcal{V}^P = \mathcal{V}_L^P = \mathbf{V}_{\mathcal{L}} \mathcal{V}_L = \mathbf{V}_{\mathcal{L}} \begin{pmatrix} \nu_e \\ \nu_\mu \\ \nu_\tau \end{pmatrix}_L$$

(this assignment is correct since neutrinos are massless). Thus physical fermion fields are now denoted as:

$$\mathcal{F}^P = \{\mathcal{U}^P, \mathcal{D}^P, \mathcal{L}^P, \mathcal{V}^P\} = \left\{ \begin{pmatrix} u^P \\ c^P \\ t^P \end{pmatrix}, \begin{pmatrix} d^P \\ s^P \\ b^P \end{pmatrix}, \begin{pmatrix} e^P \\ \mu^P \\ \tau^P \end{pmatrix}, \begin{pmatrix} \nu_e^P \\ \nu_\mu^P \\ \nu_\tau^P \end{pmatrix} \right\}. \quad (\text{A.31})$$

⁴Since right-handed neutrinos does not exist in the simple version of the Standard Model discussed here, there is no appropriate coupling, no mass matrix for neutrinos and finally neutrinos are massless.

A.3 The fermionic piece of electroweak Lagrangian in terms of physical fermion fields

As has been shown the fermion fields introduced initially are not the observed (physical) ones. Thus one should express the successors of (A.8) in terms of fields given by (A.31). Before doing that, it is useful to note that:

$$\bar{\mathcal{F}}^P \mathcal{F}^P = \bar{\mathcal{F}} \mathcal{F} \quad (\text{A.32})$$

Therefore the pieces that involve fields of the same flavour like in \mathcal{L}_{NC} should look as they were untouched. This is not true for the Charge Current part, which mixes f with f' . Starting from (A.9), in terms of \mathcal{F} , one gets:

$$\begin{aligned} -\mathcal{L}_{CC} &= \frac{g}{\sqrt{2}} \left\{ \bar{\mathcal{U}}_L \gamma^\mu W_\mu^+ \mathcal{D}_L + \bar{\mathcal{D}}_L \gamma^\mu W_\mu^- \mathcal{U}_L + \bar{\mathcal{V}}_L \gamma^\mu W_\mu^+ \mathcal{L}_L + \bar{\mathcal{L}}_L \gamma^\mu W_\mu^- \mathcal{V}_L \right\} \\ &\stackrel{phys. \ fields}{=} \frac{g}{\sqrt{2}} \left\{ (\bar{\mathcal{U}}_L^P \mathbf{V}_U) \gamma^\mu W_\mu^+ (\mathbf{V}_D^\dagger \mathcal{D}_L^P) + (\bar{\mathcal{D}}_L^P \mathbf{V}_D) \gamma^\mu W_\mu^- (\mathbf{V}_U^\dagger \mathcal{U}_L^P) + (\bar{\mathcal{V}}_L^P \mathbf{V}_L) \gamma^\mu W_\mu^+ (\mathbf{V}_L^\dagger \mathcal{L}_L^P) + (\bar{\mathcal{L}}_L^P \mathbf{V}_L) \gamma^\mu W_\mu^- (\mathbf{V}_L^\dagger \mathcal{V}_L^P) \right\} \\ &= \frac{g}{\sqrt{2}} \left\{ \bar{\mathcal{U}}_L^P \gamma^\mu W_\mu^+ \mathbf{V}_{CKM} \mathcal{D}_L^P + \bar{\mathcal{D}}_L^P \mathbf{V}_{CKM}^\dagger \gamma^\mu W_\mu^- \mathcal{U}_L^P + \bar{\mathcal{V}}_L^P \gamma^\mu W_\mu^+ \mathcal{L}_L^P + \bar{\mathcal{L}}_L^P \gamma^\mu W_\mu^- \mathcal{V}_L^P \right\} \end{aligned} \quad (\text{A.33})$$

The specific choice of the physical massless neutrino states allow us to keep the lepton sector unchanged (lower components of doublets couple with the upper ones). The situation differs for the quark sector. The coupling is mediated by the Cabibbo-Kobayashi-Maskawa matrix

$$\mathbf{V}_{CKM} = \mathbf{V}_U \mathbf{V}_D^\dagger, \quad (\text{A.34})$$

enabling mixing between the generations (i.e. \mathcal{L}_{CC} is no longer family conserving).

To summarise construction of the Standard Model Lagrangian, leading to the Cabibbo-Kobayashi-Maskawa matrix, let us write down all the pieces of

the Lagrangian which contain fermion fields. Dropping the index P one gets

$$\begin{aligned}
\mathcal{L}_F &= \sum \bar{\mathcal{F}} i \partial_\mu \gamma^\mu \mathcal{F} && \text{(kinetic term)} \\
&- \sum \bar{\mathcal{F}} (\mathbf{M}_F) \mathcal{F} && \text{(mass terms)} \\
&- \frac{g}{2M_W} H \sum \bar{\mathcal{F}} \mathbf{M}_F \mathcal{F} && \text{(fermion - Higgs couplings)} \\
&- e A_\mu \sum q_F \bar{\mathcal{F}} \gamma^\mu \mathcal{F} && \text{(electromagnetic current)} \\
&- \frac{g}{2 \cos \theta_W} Z_\mu \sum_F \gamma^\mu (g_V^F - g_A^F \gamma^5) \mathcal{F} && \text{(weak neutral current)} \\
&- \frac{g}{2\sqrt{2}} \left\{ \begin{aligned} &\bar{\mathcal{U}} \gamma^\mu (1 - \gamma^5) \mathbf{V}_{\mathbf{CKM}} \mathcal{D} W_\mu^+ \\ &+ \bar{\mathcal{D}} \mathbf{V}_{\mathbf{CKM}}^\dagger \gamma^\mu (1 - \gamma^5) \mathcal{U} W_\mu^- \\ &+ \bar{\mathcal{V}} \gamma^\mu (1 - \gamma^5) \mathcal{L} W_\mu^+ \\ &+ \bar{\mathcal{L}} \gamma^\mu (1 - \gamma^5) \mathcal{V} W_\mu^- \end{aligned} \right\} && \text{(weak charge current)}
\end{aligned} \tag{A.35}$$

A.4 The CP operation

The charge conjugation C, spatial reflection - parity P and time reversal T are special discrete symmetries. Their combination (CPT symmetry) is respected by quantum field theory and it is frequently emphasised that any theory violating invariance under the CPT product would neglect cherished properties of quantum field theory. For many years it was believed that Nature respects C, P and T symmetries separately (and it is a true for strong and electromagnetic interactions). The realization that C and P are not conserved in weak decays was a milestone in formulation of weak theories. A few years later it was shown that even the product of C and P (CP conjugation symmetry) is violated.

A.4.1 The parity operator P for fermion fields

The parity operation or spatial reflection consist in replacement of the spatial coordinates with the inverted ones: $\vec{r} \xrightarrow{P} -\vec{r}$ without changing the time dependence. The form of the parity operator P for fermions may be guessed from transformation of Dirac equation for a free particle:

$$(i\gamma^\mu \partial_\mu - m) \Psi(t, x) = 0 \tag{A.36}$$

The Dirac equation in the frame with inverted spatial coordinates (improper Lorentz transformation) reexpressed in coordinates of initial frame takes a form:

$$(i\gamma^0 \partial_0 - i\gamma^k \partial_k - m) \Psi'(t, -x) = 0 \tag{A.37}$$

One may show that since $\gamma^0 \gamma^k \gamma^0 = -\gamma^k$ the $\Psi'(t, -x) = \gamma^0 \Psi(t, x)$ satisfy it. Thus one may guess that under the parity operation Dirac spinors transforms:

$$\Psi(t, x) \xrightarrow{\mathcal{P}} \Psi^{\mathcal{P}}(t, x) = \underbrace{\gamma^0}_{\mathcal{P}} \Psi(t, -x) \quad (\text{A.38})$$

It should be stressed that the transformation is defined up to an arbitrary phase.

A.4.2 The charge conjugation operator C for fermion fields

The charge conjugation in relativistic quantum mechanic changes the particle to its antiparticle reversing its baryon or lepton number, charge and magnetic momentum. The form of charge conjugation operator C for fermions may be guessed from properties of Dirac equation for electron (charge -e) interacting with photon:

$$(i\gamma^\mu \partial_\mu + e\gamma^\mu A_\mu - m) \Psi(x) = 0 \quad (\text{A.39})$$

The positron satisfies similar equation but with opposite charge:

$$(i\gamma^\mu \partial_\mu - e\gamma^\mu A_\mu - m) \Psi^C(x) = 0 \quad (\text{A.40})$$

To transform equation (A.40) to (A.39) one should change the relative sing of $i\gamma^\mu \partial_\mu$ and $e\gamma^\mu A_\mu$. This may be done by taking the complex conjugate of equation (A.40). Using the relation $(\gamma^\mu)^* = \gamma^2 \gamma^\mu \gamma^2$ it turns out that $-i\gamma^2 (\Psi^C(x))^*$ satisfy the usual Dirac equation. With that one may guess (note that once again the correspondence is defined with arbitrary phase) that charge coupling acts on $\Psi(x)$ as follows:

$$\Psi(x) \xrightarrow{\mathcal{C}} \Psi^C(x) = \underbrace{i\gamma^2 \gamma^0}_{\mathcal{C}} \gamma^0 \Psi^*(x) \quad (\text{A.41})$$

A.4.3 The combined CP symmetry and its violation

To understand the attractive possibility to keep combined CP symmetry respected if C and P are separately broken it is useful to analyse a "pedagogical" picture [91] (see Fig. A.1) with left and right neutrinos.

Since neutrinos are massless solutions of Dirac equation, they are eigenvectors of helicity. The neutrinos have spin opposite to direction of momentum $J_z = -\frac{1}{2}$ or in other words they

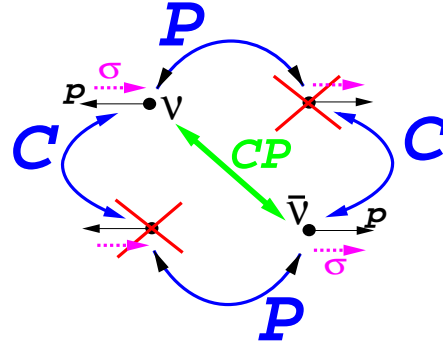


Figure A.1: C,P and CP transformation on neutrinos.

have negative helicity. It may be shown that this corresponds to the fact that they are left-handed. For their antiparticles - antineutrinos situation is opposite: the helicity is positive and they are right-handed. The parity operation P changes the sign of axes, thus the momentum is reversed while the spin is not. Hence the left-handed neutrino transformed under the parity operation with changed helicity and handedness appears as right-handed neutrino that is absent in the base version of the Standard Model (and seems to be absent in Nature). In other case C operator changes particle to its antiparticle, momentum and spin is untouched. Thus the charge conjugate of the left-handed neutrino is non-existent left-handed antineutrino. The situation changes with combined C and P together. CP changes both direction of momentum and particle to antiparticle thus right-handed antineutrino appears, that is perfectly allowed. The combined CP conservation might be respected by weak interactions. But it is not. As it will be shown the symmetry is violated in the quark sector for charge current transitions in electroweak Lagrangian.

The combined CP conjugate operation acts on fermion field as follows ((A.38) and (A.41); T -means transposed):

$$\Psi(t, x) \xrightarrow{CP} i\gamma^2\gamma^0\Psi^*(t, -x) \quad \bar{\Psi}(t, x) \xrightarrow{CP} -i\Psi^T(t, -x)\gamma^2 \quad (A.42)$$

The CP is conserved (or it is exact symmetry) if the action $\int d^4x \mathcal{L}$ is invariant under combined CP conjugation. To check that it is useful to calculate the CP operation on constituent components of the electroweak Lagrangian (A.35). Let us calculate CP transformation of scalar, vector and axialvector coupled with a vector field X_μ :

$$\begin{aligned} \bar{\Psi}_1\Psi_2 & \xrightarrow{CP} \left\{ \begin{aligned} & -i\Psi_1^T\gamma^2 i\gamma^2\gamma^0\Psi_2^* \\ & = -\Psi_1^T\bar{\Psi}_2^T = (\bar{\Psi}_2\Psi_1)^T \\ & = \bar{\Psi}_2\Psi_1 \end{aligned} \right\} \\ \bar{\Psi}_1\gamma^\mu X_\mu\Psi_2 & \xrightarrow{CP} \left\{ \begin{aligned} & -i\Psi_1^T\gamma^2 \gamma^\mu(X_\mu)^{CP} i\gamma^2\gamma^0\Psi_2^* \\ & = -\bar{\Psi}_2\gamma_\mu(X_\mu)^{CP}\Psi_1 \end{aligned} \right\} \\ \bar{\Psi}_1\gamma^\mu X_\mu\gamma^5\Psi_2 & \xrightarrow{CP} \left\{ \begin{aligned} & -i\Psi_1^T\gamma^2 \gamma^\mu(X_\mu)^{CP}\gamma^5 i\gamma^2\gamma^0\Psi_2^* \\ & = -\bar{\Psi}_2\gamma_\mu\gamma^5(X_\mu)^{CP}\Psi_1 \end{aligned} \right\} \end{aligned} \quad (A.43)$$

With that it turns out that mass term is invariant under the combined CP operation. One should note that the minus $-\Psi_1^T\bar{\Psi}_2^T = \bar{\Psi}_2\Psi_1$ disappear due to changing the order of two fermion fields. To check for the invariance of terms that involve the interaction with the (axial) vector field X_μ it is necessary to provide appropriate transformation criteria. One may find [90]:

$$\begin{aligned} \left. \begin{aligned} W_\mu^1 & \xrightarrow{CP} -W^{1\ \mu} \\ W_\mu^2 & \xrightarrow{CP} W^{2\ \mu} \end{aligned} \right\} W^\pm & \xrightarrow{CP} -W^\mp \\ \left. \begin{aligned} W_\mu^3 & \xrightarrow{CP} -W^{3\ \mu} \\ B_\mu & \xrightarrow{CP} -B^\mu \end{aligned} \right\} A_\mu, Z_\mu & \xrightarrow{CP} -A^\mu, -Z^\mu \end{aligned} \quad (A.44)$$

Assigning $X_\mu = A_\mu, Z_\mu$ electromagnetic neutral currents as well as weak neutral current pieces are invariant under CP transformation. Superimposing $H \xrightarrow{\mathcal{CP}} H$ it is also clear that the fermion-Higgs coupling term respect the symmetry. Situation differs for charge current terms, where one may obtain:

$$\begin{pmatrix} \bar{\mathcal{U}}_j \gamma^\mu W_\mu^+ (1 - \gamma^5) (\mathbf{V}_{\mathbf{CKM}})_{jk} \mathcal{D}_k \\ + \bar{\mathcal{D}}_j (\mathbf{V}_{\mathbf{CKM}}^\dagger)_{jk} \gamma^\mu W_\mu^- (1 - \gamma^5) \mathcal{U}_k \\ + \bar{\mathcal{V}}_j \gamma^\mu W_\mu^+ (1 - \gamma^5) \mathcal{L}_j \\ + \bar{\mathcal{L}}_j \gamma^\mu W_\mu^- (1 - \gamma^5) \mathcal{V}_j \end{pmatrix} \xrightarrow{\mathcal{CP}} \begin{pmatrix} \bar{\mathcal{D}}_j (\mathbf{V}_{\mathbf{CKM}})_{kj} \gamma_\mu (W^-)^\mu (1 - \gamma^5) \mathcal{U}_k \\ + \bar{\mathcal{U}}_j (\mathbf{V}_{\mathbf{CKM}}^\dagger)_{kj} \gamma_\mu (W^+)^\mu (1 - \gamma^5) \mathcal{D}_k \\ + \bar{\mathcal{L}}_j \gamma_\mu (W^-)^\mu (1 - \gamma^5) \mathcal{V}_j \\ + \bar{\mathcal{V}}_j \gamma_\mu (W^+)^\mu (1 - \gamma^5) \mathcal{L}_j \end{pmatrix} \quad (\text{A.45})$$

The above equation shows that leptonic sector is invariant under combined CP operation, while the quark one requires the following constraint for $\mathbf{V}_{\mathbf{CKM}}$: $(\mathbf{V}_{\mathbf{CKM}})_{jk} = (\mathbf{V}_{\mathbf{CKM}}^\dagger)_{kj}$. In other words, CP is conserved only if $\mathbf{V}_{\mathbf{CKM}}$ can be made real:

$$(\mathcal{CP} \text{ conserved}) \iff (\mathbf{V}_{\mathbf{CKM}}^* = \mathbf{V}_{\mathbf{CKM}}) \quad (\text{A.46})$$

$$(\mathcal{CP} \text{ violated}) \iff (\mathbf{V}_{\mathbf{CKM}}^* \neq \mathbf{V}_{\mathbf{CKM}}) \quad (\text{A.47})$$

Appendix B

The Cabibbo-Kobayashi-Maskawa matrix

B.1 CKM phases, invariants and parametrisations

Neglecting the strong CP violation problem the Cabibbo-Kobayashi-Maskawa matrix V_{CKM} is the only source of CP violation in the Standard Model. In the previous section it was shown that CP violation takes place if V_{CKM} is not real. Thus one may want to count the number of parameters in CKM matrix. The arbitrary $N \times N$ complex matrix depends on $2N^2$ real parameters (modulus or "angles" and "phases") The only theoretical constraint on CKM matrix is unitarity. The unitarity bounds sets N^2 constraints reducing the number of real parameters to N^2 i.e. $N(N-1)/2$ angles (number of independent rotations) and $N(N+1)/2$ arbitrary phases. Some of the phases may be however absorbed in the (re)definition of quark fields:

$$\mathcal{U} \rightarrow \begin{pmatrix} e^{i\alpha_u} & & \\ & e^{i\alpha_c} & \\ & & e^{i\alpha_t} \end{pmatrix} \mathcal{U} \quad \mathcal{D} \rightarrow \begin{pmatrix} e^{i\beta_d} & & \\ & e^{i\beta_s} & \\ & & e^{i\beta_b} \end{pmatrix} \mathcal{D} \quad (\text{B.1})$$

Under the above rephasing the CKM matrix elements changes as follows:

$$(V_{CKM})_{kl} \rightarrow e^{i(\alpha_k - \beta_l)} (V_{CKM})_{kl} \quad (\text{B.2})$$

Since from N u -type quarks and N d -type quarks one may compose $2N - 1$ independent combinations the number of independent phases in CKM matrix occurs to be:

$$n_{\text{phases}} = \frac{(N-1)(N-2)}{2} \quad (\text{B.3})$$

For the two family standard model $n_{\text{phases}} = 0$ and there is no room for the CP violation. This motivated Kobayashi and Maskawa to introduce a third quark

doublet. Indeed, for $N = 3$ one obtains three rotating angles and $n_{\text{phases}} = 1$. The single phase makes the model very predictable. In the three family case the CKM quark mixing matrix takes the explicit form (the u, c, t and d, s, b indexes corresponds to quarks coupled by the element):

$$V_{CKM} = \begin{pmatrix} V_{ud} & V_{us} & V_{ub} \\ V_{cd} & V_{cs} & V_{cb} \\ V_{td} & V_{ts} & V_{tb} \end{pmatrix} \quad (\text{B.4})$$

A large number of parametrisations may be composed [90]. In the standard one [92] (advocated by the Particle Data Group [29]):

$$V_{CKM} = \begin{pmatrix} c_{12}c_{13} & s_{12}c_{13} & s_{13}e^{-i\delta_{13}} \\ -s_{12}c_{23} - c_{12}s_{23}s_{13}e^{i\delta_{13}} & c_{12}c_{23} - s_{12}s_{23}s_{13}e^{i\delta_{13}} & s_{23}c_{13} \\ s_{12}s_{23} - c_{12}c_{23}s_{13}e^{i\delta_{13}} & -c_{12}s_{23} - s_{12}c_{23}s_{13}e^{i\delta_{13}} & c_{23}c_{13} \end{pmatrix} \quad (\text{B.5})$$

with $s_{ij} = \sin \theta_{ij}$, $c_{ij} = \cos \theta_{ij}$, where θ_{ij} are three angles while δ_{13} is a single phase. The above parametrisation, although strict does not well express the magnitudes of the CKM matrix elements. As one can observe the ranges of absolute values of CKM elements decrease going out of diagonal [29]:

$$|V_{CKM}| = \begin{pmatrix} 0.9745 \div 0.9757 & 0.219 \div 0.224 & 0.002 \div 0.005 \\ 0.218 \div 0.224 & 0.9736 \div 0.9750 & 0.036 \div 0.046 \\ 0.004 \div 0.014 & 0.034 \div 0.046 & 0.9989 \div 0.9993 \end{pmatrix} = \begin{pmatrix} \approx 1 & \sim \lambda & \sim \lambda^3 \\ \sim \lambda & \approx 1 & \sim \lambda^2 \\ \sim \lambda^3 & \sim \lambda^2 & \approx 1 \end{pmatrix} \quad (\text{B.6})$$

This feature was used by Wolfenstein when he proposed to write the expansion of V_{CKM} in terms of λ ($\sin \theta_{Cabibbo}$):

$$V_{CKM} = \begin{pmatrix} 1 - \frac{1}{2}\lambda^2 & \lambda & \lambda^3 A(\rho - i\eta) \\ -\lambda & 1 - \frac{1}{2}\lambda^2 & \lambda^2 A \\ \lambda^3 A(1 - \rho - i\eta) & -\lambda^2 A & 1 \end{pmatrix} + O(\lambda^4) \quad (\text{B.7})$$

In this parametrisation the CP violation arises from η in imaginary part of V_{ub} and V_{td} . The Wolfenstein parametrisation although not strict is extremely useful and its accuracy is sufficient in most cases¹.

Although plurality of different forms of CKM matrix due to rephasing exist one may calculate a set of rephasing invariants [94]-[96]. Of the special interests

¹More accurate, Wolfenstein-like parametrisation (the unitarity is kept up to λ^6) may be written as follows [93]:

$$V_{CKM} = \begin{pmatrix} 1 - \frac{1}{2}\lambda^2 - \frac{1}{8}\lambda^4 & \lambda & \lambda^3 A(\rho - i\eta) \\ -\lambda[1 + \frac{1}{2}A\lambda^4(2\rho - 1) + iA^2\lambda^4\eta] & 1 - \frac{1}{2}\lambda^2 - \frac{1}{8}(4A^2 + 1)\lambda^4 & \lambda^2 A \\ \lambda^3 A(1 - \rho - i\eta) & -A\lambda^2[1 + \frac{1}{2}\lambda^2(2\rho - 1) + i\lambda^2\eta] & 1 - \frac{1}{2}A^2\lambda^4 \end{pmatrix} \quad (\text{B.8})$$

are the nine quartet forms:

$$\Delta_{i\alpha} = (V_{CKM})_{j\beta} (V_{CKM})_{k\gamma} (V_{CKM})_{j\gamma}^* (V_{CKM})_{k\beta}^* \quad (\text{B.9})$$

$$i, j, k = u, c, t, \quad \alpha, \beta, \gamma = d, s, b \quad (\text{cyclic order})$$

The invariant $\Delta_{i\alpha}$ is obtained by crossing out the row i and the column α in the CKM matrix, taking the 2×2 submatrix with the complex conjugate of diagonal or skew diagonal. Then the elements of the submatrix should be multiplied all together. The $\Delta_{i\alpha}$ both the imaginary and the real part are invariant (i.e. numerical values holds) under the rephasing and reparametrisations. Moreover all the imaginary part of $\Delta_{i\alpha}$ are (up to a sign) the same [94].

$$\begin{aligned} J_{CP} = |\text{Im}\Delta_{i\alpha}| &= |\text{Im}(V_{ud}V_{cs}V_{us}^*V_{cd}^*)| = \cdots = |\text{Im}(V_{cs}V_{tb}V_{cb}^*V_{ts}^*)| \\ &= 2|c_{12}s_{12}c_{13}^2s_{13}c_{23}s_{23}\sin\delta_{13}| \\ &\approx A^2\lambda^6\eta \end{aligned} \quad (\text{B.10})$$

Since the Wolfenstein parametrisation is the approximate one, some care must be taken while calculating J_{CP} . One may use the $O(\lambda^6)$ parametrisation, however the correct result may be obtained from the simplified $O(\lambda^4)$ version taking for example $|\text{Im}(V_{cs}V_{tb}V_{cb}^*V_{ts}^*)|$.

All the observed phenomena involving CKM matrix elements may be described in terms on invariants. Particularly the CP violation involving observables appear to be a function of J_{CP} .

B.2 The unitary triangle

Since the unitarity is deeply rooted in the CKM matrix it is interesting to test it. The unitary condition $V^\dagger V = VV^\dagger = 1_{3 \times 3}$ requires the following twelve relations to be hold:

$$1 = |V_{ud}|^2 + |V_{cd}|^2 + |V_{td}|^2 \quad 1 = |V_{ud}|^2 + |V_{us}|^2 + |V_{ub}|^2 \quad (\text{B.11})$$

$$1 = |V_{us}|^2 + |V_{cs}|^2 + |V_{ts}|^2 \quad 1 = |V_{cd}|^2 + |V_{cs}|^2 + |V_{cb}|^2 \quad (\text{B.12})$$

$$1 = |V_{ub}|^2 + |V_{cb}|^2 + |V_{tb}|^2 \quad 1 = |V_{td}|^2 + |V_{ts}|^2 + |V_{tb}|^2 \quad (\text{B.13})$$

$$(\text{B.14})$$

$$0 = V_{ud}^*V_{us} + V_{cd}^*V_{cs} + V_{td}^*V_{ts} \quad (\text{B.15})$$

$$0 = V_{us}^*V_{ud} + V_{cs}^*V_{cd} + V_{ts}^*V_{td} \quad (\text{B.16})$$

$$0 = V_{us}^*V_{ub} + V_{cs}^*V_{cb} + V_{ts}^*V_{tb} \quad (\text{B.17})$$

$$0 = V_{ub}^*V_{us} + V_{cb}^*V_{cs} + V_{tb}^*V_{ts} \quad (\text{B.18})$$

$$0 = V_{ub}^*V_{ud} + V_{cb}^*V_{cd} + V_{tb}^*V_{td} \quad (\text{B.19})$$

$$0 = V_{ud}^*V_{ub} + V_{cd}^*V_{cb} + V_{td}^*V_{tb} \quad (\text{B.20})$$

The first three relations (B.11)-(B.13) express the fact that the sum of relative couplings must be one. The rest six (B.15)-(B.20) relations are grouped in pairs of complex coupled ones. Each of the equations (B.15)-(B.20) may be expressed as a triangle at the complex plane. However in (B.15)-(B.18) the imaginary part of the relations is small compared with the real ones and one of the elements of the sum is much smaller than other two. This makes the triangle "flat". This is not the case of equations (B.19)-(B.20) where all the three elements of the sum are of the same order. Thus, the graphical illustration of the relation (B.19) (although the choice of (B.20) is equally good) is called *unitarity triangle*². It should be mentioned that all the unitarity triangles (including the "flat" ones) have the same area equal to $\frac{1}{2}J_{CP}$ [98].

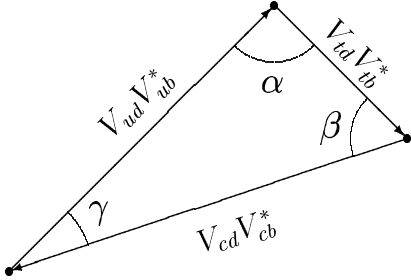


Figure B.1: The unitarity triangle.

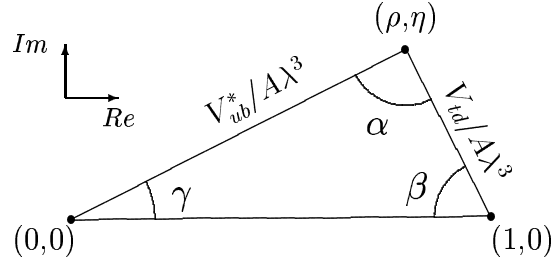


Figure B.2: The rescaled unitarity triangle in Wolfenstein parametrisation.

In the Figure B.1 the unitarity triangle is shown in arbitrary parametrisation. Any rephasing of quark fields may change the orientation of the triangle but not its shape nor area. Thus the values of its inner angles are meaningful. From that Figure B.1 one may express them in the the following general (invariant) form:

$$\alpha = \arg\left(-\frac{V_{td}V_{tb}^*}{V_{ud}V_{ub}^*}\right) = -\arg(-\Delta_{cs}) \quad (\text{B.21})$$

$$\beta = \arg\left(-\frac{V_{cd}V_{cb}^*}{V_{td}V_{tb}^*}\right) = -\arg(-\Delta_{us}) \quad (\text{B.22})$$

$$\gamma = \arg\left(-\frac{V_{ud}V_{ub}^*}{V_{cd}V_{cb}^*}\right) = -\arg(-\Delta_{ts}) \quad (\text{B.23})$$

Using explicit form for the quantities that are manifestly real in Wolfenstein $O(\lambda^4)$ parametrisation one may rewrite equation (B.19) in a form corresponding to "rescaled" unitarity triangle (Figure B.2), with a base real and equal to one:

$$\frac{V_{ub}^*}{A\lambda^3} + \frac{V_{td}}{A\lambda^3} = 1 \quad (\text{B.24})$$

²Idea introduced by J.D. Bjorken in 1987

Using the Wolfenstein parametrisation one may express the angles of unitarity triangle with CKM elements:

$$\sin \alpha = \frac{\eta}{\sqrt{(1-\rho)^2 + \eta^2} \sqrt{\rho^2 + \eta^2}} \quad (\text{B.25})$$

$$\cos \alpha = \frac{\rho(\rho-1) + \eta^2}{\sqrt{(1-\rho)^2 + \eta^2} \sqrt{\rho^2 + \eta^2}} \quad (\text{B.26})$$

$$\sin \beta = \frac{\eta}{\sqrt{(1-\rho)^2 + \eta^2}} \quad (\text{B.27})$$

$$\cos \beta = \frac{1-\rho}{\sqrt{(1-\rho)^2 + \eta^2}} \quad (\text{B.28})$$

$$\sin \gamma = \frac{\eta}{\sqrt{\rho^2 + \eta^2}} \quad (\text{B.29})$$

$$\cos \gamma = \frac{\rho}{\sqrt{\rho^2 + \eta^2}} \quad (\text{B.30})$$

With a help of the above formula, or using directly (B.22)-(B.23) the V_{td} and V_{ub} in the Wolfenstein parametrisation are related to β and γ respectively. Thus Wolfenstein parametrisation may be written in the following form:

$$V_{CKM} = \begin{pmatrix} 1 - \frac{1}{2}\lambda^2 & \lambda & |V_{ub}| \cdot e^{-i\gamma} \\ -\lambda & 1 - \frac{1}{2}\lambda^2 & \lambda^2 A \\ |V_{td}| \cdot e^{-i\beta} & -\lambda^2 A & 1 \end{pmatrix} \quad (\text{B.31})$$

B.2.1 Experimental bounds to unitarity triangle

Although the direct measurement of angles of the unitarity triangle do not exists yet, several experimental bounds may be set for the allocation of (ρ, η) vertex of the triangle, namely [99]-[101] (see Figure B.3):

- the $|\epsilon_K| = (2.280 \pm 0.013) \times 10^{-3}$ [29] parameter describing the mixing induced CP violation in neutral kaon system fixes the "hyperbola corridor", since $|\epsilon_K|$ is related to ρ and η with the formula $|\epsilon_K| = A\eta(B + C(1 - \rho))$, where A, B, C are known parameters (although some of their components are hardly calculable),
- the measurement of $|V_{ub}/V_{cb}|$ ratio defines the position of the (ρ, η) vertex between two circles around $(0,0)$. The measured value $|V_{ub}/V_{cb}| = 0.080 \pm 20\%$ [102]-[103] is based on the analysis of leptonic spectra above $b \rightarrow cl\nu_l$ kinematical endpoint. The recent measurement of exclusive $B_d \rightarrow (\pi, \rho)l\nu_l$ decays gives some discrimination between various models used in the analysis.
- the mass difference between heavy and light B_d mass eigenstates $\Delta M_d = E[(1 - \rho)^2 + \eta^2]$ (where E is calculable constant) designate the distance of (ρ, η) vertex from point $(1,0)$. The value $\Delta M_d = 0.464 \pm 0.018 \text{ ps}^{-1}$ [76] combines the results on mixing parameter χ_d with the lifetime τ_{B_d} .

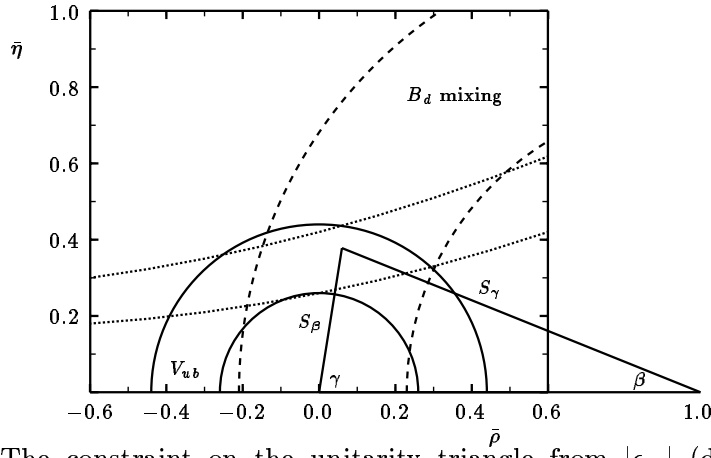


Figure B.3: The constraint on the unitarity triangle from $|\epsilon_K|$ (dotted curve) $|V_{ub}/V_{cb}|$ (solid circles) and B_d mixing (dashed circles). Figure taken from [104].

With the above experimental inputs, taking into account both experimental errors and theoretical uncertainties the preferred position of the vertex is [101]:

$$(\rho, \eta) = (0.05, 0.36) \quad (\text{B.32})$$

while the allowed region corresponding to 95% confidence level is shown in Figure B.4. Apart of measured values, additional constraint (Fig. B.5) may be set to unitarity triangle using the lower limit of $\Delta M_s > 9.2 \text{ ps}^{-1}$ [76]. Although $\Delta M_s \propto |V_{ts}^* V_{tb}|^2$ is not related to unitarity triangle, calculating the $\Delta M_s/\Delta M_d$ ratio one gains in cancellation of some uncertain variables. With that observation, the following ranges for angles of unitarity triangle may be set [101]:

$$-0.90 \leq \sin 2\alpha \leq 1.0, \quad (\text{B.33})$$

$$0.40 \leq \sin 2\beta \leq 0.94, \quad (\text{B.34})$$

$$0.34 \leq \sin^2 \gamma \leq 1.0 \quad (\text{B.35})$$

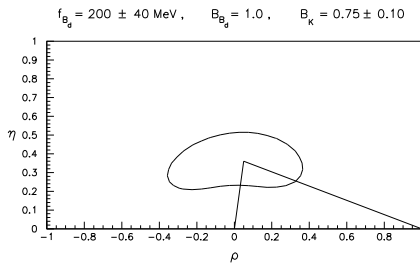


Figure B.4: The shape of the unitarity triangle preferred by experimental data. The solid curve mark the 95% C.L. allowed position of the (ρ, η) vertex. Figure taken from [100].

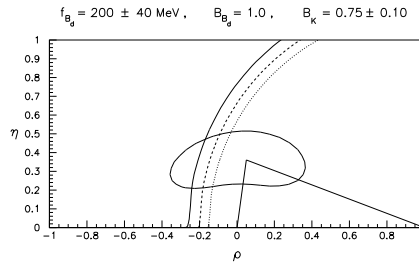


Figure B.5: Additional constraints to unitarity triangle arising from the x_s bound. The solid, dashed and dotted curves respects the freedom within the choice of hadronic matrix elements. Figure taken from [100].

Appendix C

CP violation in beauty meson decays

There¹ are three different ways to generate observable CP violation effects in beauty meson decays. All of them are caused by the interference between two or more various amplitudes contributing to the same process. One can distinguish [107]:

- Direct CP violation.
Occurs when CP violation comes from the interference of at least two diagrams with different weak and strong phases.
- Indirect CP violation.
Occurs when CP violation comes from unequal mixing rates between B^0 and \bar{B}^0 .
- CP violation due interplay between mixing and decay.
Occurs when CP violation comes from the interference of mixed and unmixed decay paths of initially produced neutral B meson.

The first mechanism may rise irrespectively of the charge of the B meson, whereas the last two involve mixing, and thus may happen only in neutral B meson systems.

C.1 Direct CP violation

The CPT symmetry implies that the total widths Γ of the particle B (not necessary being a B meson) and its antiparticle \bar{B} are equal. Let us define f_i – final state to which particle B may decay, and \bar{B}, \bar{f}_i – their CP-conjugate states. The CPT theorem requires [111, 112]:

$$\sum_{all\ i} \Gamma(B \rightarrow f_i) = \sum_{all\ i} \Gamma(\bar{B} \rightarrow \bar{f}_i) \quad (C.1)$$

¹My understanding of the CP violation in beauty sector is based on a large set of articles and reviews. The most useful for me were [105]-[110].

The requirements for the partial decay widths are much weaker. The possible inequality of partial widths arises from the CP violation. In the case of two diagrams contributing to the same transition B into f_i the amplitude can be written as:

$$\mathcal{A} = \mathcal{A}(B \rightarrow f_i) = g_1 M_1 e^{i\alpha_1} + g_2 M_2 e^{i\alpha_2}, \quad (\text{C.2})$$

where: g_i 's are relevant phases of weak couplings, α_i – strong interaction phases and M_i – real numbers. For the antiparticles the weak phases changes to the complex conjugate but strong phases remain unchanged. Thus:

$$\bar{\mathcal{A}} = \mathcal{A}(\bar{B} \rightarrow \bar{f}_i) = g_1^* M_1 e^{i\alpha_1} + g_2^* M_2 e^{i\alpha_2}, \quad (\text{C.3})$$

and the difference of partial decay widths is:

$$\Delta\Gamma = \Gamma(B \rightarrow f_i) - \Gamma(\bar{B} \rightarrow \bar{f}_i) \propto \text{Im}(g_1^* g_2) \sin(\alpha_1 - \alpha_2). \quad (\text{C.4})$$

The absence of CP violation implies equality of the g_1 and g_2 phases, and vanishing difference of partial decay widths. Hence, the CP violation arises from interference of at least two amplitudes with different weak and strong phases. There are several ways to fulfil these conditions [113]-[116]. As an example one may show interference between the spectator diagram and the single-loop (penguin) diagram (Fig. C.1). Theoretical problems due to treatment of strong phases makes the extraction of CKM phases difficult, although in some cases possible [117].

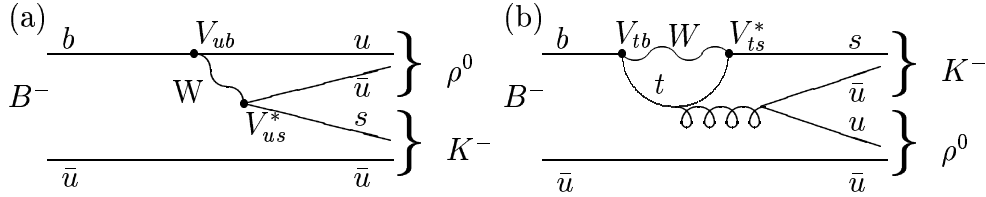
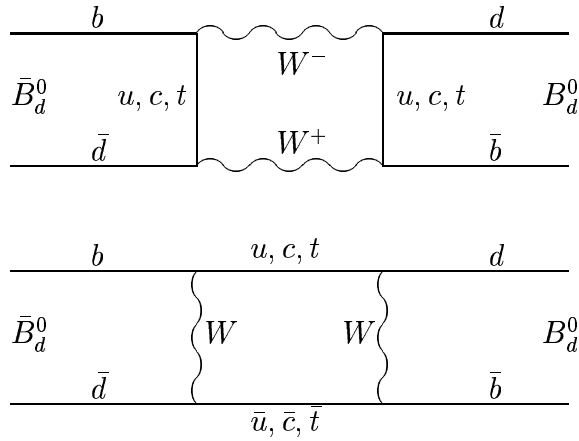


Figure C.1: (a) inner spectator diagram contributing to $B^- \rightarrow \rho^0 K^-$
 (b) example of penguin diagram contributing to $B^- \rightarrow \rho^0 K^-$

C.2 CP violation arising from mixing in neutral B meson system

The mixing of neutral B mesons ($B_d^{(+)}, B_s^{(+)}$) is known since 1987 [118, 119]. It can be described by χ_d, χ_s parameters – time integrated probabilities that a produced B^0 (or \bar{B}^0) decays as a \bar{B}^0 (B^0), e.g. for an inclusive semileptonic


 Figure C.2: $B_d^0 - \bar{B}_d^0$ mixing diagrams.

decays:

$$\begin{aligned}\chi_d &= \frac{\Gamma(B_d^0 \rightarrow l^- X \text{ (via } \bar{B}_d^0))}{\Gamma(B_d^0 \rightarrow l^\pm Y)} = \frac{x_d^2}{2 + 2x_d^2} \\ \chi_s &= \frac{\Gamma(B_s^0 \rightarrow l^- X \text{ (via } \bar{B}_s^0))}{\Gamma(B_s^0 \rightarrow l^\pm Y)} = \frac{x_s^2}{2 + 2x_s^2}\end{aligned}\quad (\text{C.5})$$

where x_d, x_s are mixing parameters for B_d, B_s mesons respectively. The measured values are^{2,3} [29]:

$$\begin{aligned}\chi_d &= 0.156 \pm 0.024 & \chi_s &> 0.49 \text{ (95\% C.L.)} \\ x_d &= 0.73 \pm 0.05 & x_s &> 9.5 \text{ (95\% C.L.)}\end{aligned}\quad (\text{C.6})$$

Since at high energies it is difficult to separate B_d and B_s the experiments [124]-[129] measure [29] an average mixing:

$$\chi_B = f_{B_d} \chi_d + f_{B_s} \chi_s = 0.126 \pm 0.008 \quad (\text{C.7})$$

The recommended [130] values for the production fractions $f_{B_d}, f_{B_s}, f_{B^\pm}, f_{\Lambda_b}$ at high energies are:

$$\begin{aligned}f_{B_d} &= (37.8 \pm 2.2)\% \\ f_{B^\pm} &= (37.8 \pm 2.2)\% \\ f_{B_s} &= (11.3 \pm_{1.9}^{1.8})\% \\ f_{\Lambda_b} &= (13.2 \pm 4.1)\%\end{aligned}\quad (\text{C.8})$$

The $B - \bar{B}$ mixing in the Standard Model arises from $\Delta B = 2$ box diagrams [131] (Fig. C.2), similarly to that in $K - \bar{K}$ system.

²Experiments [120]-[122] measure $r_d = \chi_d/(1 - \chi_d)$. The quoted values are converted from r to χ .

³The χ_s values is derived from Δm_{B_s} [123]; It cannot exceed 0.50.

Let us denote:

$$|\Psi(t)\rangle = a(t)|B^0\rangle + b(t)|\bar{B}^0\rangle$$

The quantum mechanic evolution of the $|\Psi(t)\rangle$ is governed by a Schrödinger equation $i\frac{d}{dt}|\Psi\rangle = \mathcal{H}|\Psi\rangle$, that in the B rest frame can be written as:

$$i\frac{d}{dt}\begin{pmatrix} a \\ b \end{pmatrix} = H\begin{pmatrix} a \\ b \end{pmatrix} \equiv \left(M - \frac{i}{2}\Gamma\right)\begin{pmatrix} a \\ b \end{pmatrix}, \quad (\text{C.9})$$

where M and Γ are two by two Hermitian matrices⁴ ($M = M^+$, $\Gamma = \Gamma^+$), with its diagonal elements equal ($M_{11} = M_{22}$, $\Gamma_{11} = \Gamma_{22}$) due to CPT conservation. One can introduce B_L and B_H eigenstates of the mass matrix (after a calculation of mass difference in (C.19) one may identify L -lighter, H -heavier) such as:

$$\begin{aligned} |B_L\rangle &= p \cdot |B^0\rangle + q \cdot |\bar{B}^0\rangle, \\ |B_H\rangle &= p \cdot |B^0\rangle - q \cdot |\bar{B}^0\rangle, \end{aligned} \quad (\text{C.10})$$

with p, q – complex numbers. Diagonalization of the mass matrix leads to the following relation on the q/p ratio⁵ [132]

$$\frac{q}{p} = \sqrt{\frac{M_{12}^* - \frac{i}{2}\Gamma_{12}^*}{M_{12} - \frac{i}{2}\Gamma_{12}}} \quad (\text{C.11})$$

and the time evolution of $B^0 - \bar{B}^0$ system is:

$$\begin{aligned} |\Psi(t)\rangle &= c(t)|B_L\rangle + d(t)|B_H\rangle \\ &= e^{-i\mu_L t}c(0)|B_L\rangle + e^{-i\mu_H t}d(0)|B_H\rangle \\ &= (e^{-i\mu_L t}c(0) + e^{-i\mu_H t}d(0))p|B^0\rangle + (e^{-i\mu_L t}c(0) - e^{-i\mu_H t}d(0))q|\bar{B}^0\rangle \end{aligned} \quad (\text{C.12})$$

with $\mu_{L,H} = m_{L,H} - \frac{i}{2}\gamma_{L,H}$ – eigenvalues of mass matrix:

$$\mu_{L,H} = (M_{11} - \frac{i}{2}\Gamma_{11}) \pm (M_{12} - \frac{i}{2}\Gamma_{12}) \cdot \frac{q}{p} \quad (\text{C.13})$$

The Standard Model calculations of box diagrams lead to (let us decide to use the convention $\mathcal{CP}|B_d^0\rangle = |\bar{B}_d^0\rangle$) [110],[133]-[136]:

$$M_{12} = -\frac{G_F^2 B_B f_B^2 m_B \eta_B}{12\pi^2} \cdot M_W^2 \cdot \xi_t^2 \cdot S\left(\frac{m_t^2}{m_W^2}\right) \quad (\text{C.14})$$

$$\Gamma_{12} \approx \frac{G_F^2 B_B f_B^2 m_B}{8\pi} \cdot m_b^2 \cdot \xi_t^2, \quad (\text{C.15})$$

with G_F – Fermi constant, B_B – "bag" parameter occurring while calculating box diagrams, f_B – B meson decay constant, m_B – mass of B meson, m_W –

⁴Hamiltonian operator (called mass matrix) is not Hermitian itself because of decays.

⁵The sign of q/p ratio is chosen to obtain mass difference of correct sign $m_H - m_L > 0$; a care of keeping arbitrary sing is taken in [110].

W^\pm mass, $m_t, m_b - t, b$ quark mass, $S(\cdot)$ – slowly varying function of order 1 and:

$$\xi_t = V_{tb}V_{t\alpha}^*, \quad (\text{C.16})$$

where $\alpha = d, s$ for B_d, B_s mesons respectively. Since $\frac{|\Gamma_{12}|}{|M_{12}|} \simeq \frac{m_b^2}{m_W^2} \ll 1$ expression (C.13) implies:

$$\frac{q}{p} \approx \sqrt{\frac{M_{12}^*}{M_{12}}} \approx \frac{\xi_t^*}{\xi_t} = \frac{V_{tb}^*V_{t\alpha}}{V_{tb}V_{t\alpha}^*} = e^{-2i\phi_M} \quad (\text{C.17})$$

The ϕ_M is a phase, its index M emphasised that the mixing is necessary to its occurrence. Calculating the difference of eigenvalues of mass matrix one obtains:

$$\begin{aligned} \Delta m = m_H - m_L &\approx 2|M_{12}| > 0 \\ \Delta\gamma = \gamma_H - \gamma_L &\approx -2|\Gamma_{12}| \end{aligned} \quad (\text{C.18})$$

Hence $|\Delta\gamma| \ll |\Delta m|$. This is at variance with the analogous result in the $K^0 - \bar{K}^0$ system, where $\Delta m/\Delta\gamma \approx -0.5$. A consequence of above is the similarity of lifetimes [110]:

$$\frac{\Delta\gamma}{\gamma} = \frac{\Delta\gamma}{\Delta m} \cdot \frac{\Delta m}{\gamma} = \frac{\Delta\gamma}{\Delta m} \cdot x = \begin{cases} O(10^{-2}) & \text{for } B_d^0 - \bar{B}_d^0 \text{ system} \\ \leq O(20\%) & \text{for } B_s^0 - \bar{B}_s^0 \text{ system} \end{cases} \quad (\text{C.19})$$

where $\gamma = (\gamma_L + \gamma_H)/2 \approx \gamma_L \approx \gamma_H$, $x = x_d, x_s$ defined above is the mixing parameter introduced in (C.5). Again, the above result is different from the values in $K_S - K_L$ system where $\gamma_S \gg \gamma_L$.

A special case of (C.12) is the evolution of initially pure state of defined flavour. It is described by the formulae

$$\begin{aligned} |B_{prod}^0(t)\rangle &= f_+(t)|B^0\rangle + \frac{q}{p}f_-(t)|\bar{B}^0\rangle \\ |\bar{B}_{prod}^0(t)\rangle &= \frac{p}{q}f_-(t)|B^0\rangle + f_+(t)|\bar{B}^0\rangle, \end{aligned} \quad (\text{C.20})$$

where $|B_{prod}^0(t)\rangle$ stands for $|\Psi(t)\rangle$ such that $|\Psi(0)\rangle = |B^0\rangle$, similarly for $|\bar{B}_{prod}^0(t)\rangle$. With a help of derived properties for one can find f_+, f_-

$$\begin{aligned} f_+ &= e^{-i\frac{\mu_L + \mu_H}{2}t} \cos \frac{\Delta\mu t}{2} = e^{-imt} e^{-\frac{\gamma}{2}t} \cos \frac{\Delta m t}{2} \\ f_- &= e^{-i\frac{\mu_L + \mu_H}{2}t} i \sin \frac{\Delta\mu t}{2} = e^{-imt} e^{-\frac{\gamma}{2}t} i \sin \frac{\Delta m t}{2}, \end{aligned} \quad (\text{C.21})$$

From equation (C.20) one can see that $|f_+(t)|^2$ is a probability that an initially produced B^0 (\bar{B}^0) decays as a B^0 (\bar{B}^0). In addition, in case of equal contamination ($|q/p| = 1$) of B^0 and \bar{B}^0 in B_L, B_H states, the $|f_-(t)|^2$ function gives a probability that an initial B^0 (\bar{B}^0) decays as a \bar{B}^0 (B^0).

$$\begin{aligned} |\langle B^0 | \mathcal{H}_{\text{eff}} | B_{prod}^0(t) \rangle|^2 &= |f_+(t)|^2 \\ |\langle \bar{B}^0 | \mathcal{H}_{\text{eff}} | B_{prod}^0(t) \rangle|^2 &= |f_-(t)|^2 \end{aligned} \quad (\text{C.22})$$

and (see equation (C.5)):

$$\begin{aligned}
\chi &= \frac{N(B_{prod}^0 \rightarrow \bar{B}^0)}{N(B_{prod}^0 \rightarrow B^0) + N(B_{prod}^0 \rightarrow \bar{B}^0)} = \frac{N(\bar{B}_{prod}^0 \rightarrow B^0)}{N(\bar{B}_{prod}^0 \rightarrow \bar{B}^0) + N(\bar{B}_{prod}^0 \rightarrow B^0)} \\
&= \frac{\int_0^\infty dt |f_-(t)|^2}{\int_0^\infty dt (|f_+(t)|^2 + |f_-(t)|^2)} \\
&= \frac{x^2}{2 + 2x^2}
\end{aligned} \tag{C.23}$$

A comment should be made on the q/p . Its phase is not CKM matrix invariant – thus physically meaningless. The rephasing of $|B^0\rangle, |\bar{B}^0\rangle$ would lead to changes of the phase of q/p (see for example [106, 110, 137]). Nevertheless with fixed convention $\mathcal{CP}|B^0\rangle = +|\bar{B}^0\rangle$ if CP is conserved one obtains $q/p = 1$. In that case one may assign CP eigenvalues to B_L, B_H

$$\mathcal{CP}|B_L\rangle = +|B_L\rangle \text{ and } \mathcal{CP}|B_H\rangle = -|B_H\rangle. \tag{C.24}$$

Although q/p is convention dependent its module $|q/p|$ is not. Another meaningful quantity may be obtained convoluting q/p with decay amplitudes (see C.2.2).

C.2.1 Indirect CP violation

Consider [107] B^0 (\bar{B}^0) decay to the state that specifies its flavour. An example could be the following inclusive decay (X denotes anything):

$$B^0 \rightarrow l^+ \nu_l X \quad (\bar{B}^0 \rightarrow l^- \bar{\nu}_l X). \tag{C.25}$$

Here the charge of the lepton tags the quark contents of the beauty meson (because B^0 (\bar{B}^0) does not decay to $l^- \bar{\nu}_l X$ ($l^+ \nu_l X$)). The $B - \bar{B}$ mixing offers the possibility that produced B^0 (\bar{B}^0) will decay as \bar{B}^0 (B^0). Thus the decay amplitude of initially produced B^0 (\bar{B}^0) to specified lepton state is:

$$\begin{aligned}
\langle l^+ \nu_l X | \mathcal{H}_{\text{eff}} | B_{prod}^0(t) \rangle &\propto f_+(t), \\
\langle l^+ \nu_l X | \mathcal{H}_{\text{eff}} | \bar{B}_{prod}^0(t) \rangle &\propto \frac{p}{q} f_-(t), \\
\langle l^- \bar{\nu}_l X | \mathcal{H}_{\text{eff}} | B_{prod}^0(t) \rangle &\propto \frac{q}{p} f_-(t), \\
\langle l^- \bar{\nu}_l X | \mathcal{H}_{\text{eff}} | \bar{B}_{prod}^0(t) \rangle &\propto f_+(t).
\end{aligned} \tag{C.26}$$

One can try to determine experimentally the following ratio:

$$\begin{aligned}
a_{SL} &= \frac{\int_0^\infty dt \Gamma(\bar{B}_{prod}^0(t) \rightarrow l^+ \nu_l X) - \int_0^\infty dt \Gamma(B_{prod}^0(t) \rightarrow l^- \bar{\nu}_l X)}{\int_0^\infty dt \Gamma(\bar{B}_{prod}^0(t) \rightarrow l^+ \nu_l X) + \int_0^\infty dt \Gamma(B_{prod}^0(t) \rightarrow l^- \bar{\nu}_l X)} \\
&= \frac{N(\bar{B}_{prod}^0 \rightarrow l^+ \nu_l X) - N(B_{prod}^0 \rightarrow l^- \bar{\nu}_l X)}{N(\bar{B}_{prod}^0 \rightarrow l^+ \nu_l X) + N(B_{prod}^0 \rightarrow l^- \bar{\nu}_l X)} \\
&= \frac{|\frac{p}{q}|^2 - |\frac{q}{p}|^2}{|\frac{p}{q}|^2 + |\frac{q}{p}|^2},
\end{aligned} \tag{C.27}$$

with $\frac{q}{p}$ given by (C.11). As already mentioned $|\frac{q}{p}|$ is convention independent and physically meaningful. Since B^0 (\bar{B}^0) mesons are always accompanied by a b (\bar{b}) quark (as the $b\bar{b}$ pairs are produced by strong interactions), one can use the semileptonic decay of associated beauty quark: b (\bar{b}) $\rightarrow l^- \bar{\nu}_l$ ($l^+ \nu_l$) + anything as a tag for the presence of B^0 (\bar{B}^0). Therefore, a double lepton signature may be used to determinate a_{SL} (C.27):

$$a_{SL} = \frac{N(l^+l^+) - N(l^-l^-)}{N(l^+l^+) + N(l^-l^-)} \quad (\text{C.28})$$

The non-vanishing asymmetry (C.27) mark CP violation in B^0 decays. It manifests itself as an unequal contamination of B^0 and \bar{B}^0 in eigenstates B_L, B_H of the weak Hamiltonian. This kind of CP violation is called *indirect* because one cannot observe this effect in absence of mixing.

Unfortunately in B meson system a_{SL} is very small and vanishes within approximations made in C.2. More detailed calculations shows that the Standard Model predicts $a_{SL} \sim 10^{-4}$ [107] which is far below the experimental precision $a_{SL} < 0.18$ [138].

C.2.2 CP violation arising from the interplay between mixing and decay

CP violation due to mixing allows us to measure asymmetries similar to that in equation (C.27). The asymmetries described in this section do not vanish even if $|\frac{q}{p}| = 1$, and they arise from the interference between two decay paths to a given final state f . CP violation due to mixing is more precisely called [109] CP violation due to interference between the mixed and unmixed decay paths:

$$B^0 \rightarrow f \quad \text{and} \quad B^0 \rightarrow \bar{B}^0 \rightarrow f$$

Similarly to the indirect CP violation, the mixing is required. Moreover it is necessary that both B^0 and \bar{B}^0 decay to the same final state f (note the difference with indirect CP violation).

Let us consider the state f to which both pure B^0 and \bar{B}^0 may decay. Let us define:

$$|\bar{f}\rangle = \mathcal{CP} |f\rangle \quad (\text{C.29})$$

The decay amplitudes of initially produced B^0, \bar{B}^0 to the state f, \bar{f} is:

$$\begin{aligned} \langle f | \mathcal{H}_{\text{eff}} | B_{\text{prod}}^0(t) \rangle &= f_+(t) \langle f | \mathcal{H}_{\text{eff}} | B^0 \rangle + \frac{q}{p} f_-(t) \langle f | \mathcal{H}_{\text{eff}} | \bar{B}^0 \rangle, \\ \langle \bar{f} | \mathcal{H}_{\text{eff}} | B_{\text{prod}}^0(t) \rangle &= f_+(t) \langle \bar{f} | \mathcal{H}_{\text{eff}} | B^0 \rangle + \frac{q}{p} f_-(t) \langle \bar{f} | \mathcal{H}_{\text{eff}} | \bar{B}^0 \rangle, \\ \langle f | \mathcal{H}_{\text{eff}} | \bar{B}_{\text{prod}}^0(t) \rangle &= \frac{p}{q} f_-(t) \langle f | \mathcal{H}_{\text{eff}} | B^0 \rangle + f_+(t) \langle f | \mathcal{H}_{\text{eff}} | \bar{B}^0 \rangle, \\ \langle \bar{f} | \mathcal{H}_{\text{eff}} | \bar{B}_{\text{prod}}^0(t) \rangle &= \frac{p}{q} f_-(t) \langle \bar{f} | \mathcal{H}_{\text{eff}} | B^0 \rangle + f_+(t) \langle \bar{f} | \mathcal{H}_{\text{eff}} | \bar{B}^0 \rangle \end{aligned} \quad (\text{C.30})$$

Denoting

$$\begin{aligned}\mathcal{A}_f &= \mathcal{A}(B^0 \rightarrow f) = \langle f | \mathcal{H}_{\text{eff}} | B^0 \rangle, & \mathcal{A}_{\bar{f}} &= \mathcal{A}(B^0 \rightarrow \bar{f}) = \langle \bar{f} | \mathcal{H}_{\text{eff}} | B^0 \rangle, \\ \bar{\mathcal{A}}_f &= \mathcal{A}(\bar{B}^0 \rightarrow f) = \langle f | \mathcal{H}_{\text{eff}} | \bar{B}^0 \rangle, & \bar{\mathcal{A}}_{\bar{f}} &= \mathcal{A}(\bar{B}^0 \rightarrow \bar{f}) = \langle \bar{f} | \mathcal{H}_{\text{eff}} | \bar{B}^0 \rangle\end{aligned}\quad (\text{C.31})$$

and

$$r = \frac{q}{p} \cdot \frac{\bar{\mathcal{A}}_f}{\mathcal{A}_f} \quad \bar{r} = \frac{p}{q} \cdot \frac{\mathcal{A}_{\bar{f}}}{\bar{\mathcal{A}}_{\bar{f}}}, \quad (\text{C.32})$$

the time-dependent rates transition probabilities (under conditions of equation (C.20)) for B^0 (\bar{B}^0) to decay into f (\bar{f}) are:

$$\Gamma(B_{\text{prod}}^0(t) \rightarrow f) = |\mathcal{A}_f|^2 e^{-\gamma t} \left[\cos^2 \frac{\Delta m t}{2} + |r|^2 \sin^2 \frac{\Delta m t}{2} - \text{Im} r \sin \Delta m t \right], \quad (\text{C.33})$$

$$\Gamma(\bar{B}_{\text{prod}}^0(t) \rightarrow \bar{f}) = |\bar{\mathcal{A}}_{\bar{f}}|^2 e^{-\gamma t} \left[\cos^2 \frac{\Delta m t}{2} + |\bar{r}|^2 \sin^2 \frac{\Delta m t}{2} - \text{Im} \bar{r} \sin \Delta m t \right], \quad (\text{C.34})$$

$$\Gamma(B_{\text{prod}}^0(t) \rightarrow \bar{f}) = |\mathcal{A}_{\bar{f}}|^2 e^{-\gamma t} \left[\cos^2 \frac{\Delta m t}{2} + \left| \frac{1}{\bar{r}} \right|^2 \sin^2 \frac{\Delta m t}{2} - \text{Im} \frac{1}{\bar{r}} \sin \Delta m t \right], \quad (\text{C.35})$$

$$\Gamma(\bar{B}_{\text{prod}}^0(t) \rightarrow f) = |\bar{\mathcal{A}}_f|^2 e^{-\gamma t} \left[\cos^2 \frac{\Delta m t}{2} + \left| \frac{1}{r} \right|^2 \sin^2 \frac{\Delta m t}{2} - \text{Im} \frac{1}{r} \sin \Delta m t \right], \quad (\text{C.36})$$

In the bulk of possible $\overset{(-)}{B}^0$ decay products one can separate a class of CP eigenstates. Such decays are often called *gold plated* channels because for f being a CP eigenstate (f_{CP}), relations (C.33)–(C.36) simplify significantly.

Consider CP eigenstate f_{CP} such that both B^0 and \bar{B}^0 may decay to it. Let the CP parity of f_{CP} be η_f ($\eta_f = \pm 1$).

$$\mathcal{CP} |f_{CP}\rangle = \eta_f |f_{CP}\rangle \quad (\text{C.37})$$

In that special case four decay amplitudes and widths shown above reduce to two only. Moreover \bar{r} is in straightforward relation to r

$$\begin{aligned} \begin{array}{c} \mathcal{A}_f \\ \mathcal{A}_{\bar{f}} \end{array} & \begin{array}{c} \searrow \\ \nearrow \end{array} \mathcal{A}_{f_{CP}} & r & \longrightarrow & r_{CP} \\ \begin{array}{c} \bar{\mathcal{A}}_f \\ \bar{\mathcal{A}}_{\bar{f}} \end{array} & \begin{array}{c} \searrow \\ \nearrow \end{array} \bar{\mathcal{A}}_{f_{CP}} & \bar{r} & \longrightarrow & 1/r_{CP} \end{aligned} \quad (\text{C.38})$$

To determine the relation between decay amplitudes $\mathcal{A}_{f_{CP}}$ and $\bar{\mathcal{A}}_{f_{CP}}$ one may observe [139] that Hamiltonian which governs $\overset{(-)}{B}^0 \rightarrow f_{CP}$ transitions may be factorized with $\mathcal{H} = Vh + V^*h^\dagger$, where h (h^\dagger) are operators that annihilates B^0 (\bar{B}^0) and creates f_{CP} , V and V^* are relevant CKM matrix couplings. Since

CP violation occurs due to these couplings while CP transforms h into h^\dagger and vice versa (these may be observed in eq. (A.45)), the decay amplitudes satisfy

$$\mathcal{A}_{f_{CP}} = \langle f_{CP} | \mathcal{H} | B^0 \rangle = \sum_{\alpha} V_{\alpha} \langle f_{CP}, \alpha | h | B^0 \rangle \quad (\text{C.39})$$

$$\begin{aligned} &= \sum_{\alpha} M_{\alpha} e^{i\phi_{D\alpha}} e^{i\delta_{s\alpha}} \\ \bar{\mathcal{A}}_{f_{CP}} &= \langle f_{CP} | \mathcal{H} | \bar{B}^0 \rangle = \sum_{\alpha} V_{\alpha}^* \langle f_{CP}, \alpha | h^\dagger | \bar{B}^0 \rangle \quad (\text{C.40}) \\ &= \sum_{\alpha} V_{\alpha}^* \langle f_{CP}, \alpha | (\mathcal{CP})^\dagger (\mathcal{CP}) h^\dagger (\mathcal{CP})^\dagger (\mathcal{CP}) | \bar{B}^0 \rangle = \sum_{\alpha} V_{\alpha}^* \eta_f \langle f_{CP}, \alpha | h | B^0 \rangle \\ &= \sum_{\alpha} \eta_f M_{\alpha} e^{-i\phi_{D\alpha}} e^{i\delta_{s\alpha}} \end{aligned}$$

where the index α denotes a given partial decay amplitude; M_{α} are real factors (magnitudes of amplitudes); δ_s is strong phase; ϕ_D – weak phase due to decay. One could notice that *if only one weak phase contribute to the (full) amplitude* ($\phi_{D\alpha} = \phi_D$) the weak phase could be factorized⁶ and:

$$\begin{aligned} \frac{\bar{\mathcal{A}}_{f_{CP}}}{\mathcal{A}_{f_{CP}}} &= \eta_f \frac{e^{-i\phi_D}}{e^{i\phi_D}} = \eta_f e^{-2i\phi_D} \quad (\text{C.41}) \\ &= \eta_f \frac{V_{rb} V_{kl}^*}{V_{rb}^* V_{kl}} \end{aligned}$$

where the indexes r,k,l specify the flavours of the quarks involved in the underlying weak interaction.

Equations (C.41) and (C.17) allow us to calculate r_{CP}

$$r_{CP} = \eta_f e^{-2i(\Phi_M + \Phi_D)} = \eta_f \frac{V_{tb}^* V_{t\alpha}}{V_{tb} V_{t\alpha}^*} \cdot \frac{V_{rb} V_{kl}^*}{V_{rb}^* V_{kl}} \quad (\text{C.42})$$

Finally, the decay width for the initially produced B^0 (\bar{B}^0) to the same CP eigenstate f_{CP} is given by

$$\Gamma(B_{prod}^0(t) \rightarrow f_{CP}) = |\mathcal{A}_{f_{CP}}|^2 e^{-\gamma t} [1 - \text{Im} r_{CP} \sin \Delta m t], \quad (\text{C.43})$$

$$\Gamma(\bar{B}_{prod}^0(t) \rightarrow f_{CP}) = |\mathcal{A}_{f_{CP}}|^2 e^{-\gamma t} [1 + \text{Im} r_{CP} \sin \Delta m t]. \quad (\text{C.44})$$

The r_{CP} is invariant of CKM rephasing – it may be reexpressed in terms of CKM invariants $\Delta_{i\alpha}$ defined in Appendix B. Thus, if there is no CP violation, CKM matrix is real (in some particular representation) ϕ_M and ϕ_D vanish and $r_{CP} = \pm 1$. Thus in any parametrisation r_{CP} would be ± 1 with vanishing imaginary part. If it is not the case – CP is broken. Let us also notice that non vanishing $\text{Im} r_{CP}$ disturbs the rule of exponential decays (exponential decay

⁶Often, if there are two weak phases contributing to the amplitude, one can still extract CKM phases with the isospin analysis [140]–[142].

holds if one do not distinguish the flavour of initial B). Thus one may want to look at the time dependent asymmetry:

$$\begin{aligned}
 a(t) &= \frac{N(B_{prod}^0(t) \rightarrow f_{CP}) - N(\bar{B}_{prod}^0(t) \rightarrow f_{CP})}{N(B_{prod}^0(t) \rightarrow f_{CP}) + N(\bar{B}_{prod}^0(t) \rightarrow f_{CP})} \\
 &= \frac{N(B^0)\Gamma(B_{prod}^0(t) \rightarrow f_{CP}) - N(\bar{B}^0)\Gamma(\bar{B}_{prod}^0(t) \rightarrow f_{CP})}{N(B^0)\Gamma(B_{prod}^0(t) \rightarrow f_{CP}) + N(\bar{B}^0)\Gamma(\bar{B}_{prod}^0(t) \rightarrow f_{CP})} \\
 &= -\text{Im}r_{CP} \sin \Delta m t,
 \end{aligned} \tag{C.45}$$

or time integrated one:

$$\begin{aligned}
 A &= \frac{N(B_{prod}^0 \rightarrow f_{CP}) - N(\bar{B}_{prod}^0 \rightarrow f_{CP})}{N(B_{prod}^0 \rightarrow f_{CP}) + N(\bar{B}_{prod}^0 \rightarrow f_{CP})} \\
 &= \frac{\int_0^\infty N(B^0)\Gamma(B_{prod}^0(t) \rightarrow f_{CP})dt - \int_0^\infty N(\bar{B}^0)\Gamma(\bar{B}_{prod}^0(t) \rightarrow f_{CP})dt}{\int_0^\infty N(B^0)\Gamma(B_{prod}^0(t) \rightarrow f_{CP})dt + \int_0^\infty N(\bar{B}^0)\Gamma(\bar{B}_{prod}^0(t) \rightarrow f_{CP})dt} \\
 &= \frac{\Delta m/\gamma}{1 + (\Delta m/\gamma)^2}(-\text{Im}r_{CP}) = \frac{x}{1 + x^2}(-\text{Im}r_{CP}),
 \end{aligned} \tag{C.46}$$

The above equation express asymmetry in number of decays of initially produced B^0 (\bar{B}^0) to the same final state f_{CP} . One should notice that equations holds under the assumption that B^0 and \bar{B}^0 are produced in equal amounts.

The factor $x/(1 + x^2)$ ($x = x_d, x_s$) is smaller than one and its dilutes the asymmetry hence it is called the dilution factor due to integration (D_{int}) (note its absence in (C.45)).

The number of neutral B^0 decay channels is large but one may distinguish four classes:

- B_d decays with $b \rightarrow c\bar{c}s$ transitions
Events belonging to this class are very promising because of relatively big $b \rightarrow c$ primary decay probability and small value of x_d . They may be easy to detect if one looks for c quarks combining to J/ψ . The most important channel is $\overset{(-)}{B}_d^0 \rightarrow J/\psi K_S$ allowing us to measure the β angle of unitarity triangle. This channel is discussed in Section C.2.2.a
- B_d decays with $b \rightarrow u\bar{u}d$ transitions.
Events belonging to this class generally have smaller branching ratio of primary decay because of $b \rightarrow u$ quark transitions. However the primary decay may lead to easily detectable stable state. This compensates somewhat a small primary decay probability. An example of a channel in this class is $\overset{(-)}{B}_d^0 \rightarrow \pi^+\pi^-$, sensitive to the α angle
- B_s decays with $b \rightarrow u\bar{u}d$ transitions.
Decays in this class are sensitive to the γ angle but are very difficult to measure experimentally because of large value of x_s and small $b \rightarrow u$

transition probability. One possible decay mode is $B_s^0 \rightarrow \rho K_S$ with decay products which are difficult to identify, moreover the clean interpretation is disqualified by large contributions of penguin diagrams.

- B_s decays with $b \rightarrow c\bar{c}s$ transitions.

In $B_s^0 - \bar{B}_s^0$ system the calculation of $\text{Im}r_{CP}$ with $b \rightarrow c$ transitions gives zero in first order of Wolfenstein parameterisation of the CKM matrix.

The standard example of process belonging to this class is $B_s^0 \rightarrow J/\psi \phi$ (Section C.2.2.b) which is very similar kinematically to $B_d^0 \rightarrow J/\psi K_S$. Measuring vanishing (or small) asymmetry in this channel could be a test of consistency of The Standard Model.

C.2.2.a The $B_d \rightarrow J/\psi K_S$ channel

Main diagrams contributing to the $B_d^0(\bar{B}_d^0) \rightarrow J/\psi K_S$ decay are shown in Figure C.3. Weak couplings are proportional to $V_{cb}^*V_{cs}$ for B_d^0 decays, and to $V_{cb}V_{cs}^*$ in case of \bar{B}_d^0 . The q/p parameter in the $B_d^0 - \bar{B}_d^0$ system is (C.17):

$$\left(\frac{q}{p}\right)_d = \frac{V_{tb}^*V_{td}}{V_{tb}V_{td}^*}, \quad (\text{C.47})$$

thus the CP violating parameter r_{CP} becomes:

$$r_{CP} = \eta_{J/\psi K_S} \cdot \frac{V_{tb}^*V_{td}}{V_{tb}V_{td}^*} \cdot \frac{V_{cs}^*V_{cb}}{V_{cs}V_{cb}^*} \quad (\text{C.48})$$

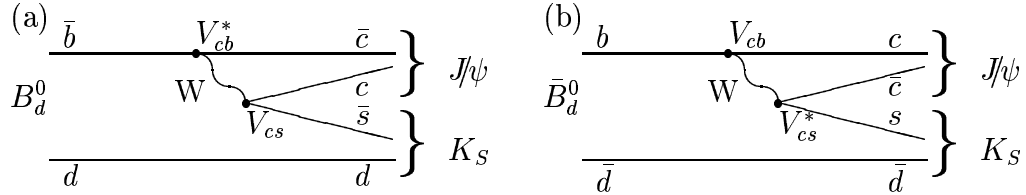


Figure C.3: $B_d^0 \rightarrow J/\psi K_S$ decay diagrams.

The calculation in the Wolfenstein parameterisation leads to:

$$\begin{aligned} \text{Im} \left[\frac{V_{tb}^*V_{td}}{V_{tb}V_{td}^*} \cdot \frac{V_{cs}^*V_{cb}}{V_{cs}V_{cb}^*} \right] &\approx \text{Im} \left[\frac{1 \cdot A\lambda^3(1 - \rho - i\eta)}{1 \cdot A\lambda^3(1 - \rho + i\eta)} \cdot \frac{(1 - \lambda^2/2) \cdot A\lambda^2}{(1 - \lambda^2/2) \cdot A\lambda^2} \right] \\ &= -2 \frac{\eta(1 - \rho)}{(1 - \rho)^2 + \eta^2} = -\sin 2\beta. \end{aligned} \quad (\text{C.49})$$

The J/ψ is a vector particle with quantum numbers $J^{PC} = 1^{--}$, with even CP parity. The K_S is a pseudo-scalar with $J^P = 0^-$. Since B_d^0 (\bar{B}_d^0) is a pseudo-scalar with spin zero the $J/\psi K_S$ from B_d decays has orbital momentum $L=1$. Neglecting CP-impurities of K_S one has:

$$\mathcal{CP} |J/\psi K_S\rangle = \eta_{J/\psi K_S} |J/\psi K_S\rangle = - |J/\psi K_S\rangle \quad (\text{CP odd state}). \quad (\text{C.50})$$

Finally the relations (C.45) and (C.46) could be written as:

$$\begin{aligned} a(t)_{B_d \rightarrow J/\psi K_S} &= \frac{\Gamma(B_d^0 \text{ prod}(t) \rightarrow J/\psi K_S) - \Gamma(\bar{B}_d^0 \text{ prod}(t) \rightarrow J/\psi K_S)}{\Gamma(B_d^0 \text{ prod}(t) \rightarrow J/\psi K_S) + \Gamma(\bar{B}_d^0 \text{ prod}(t) \rightarrow J/\psi K_S)} \\ &= -\sin 2\beta \sin \Delta m t \end{aligned} \quad (\text{C.51})$$

$$\begin{aligned} A_{B_d \rightarrow J/\psi K_S} &= \frac{N(B_d^0 \text{ prod} \rightarrow J/\psi K_S) - N(\bar{B}_d^0 \text{ prod} \rightarrow J/\psi K_S)}{N(B_d^0 \text{ prod} \rightarrow J/\psi K_S) + N(\bar{B}_d^0 \text{ prod} \rightarrow J/\psi K_S)} \\ &= -\frac{x_d}{1+x_d^2} \sin 2\beta \end{aligned} \quad (\text{C.52})$$

C.2.2.b The $B_s \rightarrow J/\psi \phi$ channel

The main diagrams contributing to the $B_s^0(\bar{B}_s^0) \rightarrow J/\psi \phi$ are shown in Figure C.4. The weak couplings appearing in the $\Delta B = \pm 1$ transitions are characterised by $V_{cb}^* V_{cs}$ ($V_{cb} V_{cs}^*$) for the decays of \bar{B}_s^0 (B_s^0). The q/p parameter in $B_s^0 - \bar{B}_s^0$ is (C.17):

$$\left(\frac{q}{p}\right)_s = \frac{V_{tb}^* V_{ts}}{V_{tb} V_{ts}^*}, \quad (\text{C.53})$$

thus the CP violating parameter r_{CP} becomes:

$$r_{CP} = \eta_{J/\psi \phi} \cdot \frac{V_{tb}^* V_{ts}}{V_{tb} V_{ts}^*} \cdot \frac{V_{cs}^* V_{cb}}{V_{cs} V_{cb}^*} \quad (\text{C.54})$$

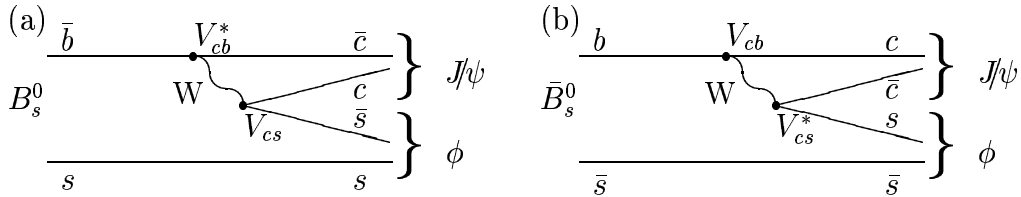


Figure C.4: $B_s^0 \rightarrow J/\psi \phi$ decay diagrams.

The calculation in the first order Wolfenstein parameterisation involves only real elements of CKM matrix. In this approximation asymmetry vanishes. More careful calculations (let us use the higher order Wolfenstein parameterisation (B.8)) leads to (phases are involved in V_{ts}):

$$\begin{aligned} \text{Im} \left[\frac{V_{tb}^* V_{ts}}{V_{tb} V_{ts}^*} \cdot \frac{V_{cs}^* V_{cb}}{V_{cs} V_{cb}^*} \right] &\approx \text{Im} \left[\frac{-A\lambda^2(1 + \frac{1}{2}\lambda^2(2\rho - 1) + i\lambda^2\eta)}{-A\lambda^2(1 + \frac{1}{2}\lambda^2(2\rho - 1) - i\lambda^2\eta)} \right] \\ &\approx 2\lambda^2\eta \approx 2\lambda^2\sqrt{\rho^2 + \eta^2} \sin \gamma \end{aligned} \quad (\text{C.55})$$

Since ϕ is a vector particle with quantum numbers same as J/ψ the $J/\psi \phi$ may form states with angular momentum $L = 0, 1, 2$. Thus both CP even

($L = 0, 2$) and CP odd ($L = 1$) amplitudes may contribute to the investigated asymmetries, diluting the effect. Nevertheless, with the help of angular distributions analysis one may separate (statistically) the longitudinally (CP even) and transverse polarised (parallel – CP even; perpendicular – CP odd) amplitudes [143]. The separation of these three components would reduce the dilution effect.

The angular analysis of the investigated decay was performed recently by CDF and the fraction of longitudinally polarisation events was measured [144]:

$$\frac{\Gamma_L}{\Gamma} = 0.56 \pm 0.21 \begin{smallmatrix} + 0.02 \\ - 0.04 \end{smallmatrix} \quad (\text{C.56})$$

The measurements of polarisation in $B_d \rightarrow J/\psi K^*$ suggests even larger contamination of CP even amplitude. With the assumption that

$$\mathcal{CP}|J/\psi\phi\rangle = +|J/\psi\phi\rangle \quad (\text{CP even dominance}) \quad (\text{C.57})$$

the time dependent and time integrated asymmetry become:

$$\begin{aligned} a(t)_{B_s \rightarrow J/\psi\phi} &= \frac{\Gamma(B_s^0 \text{ prod}(t) \rightarrow J/\psi\phi) - \Gamma(\bar{B}_s^0 \text{ prod}(t) \rightarrow J/\psi\phi)}{\Gamma(B_s^0 \text{ prod}(t) \rightarrow J/\psi\phi) + \Gamma(\bar{B}_s^0 \text{ prod}(t) \rightarrow J/\psi\phi)} \\ &= -2\lambda^2\eta \sin \Delta m t \end{aligned} \quad (\text{C.58})$$

$$\begin{aligned} A_{B_s \rightarrow J/\psi\phi} &= \frac{N(B_s^0 \text{ prod} \rightarrow J/\psi\phi) - N(\bar{B}_s^0 \text{ prod} \rightarrow J/\psi\phi)}{N(B_s^0 \text{ prod} \rightarrow J/\psi\phi) + N(\bar{B}_s^0 \text{ prod} \rightarrow J/\psi\phi)} \\ &= -\frac{x_s}{1 + x_s^2} 2\lambda^2\eta \end{aligned} \quad (\text{C.59})$$

Appendix D

The credibility of simulation

The¹ reliability of the PYTHIA event generator predictions have deep consequences for the required detector performance. Therefore the efforts were taken to check whether PYTHIA predictions agree with the existing data taken at hadron machines. Especially, the muon and b -quark spectra were compared with experimental results from UA1, CDF and D0. For this comparison, the 5.7 version of PYTHIA was used with the CTEQ2L (PYTHIA default) structure functions.

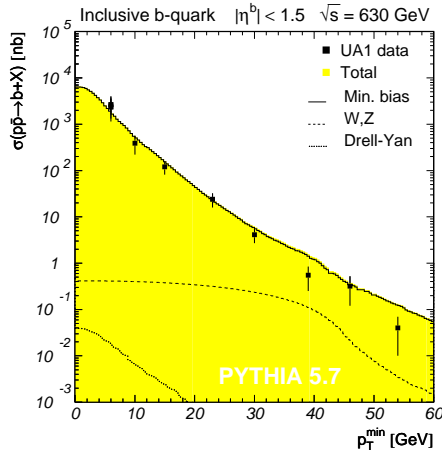


Figure D.1: Cross section for the integrated inclusive b -quark production in $|\eta^b| < 1.5$ at the SPS energy of $\sqrt{s} = 630$ GeV. At the top of PYTHIA predictions the UA1 data are shown. Figure taken from [145].

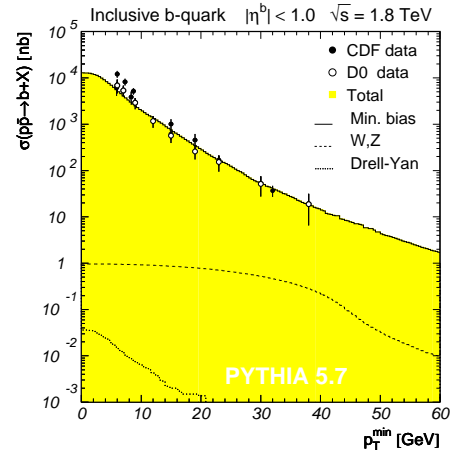


Figure D.2: Cross section for the integrated inclusive b -quark production in $|\eta^b| < 1.0$ at the Tevatron energy of $\sqrt{s} = 1.8$ TeV. At the top of PYTHIA predictions CDF and D0 data are shown. Figure taken from [145].

¹This Appendix refers to the work done by M.Ćwiok and G.Wrochna, described with more detail in [145].

Several samples of minimum bias events were simulated with varying kinematical cuts at $\sqrt{s}=630$ and 1800 GeV. At the top of that the rare processes were superimposed. The samples were normalise to the cross sections calculated internally in PYTHIA. The results for b -quark spectra are shown in Figures D.1-D.2. The PYTHIA follows UA1 points with satisfactory precision, D0 data are well reproduced whereas the CDF cross section at low p_t 's surpasses the PYTHIA one. The results for muonic spectra are shown in Figures D.3-D.4. In order to obtain better agreement with experimental data the muonic spectra were smeared to fake the detector resolution. Generally, both the D0 and UA1 data match well with PYTHIA 5.7.

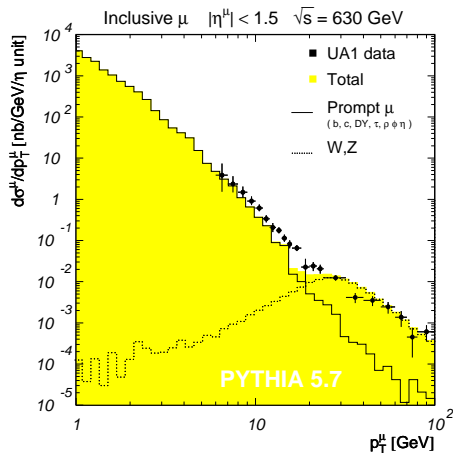


Figure D.3: The differential cross section for the inclusive muon production $p\bar{p} \rightarrow \mu X$ in $|\eta| < 1.5$ at the SPS energy $\sqrt{s} = 630$ GeV. The PYTHIA predictions are compared with UA1 data. The π/K contribution is not included. Figure taken from [145].

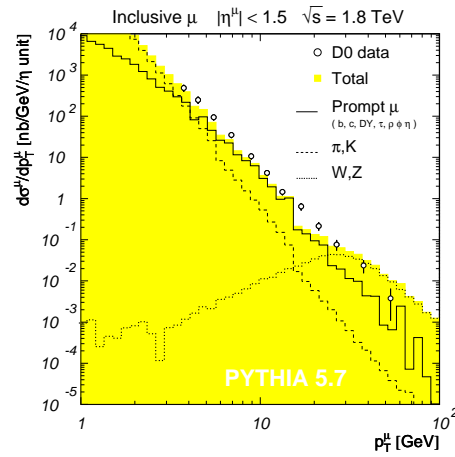


Figure D.4: The differential cross section for the inclusive muon production $p\bar{p} \rightarrow \mu X$ in $|\eta| < 1.5$ at the Tevatron energy $\sqrt{s} = 1.8$ TeV. The PYTHIA predictions are compared with the D0 data. Figure taken from [145].

Acknowledgements

First of all I would like to thank my supervisor, professor *Jan Królikowski* who guided me through the field of experimental physics, serving his patience and support since I met him as an undergraduated student in 1990. He introduced me to the CMS collaboration giving an opportunity to contribute to the RPC trigger project and motivated me in having "a closer look" at the CP violating phenomena. He gave me substantial degree of freedom in my research. My aspiration to continue to be a particle physicist is partially his merit.

I am very grateful to *Grzegorz Wrochna*, always ready to help, for the long fruitful discussions, common work, reading this thesis and much more.

I would like to thank *Daniel Denegri* – the head of CMS physics group for worm admission, bright comments and inspiration. I am very thankful to all my colleagues from *B*-physics group for enjoyable collaboration and helpful discussions. I would like to mention the group leader *Yves Lemoigne*, *Andrei Starodumov*, *Avto Kharchilava* and *Pascal Pralavorio*.

I would like to thank professor *Bohdan Grzadkowski* for his comments to the phenomenological appendices.

This work was supported in part by polish KBN grants.

Bibliography

- [1] S. L. Glashow, *Nucl. Phys.* **10** (1959) 107; *Nucl. Phys.* **22** (1961) 579.
- [2] S. Weinberg, *Phys. Rev. Lett.* **19** (1967) 1264.
- [3] A. Salam, in *Proc. 8th Nobel Symposium, Aspenäsgråden*,
ed. N. Svartholm, (Almqvist and Wiksell, Stockholm, 1968) 367.
- [4] M. Gell-Mann, *Acta Phys. Austriaca* Suppl. IX (1972) 733.
- [5] H. Fritzsch and M. Gell-Mann, in *Proc. 16th Int. Conf. on High Energy
Physics, Batavia, 1972* (NAL, Batavia, Ill., 1973) Vol. 2, 135.
- [6] H. Fritzsch, M. Gell-Mann and H. Leutwyler, *Phys. Lett.* **47B** (1973)
365.
- [7] P. W. Higgs, *Phys. Rev. Lett.* **12** (1964) 132.
- [8] F. Englert and R. Brout, *Phys. Rev. Lett.* **13** (1964) 321.
- [9] P. W. Higgs, *Phys. Rev.* **145** (1966) 1156.
- [10] T. D. Lee and C. N. Yang, *Phys. Rev.* **104** (1956) 254.
- [11] C. S. Wu et al., *Phys. Rev.* **105** (1957) 1413.
- [12] J. H. Christenson, J. W. Cronin, V. L. Fitch and R. Turlay, *Phys. Rev.
Lett.* **13** (1964) 138.
- [13] L. Wolfenstein, *Phys. Rev. Lett.* **13** (1964) 562.
- [14] J. M. Gillard et al., *Phys. Rev. Lett.* **18** (1967) 20.
- [15] J. Cronin et al., *Phys. Rev. Lett.* **18** (1967) 25.
- [16] S. Bennett et al., *Phys. Rev. Lett.* **19** (1967) 993.
- [17] D. Dorfman et al., *Phys. Rev. Lett.* **19** (1967) 987.
- [18] *CP violation*, ed. C. Jarlskog (World Scientific, Singapore, 1989).
- [19] A. D. Sakharov, *ZhETF pis. Red.* **5** (1967) 32; *JETP Lett.* **5** (1967) 24.

- [20] G. C. Callan, R. Dashen, D. Gross, *Phys. Lett.* **63B** (1976) 334.
- [21] R. Jackiw and C. Rebbi, *Phys. Rev. Lett.* **37** (1976) 172.
- [22] R. D. Peccei, in [18].
- [23] M. Kobayashi and T. Maskawa, *Prog. Theor. Phys.* **49** (1973) 652.
- [24] N. Cabibbo, *Phys. Rev. Lett.* **10** (1963) 531.
- [25] Barr et al., (NA31 coll.) *Phys. Lett.* **B317** (1993) 233.
- [26] Gibbons et al., (E731 coll.) *Phys. Rev. Lett.* **70** (1993) 1203.
- [27] Daniel Denegri, private communications.
- [28] T. Sjöstrand, *Comput. Phys. Commun.* 82 (1994) 74; preprint LU TP 95-20, CERN-TH.7112/93 (1993, revised August 1995)
- [29] *Review of Particle Physics*, ed. E. J. Weinberg and D. L. Nordstorm, *Phys. Rev.* **D54** (1996).
- [30] *ECFA-CERN Workshop on the Large Hadron Collider in the LEP Tunnel* (Lausanne and Geneva, 1984), ECFA 84/85, CERN 84-10.
- [31] *Proceedings of the Large Hadron Collider Workshop*, ed. G. Jarlskog and D. Rein (Aachen, 4-9 October 1990), CERN 90-10, ECFA 90-133.
- [32] *Design Study of the Large Hadron Collider*, CERN 91-03 (1991).
- [33] *The Large Hadron Collider Accelerator project*, CERN AC/93-03 (1993).
- [34] *The Large Hadron Collider - Conceptual Design*, ed. P. Lefevre and T. Pettersson, CERN/AC/95-05 (1995).
- [35] CERN press releases of 16 Dec 1994.
- [36] D. Denegri, in [31], vol 1, p. 56.
- [37] F. Pauss, in [31], vol 1, p. 118.
- [38] G. Altarelli, in [31], vol 1, p. 153.
- [39] H. P. Nilles, *Phys. Rep.* **110** (1984) 1.
- [40] H. Haber, G. Kane, *Phys. Rep.* **117** (1985) 75.
- [41] R. Barbieri, *Riv. Nuovo Cimento* **11** (1988) 1.
- [42] A. B. Lahanas and D. V. Nanopoulos, *Phys. Rep.* **145** (1987) 1.
- [43] *CMS Technical Proposal* CERN/LHCC 94-38, LHCC/P1, 1994.

- [44] R. Casalbuoni et al., *Phys. Lett.* **B155** (1985) 95; *Nucl. Phys.* **B282** (1987) 235.
- [45] A. Dobado and M. J. Herrero, *Phys. Lett.* **B228** (1989) 495; *Phys. Lett.* **B233** (1989) 505.
- [46] A. Dobado, M. J. Herrero and J. Terron, *Z. Phys* **C50** (1991) 205; *Z. Phys* **C50** (1991) 465.
- [47] G. G. Ross and F. Zwirner, in [31], vol 2, p. 605.
- [48] Feldman, SLAC-PUB-2839 (1981).
- [49] K. Winter, in [31], vol 2, p. 37.
- [50] P. Ciappetta and M. Greco, in [31], vol 2, p. 685.
- [51] S. Dimopoulos and M. Linder, in [31], vol 2, p. 758.
- [52] *Atlas Letter of Intent for a General-Purpose pp Experiment at the Large Hadron Collider at CERN*, CERN/LHCC 92-4, LHCC/I2 (1992).
- [53] *CMS Letter of Intent*, CERN/LHCC 92-3, LHCC/I1 (1992).
- [54] *ALICE Letter of Intent*, CERN/LHCC 93-16 (1993),
- [55] *LHC-B Letter of Intent*, CERN/LHCC 95-5, LHCC/I8 (1995),
- [56] M. Pimiä et al., in [31], vol 3, p. 547.
- [57] *CMS Expression of Interest*, in *Proceedings of the General Meeting on LHC Physice and Detectors* Evian (1992), p. 165.
- [58] Recommendations of the LHC committee, CERN/LHCC 93-31 (1993).
- [59] CMS Bulletin 97-03.
- [60] Tracker Layout Optimisation Group, CMS note CMS-NOTE 1996/013.
- [61] P. Billoir, *Nucl. Instrum. Meth.* **A225** (1984) 352,
R. Frühwirth, *Nucl. Instrum. Meth.* **A262** (1987) 444,
P. Billoir and S. Qian, *Nucl. Instrum. Meth.* **A294** (1990) 219,
P. Billoir and S. Qian, *Nucl. Instrum. Meth.* **A295** (1990) 492.
- [62] A. Khanow and N. Stepanov, CMS note CMS-TN/94-181; CMS note CMS-TN/94-309.
- [63] J. F. Hassard and S. Margetides, *Tracking for B Physics in CMS*, in *Snowmass Meeting on B Physics in Hadron Colliders*, 1993.
- [64] F. D. van der Berg et al., *Nucl. Instrum. Meth.* **A349** (1994) 438.

- [65] N. Stepanov, presented at CMS B -physics internal meeting.
- [66] M. Konecki, CMS note CMS-TN/96-105.
- [67] A. De Rujula et al., in [31], vol 2, p. 201.
- [68] D. Denegri, Y. Lemoigne, A. Fridman, C. Racca, A. Rubbia, G. Wrochna, J. Hassard, S. Margetides, T. S. Virdee V. Karimaki, M. Pimia, A. Karchilava, M. Konecki, N. Neumeister, N. Sinanis, A. Starodumov, *International Journal of Modern Physics A*, Vol.9, No.24 (1994) 4211.
- [69] M. Konecki and A. Starodumov, CMS note CMS-TN/94-237.
- [70] D. Denegri, M. Konecki, A. Rubbia and A. Starodumov, *Nucl. Instrum. Meth.* **A351** (1994) 95; CMS note CMS-TN/94-229.
- [71] M. Konecki and A. Starodumov, *$b\bar{b}$ Events Simulation Package, Users Manual*, available on WWW under <http://cmsdoc.cern.ch/user/b/bphys/BPHYS/TNCMS/manual.ps>
- [72] J. Botts et al., *Phys. Lett.* **B304** (1993) 159.
- [73] C. Peterson et al., *Phys. Rev.* **D27** (1983) 218.
- [74] M. Konecki, J. Królikowski and G. Wrochna, CMS note CMS-TN/96-104.
- [75] V. Karimaki, CMS note CMS-TN/94-275.
- [76] L. K. Gibbons, in *Proceedings of the 28th International Conference on High Energy Physics*, ed. Z. Ajduk and A. K. Wróblewski, World Scientific, Singapore (1997), p. 183.
- [77] D. Denegri, CMS note CMS-TN/95-167, preprint CERN-PPE/95-183.
- [78] A. Kharchilava and P. Pralavorio, CMS note CMS-TN/96-116.
- [79] A. Kharchilava, *Nucl. Instrum. Meth.* **A384** (1996) 100.
- [80] A. Starodumov, CMS note CMS-TN/96-108.
- [81] F. Charles, CMS note CMS-CR 1996/009.
- [82] A. Starodumov, CMS note CMS-NOTE 1997/072.
- [83] R. Kinnunen and D. Denegri, CMS note CMS-NOTE 1997/057.
- [84] R. Kinnunen and D. Denegri, CMS note CMS-TN/96-045.
- [85] K. Kleinknecht, *Nucl. Instrum. Meth.* **A384** (1996) 253.
- [86] A. Pich, preprint FTUV/94-62, IFIC/94-59, hep-ph/9412274.

- [87] C. Jarlskog, CERN Yellow Report CERN 82-04 (1982) 63; CERN Yellow Report CERN 85-11 (1985) 277; CERN Yellow Report CERN 85-11 (1985) 260.
- [88] J. F. Donoghue, E. Golowich and B. R. Holstein, *Dynamics of the Standard Model* (Cambridge Univ. Press, 1992).
- [89] S. Rudaz, CERN Yellow Report CERN 87-02 (1987) 1.
- [90] C. Jarlskog, in [18] p. 3.
- [91] D. H. Perkins, *Introduction to High Energy Physics*, 3rd edition, (Addison-Wesley, 1987), p. 84.
- [92] L.-L. Chau and W.-Y. Keung, *Phys. Rev. Lett.* **53** (1984) 1802.
- [93] Z. Z. Xing, preprint LMU-21/94, hep-ph 9411340 (1994).
- [94] C. Jarlskog, *Phys. Rev. Lett.* **55** (1985) 1039.
- [95] I. Dunietz, O. W. Greenberg and D. D. Wu, *Phys. Rev. Lett.* **55** (1985) 2935.
- [96] D. D. Wu, *Phys. Rev.* **D33** (1986) 860.
- [97] D. Du, I. Dunietz, D. Wu, *Phys. Rev.* **D34** (1986) 3414.
- [98] C. Jarlskog and R. Stora, *Phys. Lett.* **B208** (1988) 268.
- [99] A. Ali and D. London, preprint DESY 95-148, UdeM-GPP-TH-95-32.
- [100] A. Ali and D. London preprint DESY 96-140, UdeM-GPP-TH-96-38.
- [101] A. Ali, preprint DESY 96-248.
- [102] T. Skwarnicki, preprint hep-ph/9512395.
- [103] M. Artuso, *Nucl. Instrum. Meth.* **A384** (1996) 39.
- [104] A. Pilaftsis, preprint hep-ph/9606322.
- [105] E. H. Thorndike, *Ann. Rev. Nucl. Part. Sci.* **35** (1985) 195.
- [106] I. Dunietz and J. L. Rosner, *Phys. Rev.* **D34** (1986) 1404.
- [107] R. Aleksan et al., in *ECFA Workshop on a European B-Meson Factory*, ed. R. Aleksan and A. Ali, ECFA 93/151, p. 9.
- [108] M. Neubert, preprint CERN-TH/96-55, hep-ph/9604412.
- [109] H. R. Quinn, in [29], p. 507.

- [110] A. Buras and R. Fleischer, preprint TUM-HEP-275/97, TTP97-15, hep-ph/9704376.
- [111] A. B. Carter and A. I. Sanda, *Phys. Rev.* **D23** (1981) 1567.
- [112] A. Pais and S.B. Treiman, *Phys. Rev.* **D12** (1975) 2744.
- [113] M. Bander, D. Silerman and D. Soni, *Rev. Lett.* **43** (1979) 242.
- [114] C. Bernabeu and C. Jarlskog, *Z. Phys.* **C8** (1981) 233.
- [115] A. B. Carter and A. I. Sanda, *Phys. Rev. Lett.* **45** (1980) 952.
- [116] I. I. Bigi and A. I. Sanda, *Nucl. Phys.* **B193** (1981) 85.
- [117] M. Gronau and D. Wyler, *Phys. Lett.* **B265** (1991) 172.
- [118] C. Albajar et al. (UA1 collaboration), *Phys. Lett.* **B186** (1987) 247.
- [119] H. Albrecht et al. (ARGUS collaboration), *Phys. Lett.* **B192** (1987) 245.
- [120] H. Albrecht et al. (ARGUS collaboration), *Z. Phys.* **C55** (1992) 357.
- [121] Bartelt et al. (CLEO collaboration), *Phys. Rev. Lett.* **71** (1993) 1680.
- [122] H. Albrecht et al. (ARGUS collaboration), *Phys. Lett.* **B324** (1994) 249.
- [123] D. Buskulic et al. (ALEPH collaboration), *Phys. Lett.* **B356** (1995) 409.
- [124] Abreu et al. (DELPHI collaboration), *Phys. Lett.* **B322** (1994) 459.
- [125] Acciarri et al. (L3 collaboration), *Phys. Lett.* **B335** (1994) 542.
- [126] D. Buskulic et al. (ALEPH collaboration), *Z. Phys.* **C61** (1994) 179.
- [127] Akers et al. (OPAL collaboration), *Z. Phys.* **C60** (1993) 199.
- [128] Abe et al. (CDF collaboration), *Phys. Rev. Lett.* **67** (1991) 3351.
- [129] Albajar et al. (UA1 collaboration), *Phys. Lett.* **B262** (1991) 171.
- [130] K. Honscheid, in [29], p. 477.
- [131] M. K. Gillard and B. W. Lee, *Phys. Rev.* **D10** (1974) 897.
- [132] D. Wu, *Phys. Lett.* **B90** (1980) 451.
- [133] J. Ellis, M. K. Gillard, D. V. Nanopoulos and S. Rudaz, *Nucl. Phys.* **B131** (1977) 285.
- [134] J. S. Hagelin, *Nucl. Phys.* **B193** (1981) 123.

- [135] T. Inami and C. S. Lim, *Prog. Theor. Phys.* **65** (1981) 297; *Prog. Theor. Phys.* **65** (1981) 1772.
- [136] A. J. Buras, W. Słonimski and H. Steger, *Nucl. Phys.* **B245** (1984) 369.
- [137] A. Pich, preprint FTUV/95-50, IFIC/95-52, hep-ph/9601202.
- [138] Bartelt et al. (CLEO coll.), *Phys. Rev. Lett.* **71** (1993) 1680.
- [139] I. Dunietz, *Phys. Rev.* **D52** (1997) 3048.
- [140] Y. Nir and H. R. Quinn, in *B-decays*, ed. S. Stone, (World Scientific, Singapore 1992), p. 362.
- [141] M. Gronau and D. London, *Phys. Rev. Lett.* **65** (1990) 3381.
- [142] Y. Nir and H. R. Quinn, *Phys. Rev. Lett.* **67** (1991) 541.
- [143] A. S. Dighe, I. Dunietz, H. J. Lipkin and J. L. Rosner, *Phys. Lett.* **B369** (1996) 144.
- [144] Abe et al., *Phys. Rev. Lett.* **75** (1995) 3068.
- [145] M. Ćwiok, G. Wrochna, CMS note CMS-TN/95-150 (1995).

